Fall 1989

The effect of reagent rotation on gas phase reactions

Judith Agnes Harrison
University of New Hampshire, Durham

Order Number 9004862

The effect of reagent rotation on gas phase reactions

Harrison, Judith Agnes, Ph.D.

University of New Hampshire, 1989

U·M·I

300 N. Zeeb Rd.
Ann Arbor, MI 48106

THE EFFECT OF REAGENT ROTATION ON GAS PHASE REACTIONS

BY

Judith A. Harrison
B.A. Saint Anselm College, 1984

DISSERTATION

Submitted to the University of New Hampshire
in Partial Fulfillment of
the Requirements for the Degree of

Doctor of Philosophy
in
Chemistry

September, 1989

This dissertation has been examined and approved.

Dissertation director, Howard R. Mayne
Assistant Professor of Chemistry

Christopher F. Bauer
Associate Professor of Chemistry

Frank L. Pilar
Professor of Chemistry

Gary R. Weisman
Associate Professor of Chemistry

Harvey K. Shepard
Professor of Physics

June 22, 1989
Date

DEDICATION

This work is dedicated to my parents, Robert J. and Dorothea M. Harrison. They have given me many things over the years. This work is my gift to them.

ACKNOWLEDGEMENTS

First and foremost, I would like to thank Dr. Howard R. Mayne for his patience, careful guidance, and advice throughout the course of my studies. There were many occasions which Dr. Mayne took time away from his personal life in order to work with me on one project or another. I feel it is this quality which makes him an extraordinary professor.

I would also like to thank the Graduate School of the University of New Hampshire for the monetary support which I received in my final year of graduate work.

Finally, I would like to thank my good friend, Heidi Wentrup, for helping me with the preparation of this manuscript.

TABLE OF CONTENTS

DEDICATION..... iii

ACKNOWLEDGEMENTS..... iv

LIST OF FIGURES..... vii

LIST OF TABLES..... xiv

ABSTRACT..... xv

CHAPTER I PAGE

INTRODUCTION..... 1

CHAPTER II.

Introduction..... 9

Model Description..... 9

Reduced Potential..... 13

Analytical Form of the Reduced Potential..... 17

CHAPTER III

Introduction..... 47

Exact Scattering Formalism..... 52

Approximate Scattering Formalism..... 66

Results and Discussion..... 74

CHAPTER IV

Introduction..... 96

Model Classical Trajectories: Method of Calculation..... 99

Comparison of Classical and Quantal Results.... 101

Classical Centrifugal Sudden..... 103

Classical Infinite Order Sudden..... 104

Comparison of Classical Exact and Approxiamate Results..... 105

Conclusions..... 115

CHAPTER V

Introduction..... 144

Classical Trajectories: Method of Calculation.. 147

Model Trajectories: Method of Calculation..... 148

Results and Discussion..... 148

Conclusions..... 164

CHAPTER VI

Introduction..... 216

Results and Discussion..... 219

Conclusions..... 231

APPENDICES..... 266

LIST OF REFERENCES..... 320

LIST OF FIGURES

FIGURE		PAGE
II.1	Jacobi coordinates for an atom-diatom reaction	22
II.2	Center of mass coordinates for a diatom-diatom reaction.....	24
II.3	Contour plot of the SE1 surface in skewed coordinates.....	26
II.4	Schematic representation of a LEPS surface in skewed coordinates.....	28
II.5	Contour plot of the LEPS I, O+HCl surface in skewed coordinates.....	30
II.6	Contour plot of the symmetric reduced potential.	32
II.7	Contour plot of the reduced SE1 surface.....	34
II.8	Contour plot of the SE1 surface in (s,γ) coordinates.....	36
II.9	Contour plot of the reduced SE4 surface.....	38
II.10	Contour plot of the SE4 surface in (s,γ) coordinates.....	40
II.11	Contour plot of the RB and the SE surfaces in (s,θ) coordinates.....	42
II.12	Contour plot of the RB and the SE surfaces in (s,ϕ) coordinates.....	44
III.1	Exact quantum mechanical reaction probabilities as a function of E_t with J=j=0.....	79

III.2 Exact quantum $P^R(j)$ with $J = j$..... 81

III.3 Exact quantum reaction probabilities as a function of total angular momentum with j=0.... 83

III.4 Exact quantum $P^R(j)$ with $J \neq j$..... 85

III.5 Centrifugal Sudden, CS, $P^R(j)$ with $J \neq j$..... 87

III.6 Infinite Order Sudden, IOS, $P^R(j)$ for $J \neq j$.. 89

IV.1 Exact classical and exact quantal $P^R(j)$ with $J = j$..... 121

IV.2 Exact classical and exact quantal probabilities of reaction as a function of J with j =0..... 123

IV.3 Exact classical and exact quantal $P^R(j)$ for $J \neq j$..... 125

IV.4 Exact, CCS and CIOS $P^R(j)$ for the **L + LL** mass combination at 0.15 eV..... 127

IV.5 Exact, CCS and CIOS $P^R(j)$ for the **L + LL** mass combination at 0.35 eV..... 129

IV.6 Exact, CCS and CIOS $P^R(j)$ with l = 0 for the **L + HH** mass combination at 0.15 eV..... 131

IV.7 Exact, CCS and CIOS $P^R(j)$ with l = 0 for the **H + LL** mass combination at 0.15 eV..... 133

IV.8 Exact, CCS, and CIOS $P_R(j)$ for the **L + LL**, **L + HH**, and the **H + LL** mass combinations with $B_o = 0.82$ and $B_o = 2.45$ eV..... 135

IV.9 CIOS probabilities of reaction as a function of rotational energy, $P^R(E_j)$, for the **L + LL** mass combination at 0.15 eV and fixed a..... 137

IV.10 CIOS probabilities of reaction as a function of rotational energy for the L + LL mass combination at 0.15 eV at fixed B_o and a = 1.0..... 139

IV.11 CIOS probabilities of reaction as a function of rotational energy for the L + LL mass combination at 0.15 eV at fixed B_o and a = 0.0. 141

IV.12 Geometrical interpretation of the orientational and the energy effects..... 143

V.1 Reactive cross sections as a function of j, $S^R(j)$, on the SE1 surface..... 167

V.2 Reactive cross sections as a function of j on the SE4 surface..... 169

V.3 Reaction cross sections as a function of rotational energy for the SE1 surface..... 171

V.4 Probabilities of reaction as a function of j on the reduced SE1 surface..... 173

V.5 Probabilities of reaction as a function of j on the reduced SE4 surface..... 175

V.6 Probabilities of reaction as a function of j on the reduced SE1 surface for fixed c_o..... 177

V.7 Probabilities of reaction as a function of j on the reduced SE4 surface for fixed c_o..... 179

V.8 Probabilities of reaction as a function of j on the SE1 surface for fixed l..... 181

V.9 Probabilities of reaction as a function of j on the SE4 surface for fixed l..... 183

V.10 Reactive cross sections for 3D trajectories and trajectories which had the diatomic molecule initially polarized on both the SE1 and the SE4 surfaces..... 185
V.11 Probabilities of reaction as a function of j for coplanar trajectories on the SE1 surface at fixed l..... 187
V.12 Probabilities of reaction as a function of j for coplanar trajectories on the SE4 surface at fixed l..... 189
V.13 Probabilities of reaction as a function of j on the reduced SE1 surface for fixed l..... 191
V.14 Probabilities of reaction as a function of j on the reduced SE4 surface for fixed l..... 193
V.15 Differential cross sections for $F+H_2(0,j)$ on the SE1 surface..... 195
V.16 Differential cross sections for $F+H_2(0,j)$ on the SE4 surface..... 197
V.17 Opacity functions for $F+H_2(0,j)$ on both the SE1 and the SE4 surfaces..... 199
V.18 Maximum impact parameter leading to reaction as a function of j for $F+H_2(0,j)$ on both the SE1 and the SE4 surfaces..... 201
V.19 Product rotational distributions on the SE1 surface..... 203
V.20 Product rotational distributions on the SE4

surface..... 205
V.21 First moments of the HF and the DF product rotational quantum number versus j on the SE1 surface..... 207
V.22 First moments of the HF and the DF product rotational quantum number versus j on the SE4 surface..... 209
V.23 Product rotational distributions for coplanar trajectories on the SE1 surface..... 211
V.24 Product rotational distributions for coplanar trajectories on the SE4 surface..... 213
V.25 Product rotational distributions for $F+H_2(0,j)$ at fixed center of mass scattering angle on the SE1 surface..... 215
VI.1 Reaction cross sections as a function of j' for the $OH(0,0) + H_2(0,j')$ reaction on the RB surface..... 234
VI.2 Reaction cross sections as a function of j for the $OH(0,j) + H_2(0,0)$ reaction on the RB surface..... 236
VI.3 Reaction cross sections as a function of j for the $OH(0,j) + H_2(0,0)$ reaction on the SE surface..... 238
VI.4 Contour plot of the RB-V42 surface in (s,θ) coordinates..... 240

VI.5 Probabilities of reaction as a function of j for coplanar b = 0 trajectories on the RB and the RB-V42 surface..... 242
VI.6 Reaction cross sections as a function of j for 3D trajectories on the RB-V42 surface with the classical vibrational quantum number of both diatoms set to -1/2..... 244
VI.7 Reaction probabilities as a function of j for the RB model system..... 246
VI.8 Schematic contour plot showing the effect of bumps in the entrance valley of the RB model. 248
VI.9 Reaction probabilities as a function of j for the SE model system..... 250
VI.10 Schematic contour plot showing the effect of wells in the entrance valley of the SE model. 252
VI.11 Reaction cross sections as a function of j for isotopically substituted H in OH for the RB surface..... 254
VI.12 Reaction cross sections as a function of j for $OX(0,j) + H_2(0,0)$ where X is muonium..... 256
VI.13 Classical rotational quantum number at the max/min in the $S^R(j)$ function versus the mass of the isotopically substituted H in OH..... 258
VI.14 Reaction probabilities as a function of j for the isotopically substituted H in OH

for the model RB potential..... 260

VI.15 Reaction cross sections as a function of j for the reaction OH(0,j) + HD(0,0) on the RB surface..... 262

VI.16 Reaction cross sections as a function of j for the reaction OH(0,0) + HD(0,j') on the RB surface..... 264

A.1 Transformation from Jacobi coordinates to internuclear coordinates for an atom-diatom system..... 286

A.2 Pictorial representations of the polarization of the angular momentum vector of a diatom... 288

A.3 Definition of reagent and product Jacobi coordinates for the reaction A+BC --> AB + C. 290

A.4 Center of mass and internuclear coordinates for a diatom - diatom reaction (AB+CD)..... 292

B.1 Schematic representation of a LEPS potential in rectilinear coordinates..... 300

B.2 Schematic representation of a LEPS potential in skewed coordinates..... 302

B.3 Schematic representation of a LEPS potential in skewed and scaled coordinates..... 304

B.4 Mathematical definitions of the skewed and scaled variables Q_1 and Q_2..... 306

LIST OF TABLES

TABLE		PAGE
II.1	Parameter values for the reduced SE1, SE4, and symmetric surfaces.....	45
II.2	Parameter values for the reduced RB and SE potentials.....	46
III.1	State to state quantum reaction probabilities for J=0, j=0 at a total energy of 0.10 eV....	90
III.2	State to state quantum reaction probabilities for J=0, j=0 at a total energy of 0.35 eV....	91
III.3	State to state quantum reaction probabilities for J=20, j=12 at a total energy of 0.15 eV..	92
III.4	State to state quantum reaction probabilities for J=20, j=12 at a total energy of 0.35 eV..	93
III.5	Comparison of basis set size for J = j. The total energies examined are 0.15 and 0.35 eV..	94
III.6	Comparison of basis set size for J ≠ j. The total energies examined are 0.15 and 0.35 eV..	95
VI.1	Mean internuclear distance for the OH(-1/2,j) molecule.....	265
C.1	Atomic Unit conversion factors.....	319

ABSTRACT

THE EFFECT OF REAGENT ROTATION
IN GAS PHASE REACTIONS

by

Judith A. Harrison
University of New Hampshire, September, 1989

This dissertation examines the effect of reagent rotation in elementary gas phase reactions. Historically, the effect of rotational excitation of the reagents of a chemical reaction on the reactive cross section has been poorly understood. One of the major reasons for this was the lack of a simple model in which the dynamics could be visualized. In this work, such a model is developed and utilized in order to elucidate trends in reactivity observed upon rotational excitation. Within the context of this model, exact quantum mechanical scattering calculations are performed for a simple atom-diatom system. These exact quantum mechanical probabilities of reaction as a function of rotational quantum number, $P^R(j)$, exhibit the characteristic "dip and climb" behavior observed in many classical trajectory calculations. These exact $P^R(j)$ are then compared to $P^R(j)$ obtained via several approximate quantum mechanical methods, for example, the Centrifugal Sudden (CS) and the Infinite Order Sudden (IOS). We find that, in general, the CS method does a good job

reproducing exact $P^R(j)$. In contrast, the IOS method only reproduces the correct qualitative trends when the collision is "sudden" like.

The applicability of classical mechanics as it relates to rotational excitation is also investigated. Classical $P^R(j)$ obtained using the model are compared to the exact quantum mechanical $P^R(j)$. The viability of several classical mechanical approximate scattering techniques is also investigated. The classical CS approximation reproduces qualitative trends observed in the exact classical $P^R(j)$, while the classical IOS only reproduces the correct qualitative trends under "sudden" conditions.

Having established the accuracy of classical mechanics in dealing with rotational excitation we then utilized it to fully define the phenomena responsible for the trends observed in the classical $P^R(j)$. Lastly, full 3D classical trajectories are carried out for the $F+H_2(0,j)$ and $OH(0,j) + H_2(0,j')$ reactions. The model qualitatively reproduces the trends observed in the classical reaction cross section as a function of j, $S^R(j)$, for both reactions.

CHAPTER I

INTRODUCTION

An understanding of the dynamic behavior of a system at the molecular level is the key to the interpretation of the "macroscopic" kinetics of the bulk system. Intermolecular collisions serve as the microscopic mechanism behind all the observed rate phenomena involving gases and liquids [1-5]. Historically, the development of the supersonic nozzle and the laser as well as the improvements in computer technology have brought us to the state where we can investigate these collision processes at the molecular level, both experimentally and theoretically.

Ideally, one would like to investigate state to state reaction dynamics. In other words, one would like to examine the effect of energy in a specified quantum state in the reagents on the cross section to a specified quantum state in the products. This subject has been the focus of a considerable amount of experimental and theoretical interest in the last 15 years [6,7].

The effect of reagent vibration and translational energy on reactivity for several elementary reactions (A + BC --> AB + C; where A, B, and C represent atoms) has been studied a great deal [6,7]. Experimentally, the major reason for is the

availability of infrared and ultraviolet lasers and the development of the supersonic nozzle. Early theoretical work on the effects of vibration and translation was done by Polanyi. This work has been summarized in several articles [8,9]. He determined the following with regard to reagent vibration and translation. For a potential energy surface with the saddle point in the product valley (late barrier) increasing the vibrational energy, in general, enhances the reactivity to a much greater extent than does increasing the translational energy. For a surface with the saddle point in the reagent valley (early barrier), increasing the translational energy, in most cases, increases the reactivity to a greater extent than does increasing the vibrational energy. Additionally, Polanyi examined the role played by the reagent masses in reactivity and the effect these masses have on the potential energy surface [10]. The so-called "skewed and scaled" (Appendix B) potential energy surface is well suited to the representation of vibrational and translational motion. In this representation, the dynamics can be visualized as motion of a frictionless particle over the surface. It is precisely this skewed and scaled representation of the potential energy surface which has been the greatest conceptual aid in understanding the effects of vibration and translation.

Traditionally, the role of reagent rotational energy in elementary gas phase reactions has received much less

attention. Experimentally, probably the biggest roadblock to the examination of rotational effects is the difficulty associated with the preparation of molecules in selected rotational states. The theoretical study of the effect of reagent rotation on reactivity has historically been accomplished with the aid of the quasiclassical trajectory method [11-13]. However, a real understanding of how rotation affects the dynamical process has been hampered, we feel, by the lack of a simple model in which the dynamics could be easily visualized, as in the case of vibration and translation. That is, the skewed and scaled representation which was mentioned previously.

Early experimental and theoretical work concerned with the effect of reagent rotation on reactivity has been reviewed by Sathyamurthy [14]. In recent years, this problem has been addressed by several experimental groups. From a theoretical standpoint, more extensive trajectory calculations have been carried out and progress has been made towards quantum dynamical calculations.

Experimental data suggest that rotation frequently enhances reactivity and often leads to excited product species. Loesch et. al. [15,16] have examined the reactions M + HF(v=1,j) --> MF + H (M = Li,K) and find that, in general, rotation enhances reaction. At low translational energy for M=K, rotation inhibits reaction at low j, but enhances it at high j. Zare and coworkers [17,18] have investigated the

reactions M + HF(v=1,j) --> MF + H (M=Ca,Sr). They found that rotation enhances reactivity and produces vibrationally excited products. Further, they also found for the reaction $O(^3P)$ + HCl(v=2,j) --> OH + Cl [19] that rotation enhances reactivity and product rotation. A weak enhancement in reactivity was observed on going from j=1 to j=2 in Ba + N_2O --> BaO^* + N_2 by Stolte and coworkers [20].

There has also been a considerable amount of theoretical work devoted to rotational effects. Recent trajectory studies have been carried out on H + H_2(j) [21,22], D + H_2(v=1) [23], O + HCl(j) [24], Cl + HCl(j) [25,26], Li + HF(v,j) [28], Be + HF(v=0,1), X + ICH_3 --> XI + CH_3 (0,j) (X+Na,F) [28], and H + HD (0,j) [29]. In this work, we will make the following additions to the above list, F + H_2(j), and OH(j) + H_2(j').

It is not easy to make simple pronouncements on how rotation will affect the reaction cross section or rate constant. Most of the experimental studies, discussed previously [15-20], show that rotation enhances reactivity, as do most of the calculations [21-29]. However, on one potential energy surface (LEPS II of ref 24) for O + HCl, rotation was found to dramatically inhibit reaction.

Rather different trends have been observed for H + H_2 [21,25] and, in this work, for both F + H_2 (j) and OH + H_2 (j). In these studies, it was found that near threshold the cross section initially decreased with j, reached a minimum near j = 4, then increased. At higher translational energies, the

cross section increased monotonically with j. This differing behavior has been traditionally explained as the result of a competition between two dynamic effects, the "orientational" and the "energy" effects. These effects, however, have traditionally been rather vaguely defined.

The orientational effect was defined as the tendency for the molecule to rotate out of the preferred collision geometry and was therefore thought to responsible for the dip in the cross section at low j. The energy effect was thought to be responsible for the upward tendency of the cross section at large j. This was thought to be due to the increased total energy of the system concomitant with an increase in j.

Ideally, we would like to have a model which would elucidate the aforementioned behavior of the cross section with j. Of course, the model should be kept as simple as possible in order to isolate the effects due to rotation. Two of the more obvious simplifications are; 1) coplanarity and 2) the vibrational degree of freedom should be ignored.

Loesch has introduced one such model, i.e. the rotational sliding mass model (RSMM) [30]. In this model, the target diatom's bond length is held fixed at its equilibrium distance (r_e), the impact parameter, i.e. the "miss" distance between the atom and the diatoms center of masses (Appendix A), is set to zero, and coplanar trajectories are followed across a scaled, R versus γ, potential surface. The coordinates, R and γ, are defined as follows: R is the distance from the atom to

the center of mass of the diatomic molecule and γ is the angle between R and the diatom's internuclear bond, r (Fig A.1). This model did enjoy some success [31] in explaining the contrasting behavior with reagent rotation obtained by Persky and Broida [24] for the O + HCl(j) --> OH + HCl reaction on two different LEPS surfaces. However, this model has yet to be applied to other elementary systems.

In Chapter II of this work we develop a similar model in which the angle γ is plotted as a function of the reaction coordinate (s), i.e. the minimum energy path. Recently, this model has had great success in predicting the qualitative rotational trends observed in the H + H_2 (j) system [22,25]. It was this recent success which is responsible, in part, for motivating this work, where we shall determine the applicability of this model to other systems.

While the most convenient dynamical method for investigating dynamics at a molecular level is the classical trajectory method, it is still preferable to carry out quantum mechanical computations for accurate work - particularly on systems containing hydrogen. However, quantum mechanical scattering calculations which take into account rotational excitation are, in general, difficult. This difficulty stems from the fact that, in addition to the radial part of the scattering problem, the angular part must also be included. That is, for a given total angular momentum, J, the orbital angular momentum, l, the rotational angular momentum, j, as

well as the projection of j, m_j, must all be included in the calculation [32-36]. It is due to this fact that few three dimensional, converged, quantum scattering calculations have been performed [37-41]. Further, despite recent advances in quantal scattering theory [42-46], the exact treatment of high rotational states is still probably far in the future.

In an attempt to circumvent this problem, several approaches have been tried. First, various angular momentum decoupling approximations have been developed. These methods simplify the computation by approximating the various angular momenta involved in the problem of interest [47-50]. These methods are discussed more fully in Chapters III and IV. Secondly, coplanar geometries simplify quantum mechanical calculations by forcing the magnetic quantum numbers to be zero.

The organization of this work is as follows. In Chapter II we derive our model. We then use this model to perform quantum mechanical scattering calculations in order to determine the effect of reagent rotation on reactivity. This is done in Chapter III. Also in Chapter III, the viability of several angular momentum decoupling approximations is investigated with our model. The accuracy of classical mechanics in regard to rotational excitation is tested in Chapter IV via a comparison of the model classical reaction probabilities as a function of j to their quantum mechanical counterparts. As in Chapter III, the validity of several

classical mechanical angular momentum decoupling approximations is also examined. As we shall see, the use of the model, in general, and the angular momentum decoupling approximations, in particular, allow for the precise definition of the so-called orientational and energy effects. Finally, in Chapters V and VI, we apply our newly found understanding of rotational excitation to other systems. Here we investigate F + $H_2(j)$ in Chapter V and OH(j) + $H_2(j')$ in Chapter VI using classical trajectories.

CHAPTER II

THE EFFECT OF REAGENT ROTATION ON REACTIVITY:

MODEL DESCRIPTION

Introduction

In what follows, the model, which has been used throughout this work to investigate rotational excitation, is derived. It is derived for the simple A+BC(j) system as well as the more complicated AB(j) + CD(j') system. Further, the method for obtaining the model, or reduced, potential is described.

Model Derivation

A + BC Reactions

Throughout this work, a model system for gas phase A + BC(j) type reactions has been used to help understand trends observed in trajectory calculations which examined the effect of reagent rotation on reactivity.

This model was originally developed [51] for zero impact parameter coplanar atom-diatom reactive systems in which the symmetric stretch is vibrationally adiabatic. The model was later adapted for nonzero impact parameter collisions [22].

Briefly, the model is derived as follows [22]. The Hamiltonian for an A+BC collision can be written in the general form [11]

$$H = \underline{p}_R \cdot \underline{p}_R/2\mu + \underline{p}_r \cdot \underline{p}_r/2m + V(\underline{r},\underline{R}) \qquad \text{(II.1)}$$

where $\underline{R}$ is the displacement from the atom A to the center of mass of BC, $\underline{r}$ is the BC bond displacement (Fig II.1), μ is the translational reduced mass, m is the diatom's reduced mass, and $\underline{p}_r$ and $\underline{p}_R$ are the momenta conjugate to $\underline{r}$ and $\underline{R}$, respectively. Decomposing the vectors into components parallel to and perpendicular to $\underline{r}$ and $\underline{R}$ the Hamiltonian (II.1) has the form

$$H = (p_R^2 + \underline{l} \cdot \underline{l}/R^2)/2\mu + (p_r^2 + \underline{j} \cdot \underline{j}/r^2)/2m + V(r,R,\gamma) \qquad \text{(II.2)}$$

where $\underline{l} = \underline{R} \times \underline{p}_R$ is the orbital angular momentum, $\underline{j} = \underline{r} \times \underline{p}_r$ is the diatom rotational angular momentum. The total angular momentum is $\underline{J} = \underline{l} + \underline{j}$. Substituting for $\underline{l}$ in (II.2) gives

$$H = (p_R^2 + (\underline{J}-\underline{j})^2/R^2)/2\mu + (p_r^2 + \underline{j}^2/r^2)/2m + V(r,R,\gamma) \qquad \text{(II.3)}$$

Transforming p_r and p_R into natural collision coordinates [52,53] and assuming that there is zero curvature of the reaction path, i.e. the trajectory remains on the minimum energy path during the course of the collision, the Hamiltonian (II.3) becomes

$$H = p_s^2/2\mu + \underline{j}^2/2mr^2 + (\underline{J}-\underline{j})^2/2\mu R^2(s,\gamma) + V(s,\gamma) \qquad \text{(II.4)}$$

where s is the so-called reaction coordinate which runs from $-\infty$ (reagents) to $+\infty$ (products), p_s is the momentum conjugate to s, and $V(s,\gamma)$ is the reduced potential. The rotational motion of the diatom is described by the angle, γ. Asymptotically γ corresponds to free rotation of the reagent

or product diatomic molecule. At the transition state, s = 0, γ corresponds to the bending angle of the complex. Lastly, ignoring the dependence of R on γ, a particularly simple functional form is given by $R^2(s) = (R_m^2 + s^2)$ [22], where R_m is the distance from the atom to the molecule's center of mass at the saddle point. The lower limit of R is determined by the value of R_m. In practice it has been determined that the term which contains R_m is usually small. Further, it has been determined that the results are fairly insensitive to the value of R_m. For coplanar collision geometries the Hamiltonian (II.4) becomes

$$H = p_s^2/2\mu + j^2/2I(s) + (J-j)^2/[2\mu(R_m^2+s^2)] + V(s,\gamma) \qquad \text{(II.5)}$$

where the rotational quantum number j is the momentum conjugate to γ, and I(s) is the diatom's moment of inertia, which is given by

$$I(s) = I_o \{ 1 + a \exp [-(s/L)^2] \qquad \text{(II.6)}$$

where I_o is the diatom's asymptotic moment of inertia, mr_e^2, L is a length parameter, and a is the fractional increase in I at the saddle point (s=0) over its asymptotic value. The method for calculating the reduced potential is discussed in a subsequent section.

AB + CD Reactions

For diatom-diatom (AB + CD) collisions (Fig II.2), the classical Hamiltonian can be written as

$$H = \underline{p}_R \cdot \underline{p}_R/2\mu + \underline{p}_1 \cdot \underline{p}_1/2m_1 + \underline{p}_2 \cdot \underline{p}_2/2m_2 + V(\underline{R},\underline{r}_1,\underline{r}_2) \qquad \text{(II.7)}$$

Substituting the definitions of angular momenta, i.e. $\underline{l} = \underline{R} \times \underline{p}_R$, $\underline{j} = \underline{r}_1 \times \underline{p}_1$, and $\underline{j}' = \underline{r}_2 \times \underline{p}_2$, paralleling the A+BC derivation, the Hamiltonian becomes

$$H = (p_R^2 + \underline{l}^2/\underline{R}^2)/2\mu + (p_1^2 + \underline{j}^2/\underline{r}_1^2)/2m_1 + (p_2^2 + \underline{j}'^2/\underline{r}_2^2)/2m_2 + V(R, r_1, r_2, \theta, \phi, \psi) \qquad \text{(II.8)}$$

where $\underline{r}_1$ is the AB bond displacement, $\underline{r}_2$ is the CD bond displacement, $\underline{R}$ is the vector from the center of mass of AB to the center of mass of CD, the $\underline{p}$'s are the respective conjugate momenta, μ is the translational, AB+CD, reduced mass, and m_1 and m_2 are the reduced masses of the AB and CD diatoms, respectively. The angles, θ, ϕ, and ψ, are defined as follows (Fig II.2); $\theta = \arccos(\underline{r}_1 \cdot \underline{R}/r_1 * R)$, $\phi = \arccos(\underline{r}_2 \cdot \underline{R}/r_2 * R)$, and ψ is the dihedral angle between $\underline{r}_1$ and $\underline{r}_2$. The unit vector perpendicular to $\underline{r}_1$ and $\underline{R}$ is $\hat{\underline{u}}_1$, similarly the unit vector perpendicular to $\underline{R}$ and $\underline{r}_2$ is $\hat{\underline{u}}_2$. Using the definitions of $\hat{\underline{u}}_1$ and $\hat{\underline{u}}_2$, $\hat{\underline{u}}_1 = \hat{\underline{r}}_1 \times \hat{\underline{R}}$ and $\hat{\underline{u}}_2 = \hat{\underline{R}} \times \hat{\underline{r}}_2$, the dihedral angle is given by $\psi = \arccos(\hat{\underline{u}}_1 \cdot \hat{\underline{u}}_2)$.

Assuming that the r_2 bond is broken and that the r_1 coordinate is only weakly coupled to the reaction coordinate allows the terms in p_R and p_2 can be transformed into natural collision coordinates [52,53] (note that this is the case in the OH + H_2 reaction since the OH bond is a spectator bond). Further assuming there is no "bobsledding" [52] during the collision and substituting for $\underline{l}$ in (II.8) the Hamiltonian takes the form

$$H = p_s^2/2\mu + (p_1^2 + \underline{j}^2/\underline{r}_1^2)/2m_1 + \underline{j}'^2/2m_2 r_2^2$$

$$+ (\underline{J} - \underline{j} - \underline{j}')^2/2\mu R^2 + V(s,r_1,\theta,\phi,\psi) \qquad \text{(II.9)}$$

where the total conserved angular momentum is given by $\underline{J} = (\underline{l} + \underline{j} + \underline{j}')$. Finally, since motion along the r_1 bond does not materially affect the rest of the system this allows the terms in p_1 and r_1 to be separated out. For coplanar collision geometries, i.e. $\psi = 0$, the Hamiltonian becomes

$$H = p_s^2/2\mu + j^2/2m_1r_1(s)^2 + j'^2/2m_2r_2(s)^2$$
$$+ (\underline{J} - \underline{j} - \underline{j}')^2/2\mu R(s,\theta,\phi)^2 + V(s,\theta,\phi). \qquad \text{(II.10)}$$

Ignoring the angular dependence of $R(s,\theta,\phi)$, it is approximated, as in the A+BC case, by $R^2 = R_m^2 + s^2$.

If there is rotation in only one of the diatoms, either j or j' is zero, there will be no coupling between angles via the potential then the angle corresponding to the "frozen" rotor is constant. In this case equation (II.10) reduces to (II.5) for the atom-diatom system, and the potential is calculated with the appropriate angle held fixed.

Reduced Potential

A + BC Reactions

Before the model can be of any use the actual potential must be transformed to the model or reduced potential, $V(s,\gamma)$.

The interactions of an atom and a diatom are often represented by a LEPS functional form [50,54-56,60,185], which is a function of the three internuclear distances, x_1, x_2, and x_3 (Fig A.1). Although the internuclear coordinates are natural coordinates for the potential they are not well suited to represent the collision process [3] (Appendix B). Better

coordinates to represent the collision process are the Jacobi coordinates, ($\underline{r}$,$\underline{R}$) or (r,R,γ), shown in Fig II.1. Equations (A.14-A.16) allow one to make the coordinate transformation from the Jacobi coordinates to the internuclear distances. When γ = 0 the three atoms are in the collinear arrangement and a LEPS surface, plotted in Jacobi coordinates typically would have the form shown in Fig II.3. It should be noted that once the reaction products are formed, the Jacobi coordinates although still defined, do not have the same significance. For example, $\underline{r}$ is no longer the diatom internuclear displacement since the diatom is now AB instead of BC (Fig A.4). Therefore in what follows no attempt has been made to map the potential in the product region to the reduced potential.

Before the "mapping" of the actual potential, $V_{LEPS}(\underline{R},\underline{r})$, to the reduced potential, $V(s,\gamma)$, is described, the pertinent variables will be defined. In order to illustrate this procedure a schematic LEPS type surface will be used (Fig II.4). First an arbitrary fixed point, i.e. a swing point (R_s,r_s), must be defined. The line segment from the swing point which is perpendicular to the R axis is referred to as r_s. Similarly the line segment from the swing point which is perpendicular to the r axis is referred to as R_s. Further, ρ is the line segment from the swing point to any point on the reaction path and Φ is the angle between ρ and r_s, thus

$$r = r_s - \rho \cos(\Phi) \qquad \text{(II.11)}$$

$$R = R_s - \rho \sin(\Phi) \qquad \text{(II.12)}$$

For a given a γ value, say γ = 0 (Fig II.1), the "mapping" is achieved as follows. The minimum energy path when γ = 0 is represented by the solid line which goes from the reagent valley into the product valley in Figure II.4. The value of the potential along this line is desired, this amounts to minimizing the potential along ρ for a given Φ value. Incrementing Φ allows one to move along the minimum energy path toward the saddle point, i.e. the transition state (denoted with an X in Figure II.4).

For example, to begin the mapping Φ is set to zero and ρ_g, that is the first guess at ρ, is given the value $r_s - r_e$, where r_e is the equilibrium internuclear distance of the diatom. The distance, ρ_g must be bracketed by a higher, ρ_U, and a lower, ρ_L, value. Bracketing is choosing the upper and lower ρ values so that the minimum value of the potential is somewhere between these two values [94]. Using ρ_g, ρ_L, and ρ_U, a golden section search [94] is performed to determine the minimum value of the potential along ρ. Once the minimum value of the potential, and thus the corresponding ρ_m value (note ρ_m is the value of ρ along the minimum energy path, is determined the value is recorded. The angle Φ is then incremented. The value of ρ_m at the minimum determined in the previous step is used as an initial guess for ρ_g. This value is bracketed and the golden section search is performed. This process of incrementing Φ and minimizing along ρ is repeated until the saddle point is bracketed. Once the saddle point is

bracketed a golden section search for the maximum value of the potential is performed, in order to determine its exact location.

The s points are determined as follows. The saddle point is assigned an s = 0 value, and by convention the reagent valley will be given negative s values and the product valley positive s values. Beginning at the saddle point and stepping along the minimum energy path into the reagent valley the s values are assigned using the approximation for the arc s

$$s_{new} = s_{old} - [(\rho_m)_{old} + (\rho_m)_{new}] * 1/2 * d\Phi \qquad (II.13)$$

where s_{old} is the value of s from the previous step, s_{new} is the value of s at the present step, $d\Phi$ is the Φ increment, and $(\rho_m)_{old}$ and $(\rho_m)_{new}$ are the ρ_m values from the previous and the present step. The increment, $d\Phi$, should be small to insure that the segment $\rho d\Phi$ is approximately a straight line. Once the s values have been determined the reduced potential, $V_o(s,\gamma=0)$, has been determined for γ = 0. The angle, γ, is incremented and the process repeated, this results in the $V(s,\gamma)$ values. A contour plot is created using these values. These points can also be fit to a simple analytical form.

It should be noted that there are instances when this "mapping" procedure breaks down. For example, highly skewed and scaled potentials (Appendix B), e.g. O+HCl, the LEPS potential [24] can be represented by Fig II.5. From analysis of Fig II.5 it is apparent that the placement of the swing point so that ρ will only cut though the reaction path is

difficult. If ρ were to slice through both the product and reaction valleys unique determination of the minimum energy path is nearly impossible.

AB + BC Reactions

In principle, the procedure for fitting a four body (AB + CD) potential such as OH + H_2 [57,58] is the same as it is in the three body case. However, due to the increased number of variables there are differences which merit discussion.

In the case of CD rotation, i.e. H_2, ϕ is the angular coordinate of interest (Fig II.2). The other angle, θ, is held constant. In the OH + H_2 system, θ was fixed at its saddle point value of 116° [57]. The bond length of the AB diatom is fixed at its equilibrium value for the isolated diatom [57]. The "mapping" process can now be carried out as in the A + BC case, by scanning the plot of r_2 versus R at fixed ϕ then incrementing ϕ and repeating the process to generate the $V(s,\phi)$ values.

In the case of AB rotation, θ is the angular coordinate of interest and ϕ is fixed. The r_2 distance is fixed at its equilibrium value and ϕ is fixed at 0°. The reduced potential points, $V(s,\theta)$, are then generated as before.

Analytical Form of the Reduced Potential

A + BC Reactions

In general, the γ dependence of A+BC type reactions can be approximated by a $\sin^N(\gamma)$ (where N is even) function. For symmetric reactions, i.e. A=C, the s dependence is fit with

a symmetric Eckart function. Asymmetric reactions, i.e. A≠C, are fit with an asymmetric Eckart function [59], this accounts for the exothermicity of the F+H_2 reaction.

Previous work on the H+H_2(j) reaction [51] demonstrated that a reduced potential of the form

$$V(s,\gamma) = B_o * \sin^2(\gamma)/\cosh^2(s/L) \qquad \text{(II.14)}$$

reproduced qualitative trends seen in classical trajectory calculations. Here, B_o is the height of the barrier at $\gamma = 0$ along the reaction coordinate, s, and L is a length parameter. A contour plot of (II.14) is shown in Figure II.6.

Two LEPS surfaces for the asymmetric F+H_2 reaction have been fit in this work, the SE1 and the SE4 potentials [60]. The reduced SE1 surface is shown in Figure II.7. This can be compared to the actual SE1 surface is shown in Fig II.8. The reduced SE1 surface has the form

$$V(s,\gamma)=B_o\, y/(1+y)^2 + A_o\, y/(1+y) + c_o \exp(-\alpha s^2)\, \sin^N(\gamma) \qquad \text{(II.15)}$$

with $y = \exp((s-s_o)/L)$. The first two terms combine to form the asymmetric Eckart barrier in the collinear reaction coordinate ($\gamma = 0$). The exothermicity of the process is represented by A_o. The parameter, s_o, is used to center the position of the barrier to reaction at s = 0. Both the parameters, α and c_o, depend on the stiffness of the bend potential at the transition state. The SE4 surface has a well in the entrance valley, therefore in order to model this surface a gaussian well was added to the reduced form. The

reduced SE4 potential is shown in Figure II.9 and the actual SE4 surface is shown in Figure II.10. The reduced SE4 has the form

$$V'(s,\gamma) = V(s,\gamma) + D_o \exp\left[-c_1(s-s_{min})^2\right] \qquad (II.16)$$

where D_o is the depth of the well, s_{min} is the position of the minimum in the well along s, and c_1 is the gaussian shape parameter. It should be noted that the SE1 and the SE4 potentials are the only potentials where an attempt to fit the $V(s,\gamma)$ points was made. In all other cases the functional form was chosen to qualitatively represent the actual reduced potential.

AB + CD Reactions

Shown in Figures (II.11) and (II.12) are the contour plots of the $V(s,\theta)$ and the $V(s,\phi)$ potentials for both the Schatz-Elgersma (SE) [57] and the Rashed-Brown (RB) [58] OH + H_2 potentials, both of which have been used in this work. The reduced form of the potential given below was found to reproduce the qualitative functional form of the reactive cross section with j. The model form used for both the SE and the RB surfaces is given by

$$V(s,\gamma) = \{B_o/\cosh^2(s/L) + D_o \exp[-c_1(s - s_{min})^2]\} * \sin^2(\gamma) \qquad (II.17)$$

where the D_o can be used to create gaussian wells or bumps in the entrance valley.

Table II.1 contains all the reduced potential parameters, i.e symmetric H+H_2 and both asymmetric F+H_2 potentials. Table

II.2 contains the parameters for both four body $OH+H_2$ potentials, i.e. the Schatz-Elgersma (SE) potential and the Rashed-Brown (RB) potential.

Fig. II.1 Jacobi coordinates (R, r, γ) for an atom-diatom, A + BC, reaction.

II.1

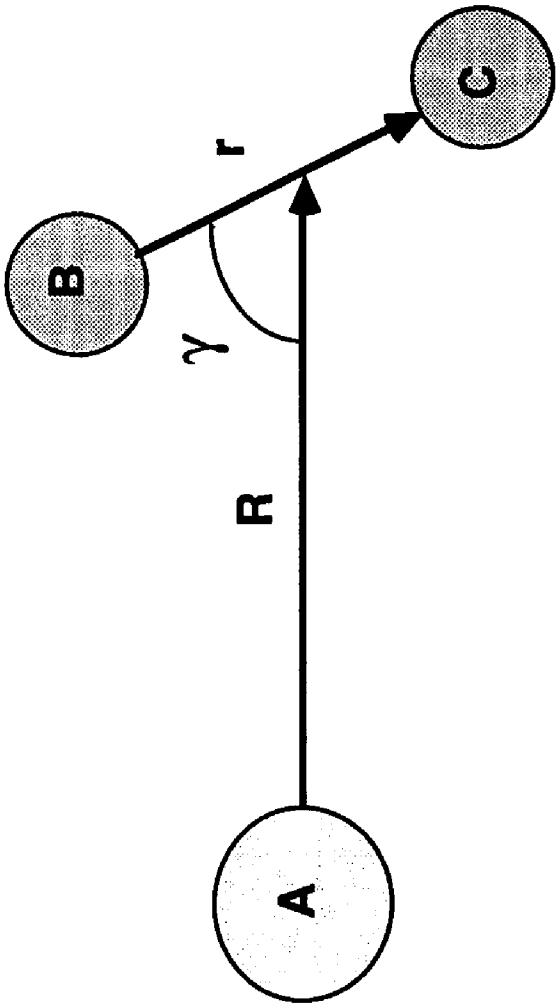

Fig. II.2 Center of mass coordinates ($\underline{r}_1, \underline{r}_2, \underline{R}$) for a diatom-diatom (AB + CD) reaction.

II.2

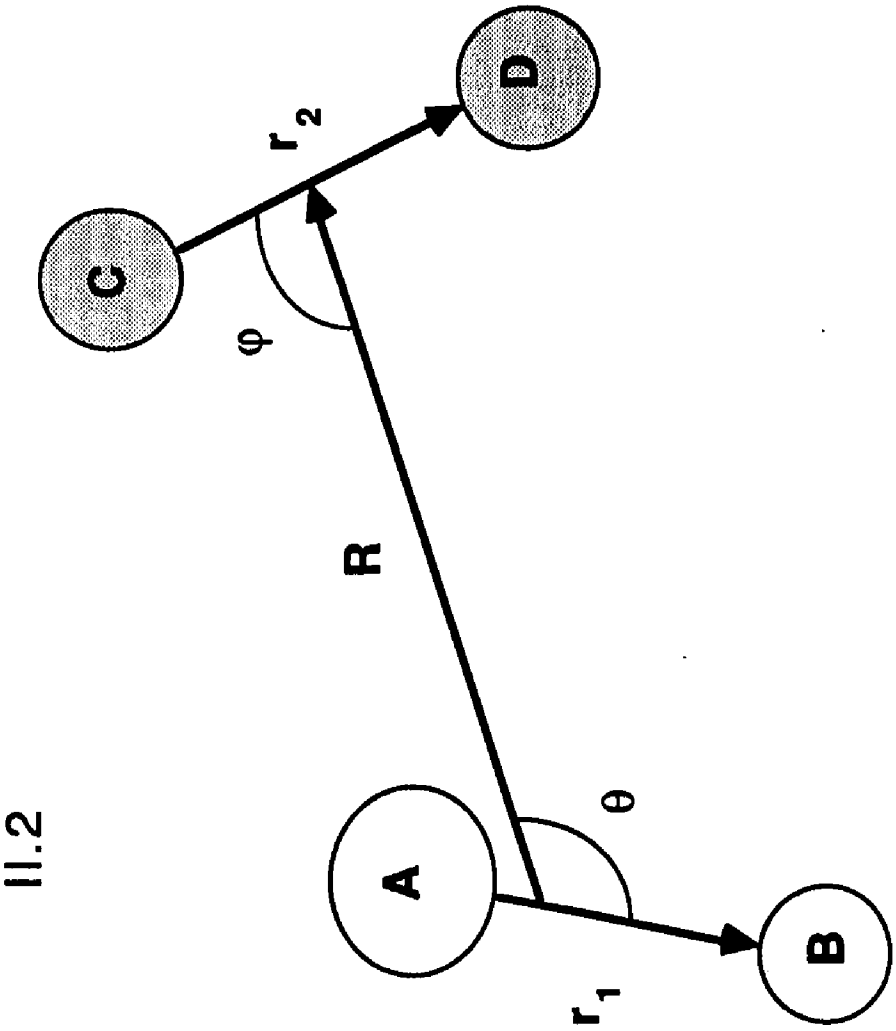

Fig. II.3 Potential energy contour diagram of the SE1 surface in skewed coordinates. The contour values are -1.08, -0.86, -0.43, 0.0433, 0.0866, 0.43, and 1.08 eV. Broken lines signify energies less than zero. The coordinates R, R2, correspond to R, r of Figure II.1, respectively.

II.3

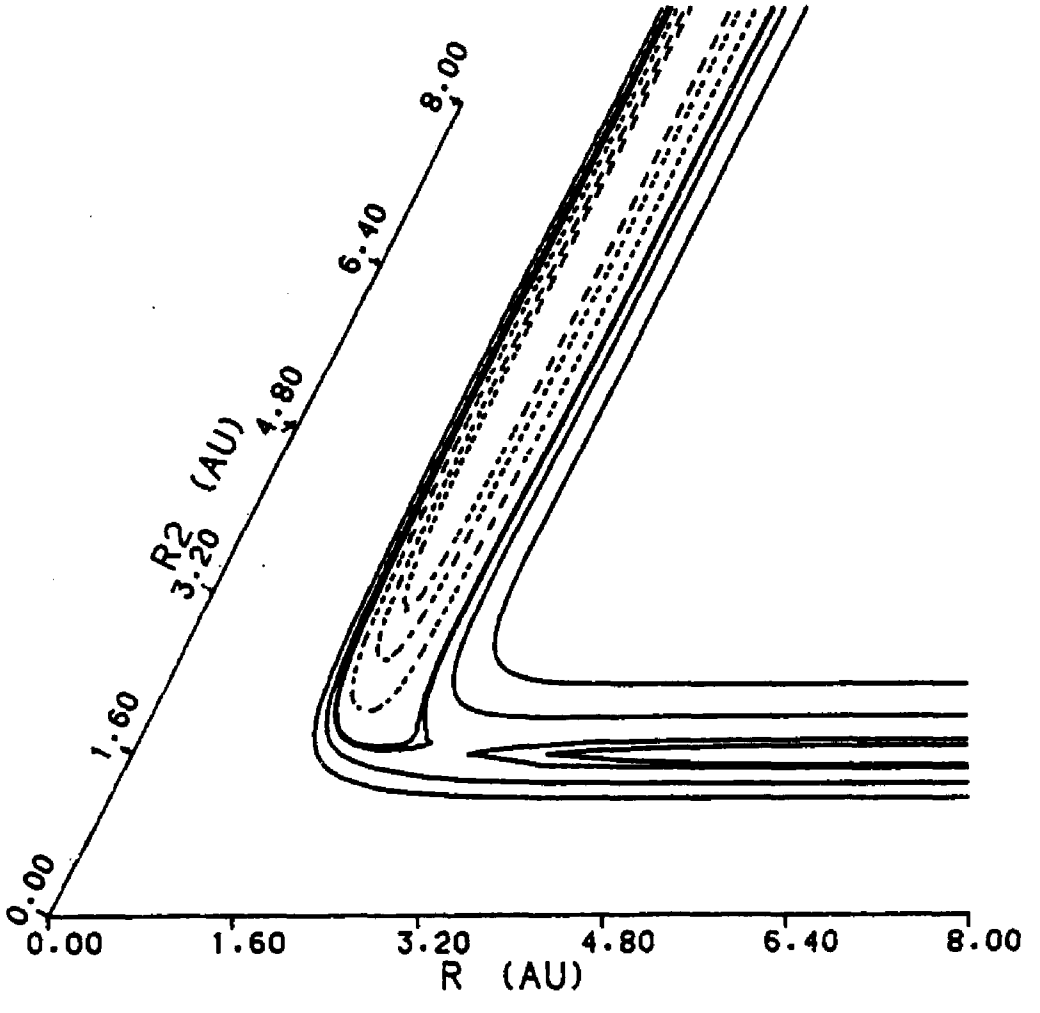

Fig. II.4 Schematic representation of a LEPS surface in skewed coordinates defining the variables (R_s, r_s), ρ and Φ. The minimum energy path is represented by solid line running from reagents to products. The saddle point is denoted with an X.

II.4

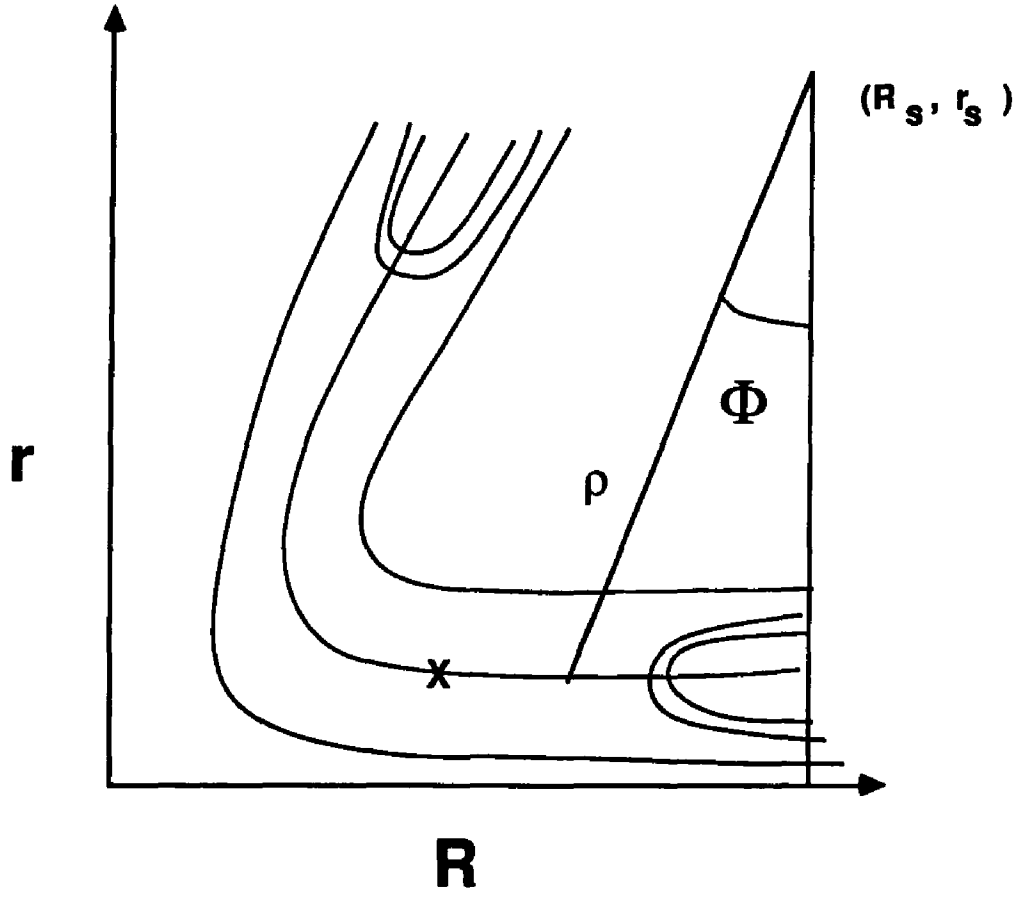

Fig. II.5 Potential energy contour diagram of the O + HCL surface (I) in skewed coordinates. The contour values are 0.2, 0.4, 0.6, 0.8, 1.0, 3.0, and 5.0 eV. The coordinates R and R2 correspond to R and r of Figure II.1, respectively.

II.5

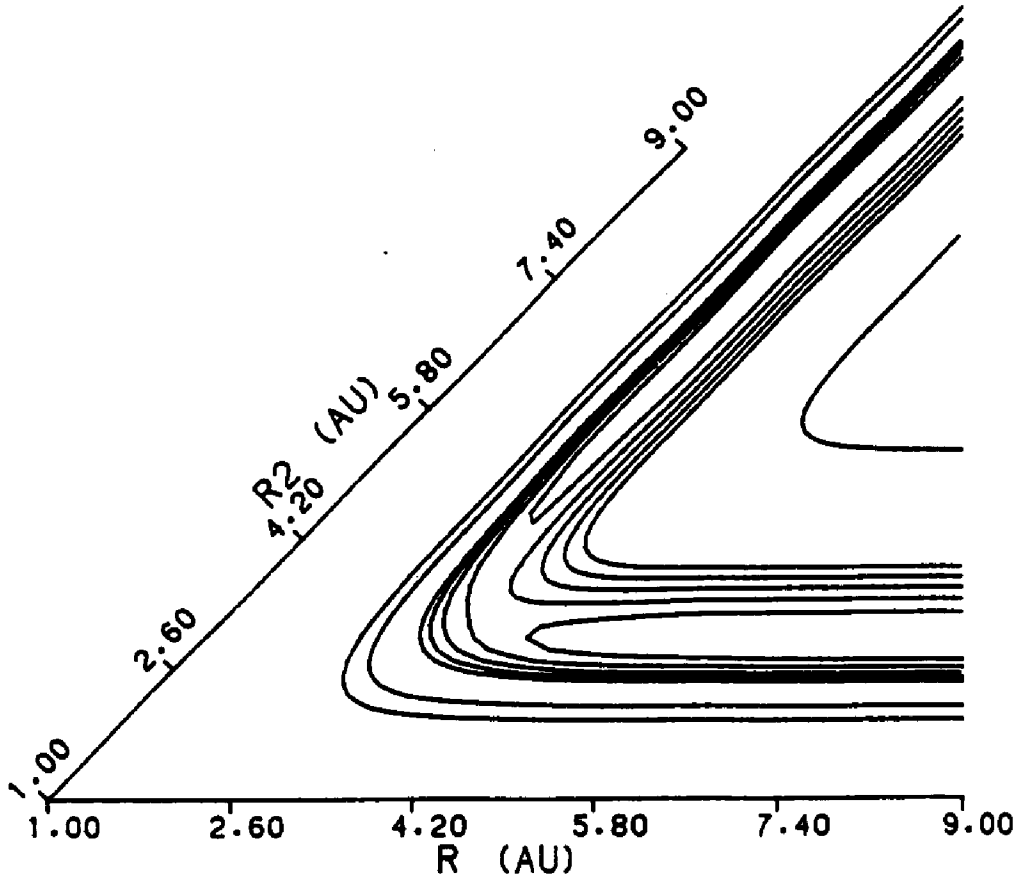

Fig. II.6 Potential energy contour diagram of the symmetric reduced potential (eqn II.14) in (s,γ) coordinates. Contour values are 0.1, 0.2, 0.3, 0.4, 0.5, 0.6, 0.7, 0.8, 0.9, and 1.0 eV.

Fig. 6

Fig. II.7 Potential energy contour diagram of the reduced SE1 surface in (s,γ) coordinates. The contour values are -1.00, -0.4, -0.16, -0.12, -0.08, -0.04, 0.02, 0.06, 0.1, 0.14, 0.16, 0.2 and 0.5 eV. Broken lines signify energies less than zero.

II.7

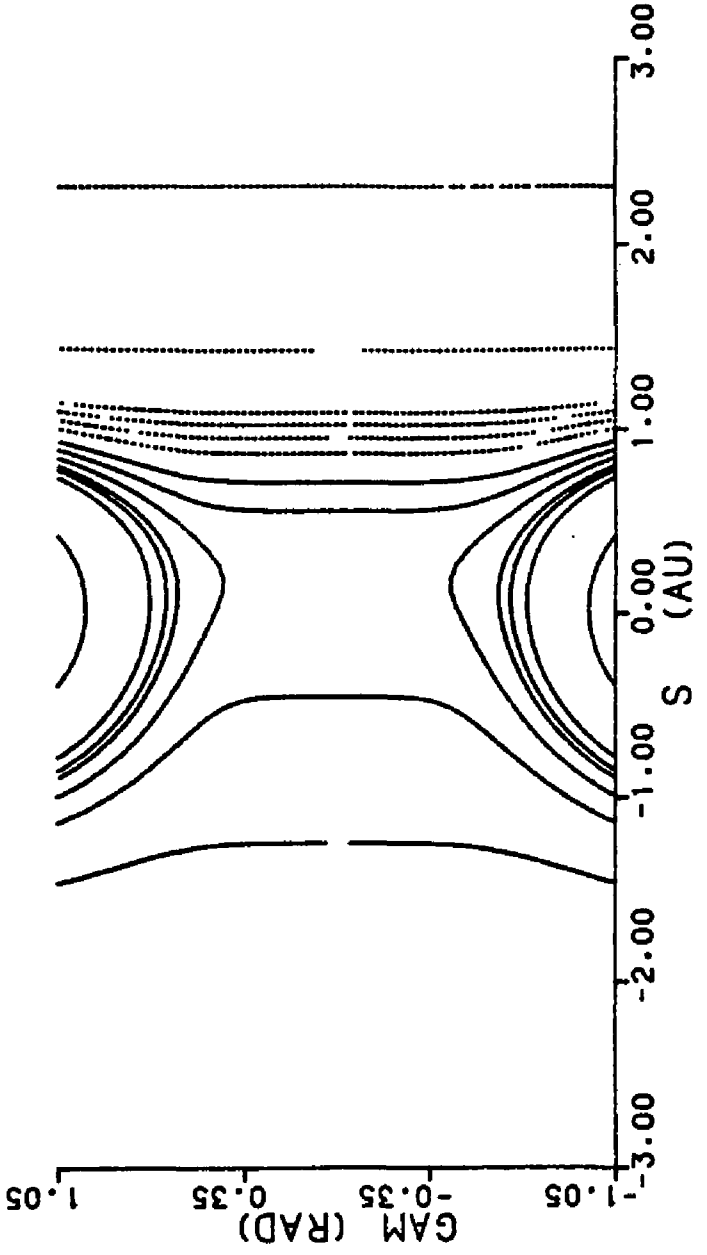

Fig. II.8 Potential energy contour diagram of the SE1 surface in (s,γ) coordinates. Contour values are as in Figure II.7.

II.8

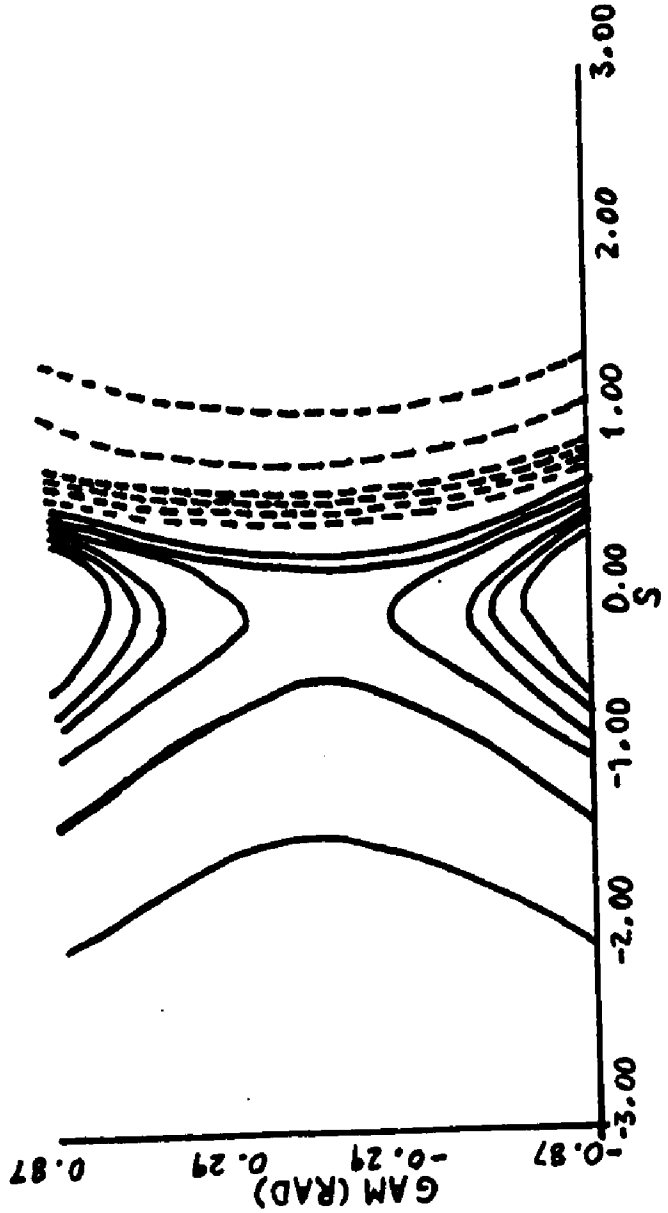

Fig. II.9 Potential energy contour diagram of the reduced SE4 surface in (s,γ) coordinates. Contour values are as in Figure II.7.

Fig. 9

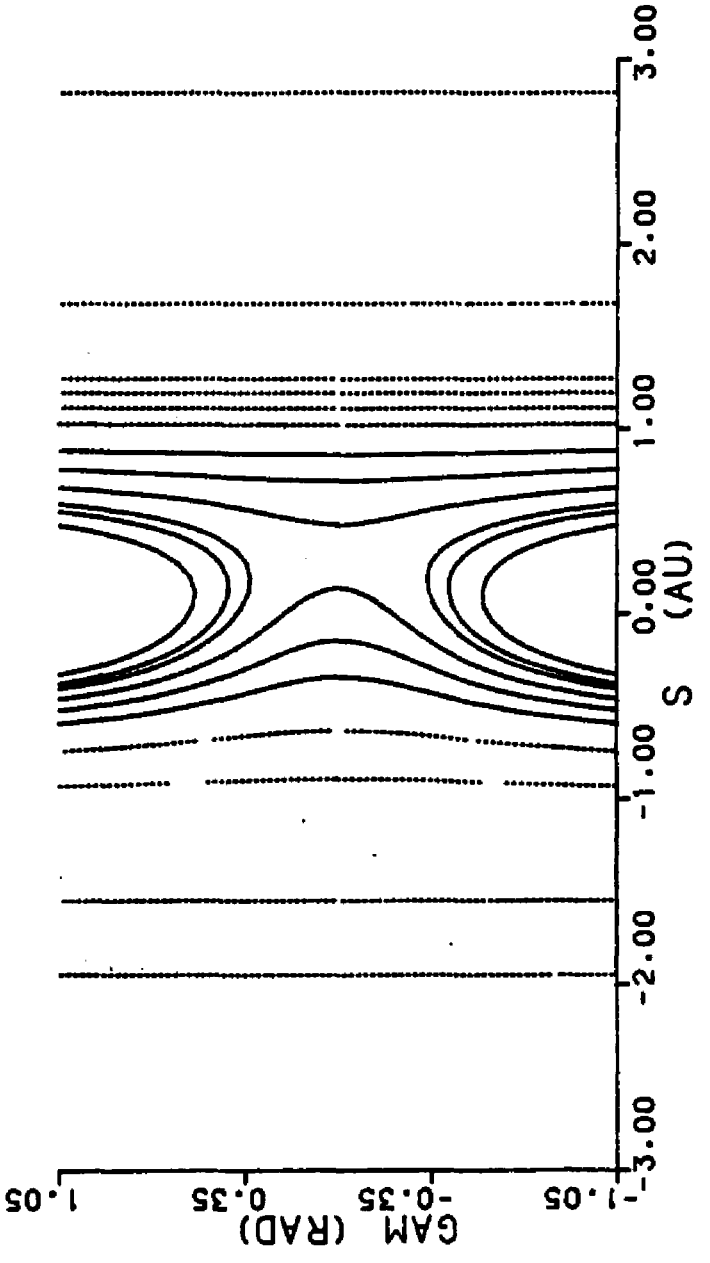

Fig. II.10 Potential energy contour diagram of the SE4 surface in (s,γ) coordinates. Contour values are as in Figure II.7.

II.10

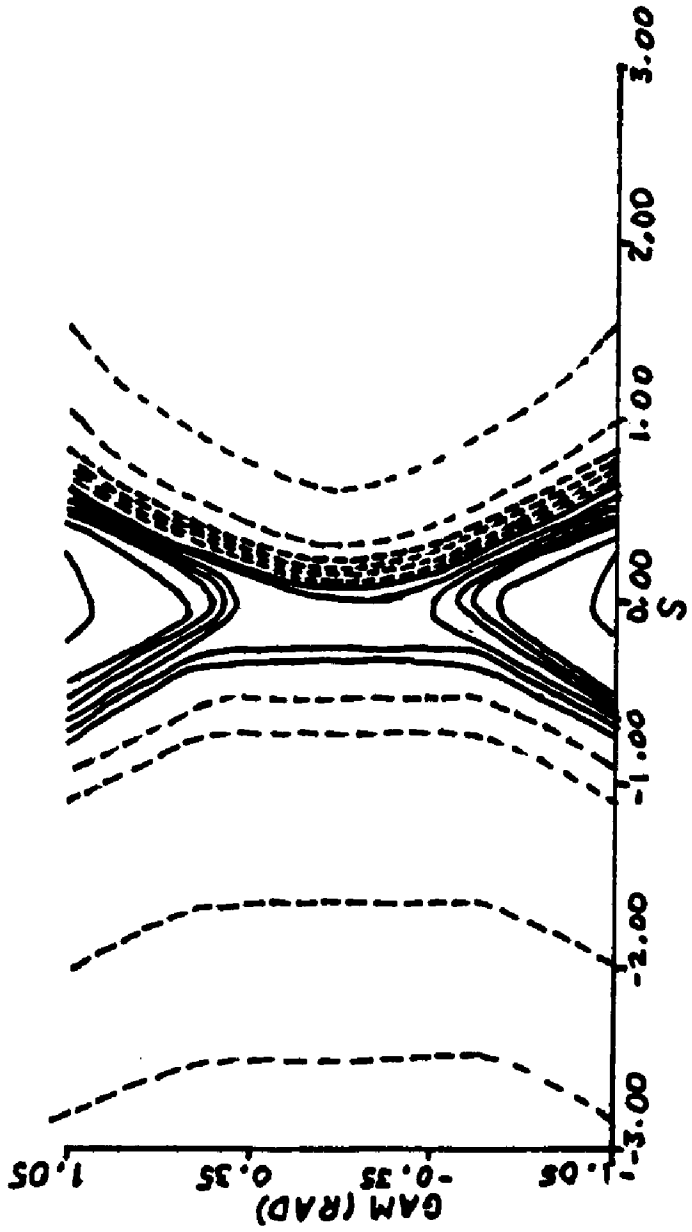

Fig. II.11 Potential energy contour diagram of the RB (top panel) and the SE (bottom panel) surfaces in (s,θ) coordinates. The angle ϕ is fixed at zero and $r_1 = r^{e}_{OH}$. Contour values are -0.4, -0.04, 0.1, 0.2, 0.5, and 0.9 eV. Broken lines signify energies less than zero.

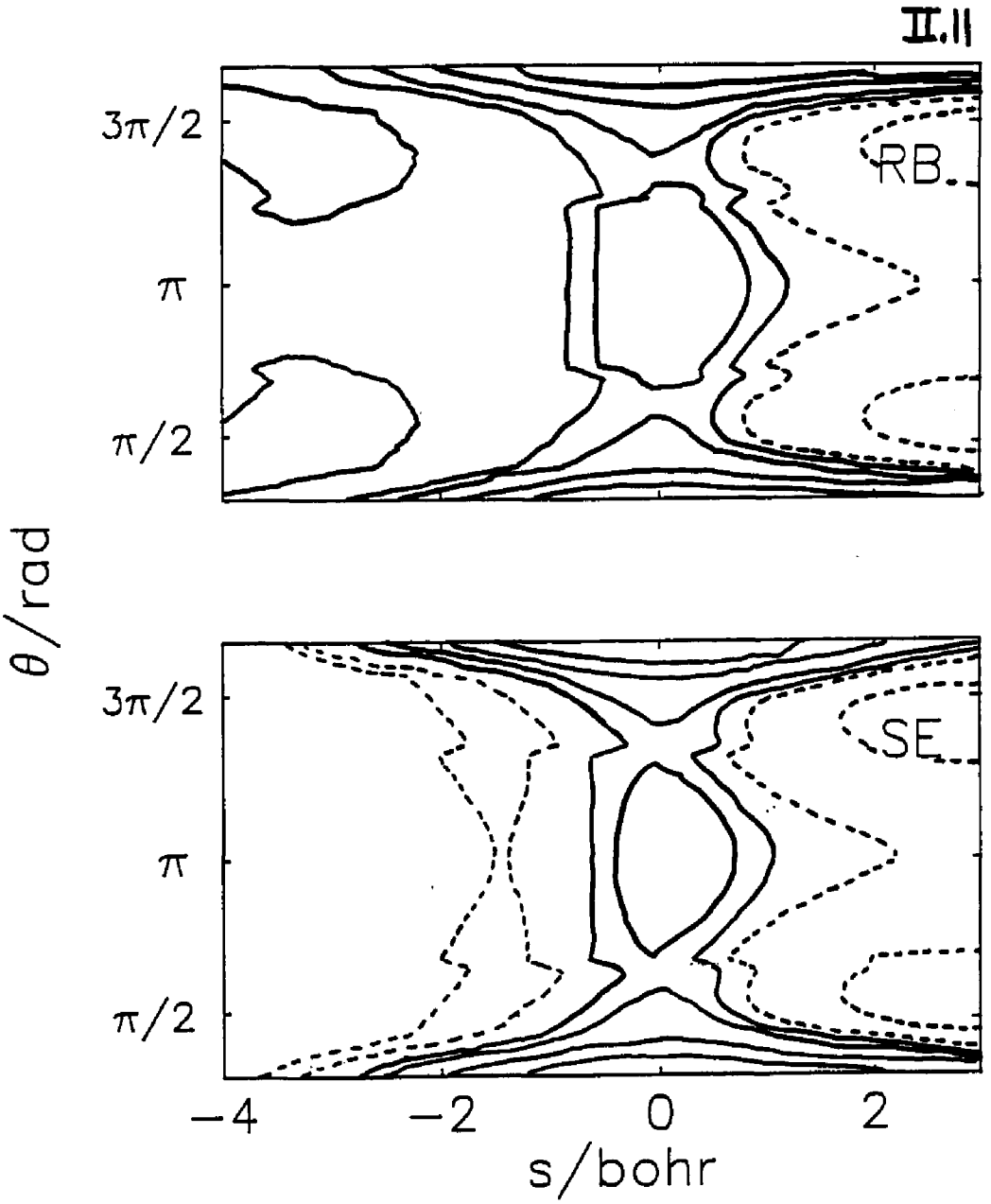
II.11
3π/2
π
π/2
RB
3π/2
π
π/2
SE
θ/rad
−4
−2
0
2
s/bohr

Fig. II.12 Potential energy contour diagram of the RB (top panel) and the SE (bottom panel) surfaces in (s,ϕ) coordinates. The angle θ is fixed at 116° and $r_1 = r^{e}_{OH}$. Contour values are -0.4, -0.04, 0.2, 0.5, and 0.9 eV. Broken lines signify energies less than zero.

II.12

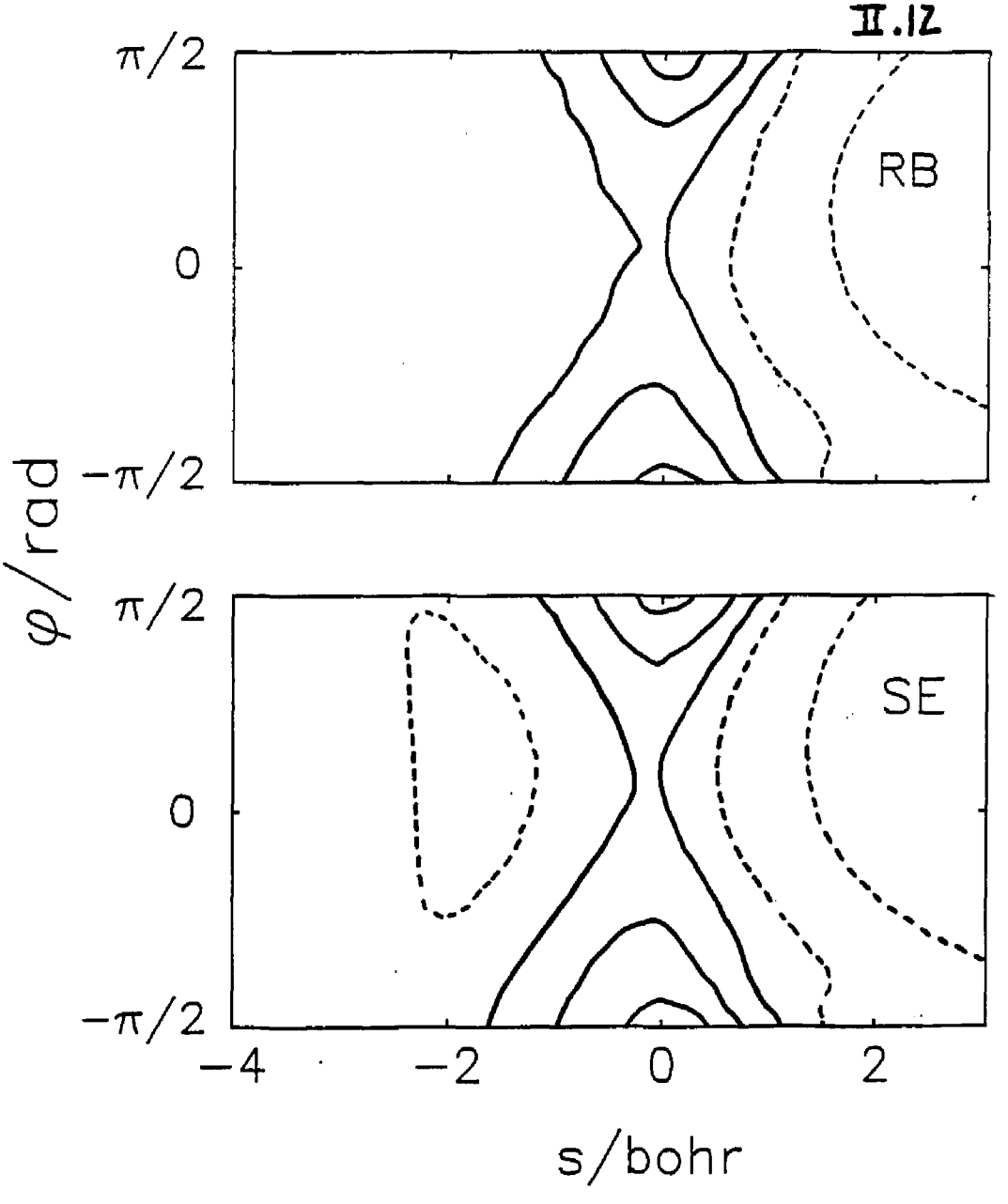

TABLE II.1

PARAMETER	*SE1*	*SE4*	*SYMMETRIC*
B_0 (hartree)	0.830(-1)	0.920(-1)	0.059905
A_0 (hartree)	-0.49295(-1)	-0.49231(-1)	- - -
C_0 (hartree)	-0.535(-1)	0.150(-1)	- - -
s_0 (bohr)	1.00	1.00	- - -
L (bohr)	0.600	0.800	0.5
α (1/bohr ^{2})	2.20	5.00	- - -
d_0 (hartree)	---	-0.600(-2)	- - -
c_1 (1/bohr ^{2})	- - -	1.00	- - -
s_{min} (bohr)	- - -	-1.00	- - -
N	6	2	2
R_m (bohr)	2.434	2.434	2.100
a	0.5	0.5	1.00

TABLE II.2

PARAMETER	*RB*	*SE*
B_0 (hartree)	1.0	1.0
L (bohr)	0.20	0.10
d_0 (hartree)	0.0, 0.03, 0.05	0.0, -0.1, -0.2
c_1 (1/bohr ^{2})	2.500	2.500
s_{min} (bohr)	-2.0	-2.0
N	6	6
a	1.0	1.0

CHAPTER III

THE EFFECT OF REAGENT ROTATION ON REACTIVITY: QUANTUM MECHANICAL SCATTERING CALCULATIONS

Introduction

In order to obtain quantum mechanical reaction probabilities or differential cross sections one must numerically solve the Schroedinger equation. There are several basic approaches which can be used in order to obtain a solution. Two of these include; 1) direct solution of the partial differential equations corresponding to the Schroedinger equation by finite difference methods on a mesh [61,62]; and 2) utilization of basis set expansions for all but one variable, resulting in a set of coupled equations equivalent to the original Schroedinger equation (except for truncation errors) in several variables [63-66].

It is this second approach which has proven to be the most productive for accurate quantum calculations of chemical reactions. This approach is know as the "close coupling" or "coupled channels" method. After all the degrees of freedom except one are expanded in a set of square integrable functions [63-66], the coupled equations are then solved numerically for motion in the final degree of freedom, referred to as either the reaction, propagation, or the

translational coordinate [65,67].

If one is concerned with inelastic scattering, that is a collision in which the internal energy of the species changes but there are no chemical changes, the major prospective problems associated with the close coupling method are as follows. As the mass of the molecule of interest increases, vibrational and rotational states become more closely spaced and the number of channels which must be included in the expansion increases. This increases the computational effort required to solve the scattering problem. Further, as the total energy of the system increases, the number of energetically accessible states (open channels) also increases. As before, the result is an increase in computational effort. Therefore, for very heavy molecules this method quickly becomes intractable.

These inherent difficulties are not of major concern, however, since quantum dynamics is mostly concerned with light mass systems close to threshold, since this is the region which will show the most pronounced quantum effects [46,67]. In a recent review, Schatz [46] discusses quantum effects, e.g. tunneling and resonances, in gas phase bimolecular reactions.

In addition to the difficulties mentioned above, reactive collisions possess their own set of complications. One major problem is due to the fact that the reagents differ from the products, i.e. A+BC --> AB + C. As a result, the coordinate

system is different in the reagent and product channels, which implies the use of a different basis set expansion in each channel. Two common strategies have been pursued in order to address this problem.

First, it is common to deform the internal basis, either continuously or by segments, in going from reagents to products [67,68-70]. This is done in an attempt to make the basis equally efficient in representing product or reagent vibrational or rotational motions. In this method the wavefunction and its derivative must be "matched" in going from the reagent to the product channel. This method is complicated, especially if a third rearrangement channel is present, for instance, if both products A+BC -->AB+C or AC+B are allowed.

The second approach is the use of natural collision coordinates [4,52,53], which circumvents this matching problem since these coordinates go smoothly from reagents to products.

As one might expect, the symmetric $H+H_2$ reaction is the benchmark system for quantum mechanical calculations due to its light mass and the availability of an accurate potential energy surface [71,72]. This reaction is the subject of a recent review by Schatz [79]. There has been a multitude of collinear studies of this system [73-78]. There are also several accurate, fully converged, 3D $H+H_2$ studies [37-41]. These studies have mostly been concerned with the determination of differential cross sections, total cross

sections, and rate constants.

There have been relatively few quantum mechanical studies explicitly devoted to the effect of reagent rotation on reactivity [51,80]. This is due, in large part, to the rapid proliferation of quantum channels associated with the degenerate orbital angular momentum states, l, and with the 2j+1 degeneracy of the energy levels of the rotor. Because of this, the number of coupled equations one must solve increases non-linearly with j. For an atom-homonuclear diatomic molecule with j = 50 the number of coupled equations that must be solved is approximately 1275 [49]. The computational effort required to solve coupled equations varies as the cube of the number of equations, so it is clear that the problem rapidly becomes intractable even for modest j [49].

In light of this, various approximate methods for dealing with angular momenta have been developed. Chief among them are the angular momentum decoupling approximations, e.g. the centrifugal sudden approximation, CS, and the infinite order sudden approximation, IOS. These methods have been reviewed by Kouri [49] and Baer [50]. Briefly they can be described as follows.

McGuire and Kouri [81] developed the l-labeled j_z-conserving coupled states (CS) approximation, and independently and simultaneously, Pack [82] developed the J labeled centrifugal sudden (CS) approximation for inelastic scattering. For inelastic scattering the CS approximations can

be made directly by replacing orbital angular momentum operator in a space fixed coordinate system by an average eigenvalue, $l_o(l_o+1)\hbar$. Generalizing this approximation to reactive scattering is made difficult because body fixed axes of reagents and products must differ. Elkowitz and Wyatt [83] resolve this problem by using natural collision coordinates. Kuppermann et. al. [84] solves it by deforming the basis functions as the propagation proceeds.

The IOS approximation for rotationally inelastic scattering consists of replacing the eigenvalues of the rotational angular momentum operator (in the CS equations) by a single effective energy [49,50,85-88]. This method has been extended to reactive collisions by Bowman and Lee [181], Barg and Drolshagen [87], and Jellinek and Baer [89].

Clary [80] used an approximate 3D quantum scattering method based, in part, on the CS approximation in order to investigate the effect of reagent rotation on reactivity for the $H+H_2$ system. His results were in good agreement with the exact quantum mechanical results for the j values which were calculated (j = 0- 3).

An alternative way to reduce the number of close coupled equations which must be dealt with is to reduce the number of degrees of freedom of the problem, i.e. reduce the dimensionality of the problem. Mayne [51] examined the effect of reagent rotation on reactivity with the aid of a coplanar model Hamiltonian. In that work, the wavefunction was expanded

in terms of the internal states of the rotor, i.e. planar free rotor basis. The close-coupled equations were then solved exactly for motion in the translational coordinate. Classical reaction probabilities obtained from the same model Hamiltonian were found to be in good agreement with the exact quantum reaction probabilities. This model, however, did not take into account the total angular momentum of the system, J.

In this work, exact quantum reaction probabilities will be obtained for the model system developed in Chapter II, which, although very similar to that of Mayne, takes J into account. This will be done in an effort to determine; 1) the effect of reagent rotation on reactivity; and 2) the effect of nonzero J. Further, the validity of the CS and the IOS approximations will be investigated.

Exact Scattering Formalism

The main objective of this work is to obtain reaction probabilities as a function of j, $P^R(j)$, by solving the Schroedinger equation for the model A+BC system (II.5) via an exact close-coupling method. Once obtained, these exact reaction probabilities can be used as a benchmark to compare with probabilities obtained from solving the Schroedinger equation utilizing an approximate method, e.g. Centrifugal Sudden (CS) and Infinite Order Sudden (IOS).

The time-independent Schroedinger equation for any system is

$$H\,\Psi\,(s,\gamma) = E\,\Psi\,(s,\gamma) \qquad \text{(III.1)}$$

where H is the quantum mechanical Hamiltonian operator, E is the total energy of the system, and $\Psi(s,\gamma)$ is the total wavefunction. The quantum mechanical form of the model Hamiltonian (II.5) is given by

$$H = (-1/2\mu)d^2/ds^2 - (1/2I(s))d^2/d\gamma^2 + F(s)\,[J^2 - d^2/d\gamma^2 - (2J/i)d/d\gamma]/2\mu(R_m^2 + s^2) + V(s,\gamma) \qquad \text{(III.2)}$$

where $I(s)$, μ, J, and $V(s,\gamma)$ have been previously defined in Chapter II. The complex number, i, has its usual value of $(-1)^{1/2}$. Note that atomics units are used throughout this derivation, therefore $\hbar = 1$ has been omitted. The function F(s) [183] is a step function equal to unity if $|s| < s_\infty$, and equal to zero otherwise. This is needed to simplify the asymptotic form of the wavefunction. It is discussed later. In this work, since we are interested in performing a benchmark calculation for $H+H_2(j)$, the model potential for a symmetric exchange reaction will be used. The form of the symmetric reduced potential $V(s,\gamma)$ is given by equation (II.14).

The numerical solution of the Schroedinger equation for $\Psi(s,\gamma)$ is carried out by expanding $\Psi(s,\gamma)$ in an infinite basis set [65]

$$\Psi\ (s,\gamma) = \underline{g}_n\ (s;\gamma)\ \underline{\phi}_n\ (\gamma) = \sum_{n=-\infty}^{\infty} g_n(s;\gamma)\ \phi_n(\gamma) \qquad \text{(III.3)}$$

where $\underline{g}_n$ is a vector of translational coefficients and $\underline{\phi}_n$ are the basis functions.

Substitution of equations (III.2) and (III.3) into the Schroedinger equation (III.1) and left multiplying by ϕ_m^*, yields

$$\sum_{n=-\infty}^{\infty} ([< m \mid (-1/2\mu)d^2/ds^2 - (1/2I(s))d^2/d\gamma^2 + V(s,\gamma) - E + F(s)\ [J^2 - d^2/d\gamma^2 - (2J/i)d/d\gamma]/2\mu(R_m^2 + s^2)] * g_n(s;\gamma)) \mid n > \approx 0 \qquad \text{(III.4)}$$

where bra-ket notation [90,91] has been employed to represent the basis functions, ϕ_n and ϕ_m.

It is important to note that the choice for ϕ_n is arbitrary [65], but in practice a choice made with some insight into the physical nature of the problem will considerably reduce the number of terms needed in the expansion. This serves to significantly reduce the computational effort required to solve the problem. Here, since we are interested in planar rotation, we take ϕ_n to be the diabatic planar free rotor states

$$\phi_n = (1/2\pi)^{1/2} \exp(in\gamma) \quad n = 0, \pm1, \pm2, \ldots \infty \qquad \text{(III.5)}$$

which are orthogonal and normalized [165], thus

$$< m \mid n > = \delta_{mn} \qquad \text{(III.6)}$$

The planar free rotor states, ϕ_n, are eigenfunctions of the operator, $(-1/2I)\ d^2/d\gamma^2$, therefore

$$(-1/2I(s))d^2/d\gamma^2 \mid n > = E_n(s) \mid n >. \qquad \text{(III.7)}$$

where $E_n(s)$ is the eigenvalue of $\mid n >$, i.e. the energy of the rotor state, ϕ_n. The energy of the rotor is given by [165]

$$E_n(s) = n^2/2I(s). \qquad \text{(III.8)}$$

Using equations (III.6) and (III.7), equation (III.4)

simplifies to the matrix representation of the Schroedinger equation in the ϕ_n basis

$$\sum_{n=-\infty}^{\infty} \{(-1/2\mu)\ \delta_{mn} d^2/ds^2 + E_n\ \delta_{mn} + V_{mn} - E\ \delta_{mn} + F(s)\ \delta_{mn}\ (J^2 + n^2 - 2Jn)/2\mu(R_m^2 + s^2)\}\ g_n\ (s) = 0 \qquad \text{(III.9)}$$

where V_{mn} is the potential energy matrix which couples ϕ_n to ϕ_m, which is given by

$$V_{mn} = < m\ |V(s,\gamma)|\ n > \qquad \text{(III.10)}$$

Truncating the infinite basis to some finite number, $j_{max} = N$, yields 2N+1 coupled second order differential equations which run from $-j_{max}$ .. 0 .. $+j_{max}$. Rearranging equation (III.9) the coupled equations take the form

$$d^2/ds^2(g(s))_m = \{2\mu\ V_{mn} - k_n^2\ \delta_{mn}\}(g(s))_n \qquad \text{(III.11)}$$

where the translational wavenumber, k_n is given by

$$k_n = \{2\mu\ (E - E_n) - F(s)(J^2 + n^2 - 2Jn)/(R_m^2 + s^2)\}^{1/2} \qquad \text{(III.12)}$$

and g(s) is a column vector of length 2N+1 beginning with g_{-N} and ending with g_N. When k_n is real the n^{th} channel is energetically accessible and the channel is said to be open; if k_n is imaginary the channel is not energetically accessible, and the channel is said to be closed [65]. Equation (III.11) can be written in the matrix form

$$d^2/ds^2\ \underline{g} = \mathbf{W}\ \underline{g} \qquad \text{(III.13)}$$

where **W** is the matrix

$$\mathbf{W} = 2\mu\ V_{mn} - k_n^2\ \delta_{mn}. \qquad \text{(III.14)}$$

There are a variety of numerical methods which could be

adopted in order to solve equation (III.13) [62,65,166,167,170]. In this work, the matrix equation (III.13) is solved by converting the 2N+1 second order differential equations into 2(2N+1) first order differential equations [65]. Substitution of the definitions

$$\underline{g}' = d\underline{g}/ds \tag{III.15}$$

$$d\underline{g}'/ds = \mathbf{W}\,\underline{g} \tag{III.16}$$

into equation (III.13) gives the new matrix equation

$$d/ds \begin{pmatrix} \underline{g} \\ \underline{g}' \end{pmatrix} = \begin{pmatrix} 0 & 1 \\ \mathbf{W} & 0 \end{pmatrix} \begin{pmatrix} \underline{g} \\ \underline{g}' \end{pmatrix} \tag{III.17}$$

which can be solved using any standard initial value integration technique [65,94]. Since 2(2N+1) linearly independent solutions of (III.17) are needed [65], $\underline{g}$ must be expanded to a matrix, $\mathbf{g}$, the columns of which contain the 2(2N+1) linearly independent solutions. The matrix, $\mathbf{g}$, can be written in the block form

$$\mathbf{g} = \begin{pmatrix} \mathbf{G}_1 & \mathbf{G}_2 \\ \mathbf{G}_1' & \mathbf{G}_2' \end{pmatrix} \tag{III.18}$$

where each matrix, $\mathbf{G}$, is a 2N+1 square matrix and primes denote derivatives with respect to s.

In this work, the matrix equation (III.17) was integrated with 2(2N+1) initially linearly independent starting conditions by a fourth order Runge-Kutta-Gill method [94] in order to obtain the solution matrix, $\mathbf{g}$. At the start of the

integration g was taken to be the unit matrix [65]. Periodic reorthogonalization of g during the integration was used to insure the linear independence of solutions [95].

Once the solution matrix is obtained, the solutions are matched to the asymptotic boundary conditions to obtain the transmission and reflectance matrices [32,62,65,168] and ultimately the reaction probabilities.

Periodic Reorthogonalization

The problem associated with solving equation (III.17) by the numerical procedure described above is as follows. The translational solutions associated with the closed channels grow exponentially [62,65] which will result in computer overflow problems. As was mentioned above, this will destroy the linear independence of solutions [65,95].

In order to avoid this problem, during integration of the first order equations a transformation must be applied to the solution matrix at selected s points, (s_1) [95]. The transformation is given by

$$\begin{pmatrix} G_1 & G_2 \\ G_1' & G_2' \end{pmatrix} \rightarrow \begin{pmatrix} G_1(G_1)^{-1} & G_2(G_2')^{-1} \\ G_1'(G_1)^{-1} & G_2'(G_2')^{-1} \end{pmatrix} = \begin{pmatrix} 1 & G_2(G_2')^{-1} \\ G_1'(G_1)^{-1} & 1 \end{pmatrix} \qquad \text{(III.19)}$$

Application of the transformation (III.19) insures the off diagonal elements of equation (III.18) remain small.

Calculation of the Transmission and Reflectance Matrices

In the asymptotic regions, $|s| = \infty$, the system is uncoupled. Therefore the g matrix elements are now decoupled from γ and thus are only a function of s, i.e. $g_n(s)$. The consequence of this is that the $g_n(s)$ are now the translational wavefunctions and therefore are the solutions to the translation portion of the problem [62,65]

$$d^2\underline{g}_n/ds^2 = -\underline{k}_n^2\underline{g}_n \qquad \text{(III.20)}$$

where $\underline{k}_n$ is defined by equation (III.12). Since the second term in this equation complicates the asymptotic solutions, and is not physically significant for large s, we use a switching function F(s) to set it to zero outside the region of interest, $-s_\infty \leq s \leq s_\infty$. In the asymptotic region the interaction potential has gone to zero and equation (III.12) takes the familiar form $\underline{k}_n = [2\mu(E - E_n)]^{1/2}$. However, in practice the integration is carried out to $|s| = 4.0$ bohr, where the interaction potential is zero, but the second term in (III.12) has not yet gone to zero. This is due to the $1/s^2$ dependence. Reaction probabilities obtained by utilizing equation (III.12) and equation (III.12) without the F(s) term have been compared and were found to be equivalent to 3 decimal places. Thus all the exact reaction probabilities reported in this work were calculated by the method previously described using equation (III.12) to match the wavefunction in the asymptotic region.

The asymtotic solutions now become the plane waves

$$g_n(s) = \exp(\pm i\underline{k}_n s) \qquad \text{(III.21)}$$

In the entrance channel, the wavefunction consists of incoming plane waves, i.e. $\exp(+i\underline{k}_n s)$, and reflected plane waves, i.e. $\exp(-i\underline{k}_n s)$. In the product channel the wavefunction is composed of transmitted plane waves. The total wavefunction in the reagent channel is therefore given by

$$\Psi = \underline{j} - \mathbf{r}\,\underline{\eta} \qquad \text{(III.22)}$$

and in the product channel by

$$\Psi = -\mathbf{t}\,\underline{\kappa} \qquad \text{(III.23)}$$

where

$$\underline{j} = \delta_{mn} \exp(ik_m s(-)) \qquad \text{(III.24)}$$

$$\underline{\eta} = \delta_{mn} \exp(-ik_m s(-)) \qquad \text{(III.25)}$$

$$\underline{\kappa} = \delta_{mn} \exp(ik_m s(+)) \qquad \text{(III.26)}$$

where $s(-)$ denotes the value of s in the reagent valley at a point where the coupling is negligible and $s(+)$ is the s value in the product valley where the coupling is negligible, $\mathbf{r}$ is the reflectance coefficient matrix and $\mathbf{t}$ is the transmission coefficient matrix. In the asymptotic region the total wavefunction is given by a linear combination of the solutions G_1 and G_2 [65], using this fact and equations (III.22) and (III.23) yields the two relationships

$$\mathbf{A}\,G_1(-) + \mathbf{B}\,G_2(-) = \underline{j} - \mathbf{r}\,\underline{\eta} \qquad \text{(III.27)}$$

$$\mathbf{A}\,G_1(+) + \mathbf{B}\,G_2(+) = -\mathbf{t}\,\underline{\kappa} \qquad \text{(III.28)}$$

where $\mathbf{A}$ and $\mathbf{B}$ are matrices which contain the linear combination coefficients, $G_1(-)$ and $G_2(-)$ are the solution matrices at $s = -\infty$, and, similarly, $G_1(+)$ and $G_2(+)$ are the

solution matrices at $s = +\infty$.

The derivative of the wavefunction must also be matched to the asymptotic boundary conditions, giving

$$\mathbf{A}\,\mathbf{G}_1'(-) + \mathbf{B}\,\mathbf{G}_2'(-) = \underline{j}' - \mathbf{r}\,\underline{n}' \qquad \text{(III.29)}$$

$$\mathbf{A}\,\mathbf{G}_1'(+) + \mathbf{B}\,\mathbf{G}_2'(+) = -\mathbf{t}\,\underline{\kappa}' \qquad \text{(III.30)}$$

where the primes denote the derivative with respect to s, as before. The result of matching the wavefunction and its derivative in the asymptotic region is a system of four equations (III.27-III.30) and four unknown matrices, **A**, **B**, **r**, and **t**, which can be solved for using standard matrix algebra, as follows.

Rearrangement of (III.27) and (III.28) gives the expression for the transmission and reflectance coefficient matrices, respectively. They have the form

$$\mathbf{t} = -[\mathbf{A}\mathbf{G}_1(+) + \mathbf{B}\mathbf{G}_2(+)](\underline{\kappa})^{-1} \qquad \text{(III.31)}$$

$$\mathbf{r} = -[\mathbf{A}\mathbf{G}_1(-) + \mathbf{B}\mathbf{G}_2(-) - \underline{j}](\underline{n})^{-1} \qquad \text{(III.32)}$$

Equating **t** from (III.28) and (III.30) and solving for **A** yields

$$\mathbf{A} = \mathbf{BXY} \qquad \text{(III.33)}$$

where

$$\mathbf{X} = \mathbf{G}_2'(+)\ (\underline{\kappa}')^{-1} - \mathbf{G}_2(+)\ (\underline{\kappa})^{-1} \qquad \text{(III.34)}$$

$$\mathbf{Y} = [\mathbf{G}_1(+)\ (\underline{\kappa})^{-1} - \mathbf{G}_1'(+)\ (\underline{\kappa}')^{-1}]^{-1}. \qquad \text{(III.35)}$$

Eliminating **r** from (III.27) and (III.29) and using (III.33) gives the expression for **B**

$$\mathbf{B} = [\underline{j}(\underline{n})^{-1} - \underline{j}'(\underline{n}')^{-1}][\mathbf{XYC} + \mathbf{D}]^{-1} \qquad \text{(III.36)}$$

where **C** and **D** are given by

$$\mathbf{C} = \mathbf{G}_1(-)(\underline{n})^{-1} - \mathbf{G}_1'(-)(\underline{n}')^{-1} \qquad \text{(III.37)}$$

$$D = G_2(-)(\underline{n})^{-1} - G_2'(-)(\underline{n}')^{-1}. \qquad \text{(III.38)}$$

The reflection and transmission matrices, **R** and **T**, are defined as [65]

$$T_{mn} = (k_m/k_n)^{1/2}\, t_{mn} \qquad \text{(III.39)}$$

$$R_{mn} = (k_m/k_n)^{1/2}\, r_{mn}. \qquad \text{(III.40)}$$

It is important to note that T_{mn} and R_{mn} are matrix representations. In this case, since we are dealing with rotor states T_{mn} and R_{mn} can be relabeled as

$$T_{j'j} = (k_{j'}/k_j)^{1/2}\, t_{j'j} \qquad \text{(III.39)}$$

$$R_{j'j} = (k_{j'}/k_j)^{1/2}\, r_{j'j} \qquad \text{(III.40)}$$

where j represents the initial state, ϕ_j, and j' the final rotor state, $\phi_{j'}$.

The total reaction probability of going from an initial reagent state, ϕ_j, to a final product state, $\phi_{j'}$, $P^R_{j'j}$, is given by

$$P^R_{j'j} = |T_{j'j}|^2 \qquad \text{(III.41)}$$

and the state to state inelastic scattering probability is given by

$$P^I_{j'j} = |R_{j'j}|^2 \qquad \text{(III.42)}$$

both of which are symmetric functions of channel indices, due to microscopic reversibility [35,62,65]. Additionally, conservation of flux requires [65]

$$\sum_{j'} |T_{j'j}|^2 + |R_{j'j}|^2 = 1. \qquad \text{(III.43)}$$

The total reaction probability must be summed over all product states and is therefore given by

$$P^R_j = \sum_{j'} P^R_{j'j} \qquad \text{(III.44)}$$

Calculation of Reaction Probabilities: Implementation

Typically, problems of this sort are integrated from the nonclassical region to the classical region [62], that is, from s = 0 out to $-\infty$ and, similarly, from s = 0 to s = $+\infty$. In this case, since the problem of interest is symmetric, that is, the same number of channels are open in the reagent and product channels, the integration only needs to be performed from s = 0 to s = $+\infty$ or from s = 0 to s = $-\infty$. The solutions g(-) and g(+) are equal on the diagonal and differ by a sign on the off diagonal. Physically this means that the products are identical with the reagents.

Since the matching is performed at large s values, where the elements of the solution matrix for the closed channels are very small, it is only necessary to include the open channels when solving for **r** and **t** [62,65].

A word regarding the difference between the total energy, E, and the translational energy, E_t, is in order at this time. The translational energy is given by

$$E_t = E - E_n \qquad \text{(III.46)}$$

where E_n is the energy associated with the channel, n. Coupled channel, and in general quantum mechanical, calculations are carried out at fixed total energy, E. Analysis of equation (III.46) reveals that for a fixed total energy, E, each channel will have a translational energy which is less (except in the case of n = 0) than the total energy. In order to compare reaction probablities at a fixed translational energy,

E_t, the close-coupling calculation must be repeated for each channel with the total energy increased in order to yield the corresponding E_t. In this work, reaction probabilities are reported for fixed translational energies. This was done so that quantum $P^R(j)$ could be compared to classical $P^R(j)$, which are calculated at fixed translational energy.

Lastly, if one were interested in an exoergic reaction, $F+H_2$ for example, or in an endothermic reaction the number of open channels in the product channel and in the reagent channel would differ. In order to solve the close coupling equations in this case several points must be considered. Chief among them is the following. Due to the differing number of product and reagent channels the solutions matrices, $G_1(+)$ and $G_2(-)$, will be of differing dimension. In this case the integration must be performed in both channels separately. One method for obtaining the reaction probabilities in this case has been discussed by Light [62].

Calculation of the Potential Energy Matrix Elements

Before numerical integration of (III.17) can be undertaken the potential energy matrix elements, V_{mn}, i.e. the coupling matrix, must be determined. That is to say, the matrix (III.10) must be evaluated in order to carry out the propagation in s.

The symmetric model potential $V(s,\gamma)$ is given by equation (II.14). The s dependence of this model potential is given by a symmetric Eckart function [59]. An advantage to this model

form is that the model potential can be written in the separable form

$$V(s,\gamma) = V_o(s)\ \sin^2(\gamma) \qquad \text{(III.47)}$$

where $V_o(s)$ is the symmetric Eckart function. This is equivalent to writing

$$V(s,\gamma) = V_o(s)\ \{[2 - \exp(2i\gamma) - \exp(-2i\gamma)]/4\}. \qquad \text{(III.48)}$$

Substitution of (III.48) into V_{mn} (III.10) and recalling the form of the basis functions (III.5) yields matrix elements of the form

$$V_{mn}(s) = V_o(s)\ \{(2\ \delta_{m,n} - \delta_{m+2,n} - \delta_{m-2,n})/4\} \qquad \text{(III.49)}$$

which is a banded, sparse, symmetric matrix. Thus it is the off diagonal potential matrix elements (III.49) which serve to couple one channel, n to another channel, m. Substitution of (III.49) into (III.14) yields the form of the **W** matrix

$$W = V_{mn}(s) - [2\mu(E-E_n) - F(s)\ (J^2 + n^2 - 2Jn)/(R_n^2 + s^2)]\ \delta_{mn} \qquad \text{(III.50)}$$

Inspection of (III.50) reveals that for fixed total J, the orbital angular momentum, l = (J - j), will be different for each state in the 2N+1 state expansion. Further, the orbital angular momentum appears only on the diagonal.

Convergence Criteria

In order to establish the accuracy of these calculations several convergence and accuracy tests were performed. They are: 1) tests of flux conservation and microscopic reversibility and 2) invariance of the results with respect

to inclusion of additional terms in the planar rotor state expansion.

Microscopic reversibility requires that the state to state reaction probabilities, $P^R_{j',j}$ (III.41), and inelastic scattering probabilities, $P^I_{j',j}$ (III.42) are symmetric with respect to channel indices. In other words, $P^R_{j',j} = P^R_{jj'}$ and similarly for the inelastic probabilities, $P^I_{j',j} = P^I_{jj'}$.

State to state reaction probabilities for the test case E = 0.10 eV when J = j are shown in Table III.1. Analysis of this matrix shows that the $P^R_{j',j}$ matrix is symmetric with respect to channel indices, in fact the agreement in most cases is exact to 4 decimal places. This is also the case for the inelastic reaction probabilities, $P^I_{j',j}$, at E = 0.10 eV when J = j; shown in Table III.2.

As the total energy, E, of the system is increased the number of open channels will increase, thus a larger number of basis sets may be required. Typical questions include; 1) Will this have a detrimental effect on the accuracy of R and T? and 2) Will large values of total angular momentum, J, or large rotational quanta in the diatom, j, adversely affect the accuracy of these matrices? Selected $P^R_{j',j}$ and $P^I_{j',j}$ at E = 0.35 eV when J = 20 and j = 12 are shown in Tables III.3 and III.4. Although the symmetry of these matrices is not almost "exact" as in the low energy, zero angular momentum case, it is nonetheless very good. Thus, microscopic reversibility is satisfied. Flux conservation demands that the elements of any

row or column of the total $P^R_{j',j}$ and the $P^I_{j',j}$ matrices sum to 1.0. Analysis of Table III.1 or III.2 demonstrates that flux conservation is satisfied.

In order to check convergence with respect to the number of basis functions used in the expansion, a trial run was performed at E = 0.15 and one at E = 0.35 eV (results shown in Tables III.5 and III.6, respectively). Here, reaction probabilities obtained utilizing 39 basis functions are compared to those obtained using 49 basis functions. Even at high energy there is no significant difference in the $P^R(j)$ for the J = j or the J ≠ j case. The deviation of the calculated flux from the ideal value of 1.0 is also given in Tables III.5 and III.6. This value was obtained by examination of the flux associated with all the open channels for a given energy, J, and j value. The value which most deviated from unity is given in Tables III.5 and III.6. The flux deviation is greater than 1.0 % in only one instance. In most cases it is no greater than 0.5 %. These values are considered acceptable in view of comparison with other close-coupling calculations where errors of 5.0 % are considered acceptable [35].

Therefore in light of all the above data and due to the greater speed of the 39 basis function calculations, this is the number of basis functions used throughout this work.

Approximate Scattering Formalism

Centrifugal Sudden

The quantum centrifugal sudden approximation (CS) makes the assumption that all the orbital angular momentum states, l, are degenerate, that is, l is equivalent for each channel in the 2N+1 state expansion [48-50].

The consequence of this assumption is the replacement of the orbital angular momentum operator, $(J-j)^2$, in the quantum model hamiltonian (III.2) with a constant orbital angular momentum term, l_o^2. Therefore, the quantum mechanical centrifugal sudden Hamiltonian is given by

$$H_{CS} = -(1/2\mu)d^2/ds^2 - (1/2I(s))d^2/d\gamma^2 + F(s)\ l_o^2/[2\mu(R_m^2 + s^2)] + V(s,\gamma). \qquad \text{(III.51)}$$

It should be noted that in the limit of $l_o = 0$ the CS Hamiltonian reduces to the Hamiltonian of Mayne [51]. However, this is not the case for the exact Hamiltonian (III.2), since $l^2 = (J^2 + n^2 - 2Jn)$, i.e. l differs for all states in the 2N+1 expansion.

Substitution of the CS hamiltonian into the Schroedinger equation (III.1), expanding in an infinite basis, and left multiplying by $< m |$, as before, gives

$$\sum_{n=-\infty}^{\infty} \{< m |-(1/2\mu)d^2/ds^2 - (1/2I(s))d^2/d\gamma^2 + V(s,\gamma) + F(s)\ l_o^2/2\mu(R_m^2+s^2) - E|\ n >) = 0. \qquad \text{(III.52)}$$

Making use of (III.5) and (III.7), as in the exact case, after truncation of the basis and rearrangement (III.52) becomes

$$d^2/ds^2(g(s))_m = (2\mu\ V_{mn} - 2\mu(E-E_n)\ \delta_{mn} + F(s)\ l_o^2/(R_m^2 + s^2)\ \delta_{mn})\ (g(s))_n \qquad \text{(III.53)}$$

where V_{mn} is given by equation (III.10). Equation (III.53) can

be written in a form similar (III.16) where **W** is given by

$$\mathbf{W} = 2\mu\, V_{mn} + F(s)\{[l_o^2/(R_m^2 + s^2)]\ \delta_{mn} + 2\mu(E - E_n)\ \delta_{mn}\} \qquad \text{(III.54)}$$

Equation (III.53) is propagated by the same procedure outlined for the exact close coupling case. Once the solutions, **g**, are obtained the transmission and reflection matrices, **T** and **R**, are obtained as in the exact case.

Calculation of the Effective Potential Matrix Elements

The first two terms in the expression for **W** can be thought of as an effective potential [169], $V_{eff}(s,\gamma)$, which can be written in the form

$$V_{eff}(s,\gamma) = V_1(s) + V_o(s)\ \sin^2(\gamma) \qquad \text{(III.55)}$$

where $V_1(s)$ is given by

$$V_1(s) = F(s)\ l_o^2/[2\mu(R_m^2 + s^2)] \qquad \text{(III.56)}$$

and $V_o(s)$ is the symmetric Eckart function as in the exact case. The effective potential matrix elements, $(V_{eff})_{mn}$, are

$$(V_{eff})_{mn} = \{< m \mid V_1(s) \mid n > + < m \mid V_o(s)\ \sin^2(\gamma) \mid n >\}. \qquad \text{(III.57)}$$

Realizing that $V_1(s)$ is not a function of γ and using the result given in (III.49) the effective potential energy matrix elements (III.57) reduce to

$$(V_{eff})_{mn} = V_1(s)\ \delta_{mn} + V_o(s)\{(2\ \delta_{mn} - \delta_{m-2,n} - \delta_{m+2,n})/4\}. \qquad \text{(III.58)}$$

which when substituted into (III.54) yields

$$\mathbf{W} = 2\mu(V_{eff})_{mn} - 2\mu(E - E_n). \qquad \text{(III.59)}$$

Thus in the CS approximation the channels are coupled by the

potential only as in the exact case. The orbital angular momentum is a constant for each channel in the 2N+1 channel expansion in contrast to the exact scattering method, where l is different for each channel. The orbital angular momentum appears only as a constant on the diagonal of the W matrix.

Infinite Order Sudden

Taking the CS approximation further, in addition to making the assumption that all orbital angular momentum states are degenerate the quantum infinite order sudden approximation (IOS) also assumes all rotational states are degenerate, i.e. the energy sudden approximation [49]. In light of this, we begin with the CS hamiltonian (III.51) and therefore with the matrix equation (III.53). The energy sudden condition is given by [96]

$$dg(s,\gamma)/d\gamma = 0 \qquad \text{(III.60)}$$

which is equivalent to carrying out the scattering calculations at fixed γ. The consequence of the implementation of the energy sudden condition is that the form of the coupling matrix, V_{mn}, and thus the W matrix is simplified. The infinite order sudden potential matrix is given by

$$(V_{IOS})_{mn} = (V_o(s)\ \sin^2(\gamma_p) + V_1(s))\ \delta_{mn} \qquad \text{(III.61)}$$

where γ is no longer a variable but a parameter, γ_p. Note that this makes the potential matrix diagonal. Substitution of (III.61) into the right hand side of (III.53) gives the IOS form of the matrix equation

$$d^2/ds^2\ (g(s))_m = (\ 2\mu(V_{IOS})_{mn}$$

$$- 2\mu(E-E_n)\ \delta_{mn}\ )\ (g(s))_n \qquad \text{(III.62)}$$

where **W** is now equal to $2\mu(V_{IOS})_{mn} - 2\mu(E - E_n)\ \delta_{mn}$. Therefore in the IOS approximation, since the **W** matrix is diagonal, one can solve each channel separately. Due to the fact that **W** is diagonal, there is no need for periodic reorthogonalization of the **g** matrix.

The scattering solutions to (III.62) obey the same asymptotic boundary conditions [96] as the exact scattering solutions.

Before continuing, there are several points which should be made. First, in the IOS approximation there is no coupling between channels and the scattering calculation is carried out at fixed γ_p. This means that the transmission matrix elements, $T_{j'j}$ (III.41), cannot be obtained as they were in the exact case. In the IOS approximation only the diagonal elements of $T_{j'j}$, i.e. $j' = j$, are nonzero after the solution of the matrix equation (III.62). Since $j' = j$, we chose to label these matrix elements with only one index. Further, since the calculation is done at fixed γ_p we denote these matrix elements as $T_j(\gamma_p)$. In practice equations (III.22-III.33) are solved at fixed γ_p for the diagonal $T_j(\gamma_p)$ elements. After γ has been scanned from 0 to 2π we have an array of $T_j(\gamma_p)$ elements which we denote as $T_j(\gamma)$. In the IOS approximation, in order to obtain the state to state transmission matrix elements, $T_{j'j}$, the γ dependence of these elements must be built "back" into the solutions. Thus we obtain the sandwich

integral for $T_{j',j}$ [97]

$$T_{j',j} = \langle j' \mid T_j(\gamma) \mid j \rangle \qquad \text{(III.63)}$$

where the integration is over all values of γ_p. Here, the final state, j', is being projected onto the initial state, j.

Calculation of $T_{j',j}$ and the Total Reaction Probabilities

Evaluation of (III.63) is, in general, accomplished by numerical quadrature. The choice of quadrature method depends of the form of the basis involved. For example, if the total wavefunction is expanded in terms of the harmonic oscillator functions then the method of choice would be a Gauss-Hermite quadrature. In this case, since the free planar rotor states were used in the expansion, $T_{j',j}$, has the form

$$T_{j',j} = (2\pi)^{-1} \int_0^{2\pi} \exp(-ij'\gamma) T_j(\gamma) \exp(ij\gamma)\, d\gamma \qquad \text{(III.64)}$$

which can be easily evaluated by forward Fast Fourier transform [94,98].

In general the forward Fourier coefficients, C_m, are given by [98]

$$C_m = (2\pi)^{-1} \int_0^{2\pi} f(x) \exp(-imx)\, dx \qquad \text{(III.65)}$$

where f(x) must be a periodic function over the interval 0 to 2π. In this case, equation (III.65) has the form

$$T_{j',j} = (2\pi)^{-1} \int_0^{2\pi} f(\gamma)\, \exp(-ij'\gamma)\, d\gamma \qquad \text{(III.66)}$$

where

$$f(\gamma) = T_j(\gamma) \exp(ij\gamma). \qquad \text{(III.67)}$$

Therefore for a given state, ϕ_j, once the $T_j(\gamma)$ coefficients have been determined the transmission matrix elements, $T_{j',j}$,

going from an initial state, ϕ_j, to all final states, $\phi_{j'}$, are easily obtained.

The total probability of scattering out of an initial state, ϕ_j, into a final state, $\phi_{j'}$, $P^R_{j',j}$, is obtained in the following way.

First, note from an analysis of equations (III.62) and (III.63) that the only term which is dependent upon the scattering state is $2\mu(E - E_n)$. As a result, the $T_j(\gamma_p)$ elements for two initial states, say ϕ_0 and ϕ_1, at a given total energy obey the relationship

$$T_1\ (\gamma_p;E_t) = T_0\ (\gamma_p;(E_t + E_1)). \qquad \text{(III.68)}$$

The validity of equation (III.68) was proven with a trial run at E = 0.1 eV for ϕ_0 and E_t = 0.1 eV for ϕ_1. Therefore one only needs to calculate the elements $T_0(\gamma_p)$ at the appropriate E for the initial state of interest, in order to obtain the $T_j(\gamma_p)$. The total reaction probability for scattering out of the initial state, ϕ_0, into any product state [96], $\phi_{j'}$, is given by

$$P^R_{j'0} = |T_{00}|^2 + \sum_{j'>0} |T_{j'0}|^2 + \sum_{j'<0} |T_{j'0}|^2 \qquad \text{(III.69)}$$

Scattering out of the ϕ_0 state to a final state, $\phi_{j'}$, where $j' < 0$, involves a backward Fourier transform [182]. It is quite easily shown, that due to the symmetry of the functions, the backward transform is equivalent to the forward transform therefore equation (III.69) reduces to

$$P^R_{j'0} = |T_{00}|^2 + 2\sum_{j'>0} |T_{j'0}|^2 \qquad \text{(III.70)}$$

where $P^R_{j'0}$ is the total reaction probability of scattering out

of any initial state to all final states, $\phi_{j'}$, providing the total energy has been adjusted accordingly.

In actual practice, for a given initial state, ϕ_j, equation (III.62) is solved at several fixed γ_p values to obtain an array of $T_j(\gamma_p)$ [96] values. The fixed γ_p values are used as the abscissa values for the Fast Fourier transform algorithm [98].

Here, no attempt was made to optimize the FORTRAN code used to calculate the reaction probabilities. However, a few general comments can be made in regard to the simplifications inherent in the IOS approximation as compared with the exact and the CS methods.

The IOS is a simpler method than either the exact or the CS methods since one need not expand in a set of basis functions at all, but rather one only needs to propagate one channel at a time. As was shown previously this only needs to be done for the j = 0 channel. Further, in this case the fact that $V(s,\gamma)$ is a symmetric function could be utilized to reduce the number of orientations for which the propagation must be preformed. Lastly, in this case, once $T_0(\gamma_p)$ is obtained all the $T_{j'0}$ elements can be calculated with one call to the Fast Fourier Transform routine. Therefore it is apparent that the IOS is, in general, much faster and simpler than either the exact or the CS methods.

The only possible loss of computational speed might arise from the quadrature associated with the calculation of $T_{j'0}$.

Since the quadrature method is determined by the choice of basis functions, functions other than the planar free rotor states would undoubtedly involve a quadrature method which is not as powerful as the Fast Fourier transform. That is, once the $T_0(\gamma_p)$ are obtained one call to the forward transform yields all the $T_{j'0}$ elements, another quadrature method would have to be called once for each final state.

Results and Discussion

Exact reaction probabilities (III.44) as a function of translational energy ($P^R(E_t)$) when J = j = 0 for the symmetric model $H+H_2$ reaction are shown in Figure III.1. The $P^R(E_t)$ increases very rapidly between E_t = 0.05 eV and 0.125 eV, where it reaches a maximum. As the translational energy is increased further, the $P^R(E_t)$ begin to decrease slowly with E_t.

Exact reaction probabilities, $P^R(j)$, carried out with J = j, are shown in Figure III.2 for several translational energies. The $P^R(j)$, in general, exhibit two basic trends. They are: 1) At low translational energy, 0.10 eV, the $P^R(j)$ decrease with increasing j, reach a minimum, then increase as j is increased to 12; 2) At high translational energy, 0.35 eV, the $P^R(j)$ increase monotonically with increasing j. These results are in good quantitative agreement with the results of Mayne [51]. In that work, a truncated Hamiltonian which essentially forced l = 0 for all channels was used. In this work, although l=0 for the channel of interest, l is nonzero for all other coupled channels (III.11 and III.12). It is also

interesting to note that the $P^R(j)$ appear to have a bit of structure, i.e. oscillatory behavior, at low translational energies, while at high energy the $P^R(j)$ are very smooth. This is not unexpected since quantum effects, e.g. resonances and interferences, are expected to be more pronounced at low energies [46].

Exact reaction probabilities as a function of the total angular momentum, $P^R(J)$, carried out at fixed j are shown in Figure III.3. In all cases, the general trend is for the $P^R(J)$ to decrease with increasing J. This same trend was observed in exact 3D $H+H_2$ calculations carried out by Schatz and Kuppermann [38].

In Figure III.4 exact $P^R(j)$ at fixed orbital angular momentum, l, are shown. At both the translational energies examined the $P^R(j)$ decrease as l is increased for fixed j. Furthermore, at 0.35 eV as l is increased the $P^R(j)$ begin to show a significant amount of structure. This could be due to the appearance of resonances or some type of interferences [46]. These effects could also be responsible for the appearance of a spike in the $P^R(j)$ at $j = 4$ when $E_t = 0.15$ eV and $l = 6$.

Now the validity of the CS and the IOS decoupling approximations can be discussed. The $P^R(j)$ at several translational energies for zero as well as nonzero values of l, obtained via the CS approximation (III.53) are shown in Figure III.5. When $l = 0$ the CS $P^R(j)$ are in qualitative

agreement with the exact $P^R(j)$ at both low, 0.15 eV, and high, 0.35 eV, translational energies. For nonzero values of l, the agreement between the CS $P^R(j)$ and the exact $P^R(j)$ is still fairly good; however the tendency is for the agreement to become less quantitative as l is increased. This trend has also been observed by Elkowitz and Wyatt [83] and McGuire and Kouri [81].

In light of the above results, we can conclude that in general the CS approximation does a good job reproducing trends in exact $P^R(j)$. Thus it is a fairly reasonable approximation.

The $P^R(j)$ obtained via the IOS approximation (III.62 and III.70) at fixed l are shown in Figure III.5. Close to threshold, 0.15 eV, the IOS $P^R(j)$ are not in qualitative agreement with the exact $P^R(j)$. At high energy, 0.35 eV, the IOS does a better job, that is, the $P^R(j)$ are, at least, in qualitative agreement with the exact $P_R(j)$. However this result is fortuitous since in this model the IOS always yields $P^R(j)$ that increase with increasing j. In its favor, the IOS does reproduce the correct qualitative trend for nonzero l, i.e. the $P^R(j)$ decrease with increasing l.

The fact that the IOS approximation does a poor job of reproducing rotational trends is not a complete surprise in light of other work [85,99,105]. Thus the IOS is most often used in problems were $P^R(j)$ are not desired, i.e. vibrational state to state probabilities of reaction are desired, in order

to simplify the coupled equations.

The IOS approximation still may be of some use in predicting trends in $P^R(j)$ in systems where the collision is more "sudden", e.g. **L** + **HH** (Chapter IV), or when one is interested in energies far from threshold. Note that this mass combination would be difficult to use in quantum mechanical calculations due to the large basis set required for the exact $P^R(j)$. In contrast, the IOS would have no such difficulty.

Fig. III.1 Exact quantum reaction probabilities as a function of E_t calculated on the symmetric reduced potential with J=j=0.

III.1

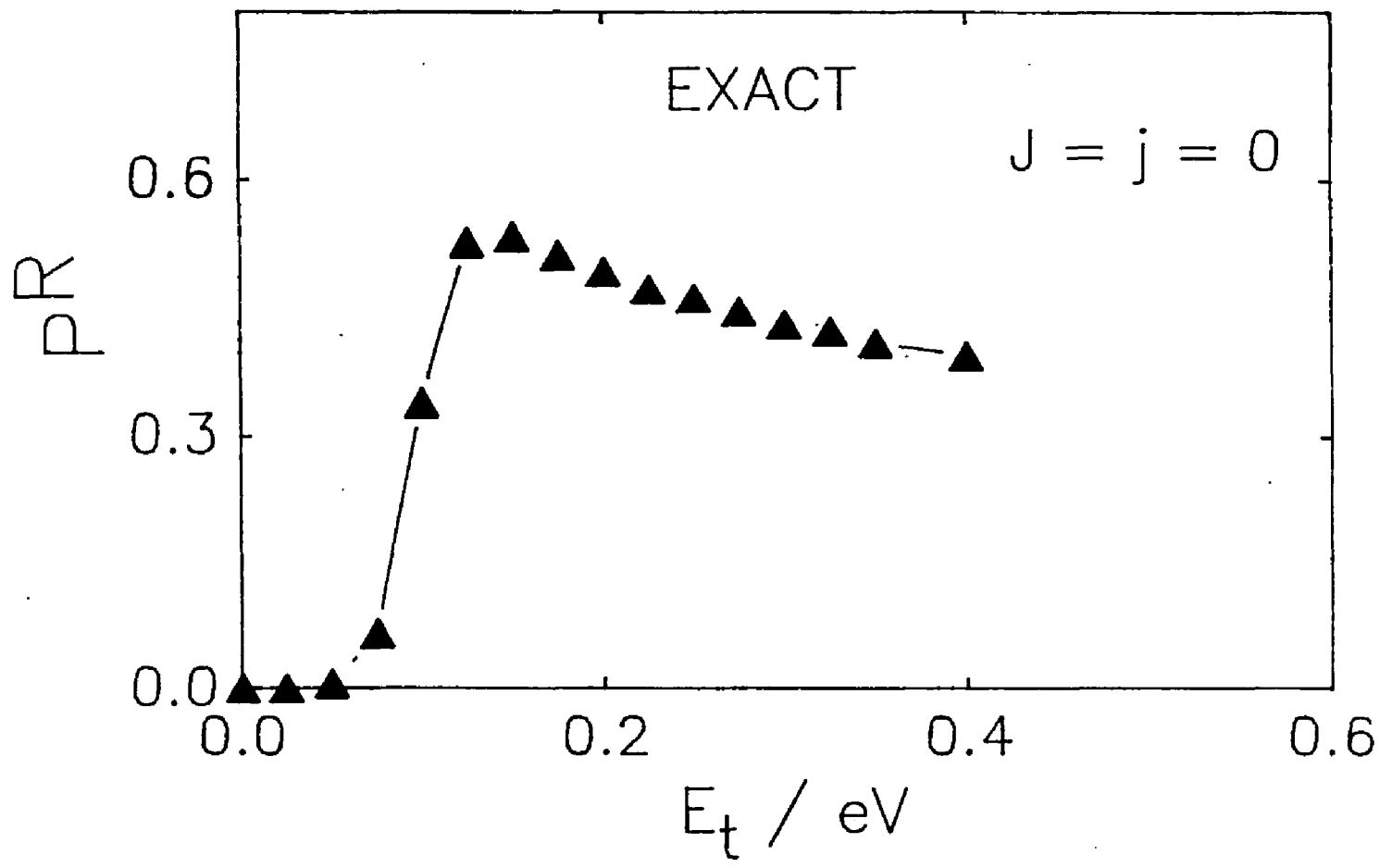

Fig. III.2 Exact quantum reaction probabilities as a function of j calculated on the symmetric reduced potential with J=j. Translational energies are 0.35, 0.15 and 0.10 eV.

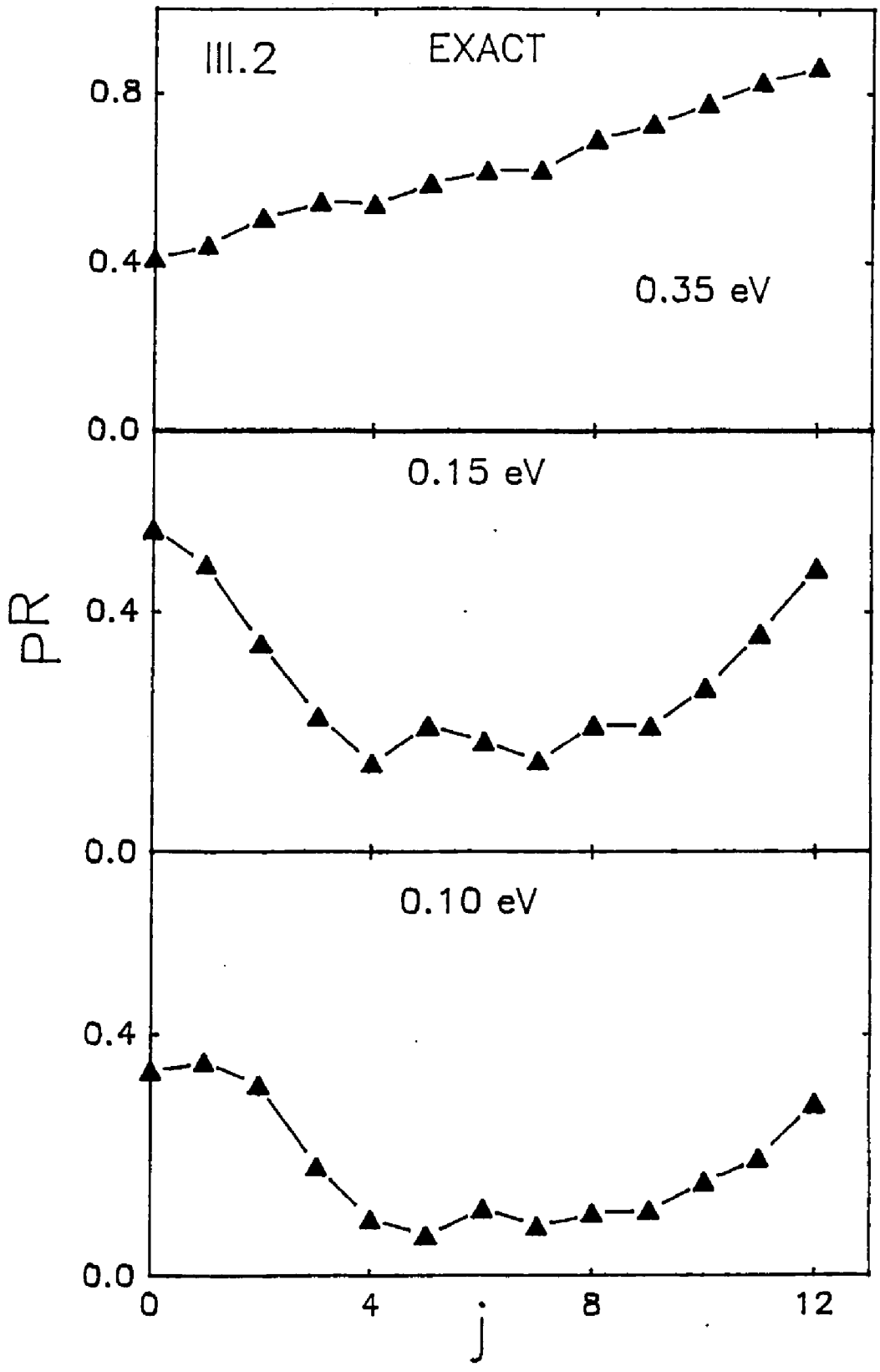
III.2
EXACT
0.8
0.4
0.0
0.35 eV
0.15 eV
PR
0.4
0.0
0.10 eV
0.4
0.0
0
4
8
12
j

Fig. III.3 Exact quantum reaction probabilities as a function of total angular momentum, J, calculated with the symmetric reduced potential for j=0. Translational energies are 0.35 and 0.15 eV.

III.3

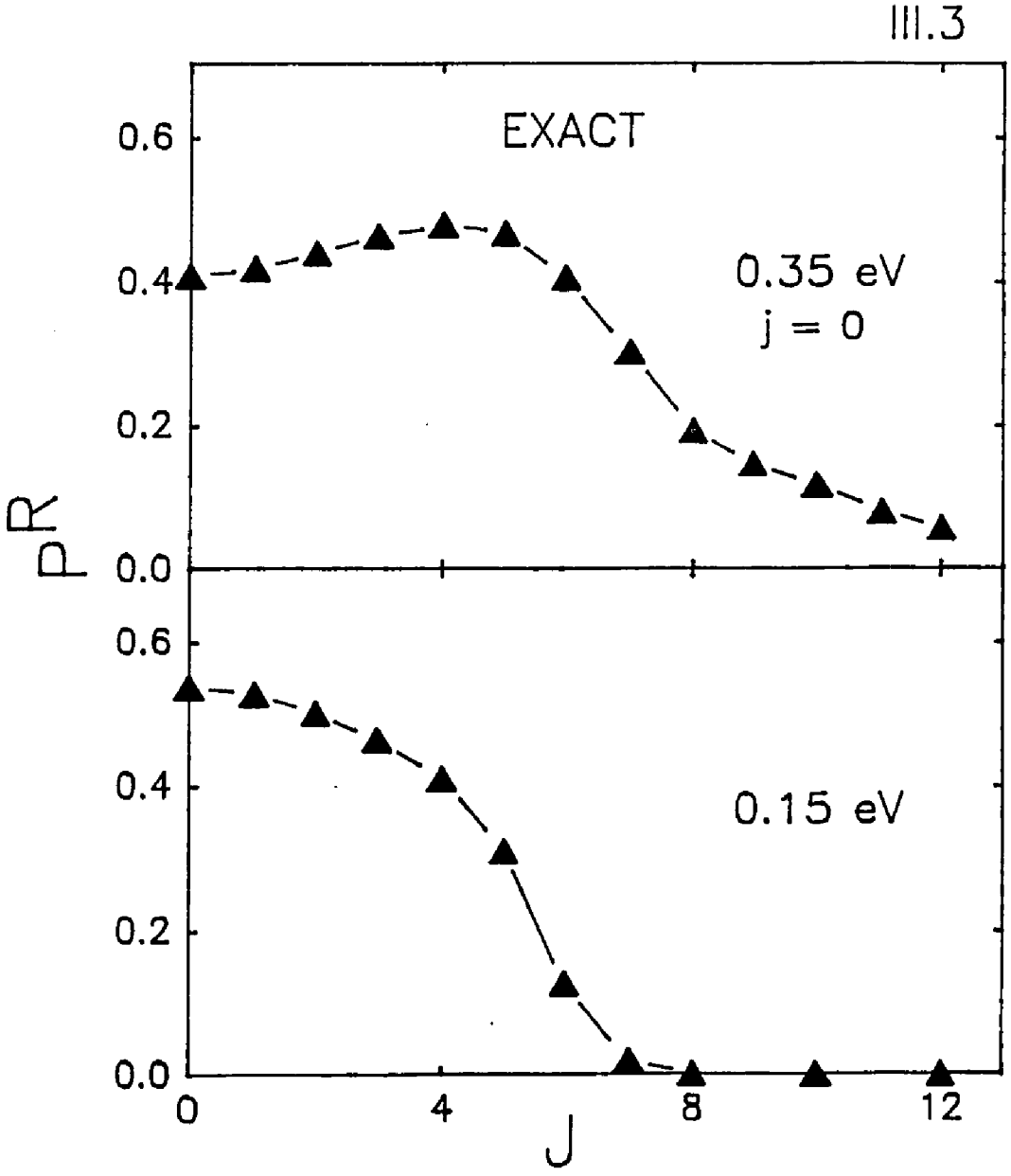

Fig. III.4 Exact quantum reaction probabilities as a function of j, calculated on the symmetric reduced potential for fixed orbital angular momentum, l. Translational energies are 0.35 and 0.15 eV.

III.4

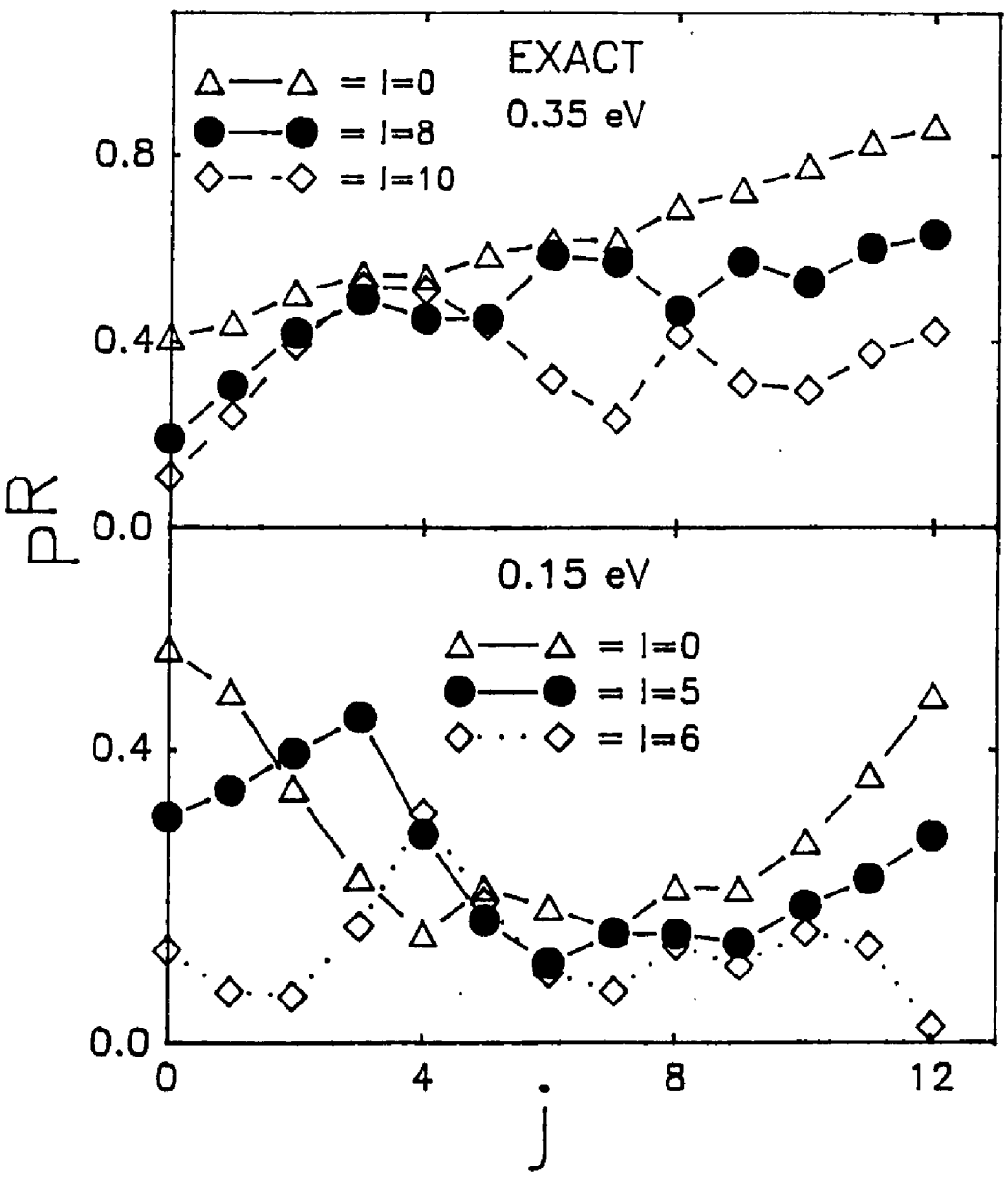

Fig. III.5 Centrifugal sudden reaction probabilities as a function of j, calculated on the symmetric reduced potential for fixed l. Translational energies are 0.35 and 0.15 eV.

III.5

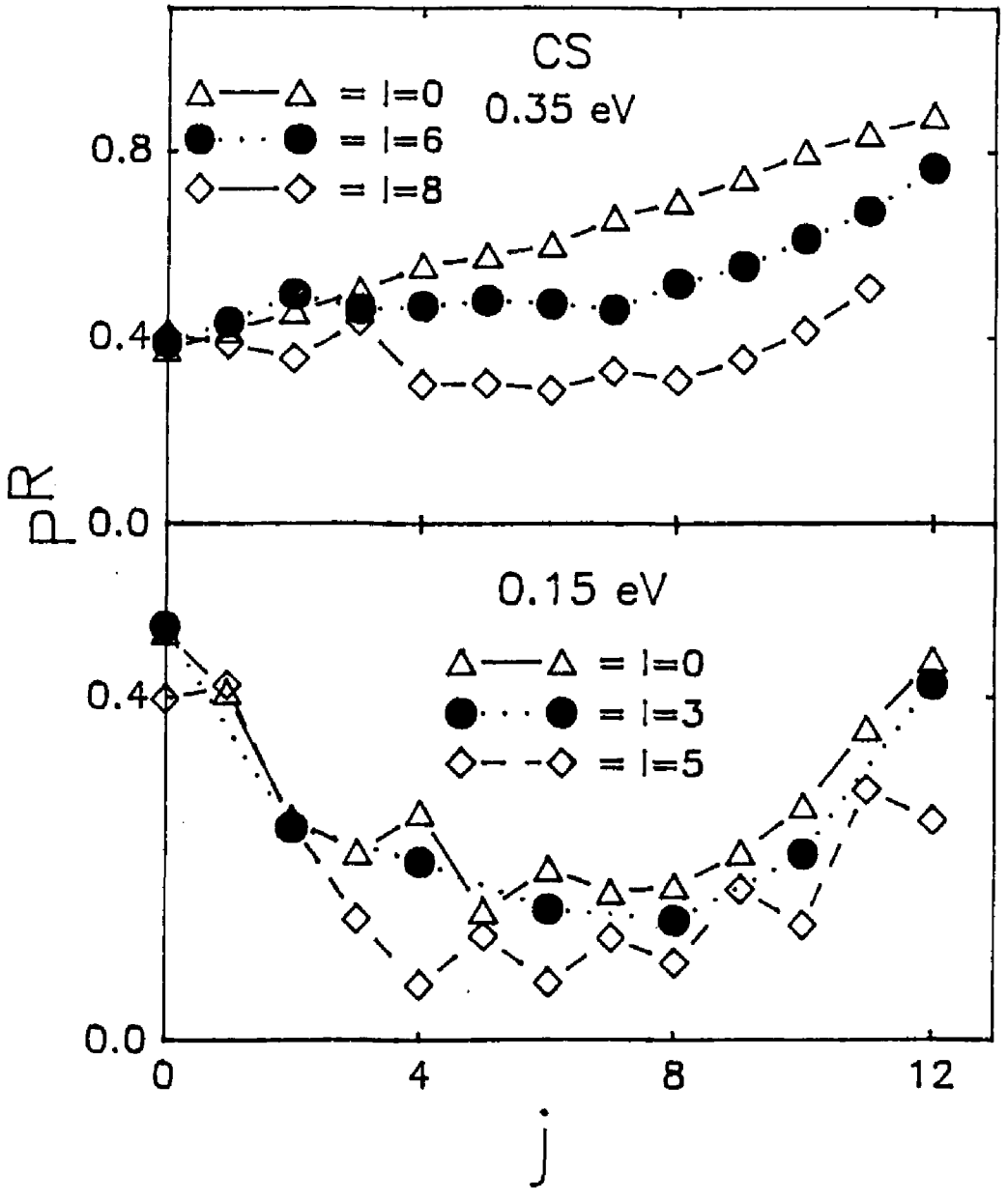

Fig. III.6 Infinite order sudden reaction probabilities as a function of j, calculated on the symmetric reduced potential for fixed l. Translational energies are 0.35 and 0.15 eV.

III.6

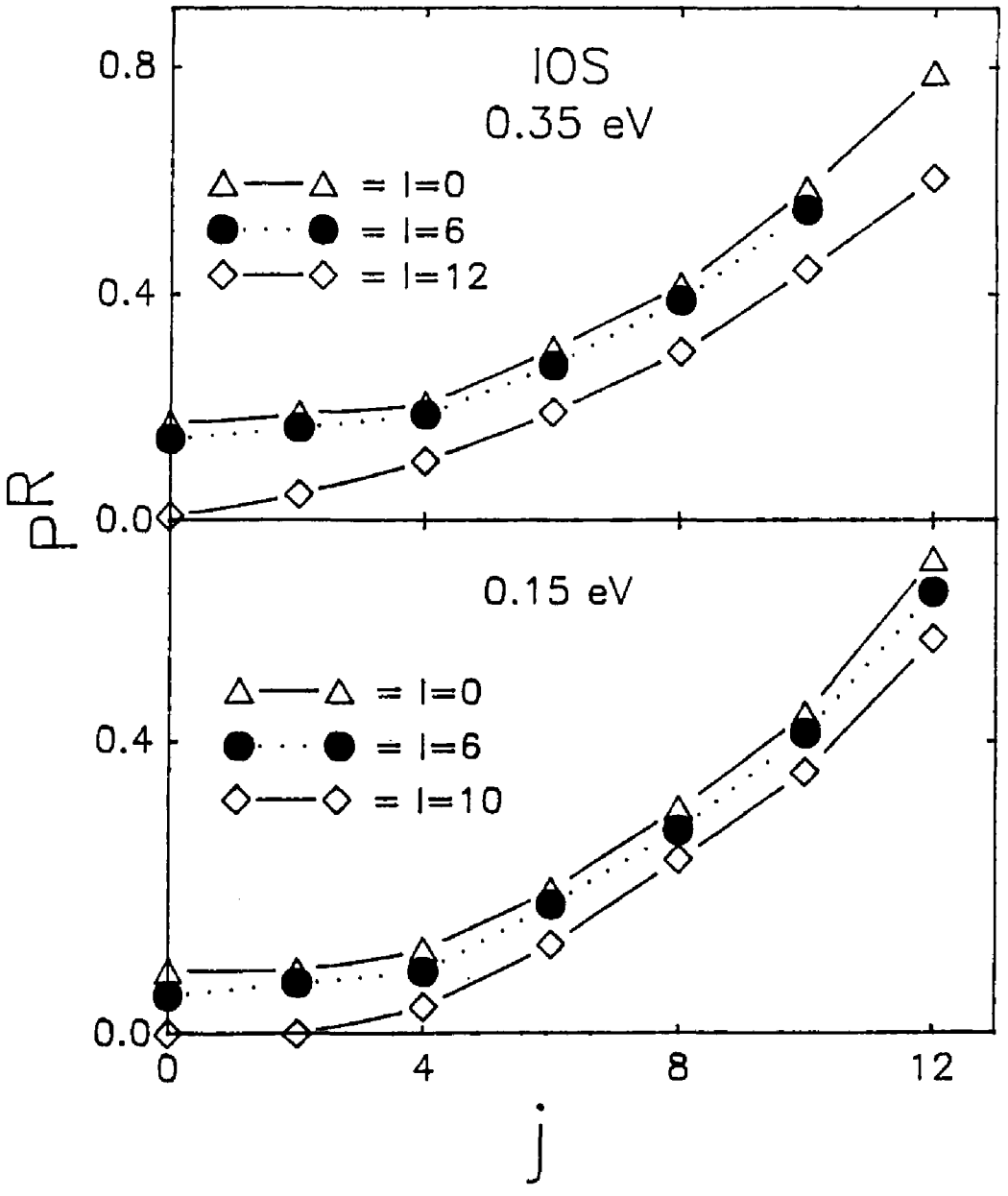

Table III.1 E = 0.10 eV, J = 0, j = 0

$P^{R}_{j'j}$

j \ j'	-3	-2	-1	0	1	2	3
-3	0.4507(-3)	0	.0.7512(-2)	0	0.7653(-2)	0	0.4766(-3)
-2	0	0.2136(-1)	0	0.6659(-1)	0	0.2186(-1)	0
-1	0.7512(-2)	0	0.1235	0	0.1243	0	0.7653(-2)
0	0	0.6659(-1)	0	0.2051	0	0.6659(-1)	0
1	0.7653(-2)	0	0.1243	0	0.1235	0	0.7512(-2)
2	0	0.2186(-1)	0	0.6659(-1)	0	0.2136(-1)	0
3	0.4766(-3)	0	0.7653(-2)	0	0.7512(-2)	0	0.4507(-3)

Table III.2 E = 0.10 eV, J = 0, j = 0,

$P^{l}_{j'j}$

j \ j'	-3	-2	-1	0	1	2	3
-3	0.8447	0.0	0.5765(-1)	0.0	0.7381(-1)	0.0	0.5035(-2)
-2	0.0	0.4067	0.0	0.2760	0.0	0.2074	0.0
-1	0.5765(-1)	0.0	0.7661(-1)	0.0	0.5288	0.0	0.7381(-1)
0	0.0	0.2760	0.0	0.1096	0.0	0.2760	0.0
1	0.7381(-1)	0.0	0.5288	0.0	0.7661(-1)	0.0	0.5765(-1)
2	0.0	0.2074	0.0	0.2760	0.0	0.4067	0.0
3	0.5035(-2)	0.0	0.7381(-1)	0.0	0.5765(-1)	0.0	0.8447

Table III.3 Some Selected Matrix Elements: E = 0.35 eV, J = 20, j = 12

$P^{R}_{j'j}$

j \ j'	-10	-6	-2	0	2	6	10
-10	0.324(-13)	0.188(-23)	0.108(-21)	0.129(-21)	0.396(-21)	0.742(-21)	0.458(-21)
-6	0.299(-23)	0.131(-12)	0.799(-8)	0.166(-7)	0.190(-7)	0.494(-7)	0.365(-7)
-2	0.109(-21)	0.795(-8)	0.998(-3)	0.359(-2)	0.786(-2)	0.205(-1)	0.120(-1)
0	0.130(-21)	0.161(-7)	0.356(-2)	0.251(-1)	0.375(-1)	0.112	0.601(-1)
2	0.383(-21)	0.187(-7)	0.780(-2)	0.375(-1)	0.358(-1)	0.105	0.528(-1)
6	0.722(-21)	0.488(-7)	0.205(-1)	0.113	0.106	0.858(-1)	0.117(-1)
10	0.458(-21)	0.365(-7)	0.122(-1)	0.610(-1)	0.558(-1)	0.118(-1)	0.251

Table III.4 Some Selected Matrix Elements: E = 0.35 eV, J = 20, j = 12

$P^{l}_{j'j}$

j \ j'	-10	-6	-2	0	2	6	10
-10	1.0	0.282(-13)	0.538(-18)	0.125(-18)	0.323(-19)	0.510(-20)	0.133(-20)
-6	0.281(-13)	0.997	0.946(-4)	0.157(-4)	0.343(-5)	0.450(-6)	0.113(-6)
-2	0.575(-18)	0.936(-4)	0.174	0.302	0.134	0.378(-1)	0.156(-1)
0	0.172(-18)	0.154(-4)	0.301	0.334(-1)	0.387	0.274(-1)	0.302(-1)
2	0.316(-19)	0.337(-5)	0.133	0.387(-1)	0.120	0.664(-1)	0.154(-1)
6	0.502(-20)	0.443(-6)	0.377(-1)	0.275(-1)	0.668(-1)	0.377(-1)	0.699(-1)
10	0.131(-20)	0.114(-6)	0.158(-1)	0.306(-1)	0.157(-1)	0.707(-1)	0.382(-1)

Table III.5 Comparison of basis set size:

39 versus 49

E_t = 0.15 eV, J = j

j	P^R (39)	Flux dev. (%)	P^R (49)	Flux dev. (%)
0	0.05364	0.0019	0.5347	0.0009
2	0.3460	0.0018	0.3462	0.0014
4	0.1447	0.0118	0.1475	0.0063
6	0.1840	0.0333	0.1842	0.0250
8	0.2115	0.0878	0.2105	0.2210
10	0.2737	0.0926	0.2717	0.221
12	0.4718	0.7230	0.4736	0.5540

E_t = 0.35 eV, J = j				
0	0.4072	0.0058	0.4082	0.0166
2	0.5050	0.0271	0.5033	0.0201
4	0.5373	0.0460	0.5377	0.0374
6	0.6160	0.1100	0.6172	0.0853
8	0.6908	0.2570	0.6926	0.1963
10	0.7751	0.5800	0.7755	0.4450
12	0.8622	1.270	0.8576	0.9740

Table III.6 Comparison of basis set size:
39 versus 49

E_t = 0.15 eV, l = 5

j	P^R (39)	Flux dev. (%)	P^R (49)	Flux dev. (%)
0	0.3049	0.0006	0.3083	0.0012
2	0.4009	0.0009	0.3949	0.0009
4	0.3019	0.0022	0.2836	0.0019
6	0.1087	0.0080	0.1086	0.0078
8	0.1452	0.0400	0.1488	0.0401
10	0.1833	0.1210	0.1875	0.1210
12	0.2826	0.2800	0.2805	0.2880

E_t = 0.35 eV, l = 8				
0	0.1913	0.0091	0.1913	0.0090
2	0.4178	0.0093	0.4178	0.010
4	0.4984	0.0148	0.4984	0.0015
6	0.5853	0.0294	0.5854	0.029
8	0.4663	0.071	0.4662	0.071
10	0.5261	0.171	0.5247	0.189
12	0.6299	0.360	0.6133	0.339

CHAPTER IV

THE EFFECT OF REAGENT ROTATION OF REACTIVITY

CLASSICAL TRAJECTORY CALCULATIONS

Introduction

In general, quantum mechanical reactive scattering calculations are difficult for light systems and nearly impossible for heavy systems or systems far above the energetic threshold to reaction. This is due to the fact that, if one is concerned with the effect of reagent rotation on reactivity in three dimensions, the degeneracy of the l and j states leads to a large number of close-coupled equations. This leads to a prohibitively large number of basis functions which must be used, which, in turn leads to very large matrices. Since the tractability of quantum mechanical calculations depends on the number of basis functions required, in cases where a large number of basis functions is involved (for instance, large j or high energy) converged results are difficult to obtain [49].

In contrast, classical mechanical dynamical calculations do not require basis set expansions; they require only initial positions and momenta of all the particles of interest and the derivatives of the potential energy function. Thus they are inherently simpler, and when the number of particles is

reasonable they are always tractable. Furthermore, the use of classical mechanics allows the dynamics to be easily visualized, a luxury not afforded by quantum mechanics.

In light of the ease of use of classical mechanics, several questions now need to be addressed. How well does classical mechanics reproduce effects observed in quantum mechanical calculations, especially when one is dealing with rotational levels? Recall, rotational levels get farther apart as the energy is increased, in contrast to vibrational levels which get closer together. Will this affect the validity of the Bohr correspondence principle which states that quantum and classical mechanics tend to agree at high energy? Further, close to threshold, where quantum effects such as resonances become more important, [46] how well will classical mechanics reproduce rotational trends observed in quantum mechanical calculations?

Mayne [51] utilized a model Hamiltonian, similar to (II.5) but which did not take into account orbital angular momentum, in order to explicitly test the accuracy of classical mechanics in dealing with rotational states. In that work, rotational quantum numbers from 0 to 12 were examined at low and high translational energy. Mayne found classical mechanics did a reasonable job, qualitatively reproducing trends observed in quantal reaction probabilities at high translational energy. In both cases, the $P^R(j)$ increased monotonically with increasing j (when a = 1.0 [eqn II.6]).

At lower translational energies both the quantal and the classical $P^R(j)$ decrease with increasing j, for low j. At high j, the $P^R(j)$ increase with increasing j. In other words, the $P^R(j)$ manifest the characteristic "dip and climb" seen in other work [21-23,29]. Apart from "adiabatic leak" [51] at low j, classical mechanics did a reasonable job reproducing quantum mechanical rotational trends at low translational energies. "Adiabatic leak" is a term coined to explain the phenomenon in which the classical threshold is lower than the quantum threshold. This is contrary to the conventional wisdom that due to tunneling the quantum mechanical threshold will always be lower. This phenomenon has been ascribed to the fact that classical mechanics ignores the adiabatic barriers imposed by quantum mechanics. Thus under certain circumstances, when the energetic bottleneck is a vibration, reaction occurs at lower translational energy in classical mechanics than in quantum mechanics. In other words, quantum mechanics demands that a diatom has a zero point energy; classical mechanics, on the other hand, has no such restriction.

For those systems where rotational dependence has been included in quantum mechanical calculations [43], e.g. $H + H_2$, classical mechanics is in good qualitative agreement with quantum results for those j states examined (j = 0 - 3). It should be noted however, that since quantum mechanical calculations are carried out at fixed energy, often the energy

associated with particular rotational states will be below the classical threshold to reaction. This makes the comparison of classical results to quantal results impossible.

As previously mentioned, Mayne's model does not take into account orbital angular momentum; i.e. the model has no impact parameter dependence. An obvious question is therefore; Will classical mechanics do an equally good job reproducing trends observed in quantal $P^R(j)$ when orbital angular momentum is included in the model?

In what follows, classical mechanical probabilities of reaction as a function of j, $P^R(j)$, will be compared to the quantum mechanical $P^R(j)$ reported in Chapter III.

Model Classical Trajectories: Method of Calculation

Recall the form of the exact model Hamiltonian (II.5) derived earlier

$$H = p_s^2/2\mu + j^2/2I(s) + (J-j)^2/[2\mu(R_m{}^2+s^2)] + V(s,\gamma) \qquad \text{(IV.1)}$$

where all variables have been defined in Chapter II. In order to facilitate comparison of the classical results obtained here with the quantum mechanical results obtained in Chapter II, the symmetric reduced potential (II.14) will be used. Furthermore, the masses appropriate for $H+H_2$ (i.e. **L** + **LL** where **L** has a mass of 1 amu) will also be used. The potential parameters for the symmetric reduced potential are given in Table II.1.

Classical trajectory calculations were carried out by

solving Hamilton's equations [100,101]. In general, for our model Hamiltonian (IV.1), Hamilton's equations take the form

$$ds/dt = dH/dp_s = p_s/\mu \qquad \text{(IV.2)}$$

$$dp_s/dt = -dH/ds = I(s)'j^2/I(s)^2 2 + (J-j)^2 s/\mu(R_m^2+s^2)^2 - dV/ds \qquad \text{(IV.3)}$$

$$d\gamma/dt = dH/dj = j/I(s) - (J-j)/\mu(R_m^2 + s^2) \qquad \text{(IV.4)}$$

$$dj/dt = -dH/d\gamma = -dV/d\gamma \qquad \text{(IV.5)}$$

where the prime denotes the derivative with respect to s. The derivatives with respect to the reduced potential have not been included specifically since their form will vary depending upon which form the reduced potential takes. Trajectories were integrated from s=-4 until it could be determined whether or not reaction occurred ($|s| > 4$). The angle γ was systematically varied between 0 and π in 100 equal increments. The momentum in the s direction, p_s, is initially given by, $p_s = (2\mu E_t)^{1/2}$, where E_t is the translational energy. The value of the rotational quantum number, j, and the total angular momentum, J, are input at the start of each trajectory. The reaction probability is the number of reactive trajectories divided by the total number of trajectories run [51].

Previously, it has been found [50,51] that agreement with trajectory calculations was obtained when the moment of inertia is allowed to increase as the transition state is approached. The form of I(s) is given in Chapter II, equation (II.6).

Comparison of Classical and Quantal Results

In Figure IV.1 classical reaction probabilities as a function of j, $P^R(j)$, calculated using equation (IV.1) are compared to the exact quantum mechanical close coupling $P^R(j)$ obtained by solving (III.11). Both the classical and the quantal $P^R(j)$ were calculated using with J = j initially. At high translational energy, 0.35 eV, the classical and the quantum $P^R(j)$ are in near quantitative agreement. At lower translational energies, 0.15 eV and 0.10 eV, the agreement between classical and quantal $P^R(j)$ becomes less quantitative. As one would expect, the classical $P^R(j)$ are smooth while the quantal $P^R(j)$ are somewhat oscillatory. Additionally, at low translational energy, 0.15 eV and 0.10 eV, the quantal probability of reaction at j = 0, $P^R(0)$, is higher than the classical $P^R(0)$. This is most likely due to tunneling. These same general observations were noted by Mayne [51].

Classical and quantal probabilities of reaction as a function of total angular momentum, $P^R(l)$, are compared when j = 0 in Figure IV.2. Again, classical mechanics reproduces the qualitative trends observed in the quantal calculations with the high energy results being rather more quantitative.

The effect of nonzero orbital angular momentum quantum number, l, on the correspondence between the classical $P^R(j)$ and the quantal $P^R(j)$ is considered in Figure IV.3. In the top panel, the exact classical $P^R(j)$ calculated using equation (IV.1) with l = 5 and l = 12 at a translational energy of 0.35

eV are shown. Also shown in the top panel (solid lines) are the quantal exact $P^R(j)$ for l = 6 and l = 10. The agreement between the classical l = 5 and the quantum l = 6 $P^R(j)$ is very good. Similarly, the agreement between the classical $P^R(j)$ when l=12 and the quantal $P^R(j)$ when l = 10 is quite good. Thus, at high energy, for nonzero values of orbital angular momentum classical mechanics does a reasonable job reproducing qualitative trends in quantal $P^R(j)$. Further, it should be noted that the classical $P^R(j)$ decrease as l is increased for a fixed j, as do the quantal $P^R(j)$. The lower panel of Figure IV.3 shows the exact classical $P^R(j)$ when l = 4 and l = 6 and the quantal $P^R(j)$ when l = 2 and l = 5 at a translational energy of 0.15 eV. The classical $P^R(j)$ still agree qualitatively with the quantum results, although agreement is worse than in the high energy case.

In conclusion it seems that, in general, classical mechanics does a good job qualitatively reproducing trends observed in quantal $P^R(j)$. Agreement tends to become worse as l is increased at both low and high translational energy. When l = 0, agreement is very good at low translational energy and becomes almost quantitative as the translational energy is increased. In three dimensions, one would expect such differences as oscillations about the classical mean to become "quenched" [51,102].

Armed with the knowledge that classical mechanics can qualitatively reproduce quantal $P^R(j)$ trends, we can extend

our work to regions where quantal calculations are difficult. For example, several nonsymmetric mass combinations can be examined which did not lend themselves to examination by close-coupling methods. Recall that for a nonsymmetric mass combination the number of energetically accessible (open) channels in the entrance and exit valley differs, thus making the quantum mechanical calculation more difficult [62]. Additionally, heavy atoms (i.e. atoms with a large number of degenerate l and j states) which would require a large number of basis functions, are easily examined within the context of classical mechanics.

Further, the validity of several classical angular momentum decoupling approximations will be tested. It will be demonstrated that these decoupling approximations allow for the unambiguous definition of the various contributions to the rotational excitation function.

Classical Centrifugal Sudden Approximation

In the classical centrifugal sudden (CCS) approximation [103] it is assumed that all the centrifugal potentials are degenerate. Therefore the dynamical variable term $(J-j)^2$ in the exact hamiltonian is replaced with a constant orbital angular momentum term l_o^2 (where $l^2 = (J-j)^2$ in eqn (IV.1)). There has been much discussion concerning the actual value of l_o to be used throughout the trajectory [89,103]. In this work, in accordance with Mulloney and Schatz [103], l_o is taken as l_i, the initial value of l, since this is easiest to

implement. As a result of this substitution the exact Hamiltonian (IV.1) reduces to the CCS Hamiltonian

$$H_{CCS} = p_s^2/2\mu + j^2/2I(s) + l_i^2/2\mu(R_m^2 + s^2) + V(s,\gamma). \qquad (IV.6)$$

Classical trajectories are calculated by solving Hamilton's equations (IV.2-IV.5), as in the exact case, however the form of dp_s/dt is now slightly different from the exact case. In the CCS approximation dp_s/dt has the form

$$dp_s/dt = -dV_{eff}(s,\gamma)/ds \qquad (IV.7)$$

where $V_{eff}(s,\gamma)$ has been previously defined as the effective reduced potential (III.55) for a given l_i. Initial conditions are identical to the exact case as is the method for calculating the probability of reaction.

Classical Infinite Order Sudden Approximation

The classical infinite order sudden approximation (CIOS) further assumes that all rotational levels are degenerate [103] (i.e. the energy sudden (ES) approximation [49]). As a result the dynamical variable, j, is replaced with a constant value. We use here the initial value, j_i. The CIOS Hamiltonian takes the form

$$H_{CIOS}=p_s^2/2\mu + j_i^2/2I(s) + l_i^2/2\mu(R_m^2 + s^2) + V(s,\gamma). \qquad (IV.8)$$

Making the approximation that the rotational levels are degenerate allows one to decouple the quantum mechanical closed-coupled equations (Chapter III) in order to solve the scattering problem. This amounts to a fixed orientation

approximation, since it is the orientational dependence which contains information about rotational excitation. As in the quantum case, the classical calculations are carried out at constant γ; the potential now depends only parametrically on γ. Further, since j is no longer a dynamical variable, $d\gamma/dt = 0$ [103,104]. It should be further noted that problems associated with matching the coordinates in the two rearrangement channels (i.e. reagents and products) experienced by Jellinek and Baer [89] are not encountered in this work due to the use of natural collision coordinates [52,53].

The equations of motion are altered from the exact case in the following way. In the CIOS approximation, in addition to dp_s/dt taking the CCS form (IV.7), $d\gamma/dt$ is given by [103]

$$d\gamma/dt = 0. \qquad \text{(IV.9)}$$

The initial conditions and the method for calculating the probability of reaction remain unchanged from the exact case.

Comparison of Classical Exact and Approximate Results

In Figures IV.4 and IV.5 the reaction probabilities, $P^R(j)$, calculated using the exact [eq (IV.1)], the CCS [eq (IV.6)], and the CIOS [eq (IV.8)] Hamiltonian for the mass combination **L + LL** (L has a mass of 1.0 amu) are shown. Various values of the orbital angular momentum quantum number, l, have been used. Both the exact and the CCS results show trends which are now familiar in the literature [21-23,27,29,51] which were also observed in the quantum

mechanical $P^R(j)$: at low translational energy, E_t, $P^R(j)$ decrease for low j, reach a minimum, then increase at high j. At higher E_t, the decrease disappears, and the $P^R(j)$ are monotone increasing functions. By contrast, the CIOS approximation fails to reproduce the "dip" at low E_t, giving always an increase in reactivity with increasing rotation, regardless of the mass combination.

The $P^R(j)$ from all three Hamiltonians show a decrease in reactivity with increasing orbital angular momentum. The exact and CCS results are in essentially quantitative agreement at $l = 0$, with agreement becoming worse as l is increased. However, the general trend in $P^R(j)$ as l increases is very similar. On the other hand, at high E_t, when the CIOS shows the same upward trend, the reactivity for $l = 0$ is significantly less than for the exact case.

It is well known from rotationally inelastic scattering that the IOS approximation works best when the collision is, indeed, sudden. This is best realized in the case of a light atom and a heavy diatom [105]. Due to the large moment of inertia of the molecule $d\gamma/dt$ is small; this is precisely the "sudden" condition [96]. Results for such a mass combination (**L** + **HH**, **H** has a mass of 19 amu) are shown in Figure IV.6. In this case, the CIOS is in virtually quantitative agreement with the CCS and both are in good agreement with the exact results. As before, reactivity decreases with l, and the agreement between the approximations is comparable at all

values of l (not shown).

By contrast, the mass combination **H + LL** should be a case where the IOS performs poorly: the translational motion is slow and the rotational states are widely separated (in other words, rotational motion is fast). This is confirmed by the results shown in Figure IV.7, in which it is clear that the CIOS bears no resemblance to the exact results. The CCS approximation, however, is in excellent agreement with the exact data for l = 0 (shown) and for higher values of l (not shown).

Now the effect of increasing or decreasing the value of B_o in equation (II.14) can be considered. Increasing B_o would make the bend mode at s=0 "tighter" in the sense that, for a given total energy, a smaller range of γ values would be accessible. Conversely, decreasing B_o would make the bend mode "floppier", increasing the range of accessible γ values. Exact, CCS, and CIOS results for all the previously used mass combinations are shown in Figure IV.8, for l = 0. It is clear that whenever the diatom contains two light atoms the tight bend causes the reactivity to decrease with j. The CCS is in good agreement with the exact results in such cases, whereas the CIOS, which always gives an increasing trend, is extremely poor. On the other hand, even with a tight bend, $P^R(j)$ increases for the **L + HH** mass combination. The CCS and the CIOS are now in at least qualitative agreement. In contrast to the tight bend mode, the floppy bend causes the reactivity

to increase with j regardless of the mass combination.

The most striking result from the above results is that, for all the mass combinations examined, $P^R(j)$ always increases in the CIOS approximation. This approximation, by definition, does not allow γ motion to be "mixed" with s motion. Therefore all of the translational energy is available to help the trajectory over the barrier. In addition to translational energy, the system also contains rotational energy which is coupled into translational motion via the I(s) term (II.6). As j is increased, more rotational energy is coupled to translational energy, therefore a higher barrier to reaction can be overcome. The result is an increase in $P^R(j)$ with increasing j. This can be defined as a pure "energy" effect.

The significance of these results can now be discussed. In particular, the effects known in the literature as the "orientational" and "energy" effects [14,21,24,106] will be addressed. These effects are usually cited as being responsible for the behavior of the $P^R(j)$; however these effects are usually rather vaguely defined. In what follows, the model will be utilized in order to clearly define both of these effects.

Recall (Chapter I) that the so-called orientational effect is thought to be responsible for the decrease in the $P^R(j)$ at low j [14,21,24]. Further, the energy effect is though to be responsible for the increase in the $P^R(j)$ at high j [14,21,24]. The characteristic "dip and climb" behavior of

the $P^R(j)$ is thought to result from a competition between these two effects. At high j the energy effect, believed to be linear in E_j, or j^2, dominates the orientational effect, which was previously thought to be linear in j [14,21].

The CIOS approximation affords a unique method in which to investigate the energy effect. Here, within the context of the model, the sensitivity of the pure energy effect to model parameters can be investigated.

In Figure IV.9 we plot the probabilities of reaction as a function of E_j, $P^R(E_j)$, for fixed values of the parameter a, which controls the stretch of the target molecule at the transition state [eqn(II.6)]. When a is equal to zero the $P^R(E_j)$ is a flat function; that is, it is the same for all values of E_j. When a is nonzero, the $P^R(E_j)$ increases with increasing E_j. From this figure it is apparent that the energy effect is, in fact, linear in E_j, i.e. j^2. The linear least squares fit to the $P^R(E_j)$ has been included in Figure IV.9 (solid line). As a is increased the slope of the $P^R(E_j)$ function, dP^R/dE_j, increases. We can now conclude the following in regard to the energy effect. First, the target molecule must stretch in order for the energy effect to manifest itself. In other words, rotational energy must couple to translational motion. Second, the energy effect increases as a is increased, the biggest increase coming at small a.

The energy effect is also apparent in exact and CCS $P^R(j)$ under "sudden" type conditions. In the CIOS approximation

$d\gamma/dt = 0$, therefore instances where γ does not change significantly before the transition state is reached can be defined as "sudden" type instances. This condition can be quantified by definition of a sudden parameter. This parameter is basically the ratio of rotational speed, $d\gamma/dt$, to translational speed, ds/dt. Using the following definitions, $d\gamma/dt = j/I$ and $ds/dt = (2E_t/\mu)^{1/2}$, we define the sudden parameter as $(\mu/E_t)^{1/2}(1/m)$, where E_t, μ, and m have all been previously defined. (Note that the ratio of $d\gamma/dt$ to ds/dt is equal to zero in the CIOS approximation.) The smaller this parameter the more "sudden" like the conditions. The mass combinations examined here, **H + LL**, **L + LL**, and **L + HH**, have the following sudden parameters, $0.063/E_t^{1/2}$, $0.038/E_t^{1/2}$, and $0.002/E_t^{1/2}$, respectively. Thus, the **L + HH** mass combination is the most "sudden" like mass combination. Instances where the sudden parameter is small include; 1) high translational energy (Fig IV.5), since the sudden parameter is inversely proportional to $E_t^{1/2}$ and 2) heavy atoms in the diatomic molecule (Figure IV.6), again due to the inverse relationship of the sudden parameter to the reduced mass of the diatomic molecule.

In contrast to these "sudden" like instances, there are cases when the sudden parameter is large. In these cases the $P^R(j)$ decrease with increasing j, this can be defined as the orientational effect. The $P^R(j)$ for one such case, the **H + LL** mass combination, are shown in Figure IV.7. In this case, due

to the large value of the sudden parameter, γ changes significantly before the transition state is reached. This is also true for the L + LL $P^R(j)$ at low energy (Figure IV.5). It is interesting to contrast these two cases, since the reduced mass of the diatomic molecule is equal in both cases. It is the translational reduced mass, μ, of the H + LL which makes the sudden parameter nearly twice as large as it is for the L + LL system. As a result, the orientational effect is much more pronounced for the H + LL mass combination; this is apparent from a comparison of Figures IV.5 and IV.7.

An advantage of our rather simple model is that it allows for the variation of the strength of the bend mode by changing the value of the parameter which multiplies the sine dependence of the reduced potential. This parameter is B_o in the symmetric reduced potential (II.14). The strength of the bend mode, or the gradient of the potential, seems to be another key in determining whether the orientational or the energy effects will dominate. It was previously determined that decreasing B_o resulted in the $P^R(j)$ which were dominated by the energy effect (Fig IV.8 top panel). Increasing B_o, on the other hand, results in the dominance of the orientational effect, except for the L + HH mass combination.

The CIOS approximation can be utilized in order to more fully determine the effect on changing the strength bend mode on the energy effect. Probabilities of reaction were calculated at several fixed values of B_o and the results

plotted as a function of rotational energy, $P^R(E_j)$ in Figure IV.10. Regarding these $P^R(E_j)$, there are several interesting points which merit discussion. First, it should be noted that the $P^R(E_j)$ are linear in E_j or j^2, as expected. The solid lines in Figure IV.10 represent the best fit line obtained by a linear least squares fit to these $P^R(E_j)$. Second, the reaction probability at $j = 0$, $P^R(0)$, increases as B_o is decreased. Since the bend is "softer" the reaction valley is, in effect, wider; thus the reaction probability increases. Finally, the slope of the $P^R(E_j)$ function, dP^R/dE_j, is similar for all the values of B_o investigated. Thus the energy effect seems to be almost independent of the strength of the bend mode.

The impact of changing the strength of the bend mode on the orientational effect is easily investigated using the exact Hamiltonian (IV.1). In order to isolate the effects which are due to the orientational effect the parameter a, which controls the energy effect, was set equal to zero. Reaction probabilities as a function of E_j at fixed B_o are shown in Figure IV.11. Also shown are the $P^R(E_j)$ for the **L + LL** mass combination when $a = 1.0$, i.e. the exact $P^R(j)$ for $l = 0$ from Figure IV.4. The $P^R(E_j)$ decrease with E_j for all values of B_o examined, i.e. the orientational effect. Further, we note that the orientational effect is almost linear in E_j, i.e. j^2. This is in contrast to early speculations, where we supposed it linear in j [21,22,29]. Increasing B_o increases the magnitude of dP^R/dE_j; that is, the tighter the bend mode

the more dominating the orientational effect becomes. Note that the slope of the $P^R(E_j)$ when a = 1.0 is significantly less than when a = 0. We can therefore conclude that, in this case, the energy effect is in competition with the orientational effect, resulting in increased $P^R(E_j)$.

The geometrical interpretation of the energy and the orientational effects is shown in Figure IV.12. Here the reduced potential is represented schematically. The bold line indicates the range of initial γ values which leads to reaction (that is, which pass through the reaction valley) for several values of j. When j is equal to zero, the motion of the trajectories across the (s,γ) plane is parallel to the s axis. The range of initial γ values which lead to reaction is denoted by W (top panel). Trajectories travel across the (s,γ) plane with a slope of χ (where $\chi = \arctan[(d\gamma/dt)/(ds/dt))]$. Trajectories only "see" a reaction valley width of W $\cos(\chi)$. As j is increased, $d\gamma/ds$ is increased, resulting in an increase in χ. Therefore the range of initial γ values which "see" the reaction valley decreases, and as a result reactivity decreases. This accounts for the decrease in probability of reaction at low j, i.e. the orientational effect. A simple calculation further illustrates this point. Using the above definition for the slope χ, and the following relationships, $d\gamma/dt = j/I$ and $ds/dt = (2E_t/\mu)^{1/2}$, simple trigonometry yields the following expression for cos (χ)

$$\cos(\chi) = (1 + j^2 A^2)^{-1/2} \qquad \text{(IV.10)}$$

where A is given by

$$A = (1/I)\ (\mu/2E_t)^{1/2} \qquad \text{(IV.11)}$$

for the L + LL system at 0.15 eV, A = 0.185 au. Therefore W $\cos(\chi)$ is given by

$$W \cos(\chi) = W\ (1 + j^2\ A^2)^{-1/2}. \qquad \text{(IV.12)}$$

Using the binomial theorem, for small $j^2\ A^2$, equation (IV.12) becomes

$$W \cos(\chi) = W(1 - j^2\ A^2/2). \qquad \text{(IV.13)}$$

Several interesting points can be made which are related to this rather simple expression for W $\cos(\chi)$ (eqn IV.13). First and foremost, as was observed in Figure IV.11, the orientational effect is approximately linear in E_j, or j^2. Second, it is well know that the orientational effect becomes less pronounced as the translational energy is increased (Figure IV.5). This is also readily apparent from the expression IV.13. Since A (eqn IV.11) is inversely proportional to the translational energy, at low translational energy, the $j^2A/2$ term is large. Thus the range of reactive angles decreases with increasing j, i.e. the orientational effect. For large translational energy, on the other hand, this term becomes negligible. Therefore the dominance of the orientational effect is diminished.

Lastly, the total energy of the system is increased by an increase in j (bottom panel IV.12). Due to the additional energy, the trajectories are no longer influenced by the contours which are lower in energy. This serves to effectively

widen the reaction valley at s=0. It is now apparent that the range of initial γ values which lead to reaction has increased, therefore the reactivity increases at large j. In other words, we see the energy effect manifest itself.

In summary, the increase in χ causes the P^R to decrease, while the increased total energy causes the reaction valley to widen. This, then, explains the characteristic behavior observed in the $P^R(j)$ here, and in other work [21,22,27,29].

In the **L + HH** system (Figure IV.6), at j = 0 the $P^R(j)$ are decreased by 20% in going from the exact to the CIOS results. This is due to the "funneling" of otherwise nonreactive trajectories into the reaction valley, a phenomenon not allowed in the CIOS (since funneling is the reverse phenomenon of the orientational effect). Mayne [180] predicted that funneling would be greatest in a **H + LL** system and least in a **L + HH** system. From Figures IV.6 and IV.7, we can see that this prediction holds for our model system; the exact $P^R(0)$ is slightly greater than the CIOS for **L + HH**, but is much greater for **H + LL**.

Conclusions

Exact classical dynamics has been compared with exact quantal dynamics for a model system. When the orbital angular momentum was equal to zero, agreement was found to be near quantitative at high translational energies and rather worse as the translational energy was decreased. For nonzero values of orbital angular momentum, quantal and classical $P^R(j)$

agreed qualitatively, with agreement becoming worse as the translational energy was decreased.

The approximate CCS and CIOS dynamics have been compared to exact classical dynamics for a variety of cases. The CCS approximation reproduces qualitative trends seen in the exact results regardless of mass combination or translational energy.

The CIOS is in general a poor approximation for examining trends in reactivity with j since it does not account for the orientational effect. Systems in which this effect is important should not be examined via this approximation. However, if one is investigating a system in which the energy effect dominates, "sudden" like conditions, the CIOS may be a useful approximation.

Additionally, it was demonstrated that the orientational and the energy effects can be easily investigated, via the use of the model (II.5) and the CIOS approximation.

Briefly, the energy effect is a result of the coupling of rotational energy to translational motion. It is uniquely defined by the CIOS. It was determined that the energy effect dominates the dynamics in the following cases; 1) At high translational energy regardless of mass combination. This is due, in part, to the fact that trajectories are higher on the surface and therefore see less of the reaction valley. It is also due to the fact that γ does not have a chance to change significantly before the transition state is reached due to

the small sudden parameter. This is aided by the fact that the orientational effect is significantly decreased at high translational energy (IV.13); and 2) When the diatomic molecule is made up of two heavy atoms, for instance, L + HH. The large reduced mass of the diatomic molecule results in a small sudden parameter, therefore γ does not change significantly before collision. By varying the strength of the bend mode it was determined that the severity of the energy effect is very nearly independent of the strength of the bend mode. However, when the bend mode is very floppy it was determined the energy effect does dominate the dynamics for all the mass combinations examined. This is due to the diminished significance of the orientational effect. The degree to which the target molecule is stretched at the transition state was found to have a pronounced effect on the severity of the energy effect.

The dynamics will be dominated by the orientational effect in the following instances; 1) The orientational effect dominates at low translational energy for low j, except when the diatom is heavy. In this case the sudden parameter is large, therefore γ changes significantly prior to reaching the transition state; 2) When the diatom contains light atoms this effect will be present for low j, i.e. the value of the sudden parameter is large due to the small reduced mass of the diatom; and 3) When the bend mode is tight. The dominance of the orientational effect was found to be dependent upon the

strength of the bend mode. The tighter the bend mode the more pronounced the orientational effect becomes. Lastly, it was determined that the orientational effect is, in fact, linear in E_j not in j as was previously thought.

In light of the results presented here, we can make some comments concerning various theories which deal with the form of the opacity function, $P^R(b)$, at fixed j [14,150]. In all cases examined here, $P^R(l;j)$ decreases with l for a given j. This is in agreement with trajectory studies [21,27]. Additionally, the functional form of $P^R(j)$ is similar for all fixed l values (i.e. at all b). This phenomenon has been observed before for O + HCl [151] and for F + H_2, this work.

This result is important in light of some previous work on the effect of reagent rotation on reactivity. This work [14,24,150] asserted that reaction occurs when the orbital angular momentum "matches" the rotational angular momentum. This implies a different functional form in $P^R(j)$ at high and low impact parameters. The previously discussed results [151] taken in conjunction with the present model results cast serious doubt on this assertion. Further doubt will be cast on this assertion in subsequent Chapters (Chapter V, F + $H_2(j)$.

Lastly, the validity of classical mechanics has been demonstrated, via the use of the model system, for cases where one is dealing with rotational excitation. Classical mechanics can now be used in the future to examine systems for which

quantal calculations are not possible. In this work, three dimensional classical trajectory calculations have been performed and the effect of reagent rotation examined for the two systems $F+H_2$ (0,j) --> HF + H and OH(0,j) + H_2(0,j') --> H_2O + H.

Fig. IV.1 Exact classical reaction probabilities, $P^R(j)$, calculated with J=j for the **L + LL** mass combination on the symmetric reduced potential at translational energies 0.35, 0.15, and 0.10 eV. Exact Quantum $P^R(j)$ (solid line) are included for comparison. Error bars are smaller than the size of the point.

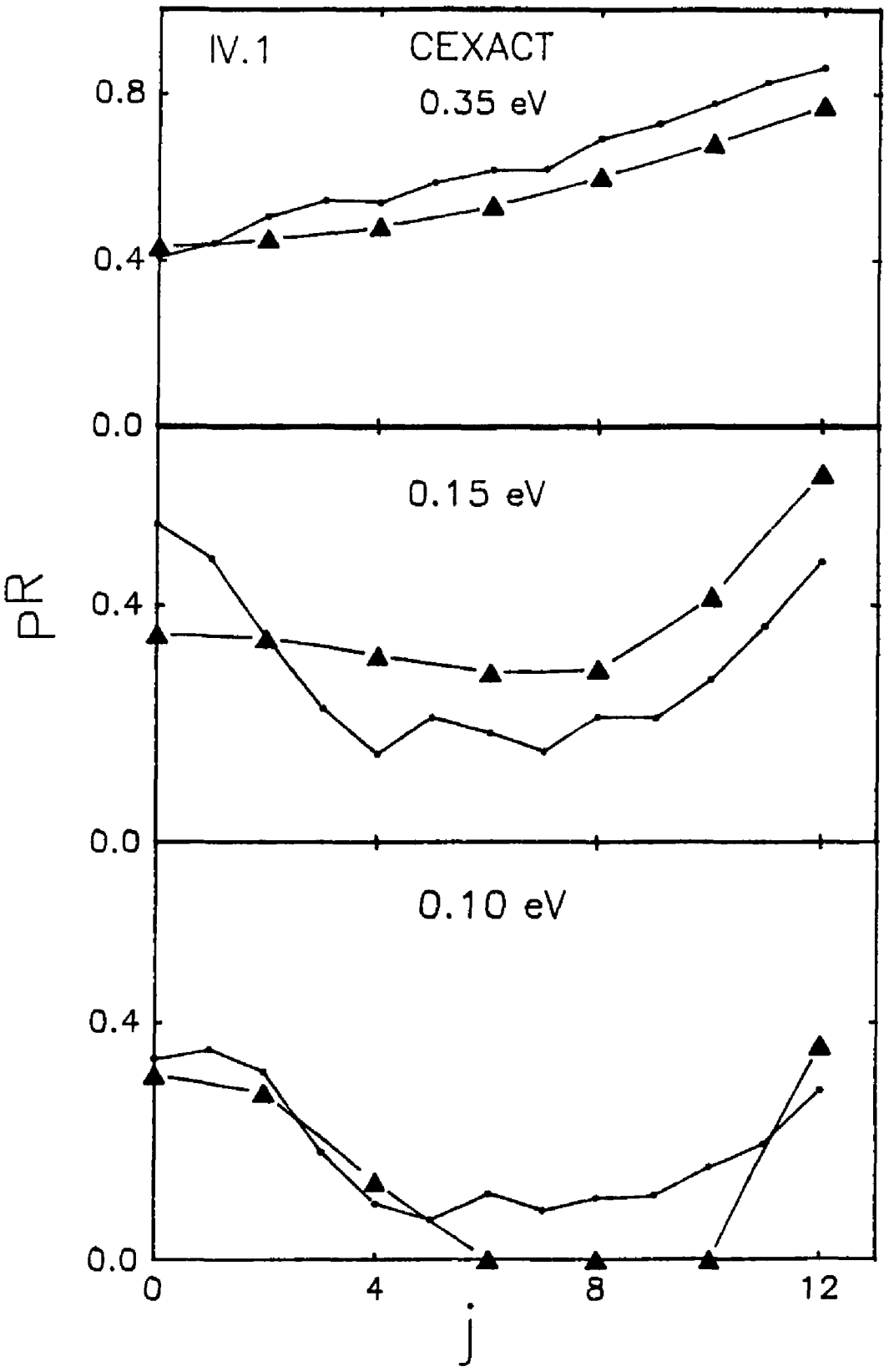
IV.1
CEXACT
0.35 eV
0.15 eV
0.10 eV
0.8
0.4
0.0
0.4
0.0
0.4
0.0
PR
0
4
8
12
j

Fig. IV.2 Exact classical reaction probabilities, $P^R(J)$, with j=0 for the L + LL mass combination on the symmetric reduced potential at translational energies 0.35 and 0.15 eV. Exact Quantum $P^R(J)$ (solid line) are included for comparison. Error bars are smaller than the size of the point.

IV.2

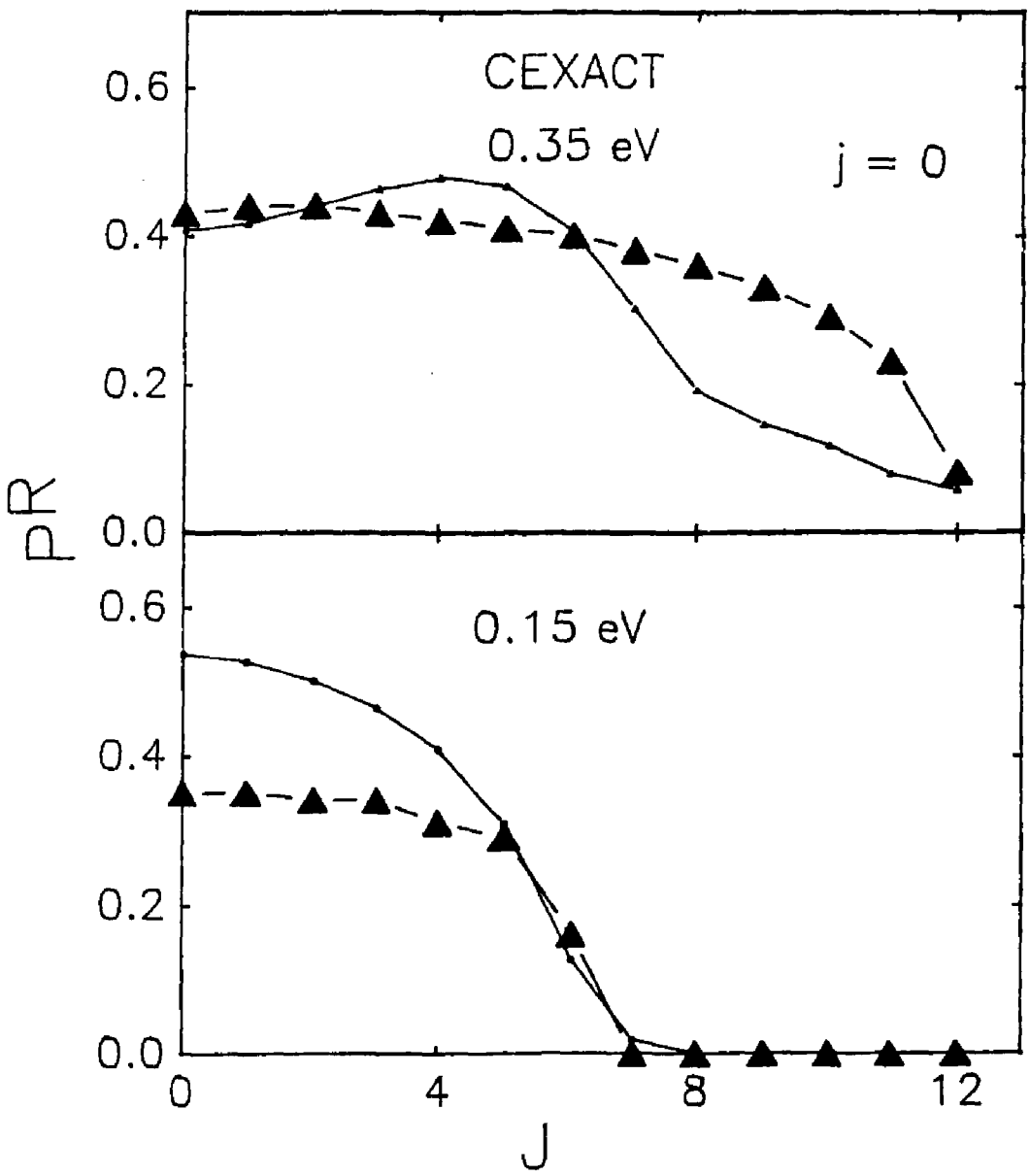

Fig. IV.3 Exact classical reaction probabilities, $P^R(j)$, for the L + LL mass combination on the symmetric reduced potential for nonzero values of l at translational energies 0.35 and 0.15 eV. Error bars are smaller than the size of the point.

IV.3

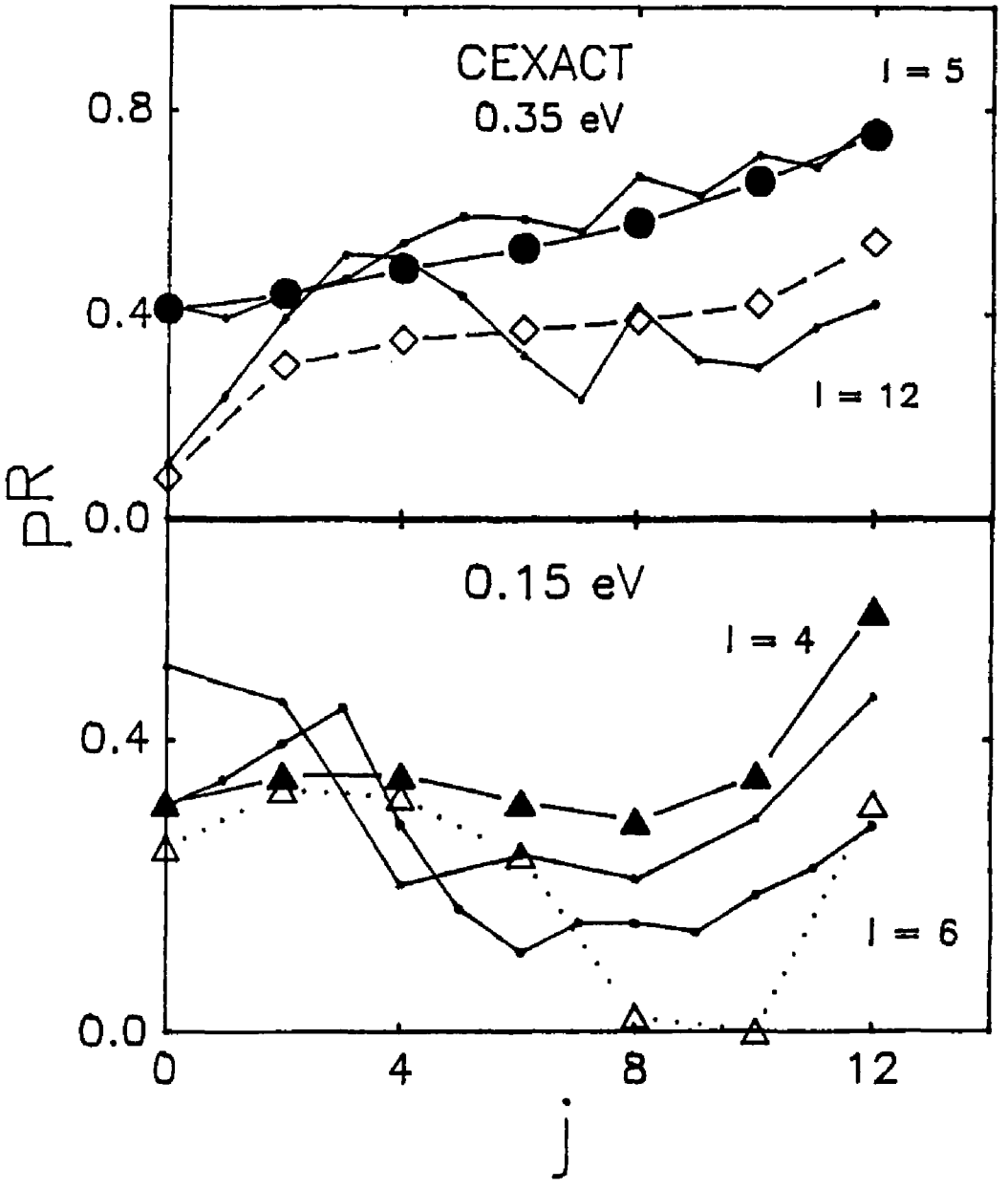

Fig. IV.4 Reaction probabilities, $P^R(j)$, obtained from the exact, CCS, and CIOS Hamiltonians for the **L + LL** mass combination at fixed **l**. The translational energy, E_t, is 0.15 eV.

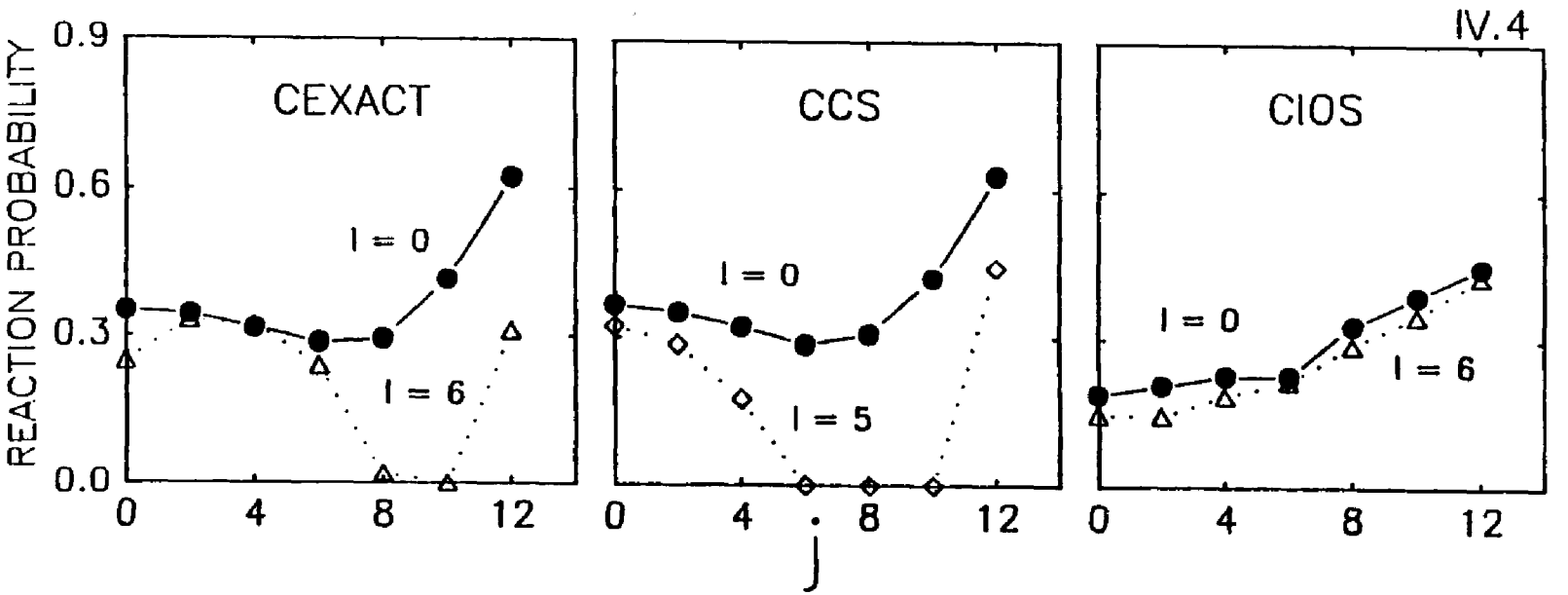
IV.4
REACTION PROBABILITY
0.9
0.6
0.3
0.0
CEXACT
CCS
CIOS
l = 0
l = 6
l = 5
0
4
8
12
J

Fig. IV.5 Reaction probabilities, $P^R(j)$, obtained from the exact, CCS, and CIOS Hamiltonians for the L + LL mass combination at fixed l. The translational energy, E_t, is 0.35 eV.

IV.5

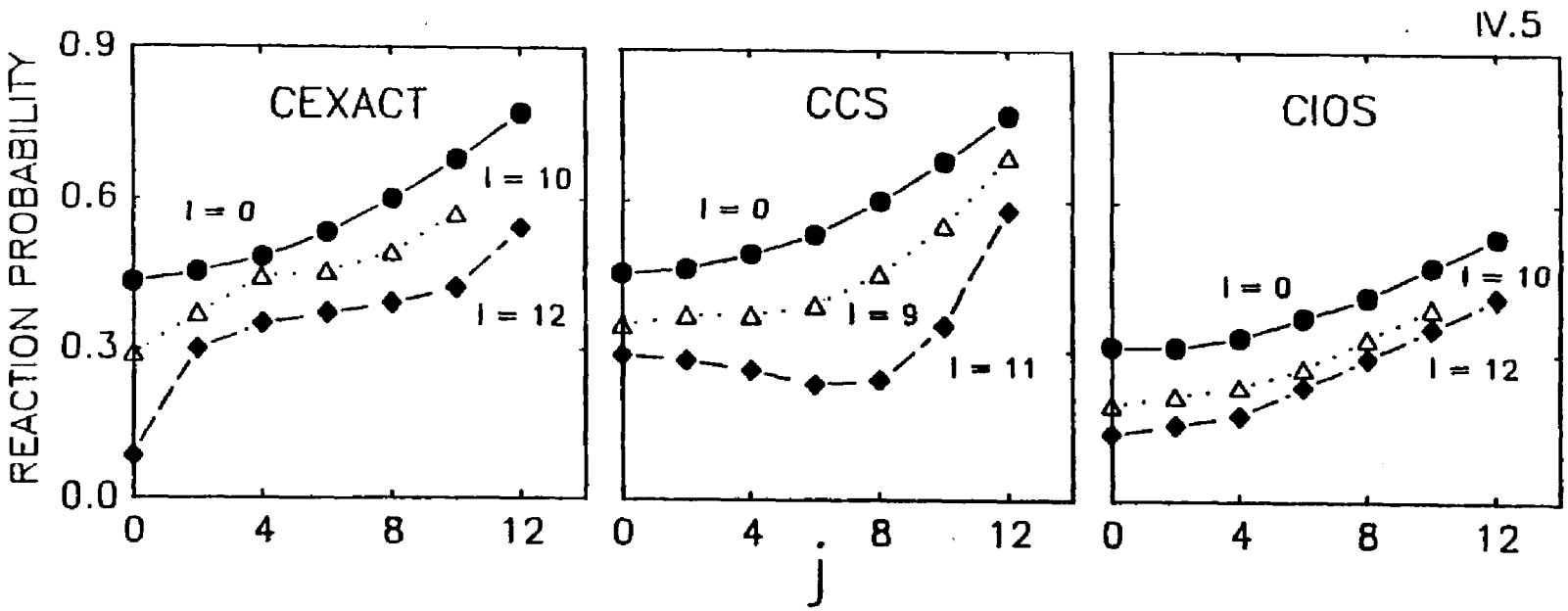
REACTION PROBABILITY
0.9
0.6
0.3
0.0
CEXACT
CCS
CIOS
l = 0
l = 10
l = 12
l = 9
l = 11
0
4
8
12
J

Fig. IV.6 Reaction probabilities, $P^R(j)$, obtained from the exact, CCS, and CIOS Hamiltonians for the L + HH mass combination. The orbital angular momentum quantum number, l=0 and E_t = 0.15 eV.

IV.6

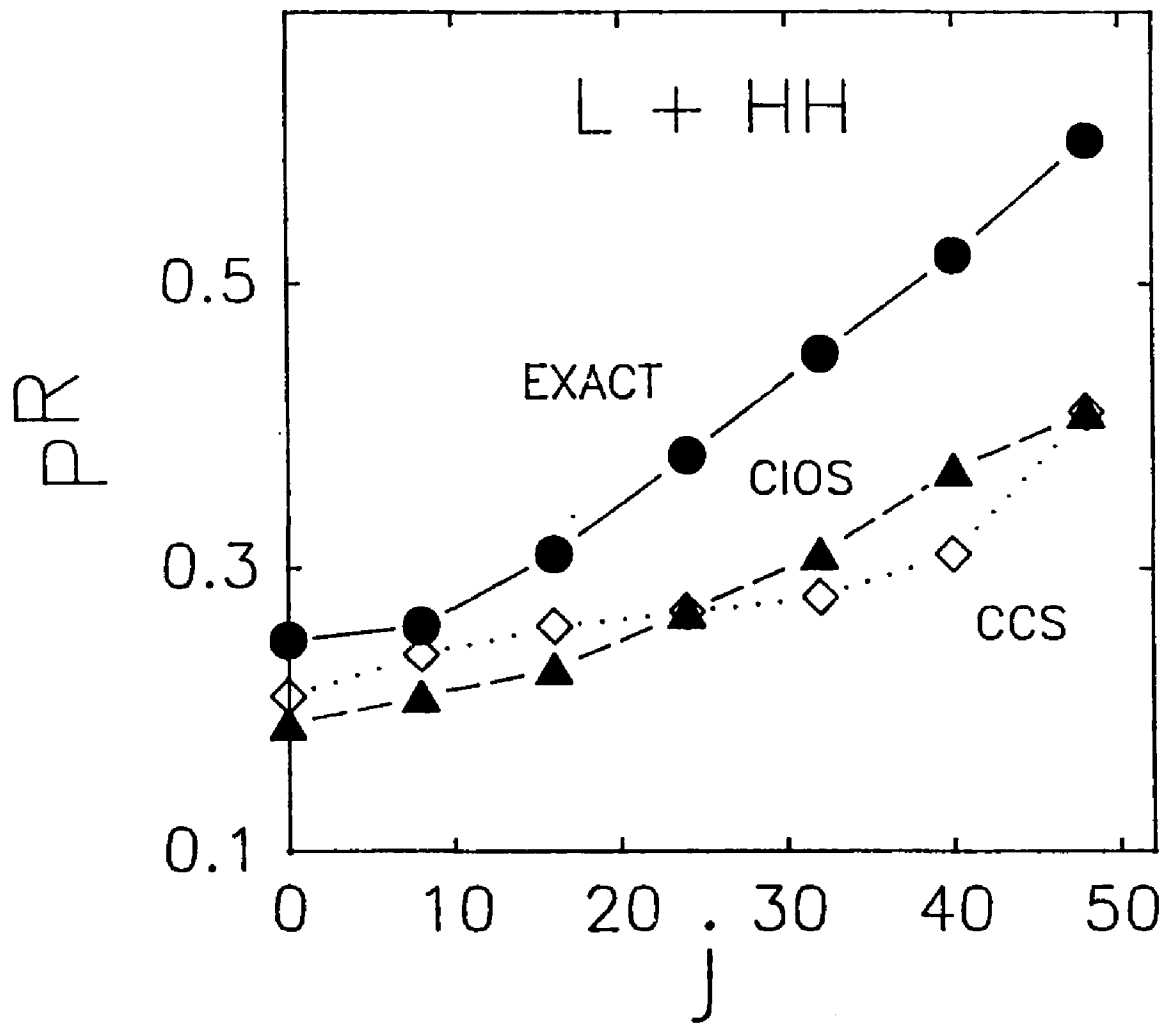

Fig. IV.7 Reaction probabilities, $P^R(j)$, obtained from the exact, CCS, and CIOS Hamiltonians for the H + LL mass combination. The orbital angular momentum, l=0 and E_t = 0.15 eV.

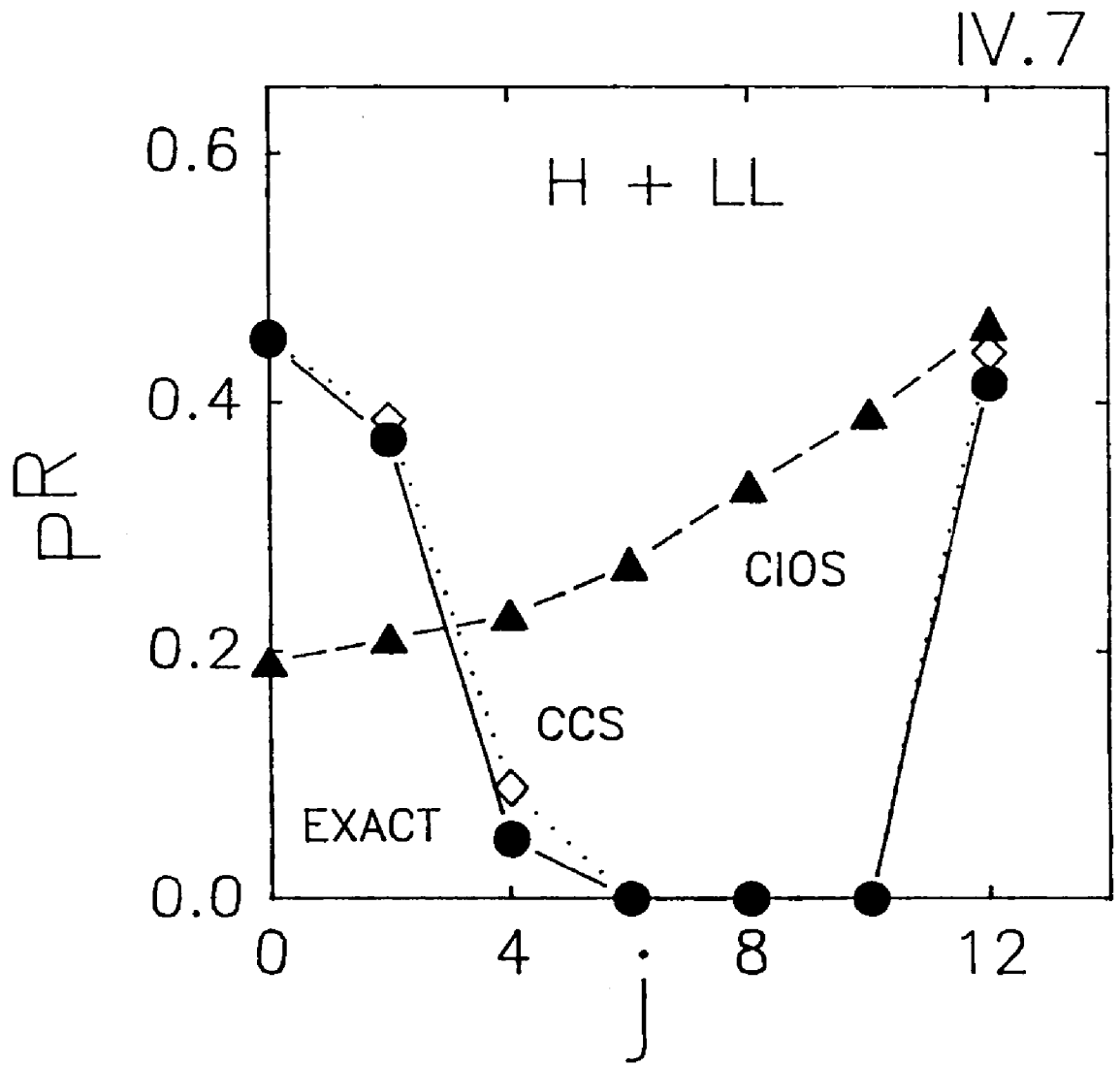
IV.7
H + LL
0.6
0.4
0.2
0.0
PR
CIOS
CCS
EXACT
0
4
8
12
j

Fig. IV.8 Reaction probabilities, $P^R(j)$, obtained from the exact, CCS, and CIOS Hamiltonians with B_o = 0.82 eV (top panel) and B_o = 2.45 (bottom panel). Exact results are denoted by solid circles, the CCS results by open triangles, and CIOS results by solid diamonds. The orbital angular momentum quantum number, l=0 and E_t = 0.15 eV.

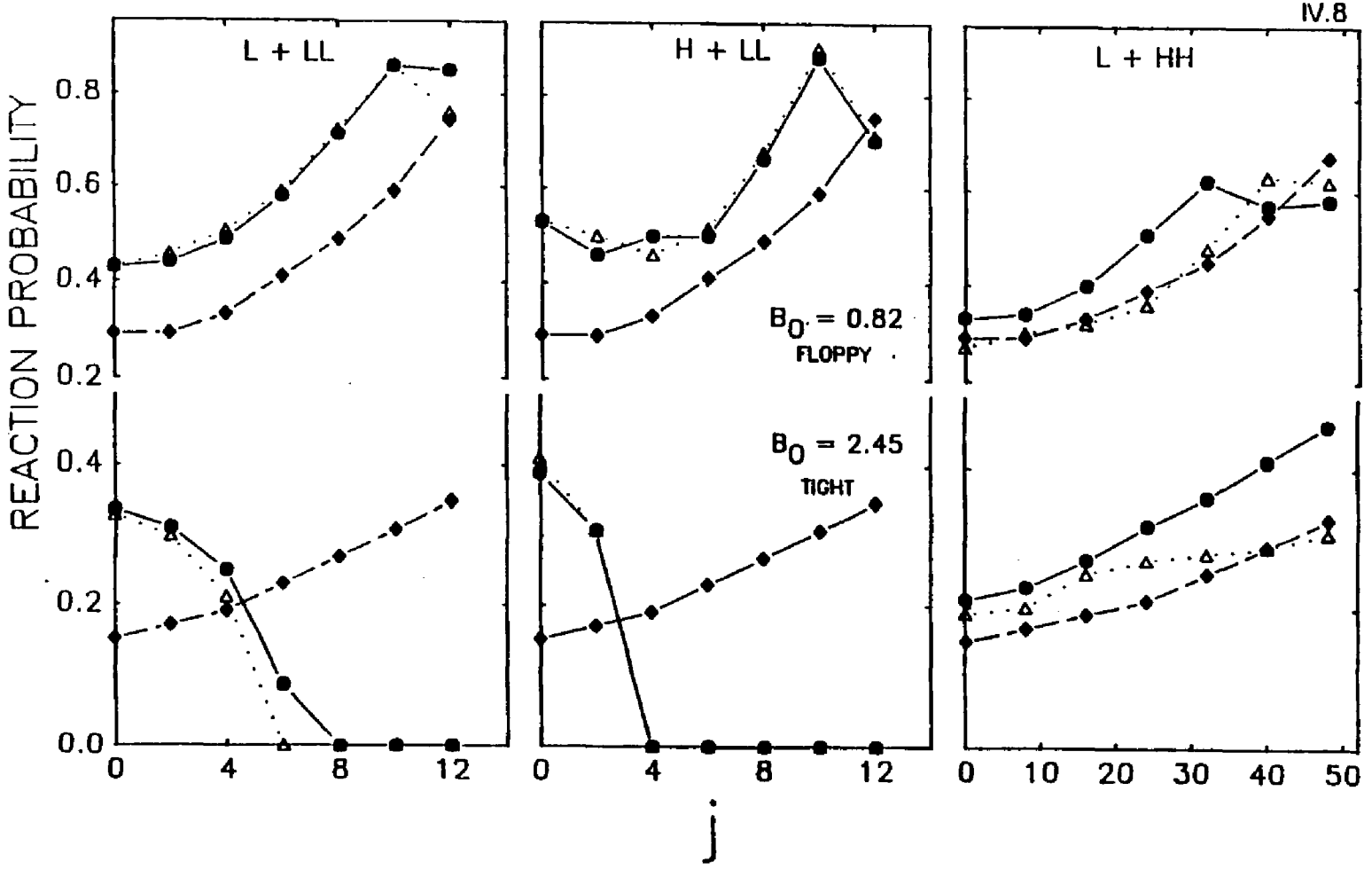
L + LL
H + LL
L + HH
REACTION PROBABILITY
0.8
0.6
0.4
0.2
0.4
0.2
0.0
B_0 = 0.82
FLOPPY
B_0 = 2.45
TIGHT
0
4
8
12
0
4
8
12
0
10
20
30
40
50
j

Fig. IV.9 Reaction probabilities, $P^R(E_j)$, obtained from the CIOS Hamiltonian for the **L + LL** mass combination at fixed a. The translational energy, E_t, is equal to 0.15 eV. and B_o = 1.63 eV.

IV.9

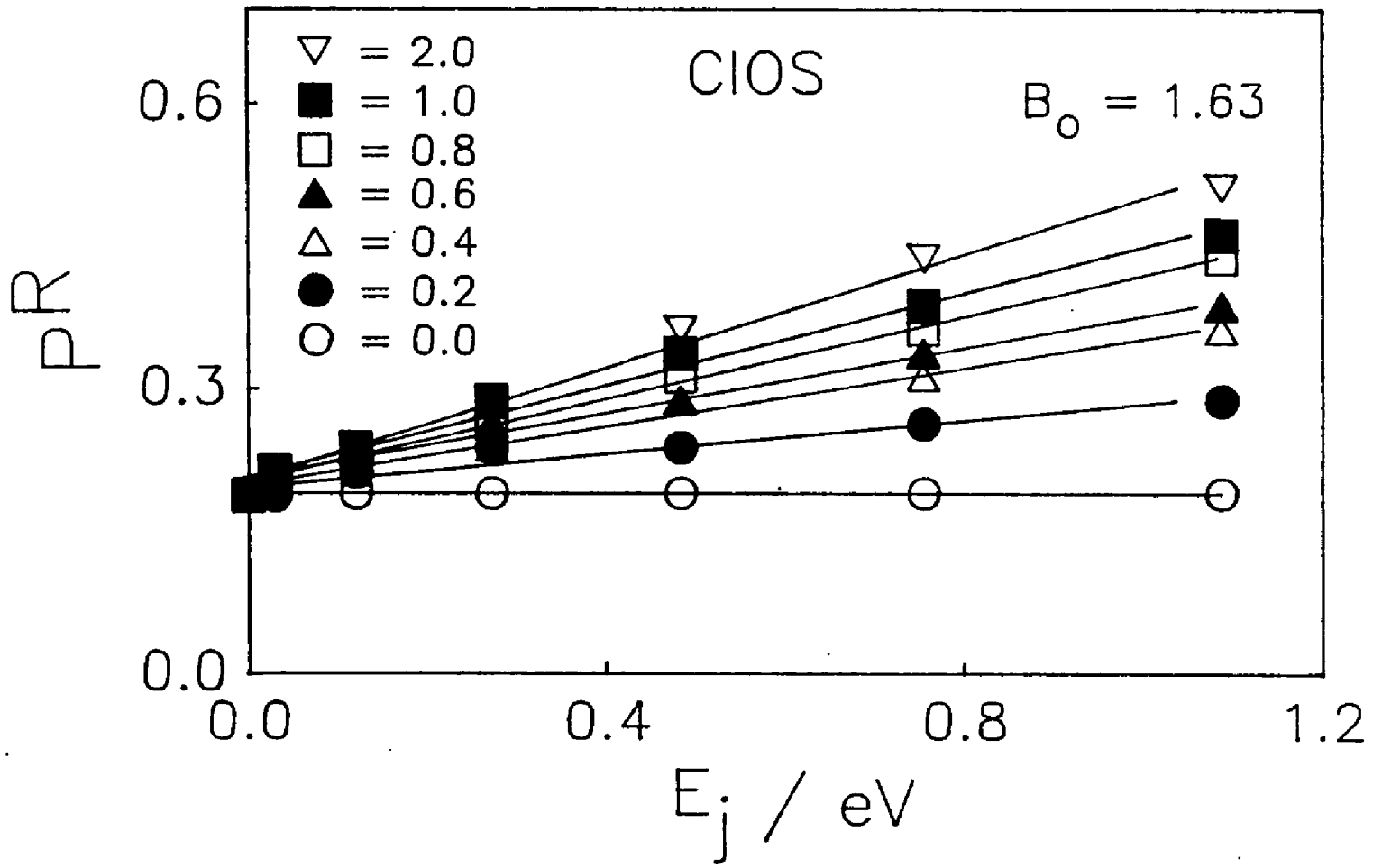

Fig. IV.10 Reaction probabilities, $P^R(E_j)$, obtained from the CIOS Hamiltonian for the **L + LL** mass combination at fixed B_o. The translational energy, E_t = 0.15 eV and the parameter a = 1.0.

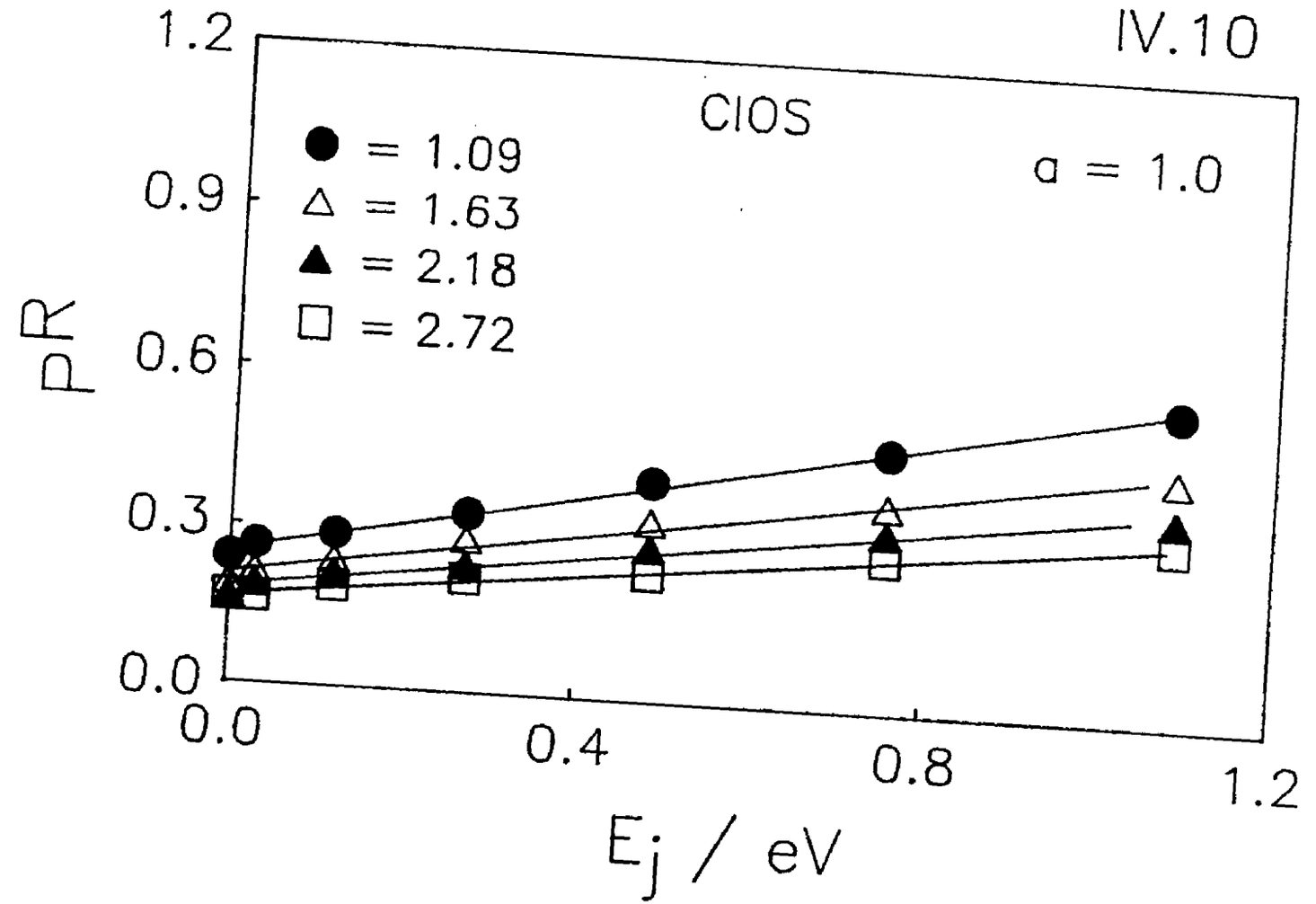
IV.10
CIOS
● = 1.09
△ = 1.63
▲ = 2.18
□ = 2.72
α = 1.0
P_R^R
1.2
0.9
0.6
0.3
0.0
0.0
0.4
0.8
1.2
E_j / eV

Fig. IV.11 Reaction probabilities, $P^R(E_j)$, obtained from the exact Hamiltonian for the **L + LL** mass combination at fixed B_o. The translational energy, E_t =0.15 eV and the parameter a = 0.0. For the trajectories with a = 1.0; B_o = 1.63 eV.

IV.11

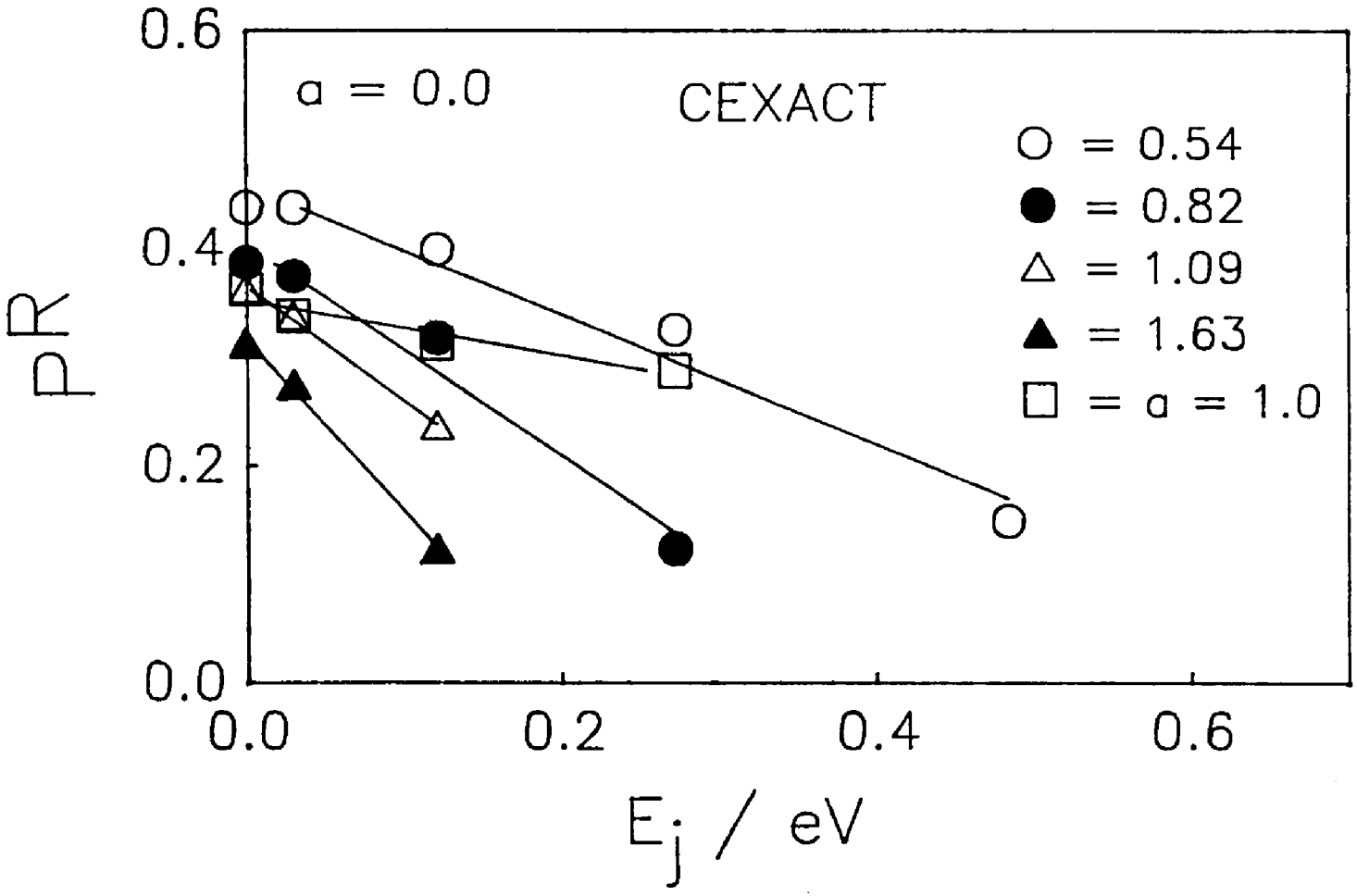

Fig. IV.12 Schematic diagram showing representative model trajectories on a model potential surface. Top panel : j = 0. The width of the reaction valley is W. The range of initial γ values which lead to reaction is shown by the dark shading on the γ axis. Reaction probability is W/π. Middle panel : j small. Here the reaction valley is assumed to be the same width, W. The reaction probability is now roughly $W\cos(\chi)/\pi$. Lower panel: j Large. Here we take into account the fact that nonzero rotation increases the total energy, thus increasing the width of the reaction valley at s = 0. The reaction probability is greater than it is for j = 0.

IV.12

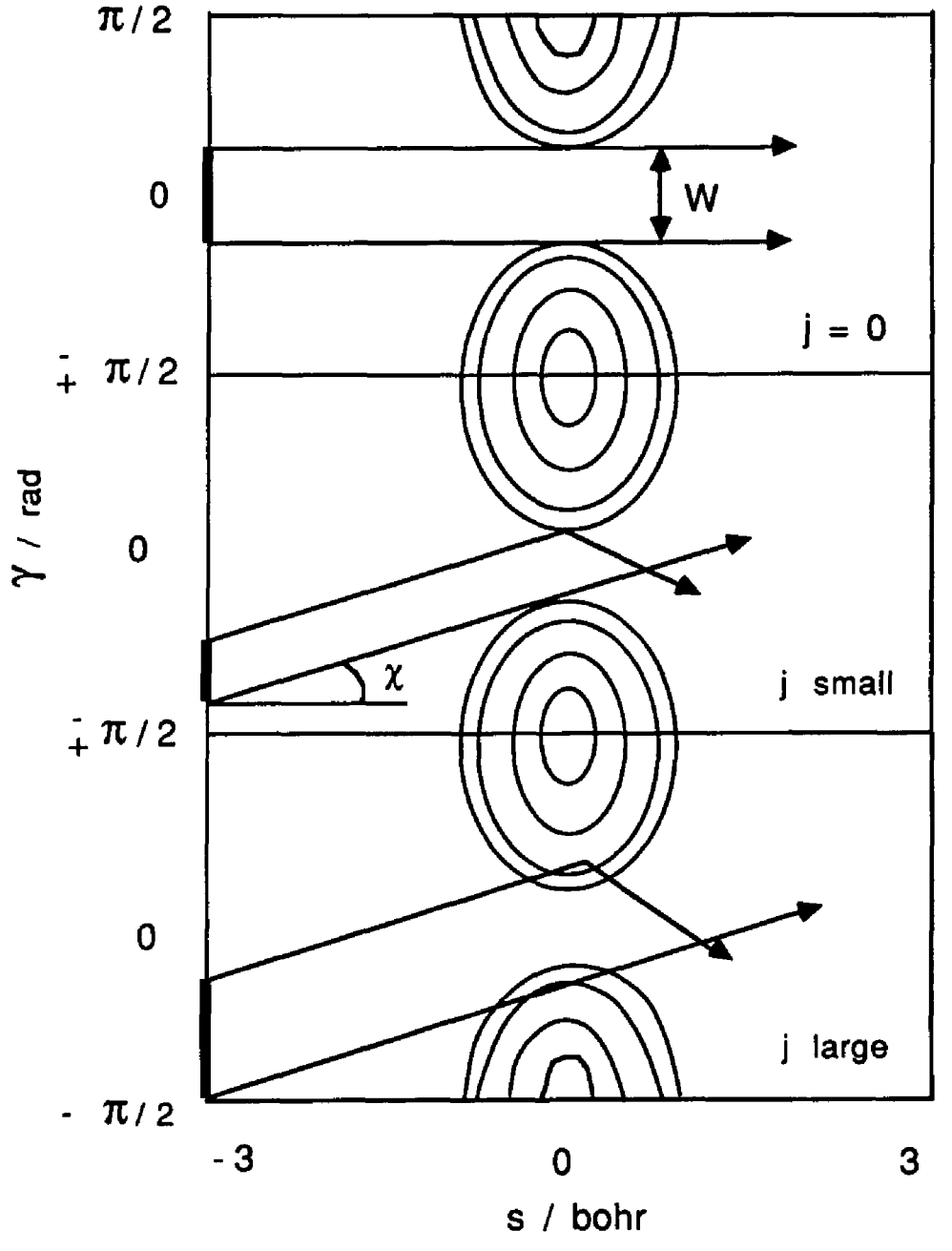

CHAPTER V

CASE STUDY: $F + H_2$

Introduction

The reaction of fluorine and hydrogen ($F + H_2$) to form hydrogen fluoride (HF) and its isotopic analogues has been the subject of considerable experimental [107,109-119] and theoretical work [108,120-148]. This work has been reviewed up to 1980 by Anderson [107]. Schaefer [108] has reviewed the theoretical work which has attempted to calculate an accurate ab initio surface for the $F + H_2$ reaction. One of the major reasons for this interest in the $F + H_2$ reaction is the use of the system as a chemical laser [121,124]. Another contributing factor is that the $F + H_2$ reaction is one of the few systems for which quantum mechanical resonances have been observed experimentally [111,118,119]. The landmark cross beam experiments were performed by Lee and coworkers on $F+H_2$ [118] and $F+D_2$ [119]. Lee and coworkers reported differential cross sections and kinetic energy distributions for product HF vibrational states. They determined for the $F+H_2$ reaction that the $v' = 1$ and $v' = 2$ (primes denote reaction product) states were predominantly backward scattered (HF scattered at 180° relative to incident F), whereas a large degree of forward scattering was observed for the $v' = 3$ state. The results

indicated that dynamical resonances play a significant role in the reaction dynamics and that they are most prominent in the v' = 3 channel. For the $F+D_2$ reaction, although weaker than for $F+H_2$, dynamic resonances were observed in the v' = 4 channel of DF. Quantal calculations [108,134-146] (most of which were done on the Muckerman 5 (M5) surface [123]) on the $F+H_2$ system predict that the v' = 2 channel is most strongly affected by resonances.

The effect of vibrational [122,124,125,131-133] and rotational [60,120,121,123,128] excitation of the hydrogen molecule on the cross section, product angular distribution, and product rotational and vibrational distributions has been examined in several theoretical studies.

Classical trajectory calculations performed on a variety of semiempirical potential energy surfaces have in general been concerned with obtaining rate information and product energy distributions [121,124-127,129-133]. Additionally, several studies have been concerned with the effect of reagent rotation on the dynamics and product attributes of the $F+H_2$ ($F+D_2$) system [60,120,121,123,128].

Muckerman performed trajectory calculations on several surfaces, most notably the M1 [121] and M5 [123] surface. Both surfaces are of the familiar LEPS form [50,54-56]. For the $F+H_2$ system both surfaces produced an increase in cross section as j went from 0 to 1, followed by a decrease as j went from 1 to 4. However for the $F+D_2$ system there was no

apparent increase in reactivity as j went from 0 to 1. Here the cross section smoothly decreased as j went from 0 to 4 on both surfaces. Trajectories on the M1 surface were given 2.0 kcal/mol collision energy at the start of the trajectory. Trajectories run on the M5 surface were given 3.0 kcal/mol collision energy initially. Similar results were obtained for the $F+H_2$ reaction on a slightly different LEPS type surface by Jaffe and Anderson [120].

Polanyi and Schreiber examined the $F+H_2(j)$ reaction on several LEPS surfaces [60]. They observed this same trend; a slight increase between j = 0 and 1 followed by a decrease, on their SE1 surface. However, on their SE4 surface they observed a marked decrease in cross section as j went from 0 to 1, followed by a increase as j went from 1 to 6. The major difference between these two surfaces is the existence of a 2.3 kcal/mole well in the entrance valley of the SE4 surface. Blais and Truhlar [128] examined the $F+D_2$ reaction on a semiemperical valence bond surface (BT) and also observed a decrease as j went from 0 to 1 followed by an increase in cross section with higher j values. Like the SE4 surface, the BT surface also has a well in the entrance valley, however at 3.8 kcal/mole it is slightly deeper. Schreiber [149] speculates that the contrasting behavior of the cross section (S^R) with j is due to the presence of this well. The reason for these seemingly different types of behavior is not at all well understood and is therefore responsible in part for

motivating this work.

Another motivating force behind this work is the applicability of the model, described previously, to the exoergic $F+H_2$ reaction. This model has enjoyed success in explaining trends in reactivity caused by reagent rotation for reactions with high barriers, e.g. $H+H_2$ (Chapters III-IV). It is therefore worthwhile to investigate the validity of the model for reactions which are significantly exothermic (therefore "early" [8,9]) and which have small barriers.

Thus, the objectives of this work are; 1) to unify the previously reported and apparently contradictory results concerning $F+H_2(j)$ and to extend this work to include results for j values > 4 (6 in the case of D_2), 2) to use the recently developed model to qualitatively reproduce the effect of rotational excitation in $F+H_2$ (D_2), and 3) to determine what, if any, experimentally determinable quantities will be useful in elucidating the cross section behavior with rotational excitation.

Classical Trajectories: Method of Calculation

The method for calculating classical trajectories is given in Appendix A. The topics addressed are; 1) the coordinate system; 2) the classical equations of motion 3) the selection of initial conditions; and 4) the calculation of final state properties. Final state properties include reaction cross section, S^R, differential cross section, $d\sigma/d\omega$, and determination of the product rotational and vibrational

quantum numbers, j' and v', respectively.

Model Trajectories: Method of Calculation

The method for calculating classical trajectories using the model Hamiltonian (IV.1) is discussed in Chapter IV. The coordinate system, the selection of initial conditions, as well as the calculation of reaction probabilities are also addressed in that chapter.

Results and Discussion

Reaction Cross Sections

Reaction cross sections as a function of initial rotational quantum number, $S^R(j)$, calculated on the SE1 surface at several collision energies are shown for $F+H_2(v=0,j)$ and $F+D_2(v=0,j)$ in Figure V.1. For $F+H_2(0,j)$ the reaction cross section decreases as j goes from 0 to 6. An important aspect of this curve not previously seen for this system, but seen for other triatomic systems [21,136], is the increase in the $S^R(j)$ as j goes from 6 to 14. While increasing the translational energy (E_t) of the system increases the cross section, it does not affect the position of the minimum. These results are in agreement with the thermally averaged cross sections of Polanyi and Schreiber [60] for those j values for which they have calculated cross sections ($j < 5$ on the SE1). Polanyi and Schreiber [60] noted an apparent increase in the cross section as j went from 0 to 1. In this work, while there is a hint of this increase at high translational energy it is within the error bars.

The reaction cross sections for $F+D_2(0,j)$ have the same qualitative shape as the $F+H_2(0,j)$ cross sections. The major difference between the two being the shifting of the minimum from about j=6 to j=8. Also shown in Figure V.1 are the $S^R(j)$ for the $M_x+H_2(0,j)$ system, where M_x is a fictitious isotope of fluorine with mass equal to 1 a.m.u.. The position of the minimum in the $S^R(j)$ is the same as it is in the $S^R(j)$ for $F+H_2(0,j)$. Thus, the position of the minimum in the $S^R(j)$ remains constant regardless of the mass of the incoming atom. However, it shifts to higher values of j when the mass of the diatom is increased. The phenomenon is addressed further on.

Reaction cross sections, $S^R(j)$ at various translational energies calculated on the SE4 surface are shown in Figure V.2 for $F+H_2$ and $F+D_2$. Like the $S^R(j)$ calculated on the SE1 surface, those calculated on the SE4 surface for $F+H_2$ are in agreement with the average $S^R(j)$ of Polanyi and Schreiber [60] (note that Polanyi and Schreiber only considered values of j to 6). There are several interesting features of these $S^R(j)$. They are: 1) The $S^R(j)$ decreases from j=0 to 1 for $F+H_2$ and then they increase as j is increased from 1 to 12. The $F+D_2$ system exhibits the same qualitative behavior with no significant shift in the position of the minimum as there was on the SE1; 2) In contrast with the SE1 surface, the $S^R(j)$ decrease as the collision energy is increased; and 3) The reactive cross sections calculated on the SE4 surface are much larger than those calculated on the SE1 surface. Each of these

points will be addressed in turn.

First, it is important to note that minima in the $S^R(j)$ calculated on the SE1 surface and those calculated on the SE4 surface are different types of minima, that is to say, they are caused by different phenomena. On the SE1 surface the minima in the $S^R(j)$ shift when going from $F+H_2(0,j)$ to $F+D_2(0,j)$ but they occur at the same value of rotational energy of the diatom. This fact is demonstrated in Figure V.3, where S^R versus E_j (rotational energy) are shown for both $F+H_2(0,j)$ and $F+D_2(0,j)$. In contrast, the minima in the $S^R(j)$ calculated on the SE4 surface do not occur at the same value of rotational energy since they occur at the same value of j. In fact, it has been determined by Isakson [171] that the minima in the $S^R(j)$ calculated on the SE4 surface are the result of the long range attractive well in the entrance valley. That is, the well causes the reactive cross section at j = 0, $S^R(0)$, to be anomalously high. In that work, Isakson determined that the range of asymptotic γ values (see Figure II.1 for a definition of γ) which lead to reaction at j = 0 is roughly two times that for nonzero j values. When j = 0 the well is able to "funnel" more trajectories into the reactive region, that is, it is able to steer more trajectories into the preferred geometry for reaction, γ = 0.

The well in the entrance valley is also responsible for the increase in the $S^R(j)$ as the E_t is decreased. This behavior is typical of surfaces which have a well in the entrance

valley. The attractive well can capture the incoming atom and therefore increase the reaction cross section [128]. As the translational energy is increased the effect of the well becomes less pronounced, that is, the well is less able to capture the incoming atom. Thus the reaction cross section decreases.

Lastly, placing a well in the entrance valley of the potential softens the bend mode. Therefore, the $S^R(j)$ are higher on the SE4 surface than those calculated on the SE1 surface (see discussion of effect of changing B_o in Chapter IV).

The significance of the position of the minima in the $S^R(j)$ calculated on the SE1 surface and the qualitative shape of the $S^R(j)$ calculated on both surfaces is best explained with the aid of our model.

The reduced SE1 and SE4 potentials have been previously given in Chapter II, equations II.15 and II.16 respectively. The method for calculating classical trajectories on these reduced surfaces is discussed in Chapter IV. The shapes of the reduced potentials are in qualitative agreement with the shape of the actual surfaces as can be seen from an examination of Figures II.7 and II.8 for the SE1 surface and Figures II.9 and II.10 for the SE4.

The $P^R(j)$ for the $F+H_2$ on the reduced SE1 surface are shown in Figure V.4 (Note: the $P^R(j)$ have been calculated with J=j). It should be pointed out that the collision energies are

much higher here than in the 3D trajectories. This is because the model system has no zero point vibrational energy available to enhance reactivity. The model does, however, qualitatively reproduce the "dip and climb" behavior of the 3D $S^R(j)$. Further, the position of the minimum is fixed regardless of the translational energy. However, the position of the minimum is shifted as compared to the 3D $S^R(j)$ from j = 6 to j = 8. The model also reproduces the shift in the minimum to larger j when D is substituted for H, i.e. j is shifted from j = 8 to j = 10.

The $P^R(j)$ for several fixed translational energies obtained using the reduced SE4 potential are shown in Figure V.5. The $P^R(j)$ increase as the translational energy is increased. Further, the $P^R(j)$ increase monotonically with increasing j. Thus, the reduced SE4 surface only reproduces the correct qualitative shape of the 3D $S^R(j)$ from j = 1 to 12. The reduced SE4 potential does not reproduce the "dip" in the $S^R(j)$ as j goes from 0 to 1 even though a well has been added to the entrance valley. The reason for this is as follows. The reduced potential's well is an isotropic well, i.e. it is equal for all values of γ. Isakson [171] has determined that the actual well present in the SE4 surface is anisotropic, with the deepest part of the well coming between $\gamma = -10^\circ$ and 10°. It is precisely this anisotropy which "funnels" the trajectories into the reactive region. In this work, the area of interest is the trends in $S^R(j)$ not the

effect of placing a well in the entrance valley. Thus, the fact the $P^R(j)$ calculated on the reduced SE4 surface do not decrease with increasing energy nor do they "dip" between j=0 and j = 1 is not of great concern. However, the fact that the correct trend from j = 1 to 12 in the $S^R(j)$ can be reproduced by the reduced SE4 potential is the important point.

The trend of a decrease in $S^R(j)$ followed by an increase, i.e. "dip and climb", has been traditionally explained as the result of the competition between the orientational effect and the energy effect [14,150]. Both these effects were fully defined in Chapter IV. In that chapter, it was determined that the orientational effect is responsible for the downward trend of the $P^R(j)$ at low j. As j is increased further the energy effect begins to dominate the orientational effect, thus the $P^R(j)$ begins to increase with j.

As was noted in Chapter IV, the strength of the bend mode can play an important role in the functional form of the $S^R(j)$. In that chapter an analysis of how the strength of the bend mode is related to both the orientational and the energy effects was undertaken. It was determined that the dominance of the orientational effect was dependent upon the strength of the bend mode. For a "tight" bend mode, the orienational effect dominates the dynamics of the system. As the bend mode becomes "softer" the dominance of the orientational effect is quickly diminished. In this case, the dynamics is dominated by the energy effect.

When the strength of the bend mode is varied the $P^R(j)$ calculated on both the reduced SE1 (Fig V.6) and the reduced SE4 (Fig V.7) surfaces exhibit the same trends as were discussed above. It should be noted that due to the slightly different form of the reduced SE1 and SE4 potentials, compared to the form of the symmetric reduced potential, the parameter which controls the strength of the bend mode is c_o (II.15 and II.16), not B_o (II.14) as it was in the case of the symmetric reduced potential.

The significance of the position of the minima in the $S^R(j)$ calculated on the SE1 surface will now be addressed. This is most easily accomplished by enlisting the aid of the model. Recall (Chapter IV) that, for nonzero j, trajectories travel across the (s,γ) plane with a slope $d\gamma/ds$. The slope is given by, $d\gamma/ds = (j/I)(\mu/2E_t)^{1/2}$. At constant translational energy $d\gamma/ds$ is proportional to $\mu^{1/2}$ j/I. It is reasonable to assume that $d\gamma/ds$ at the minimum is always the same. Evaluation of $d\gamma/ds$ at the minimum, for our model system, reveals that this is, in fact, the case. That is, $d\gamma/ds$ is equivalent for $F + H_2$ and $F + D_2$. In light of this it is apparent that j is shifted to a larger value for $F+D_2$ due to the fact that μ and I have changed upon isotopic substitution.

As was mentioned in Chapter IV, there are other theories concerned with the effect of reagent rotation on reactivity which imply a different functional form of the $S^R(j)$ at high and low impact parameters [150]. Doubt has been cast upon this

assertion by Mayne and Harrison [151] who plotted the $P^R(j)$ at fixed impact parameters for the O + HCl(0,j) --> OH + Cl system. They observed the same functional form of the $P^R(j)$ for all impact parameters examined. Additionally, this same result was observed in Chapter IV for model $P^R(j)$ calculated on the symmetric reduced potential at fixed l.

In that same spirit, probability of reaction as a function of j has been examined at constant l for the F + $H_2(0,j)$ --> HF(v',j') + H and F + $D_2(0,j)$ --> DF(v',j') + D system for both the SE1 (Figure V.8) and the SE4 (Figure V.9) surfaces. Two major points merit discussion from an analysis of these plots.

First and foremost, the functional form of the $P^R(j)$ curve at constant l is similar for l=0 (b=0) and l>0 (b>0) collisions on both surfaces (Figures V.8 and V.9). Further these $P^R(j)$ exhibit the same trends as the 3D $S^R(j)$. It is interesting to note that on the SE4 surface, for large impact parameter collisions (l=20) the effect of the well is effectively "quenched" and the probability of reaction purely rotationally enhanced.

It should be noted that as l is increased the $P^R(j)$ calculated on both surfaces decreases. This is not surprising since larger l values correspond to larger impact parameters, b ($l = \mu v b$, where v is the relative speed). There is a very simple idea which aids in the rationalization of larger impact parameter (large l) collisions being less reactive than

smaller impact parameter collisions. The larger the l value the higher the effective potential [3] (ie. $V_{eff} = l^2/2\mu r^2 + V$) and as a result of this larger potential the reactivity decreases. Or, from a different perspective, as the impact parameter becomes larger it becomes more difficult for a F atom to enter the diatom's cone of acceptance [2]. The result, here again, is a decrease in $P^R(j)$ as l is increased. In summary, we have seen from an analysis of the $P^R(j)$ at fixed l that the functional form of the $P^R(j)$ is similar regardless of the l value. This means, in essence, that the $P^R(j)$ behave in the same manner for all impact parameters. This result effectively puts to rest theories implying differing behavior at high and low b or some sort of oscillatory behavior of the $P^R(j)$ with b [14,151,152].

Polarized Trajectories

Polarization, or the polarization direction, is defined as the initial direction of the rotational angular momentum vector, $\mathbf{j}$ (see Appendix A, Fig A.2). The polarization direction can be initially selected to lie in the x direction, j_x (coplanar trajectories), in the y direction, j_y, or the z direction, j_z. Pictorial representations of these polarization directions are shown in Figure A.2. Of the three polarization directions, the j_x direction is the most important for the following reasons. First, and the most obvious, coplanar trajectories have higher cross sections and therefore fewer trajectories need to be run in order to observe the trends.

Secondly, the use of reduced dimensionality makes the dynamics of the system easier to visualize. Lastly, and most importantly for this work, if the trends in the $S^R(j)$ of the coplanar trajectories are in qualitative agreement with those observed in 3D $S^R(j)$ this would lend further support to the belief that the model developed in Chapter II accurately describes rotational behavior. [21,22,51].

Reactive cross sections calculated on the SE1 and the SE4 surfaces for $F+H_2$ for trajectories which have been initially polarized are shown in Figure V.10. The reaction cross sections for trajectories which were initially randomly oriented, j_{ran}, have been included to allow for comparison. We find trajectories with j_x polarization have a higher cross section, as might be expected, and exhibit the same trends in $S^R(j)$ as the $S^R(j)$ for the randomly oriented trajectories. Trajectories with polarization in the j_y direction are less reactive than the 3D trajectories. Finally j_z polarization, not shown on the plot, was unreactive at all j's. This is not surprising since the molecule is rotating in a plane perpendicular to the direction from which the atom approaches.

The coplanar, j_x polarization, $P^R(j)$ calculated at fixed l on the SE1 and the SE4 surfaces are shown in Figures V.11 and V.12, respectively. The coplanar $P^R(j)$ calculated on both surfaces have the same qualitative shape as their respective 3D $S^R(j)$ (Figs V.8 and V.9). That is, as l is increased the $P^R(j)$ decrease and the $P^R(j)$ have the same qualitative shape

at all l. Furthermore, as l is increased the $P^R(j)$ decrease as in the case of the 3D $P^R(j)$ at fixed l. Model trajectories calculated on both the reduced SE1 (Fig V.13) and the reduced SE4 (Fig V.14) surfaces reproduce this qualitative behavior.

Product Angular Distributions

Analysis of the center of mass scattering angle of the products of a chemical reaction can yield insight into the reaction mechanism [3]. For example, a "direct" reaction, one in which the reaction is over before the colliding molecules have time to execute one or more rotations about one another will exhibit an anisotropic scattering distribution. That is, one particular range of scattering angles will be more likely than any other, i.e. the scattering distribution will be peaked. If the reaction is "complex", the time scale of the reaction is on the order of a rotational period (picosecond), the center of mass angle scattering distribution will be symmetric about 90°.

Differential cross sections (DCS) for the $F+H_2(0,j)$ system on the SE1 surface for j = 1, 4, and 12 are shown in Figure V.15. The DCS calculated in the SE4 surface for j = 0, 1, and 4 are shown in Figure V.16. In general, the functional form of the DCS can be fit by an expression of the form [154]

$$d\sigma/d\omega\ (E,\theta) = 0, \qquad \theta > \theta_{max}$$
$$= A\ \cos^N(\pi/2 * \theta/\theta_{max}), \qquad \theta < \theta_{max}, \qquad (V.1)$$

where the normalization parameter, A, the shape parameter, N, and θ_{max}, the maximum center of mass scattering angle, all

depend on the collision energy and the initial rotational quantum number. Justification for a fit of this type derives from previous work on fitting differential cross sections [154,155]. The fits for DCS's obtained from both the SE1 and the SE4 surfaces are also plotted in Figures V.15 and V.16 (solid line). In general, for zero and small nonzero j values N is equal to 2, however for large j values N = 1. This trend was observed on both surfaces.

We can conclude the following in regard to these DCS data. First, the $F+H_2$ (0,j) reaction is a direct reaction. This is evident from the fact that the DCS is peaked in the forward direction (note: θ was measured relative to the product atom) on both surfaces. This phenomenon has been observed experimentally [111] and in other theoretical work [125]. The usual interpretation of this fact is that the reaction is dominated by the collinear geometry, whereas a shift to less forward scattering implies the bent geometry is playing the major role in the reaction [3]. It is this bent geometry which is, in part, responsible for the broadening of the DCS when j = 12 (SE1). The "Repulsive" nature [8,9] of the surface also contributes to the forward scattering of the product atom, i.e. most of the energy is released as the products separate.

Second, the product angular distributions, calculated on both surfaces, correlate extremely well with trends seen in the reactive cross sections (Figures V.1 and V.2). On the SE1

surface in going from j = 0 to 4 the reactivity decreases and the DCS becomes much narrower (i.e θ_{max} is decreasing). As j is increased further (j=12) the reactivity increases and the DCS becomes much broader. In contrast to the DCS distributions obtained on the SE1 surface, the DCS distributions on the SE4 surface show no decrease in θ_{max} as j goes from 0 to 1, but rather θ_{max} increases with increasing j (for j > 1).

This behavior of the DCS can be understood as follows. On the SE1 surface as the reaction cross section drops, so too does b_{max} (Appendix A), the maximum impact parameter leading to reaction. This fact is illustrated in Figure V.17, where the opacity functions, $P^R(l)$, for $F+H_2$ at fixed j values are shown. It has been shown, for $H+H_2$ [154], that θ_{max} has a simple almost linear dependence on b. This relationship is important since it relates the experimentally observable θ_{max} to b_{max} which is affected in the same manner as the reactive cross section, S^R, by rotational excitation (Figure V.18). The decreasing portion of the $S^R(j)$ can also be interpreted as a narrowing of the "cone of acceptance" [55]. Which corresponds to a decrease in b_{max}. Similarly, the increase in θ_{max} as j goes from 4 to 12 corresponds to a opening up of the cone of acceptance, i.e. an increase in b_{max}.

In contrast to the SE1 surface, the DCS obtained on the SE4 surface show no decrease in θ_{max} as j goes from 0 to 1. That is, the decrease in cross section from 0 to 1 is not due to a decrease in b_{max}, but rather to a decrease in the range of

initial γ values which lead to reaction. These trends in b_{max} with j are nicely summarized in Figure V.18. It is interesting to note, on the SE4 surface b_{max} is higher at E_t = 0.075 eV. This is due to the fact that, as previously mentioned, the well can "funnel" more trajectories into the reactive region at this lower translational energy. The shift in the minimum of the $S^R(j)$ when D_2 is substituted for H_2 is also present in the b_{max} versus j function (not shown). Since b_{max} shows the same trends with j as the $S^R(j)$ and is related to the experimentally observable θ_{max} this could allow the experimentalist to draw qualitative conclusions concerning how rotational excitation is affecting the system under investigation (ie. the nature of the bend mode at the transition state) from the DCS data.

Product Rotational Distributions

In a further attempt to determine what experimentally observable quantities will yield insight into the reactivity as a function of reagent rotation, product rotational distributions have been examined. The product rotational distributions for several initial j values are shown in Figures V.19 and V.20 for F + H_2 (0,j) --> HF (j') + H and its isotopic analog calculated on the SE1 (Fig V.19) and the SE4 (Fig V.20) surfaces, respectively. Rotational distributions have been summed over all v' values. Additionally, the first moment of the product rotational quantum number, <j'>, has been plotted as a function of j. These data are shown in

Figures V.21 and V.22, for both the SE1 and the SE4 surfaces. Several aspects of these data merit discussion.

First, the product rotational distributions appear to be gaussian for HF and DF on both surfaces. Second, the HF distributions are not as broad as the DF distributions. This is true also on both surfaces. Third, the value of <j'> shifts to higher values as j is increased (Figures V.19 and V.20). This is most obvious from a consideration of Figures V.21 and V.22, i.e. <j'>(j). On the SE4 surface, <j'> increases almost linearly with increasing j for both high and low translational energy. That is, the <j'> are purely kinematic, i.e. independent of potential energy [3]. On the SE1 surface, at high translational energy <j'> also increases linearly with j. However, near threshold, <j'> increases slowly initially at low j, flattens out for a time, then increases rapidly with j (as seen at higher energies). This flattening out of the function occurs in the region of the minima in the $S^R(j)$. Due to the very low reactivity in this region (at 0.125 eV), it is not clear whether this result is statistically significant. Lastly, the <j'> is larger for DF than for HF. This is not surprising since $F+D_2$ reacts at larger values of l, therefore it contains more angular momentum which can be converted into j'.

Product energy distributions were also plotted for trajectories with the diatom initially j_x polarized. On the SE1 surface (Fig V.23) the j_x polarized trajectory

distributions are in very good agreement with the 3D trajectories for both HF and DF (Fig V.19). The <j'> for all fixed j values are approximately equal in the 3D and the coplanar trajectories. Additionally, the shapes of the distributions are very similar. It should be noted that in order to determine the shape of the distribution for the coplanar trajectories a larger number of reactive trajectories must be considered than in the 3D case. On the SE4 surface (Fig V.24) the shape of the distribution is somewhat skewed, i.e. non-gaussian. However, the <j'> have approximately the same value as in the 3D trajectories. The distributions for HF are "closer" to being gaussian than those of the DF. These HF distributions were computed from a sample which contained more reactive trajectories. In light of this, and similar trends with sample population seen on the SE1 surface it is believed that these distributions would be symmetric if a larger sample size was used.

Finally one last comment concerning product rotational distributions. One interesting feature of the final rotational state distributions on the SE1 surface is that they are not a function of center of mass scattering angle, θ, (Fig V.25). In other words, for given θ the shape of the $P^R(j')$ distribution remains unchanged. This is the case for both zero and nonzero initial j values. This has important implications if one considers the experimental constraints present in a molecular beam experiment. Often only a limited

number of detection angles are possible. In light of the above result, it would still be possible to obtain the $P^R(j')$ distribution from detection at one Lab angle.

We can conclude therefore, from an analysis of these data, that there is relatively little correlation between the trends seen in the $S^R(j)$ and those observed in the product rotational distributions.

Conclusions

We have used our newly developed knowledge regarding the behavior of the $S^R(j)$ to reconcile the apparently contradictory behavior of the $S^R(j)$ calculated on the SE1 surface and those calculated on the SE4 surface. It has been determined that the SE4 surface has a weak bend mode, therefore the dynamics is dominated by the energy effect. In contrast, the SE1 surface has a somewhat stronger bend mode which gives rise to the characteristic "dip and climb" behavior of the $S^R(j)$. It was previously determined that this behavior is the result of the competition between the orientational and the energy effects. Further, it was shown that trajectories in which the diatom was initially polarized manifest the same trends as their 3D counterparts. This, of course, has significance for our coplanar model.

It was further demonstrated that our model can qualitatively reproduce trends due to rotational excitation in exoergic reactions.

Finally, an analysis of product distributions revealed

the following. Product rotational distributions on both surfaces are kinematic in nature. Further, their behavior does not correlate with the $S^R(j)$ behavior. In contrast, the DCS data on both surfaces correlated extremely well with the $S^R(j)$ behavior.

Fig. V.1 Reactive cross section as a function of j calculated on the SE1 surface for $F + H_2(0,j)$, $F + D_2(0,j)$ and $M_x + H_2(0,j)$ where $M_x = 1$ amu. The translational energies are 0.200, 0.125, and 0.100 eV. Error bars are one standard deviation.

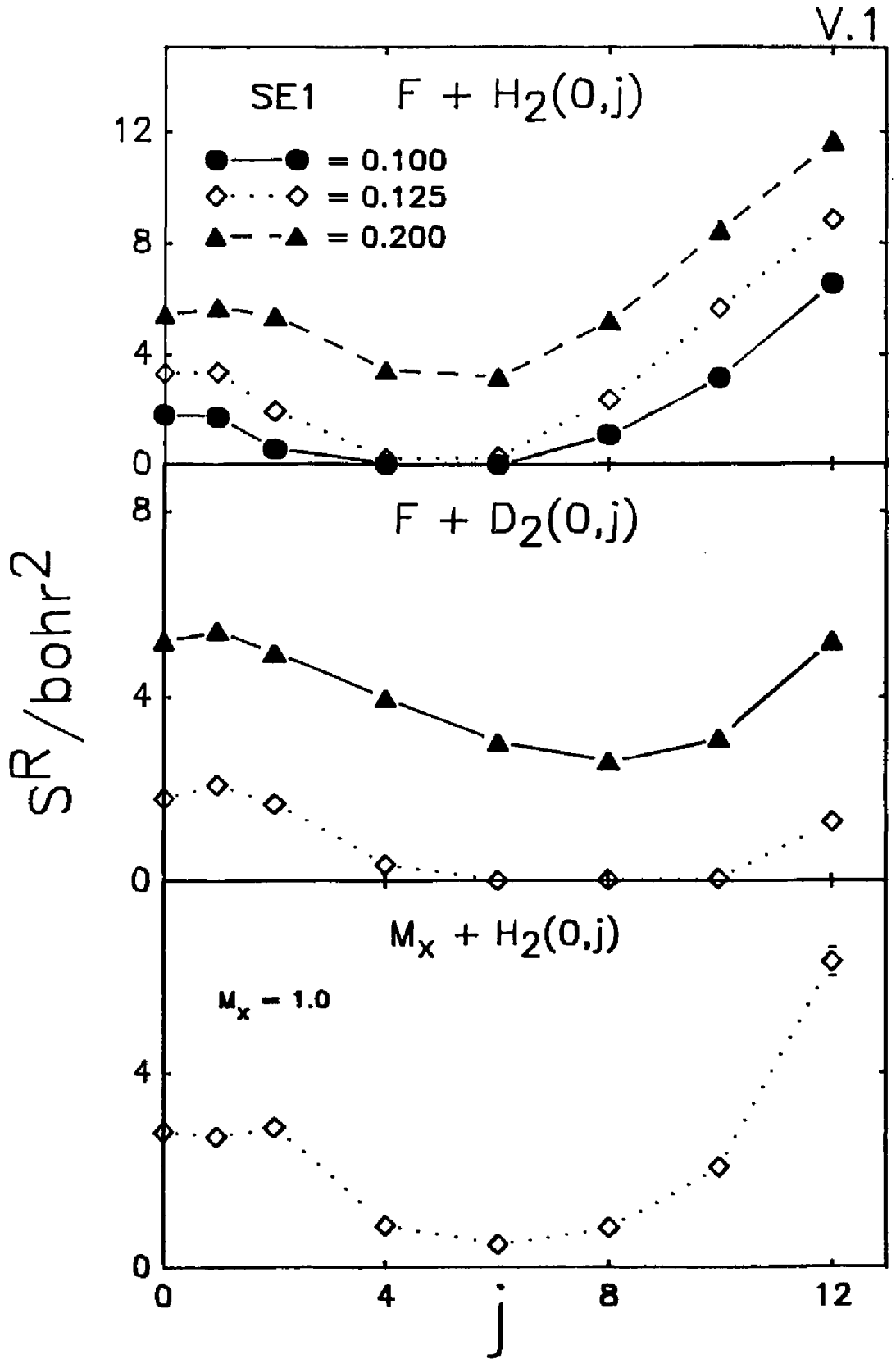
V.1
SE1 F + H2(0,j)
= 0.100
= 0.125
= 0.200
F + D2(0,j)
Mx + H2(0,j)
Mx = 1.0
SR/bohr2
j
0
4
8
12

Fig. V.2 Reactive cross sections as a function of j calculated on the SE4 surface for F + H_2(0,j) and F + D_2(0,j). The translational energies are 0.075 and 0.125 eV. Error bars are one standard deviation.

V.2

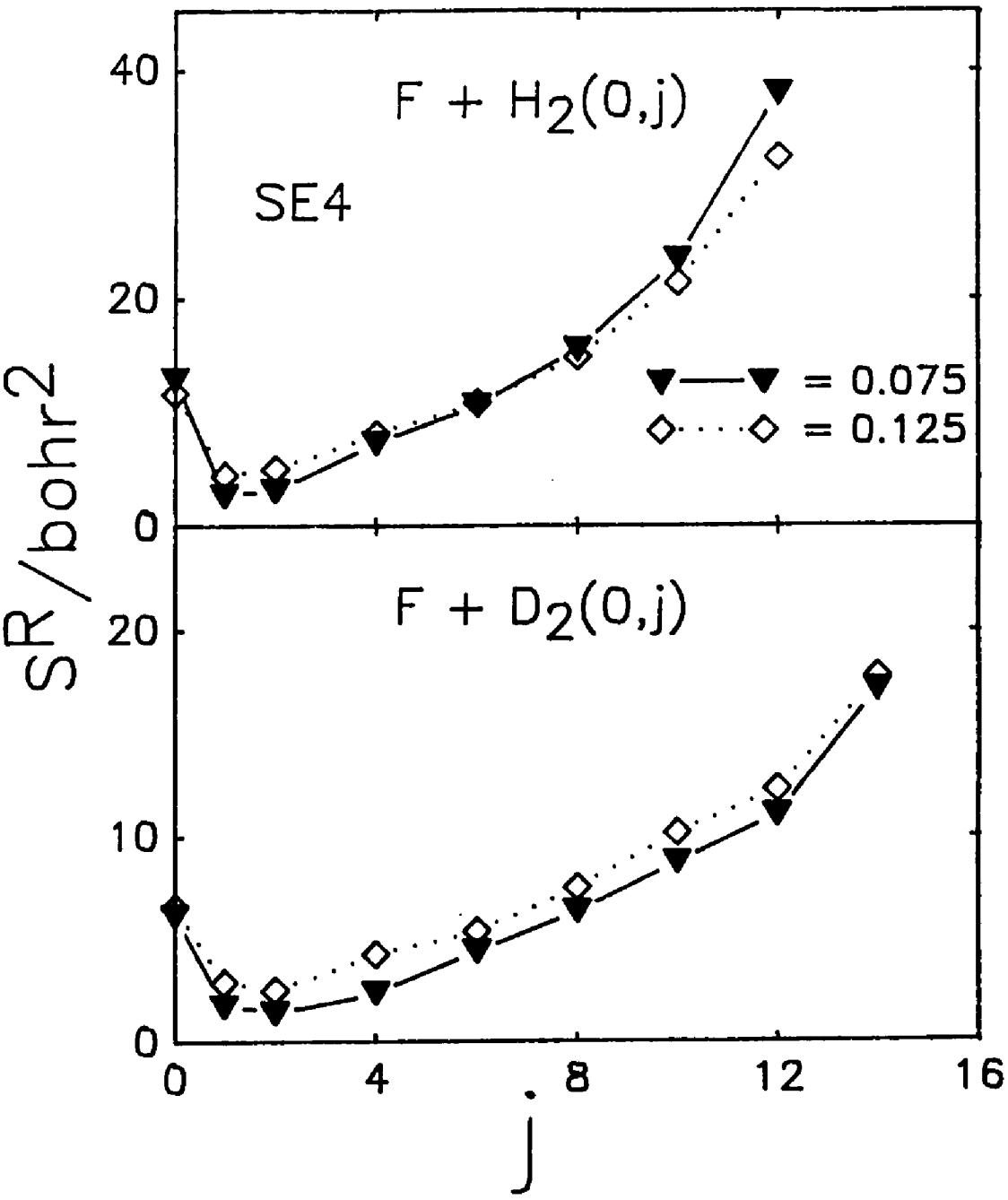

Fig. V.3 Reactive cross section as a function of rotational energy, E_j, calculated on the SE1 surface. The translational energy is 0.200 eV. Error bars are one standard deviation.

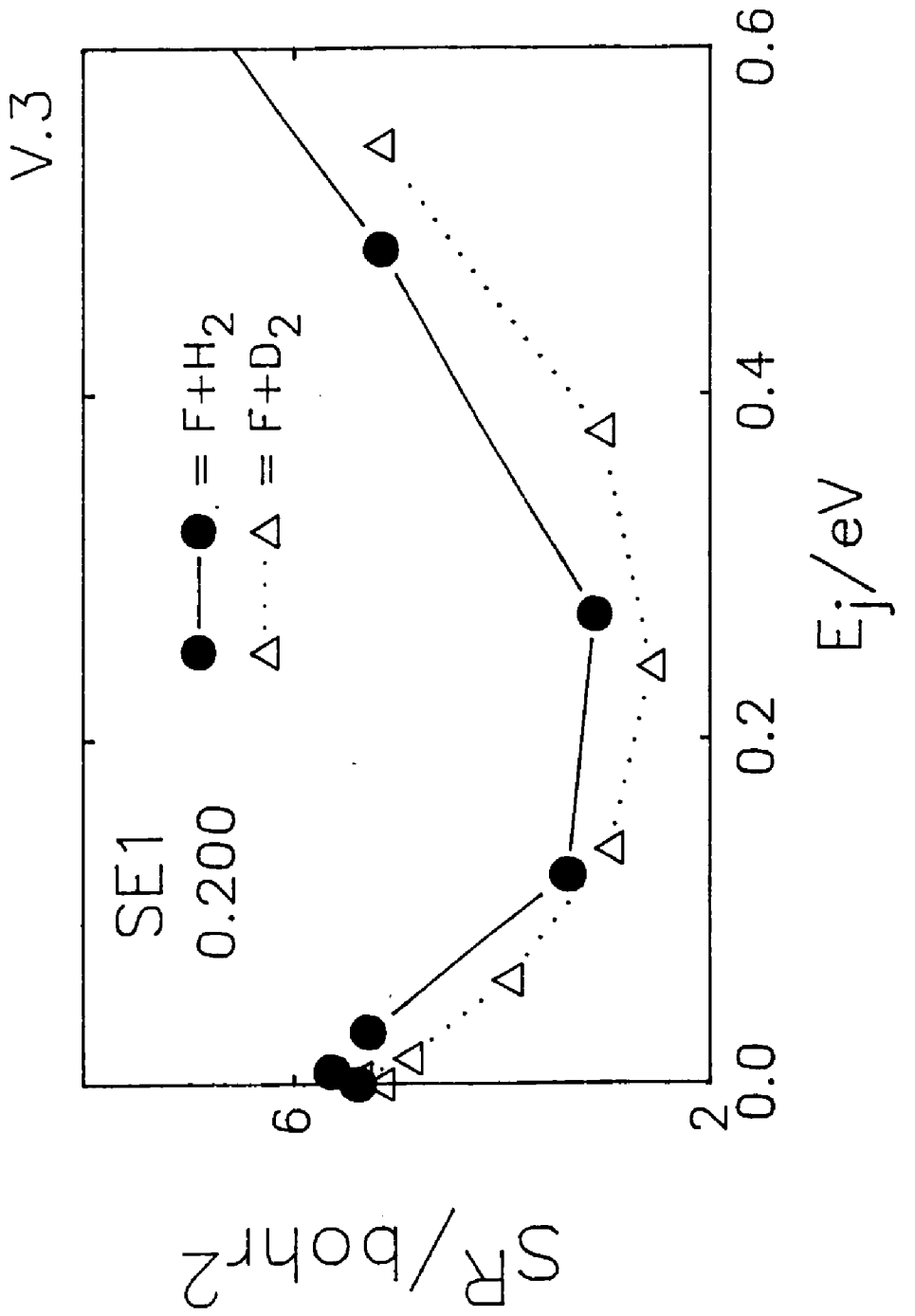
V.3
SE1
0.200
● = F+H2
Δ = F+D2
SR/bohr2
Ej/eV
0.0
0.2
0.4
0.6
2
6

Fig. V.4 Reaction probabilities as a function of j, for F + H_2(j) and F + D_2(j) calculated on the reduced SE1 surface. The translational energies are 0.45, 0.40, 0.35, and 0.30 eV. Error bars are smaller than the size of the point.

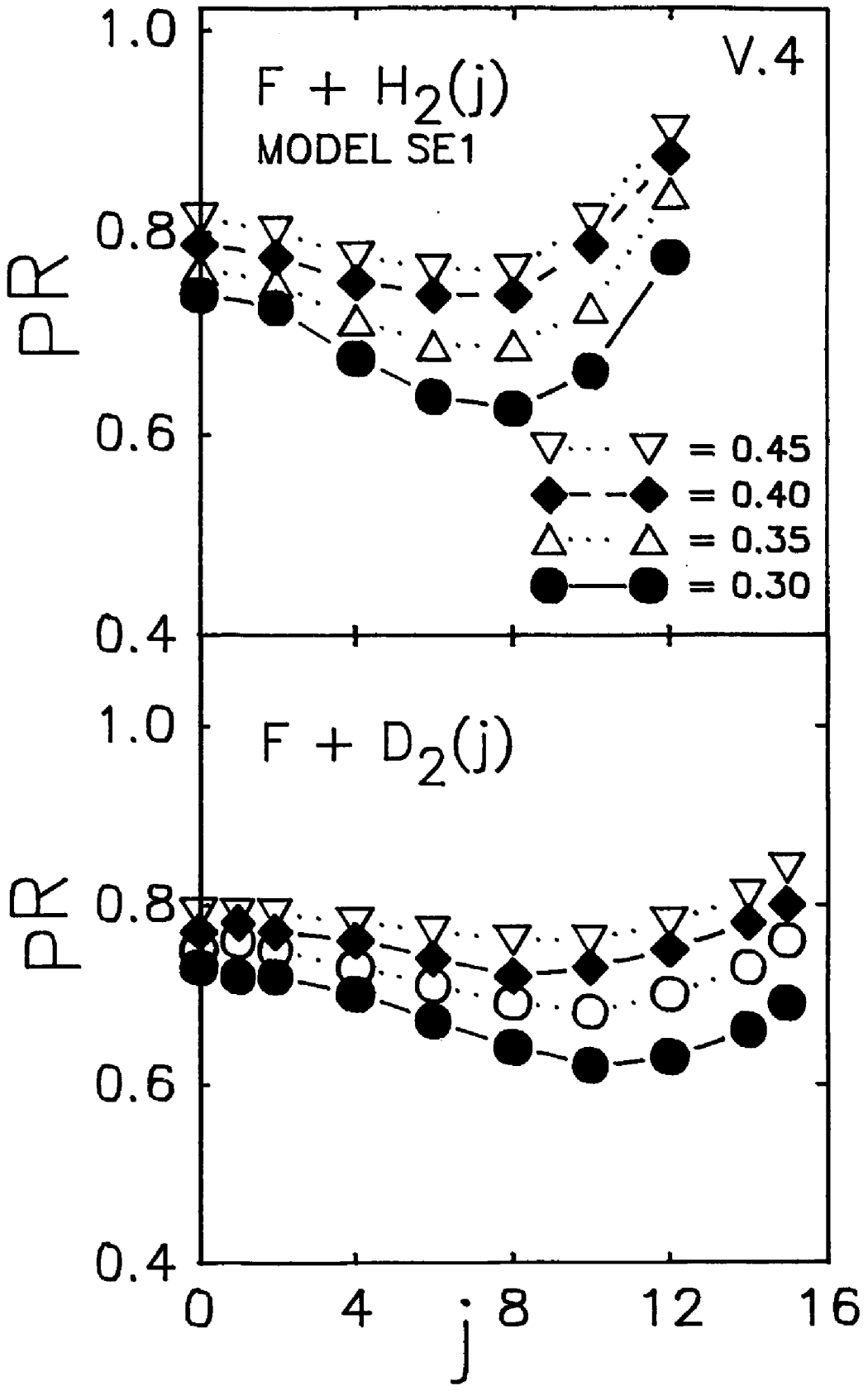
V.4
F + H2(j)
MODEL SE1
PR
1.0
0.8
0.6
0.4
= 0.45
= 0.40
= 0.35
= 0.30
F + D2(j)
PR
1.0
0.8
0.6
0.4
0
4
8
12
16
j

Fig. V.5 Reaction probabilities as a function of j for F + H_2(j) and F + D_2(j) calculated as the reduced SE4 surface. The translational energies are 0.30, 0.25, 0.20, and 0.15. eV. Error bars are smaller than the size of the point.

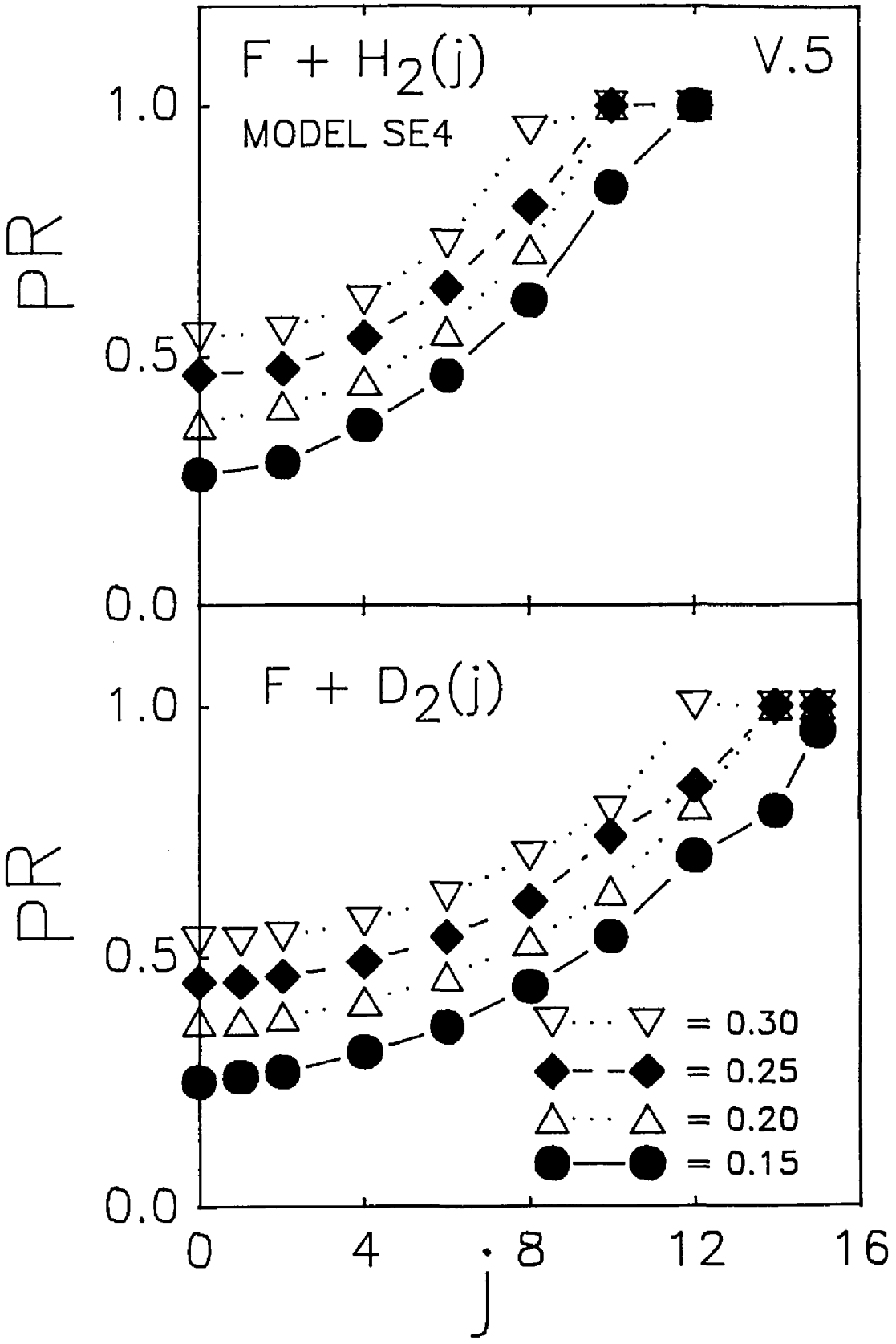
F + H2(j)
V.5
MODEL SE4
1.0
0.5
0.0
PR
F + D2(j)
1.0
0.5
0.0
PR
= 0.30
= 0.25
= 0.20
= 0.15
0
4
8
12
16
J

Fig. V.6 Reaction probabilities as a function of j for F + H_2(j) calculated on the reduced SE1 surfaces for fixed values of c_o. The values of c_o are 0.030, 0.0535, and 0.075 (au). The translational energy is 0.30 eV. Error bars are smaller than the size of the point.

V.6

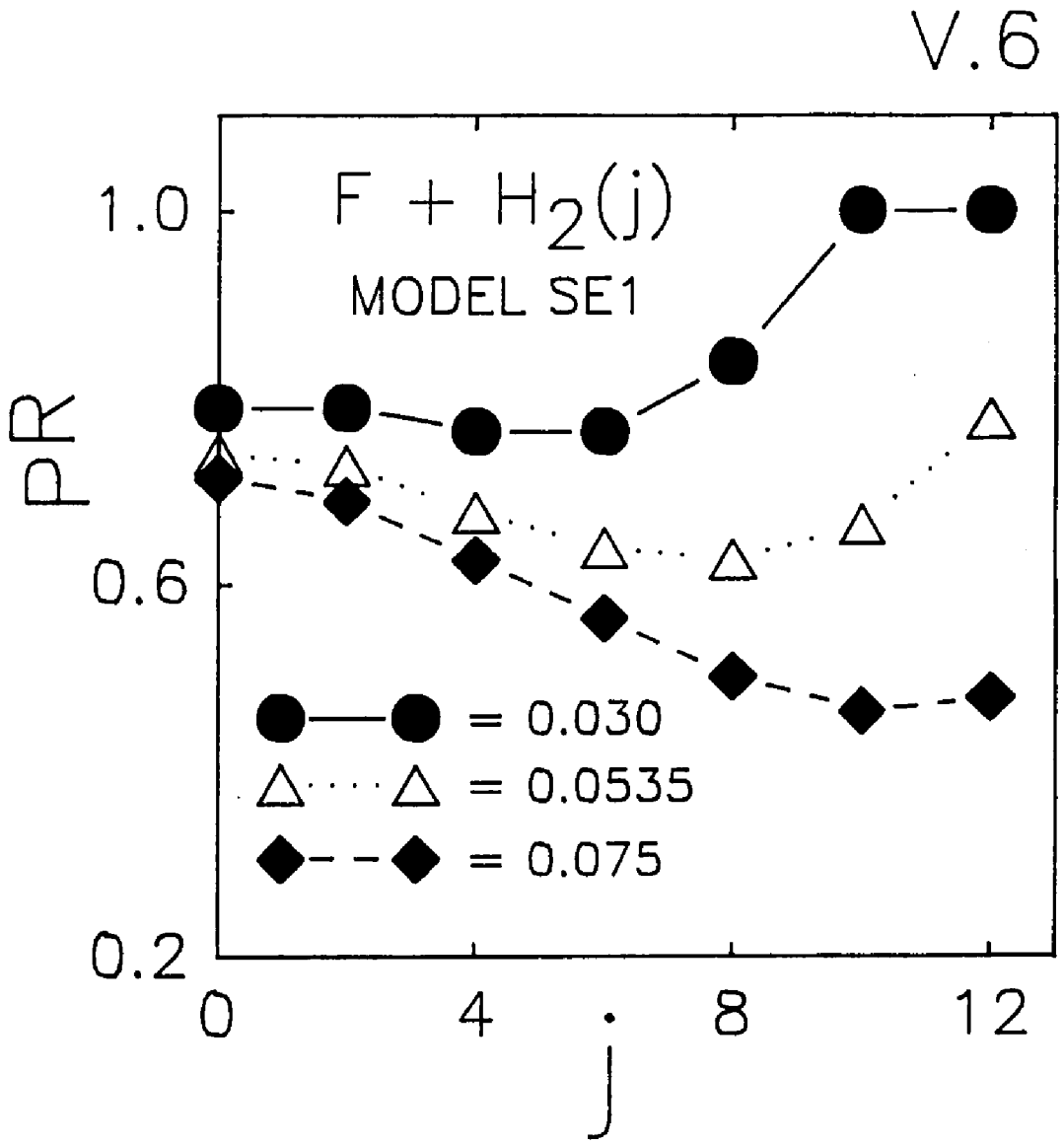

Fig. V.7 Reaction probabilities as a function of j for $F + H_2(j)$ calculated on the reduced SE4 surface for fixed values of c_o. The values of c_o are 0.015, 0.100, and 0.200 (au). Error bars are smaller than the size of the point.

V.7

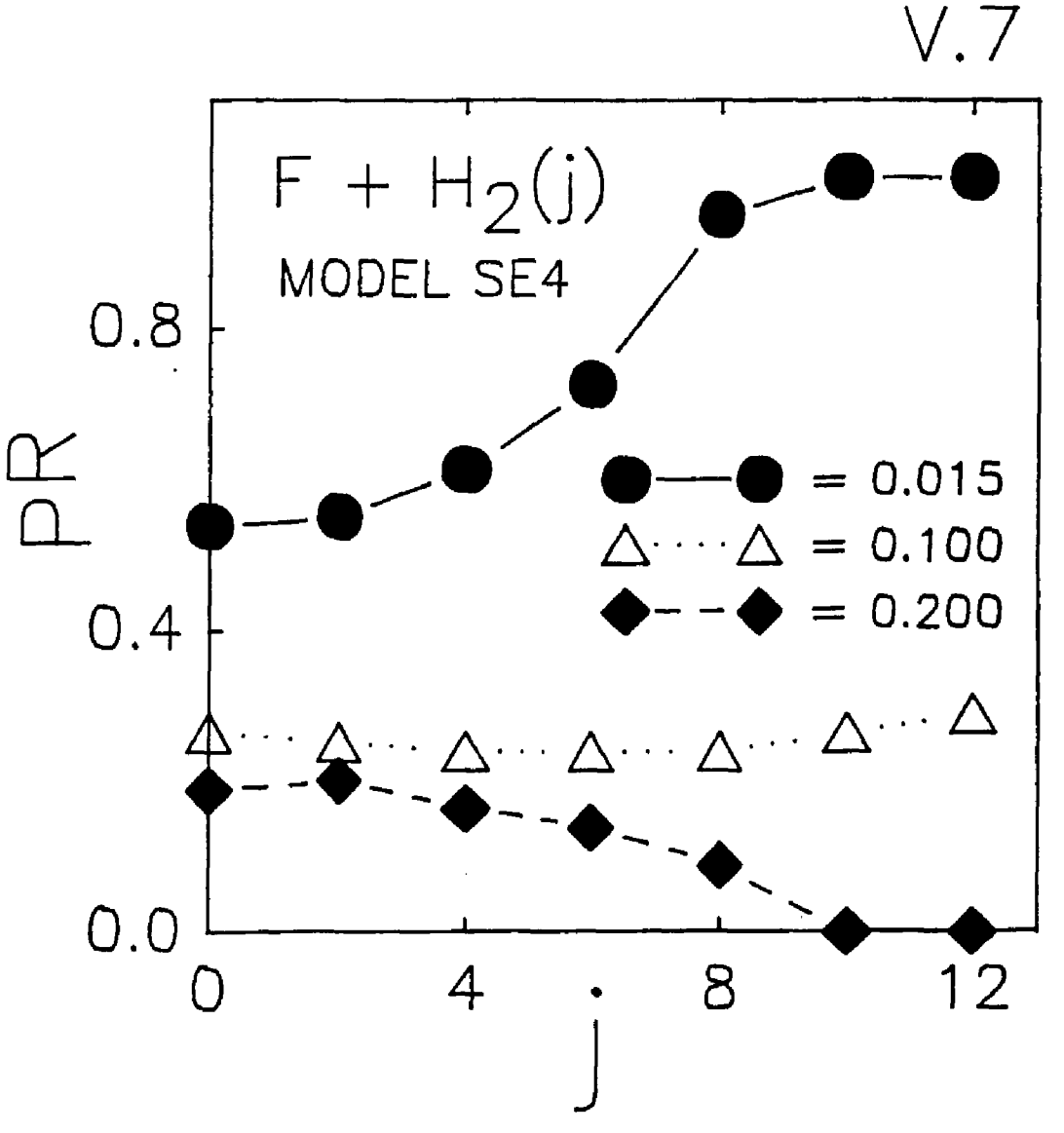

Fig. V.8 Reaction probabilities as a function of j for $F + H_2(0,j)$ and $F + D_2(0,j)$ calculated on the SE1 surface for fixed l. The translational energy is 0.125 eV.

V.8

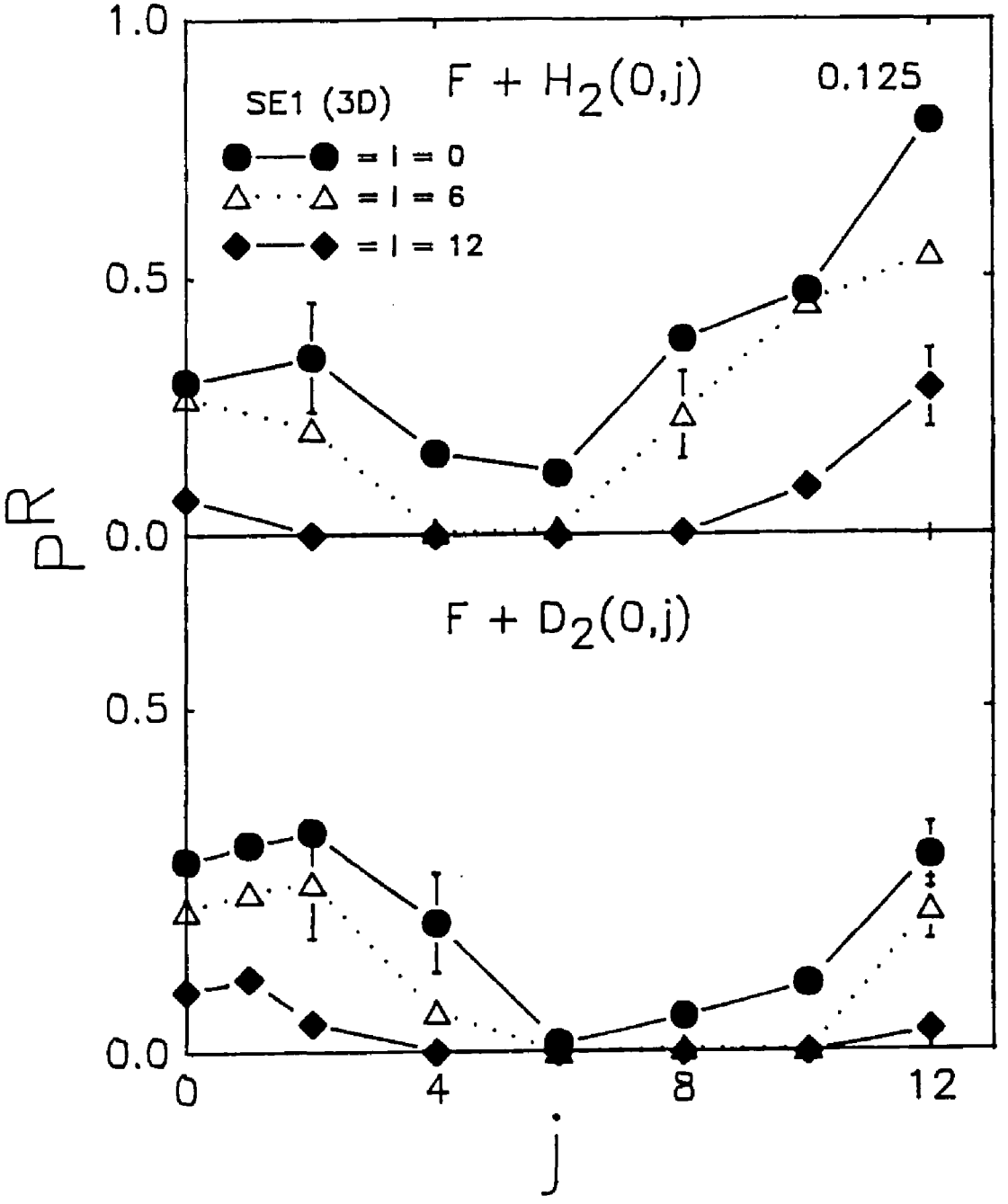

Fig. V.9 Reaction probabilities as a function of j for F + $H_2(0,j)$ and F + $D_2(0,j)$ calculated on the SE4 surface for fixed l. The translational energy is 0.125 eV.

V.9

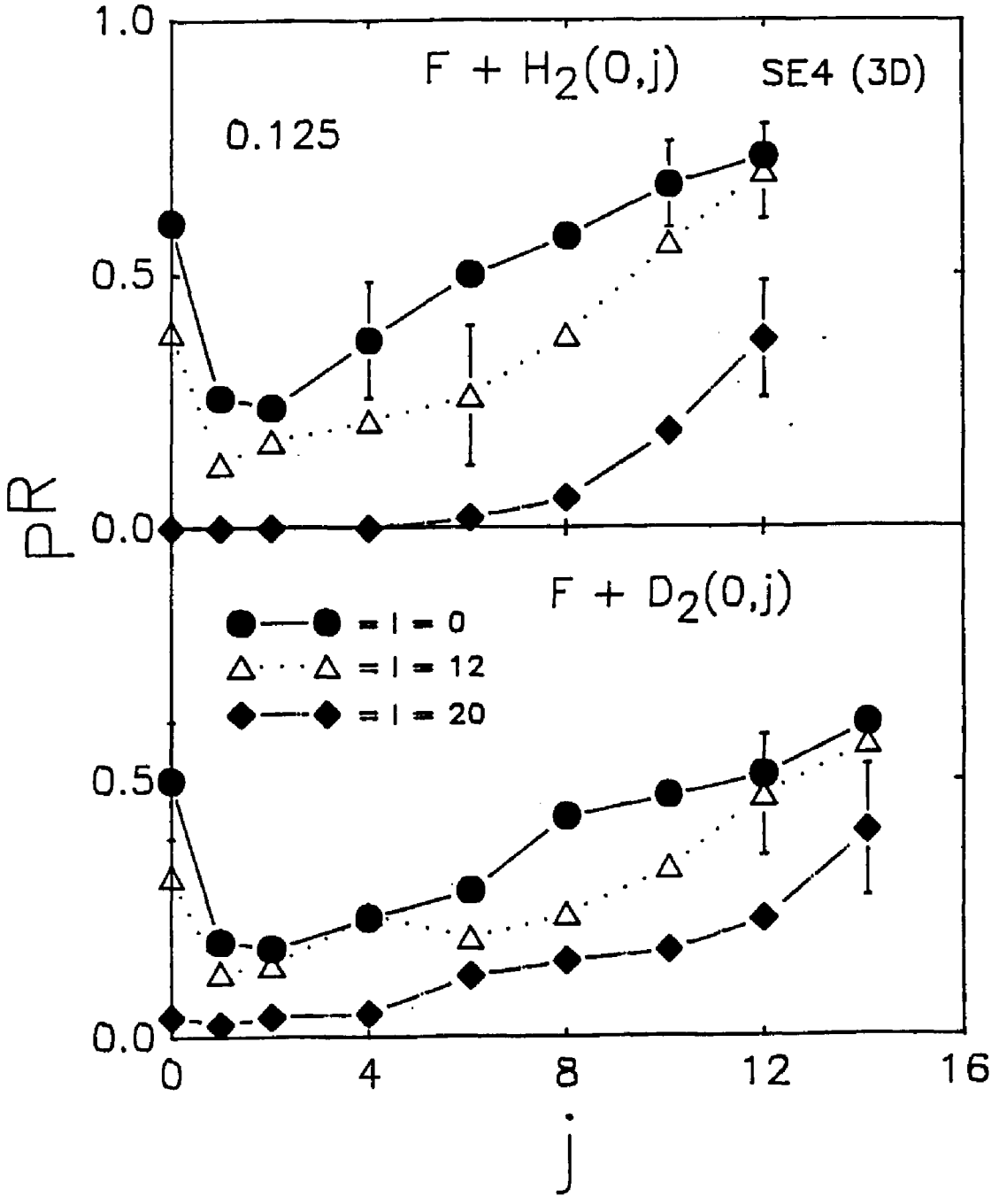

Fig. V.10 Comparison of reactive cross sections for trajectories in which the H_2 was initially polarized to those where H_2 was randomly oriented in space on both SE1 and SE4 surfaces. The translational energy is 0.125 eV. Error bars are one standard deviation.

V.10

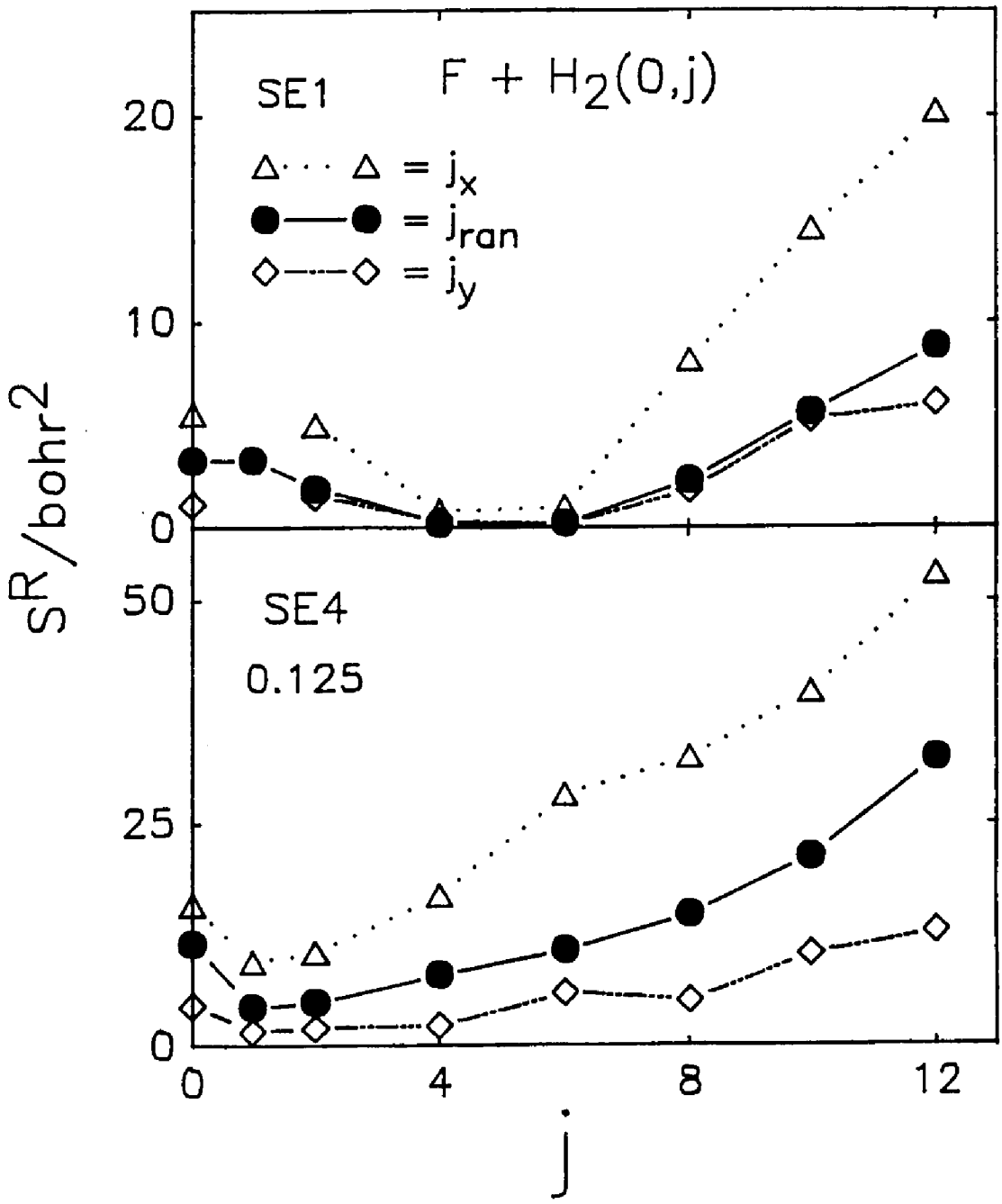

Fig. V.11 Probability of reaction as a function of j for coplanar trajectories on the SE1 surface. The $P^R(j)$ for both $F + H_2(0,j)$ and $F + D_2(0,j)$ are shown for fixed l. The translational energy is 0.125 eV.

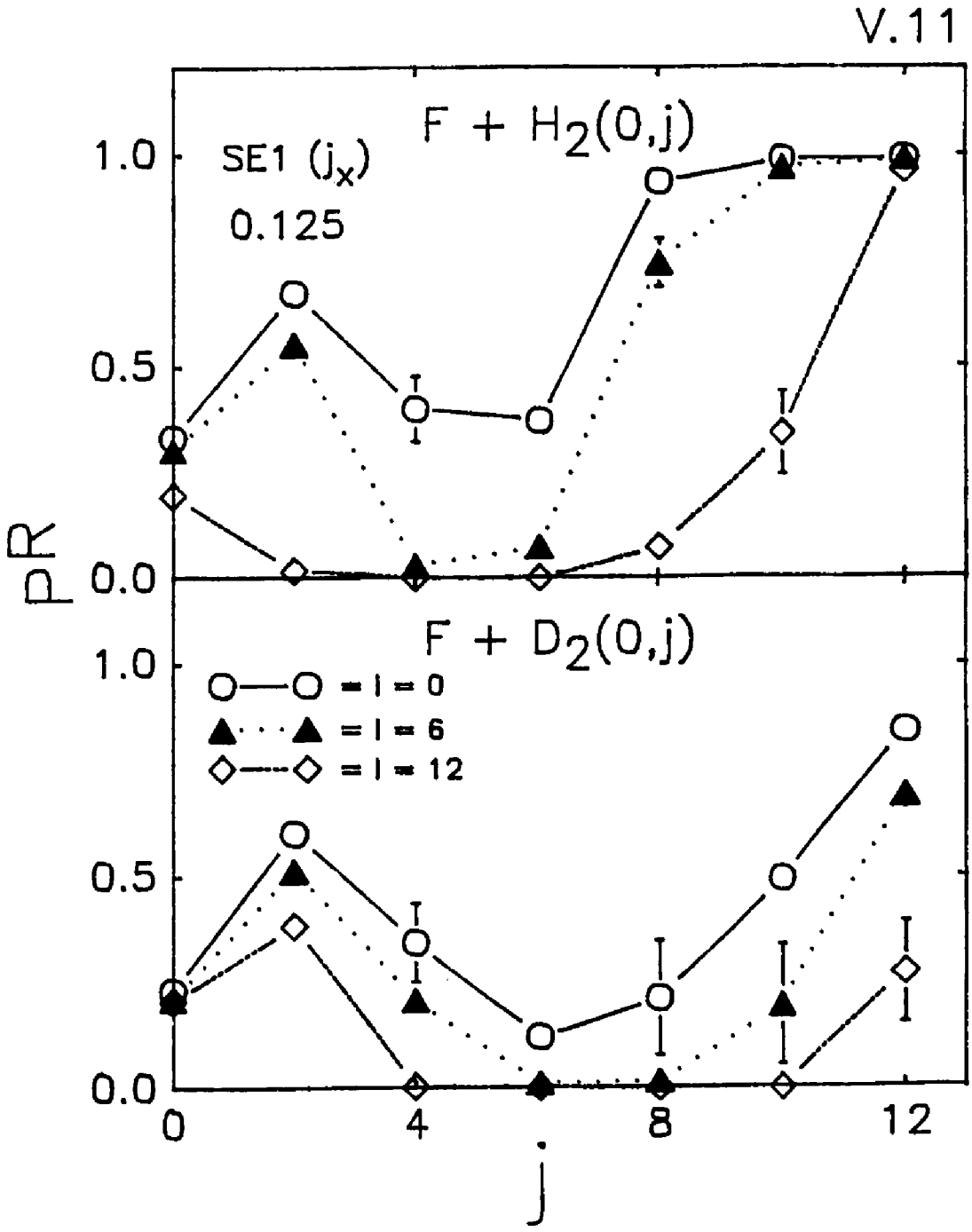
V.11
F + H2(0,j)
SE1 (jx)
0.125
1.0
0.5
0.0
PR
F + D2(0,j)
O—O = l = 0
▲···▲ = l = 6
◇—◇ = l = 12
1.0
0.5
0.0
0
4
8
12
j

Fig. V.12 Probability of reaction as a function of j for coplanar trajectories on the SE4 surface. The $P^R(j)$ for both F + $H_2(0,j)$ and F + $D_2(0,j)$ are shown for fixed l. The translational energy is 0.125 eV.

V.12

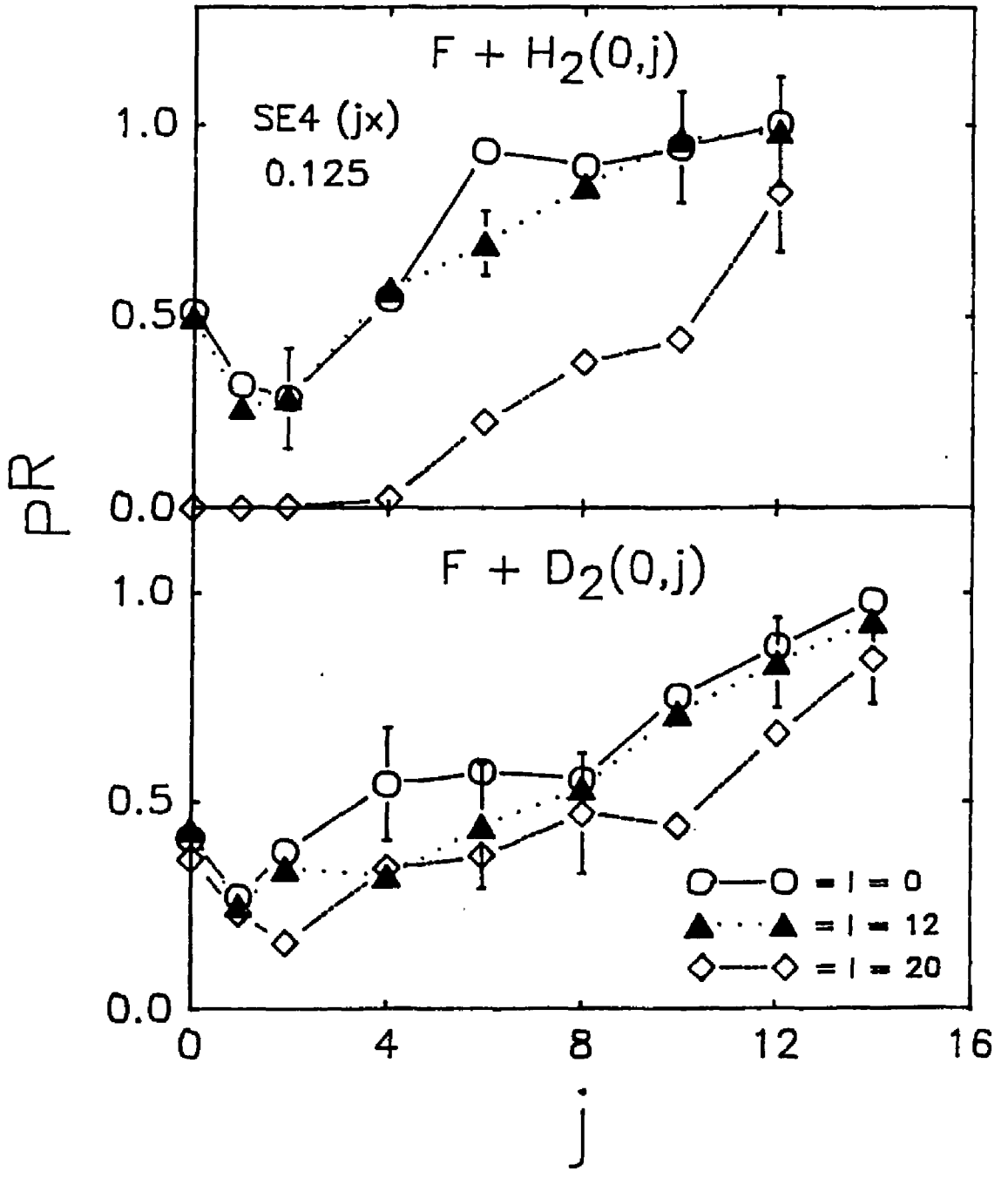

Fig. V.13 Reaction probabilities as a function of j for $F + H_2(j)$ and $F + D_2(j)$ calculated on the reduced SE1 surface at fixed l. The translational energy is 0.30 eV. Error bars are smaller than the size of the point.

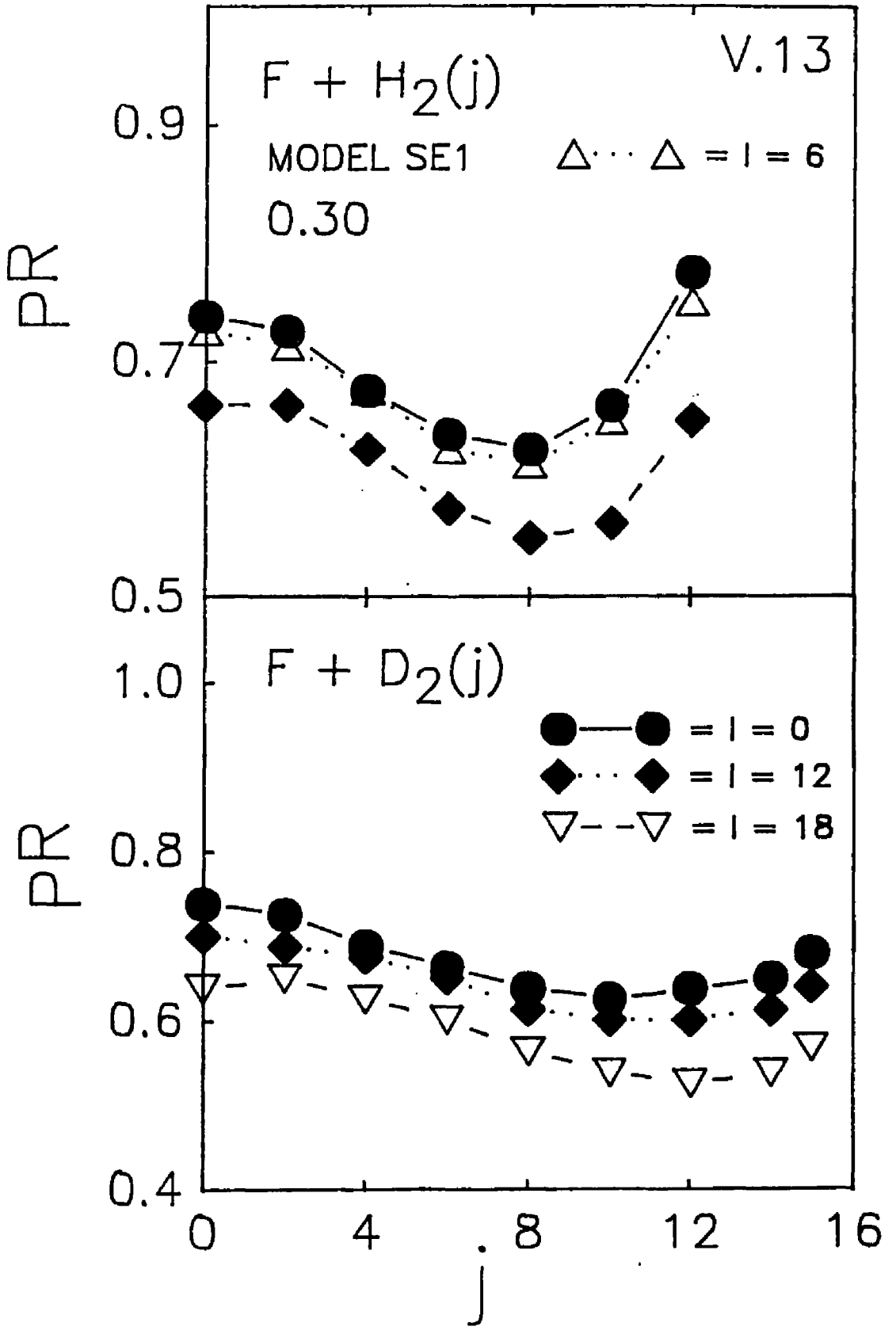
V.13
F + H2(j)
MODEL SE1
0.30
Δ··· Δ = l = 6
PR
0.9
0.7
0.5
F + D2(j)
= l = 0
= l = 12
= l = 18
PR
1.0
0.8
0.6
0.4
0
4
8
12
16
J

Fig. V.14 Reaction probabilities as a function of j for F + H_2(j) and F + D_2(j) calculated on the reduced SE4 surface at fixed l. The translational energy is 0.30 eV. Error bars are smaller than the size of the point.

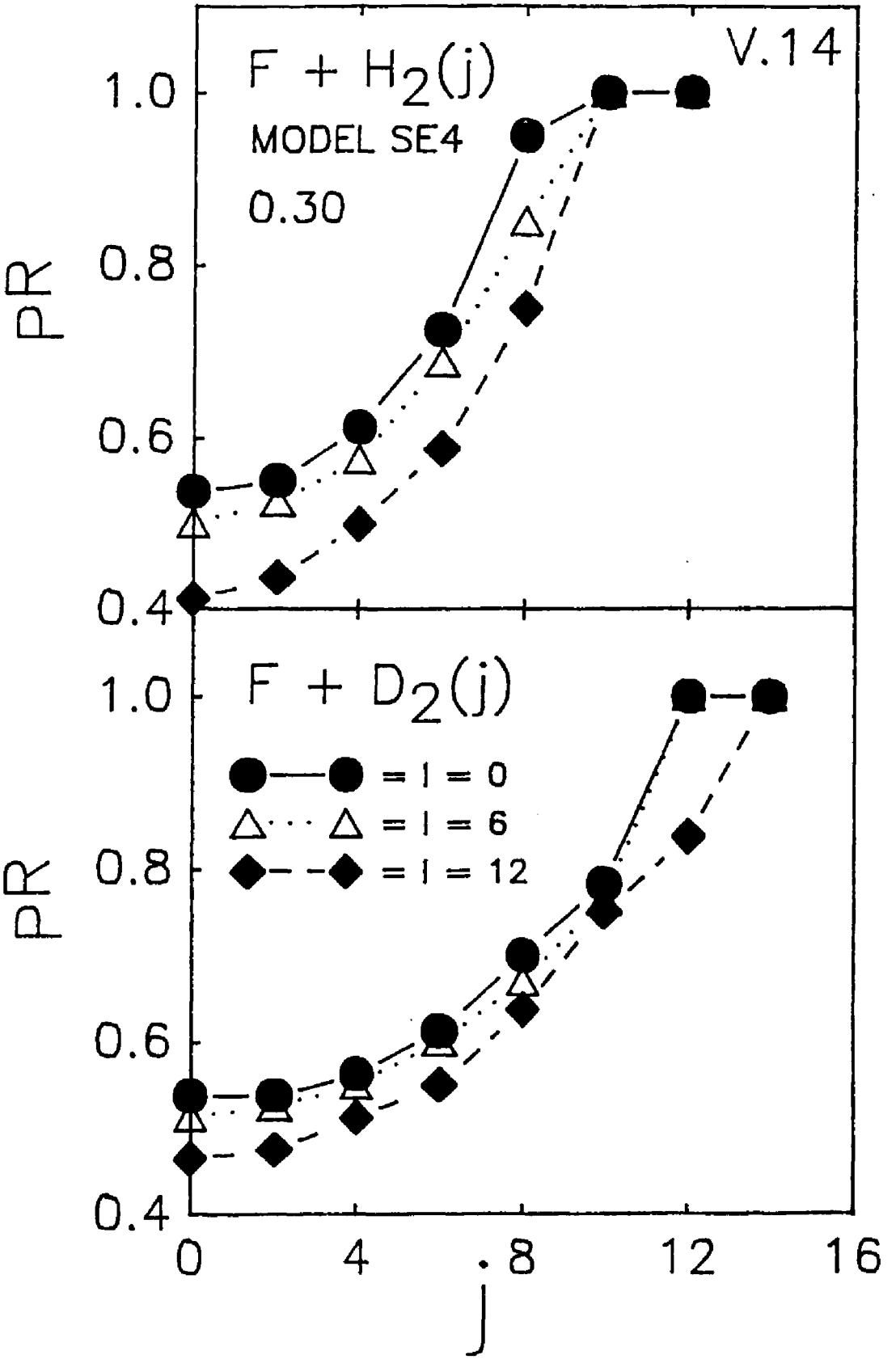
F + H2(j)
V.14
MODEL SE4
0.30
1.0
0.8
0.6
0.4
PR
F + D2(j)
= l = 0
= l = 6
= l = 12
0
4
8
12
16
J

Fig. V.15 Differential cross sections for the F + $H_2(0,j)$ reaction on the SE1 surface for j=0, 4, and 12 at translational energy 0.125 eV. The smooth curves are the fit obtained with eqn (V.1). The values used for A, N and θ_{max} are also shown on the figure. Error bars are one standard deviation.

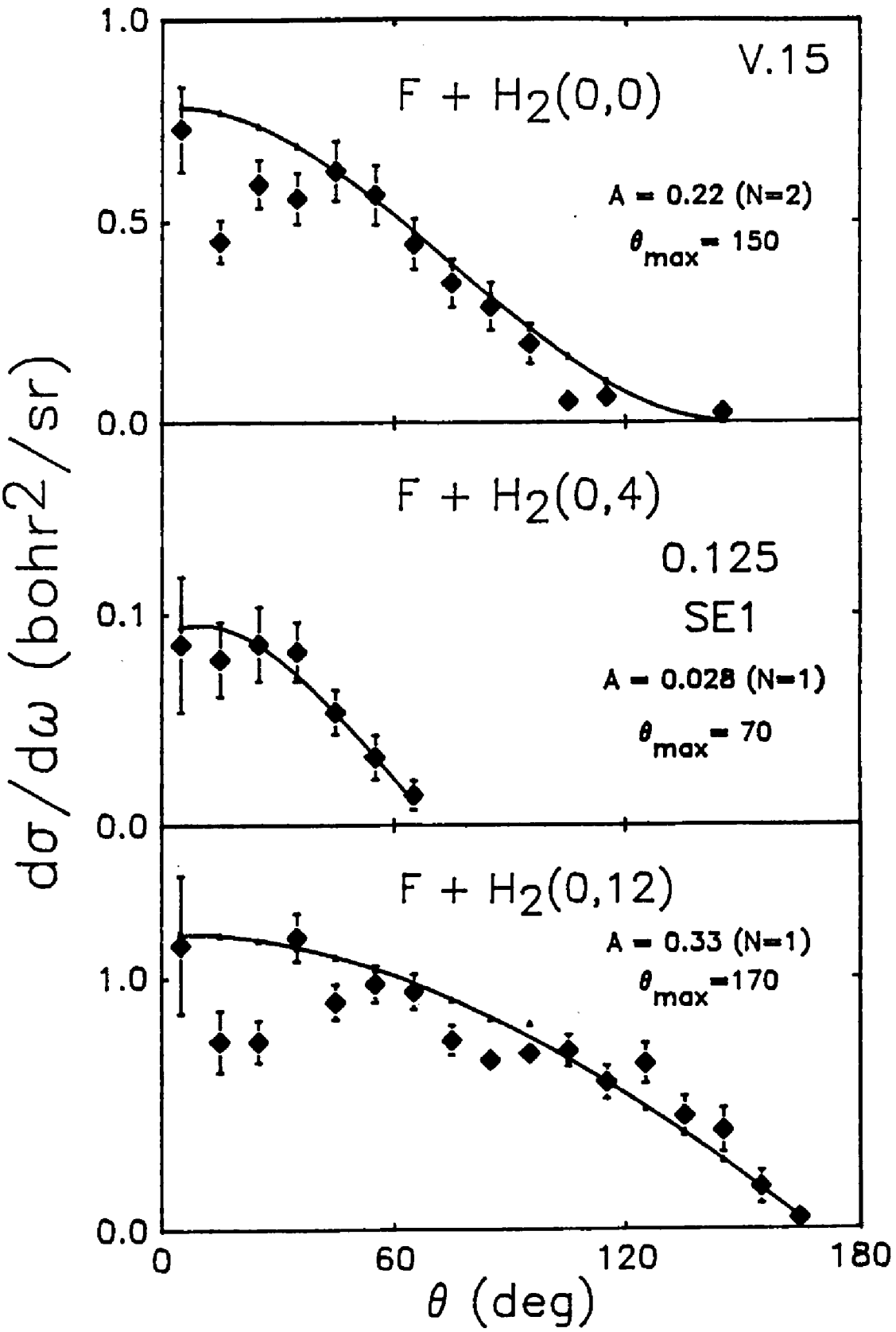
1.0
0.5
0.0
V.15
F + H2(0,0)
A = 0.22 (N=2)
θmax= 150
F + H2(0,4)
0.125
SE1
A = 0.028 (N=1)
θmax= 70
0.1
0.0
F + H2(0,12)
A = 0.33 (N=1)
θmax=170
1.0
0.0
dσ/dω (bohr2/sr)
0
60
120
180
θ (deg)

Fig. V.16 Differential cross section for the F + H_2 (0,j) on the SE4 surface for j=0, 1, and 4 at translational energy 0.125 eV. The smooth curves are the fit obtained with eqn (V.1). The values used for A, N and θ_{max} are given on the figure. Error bars are one standard deviation.

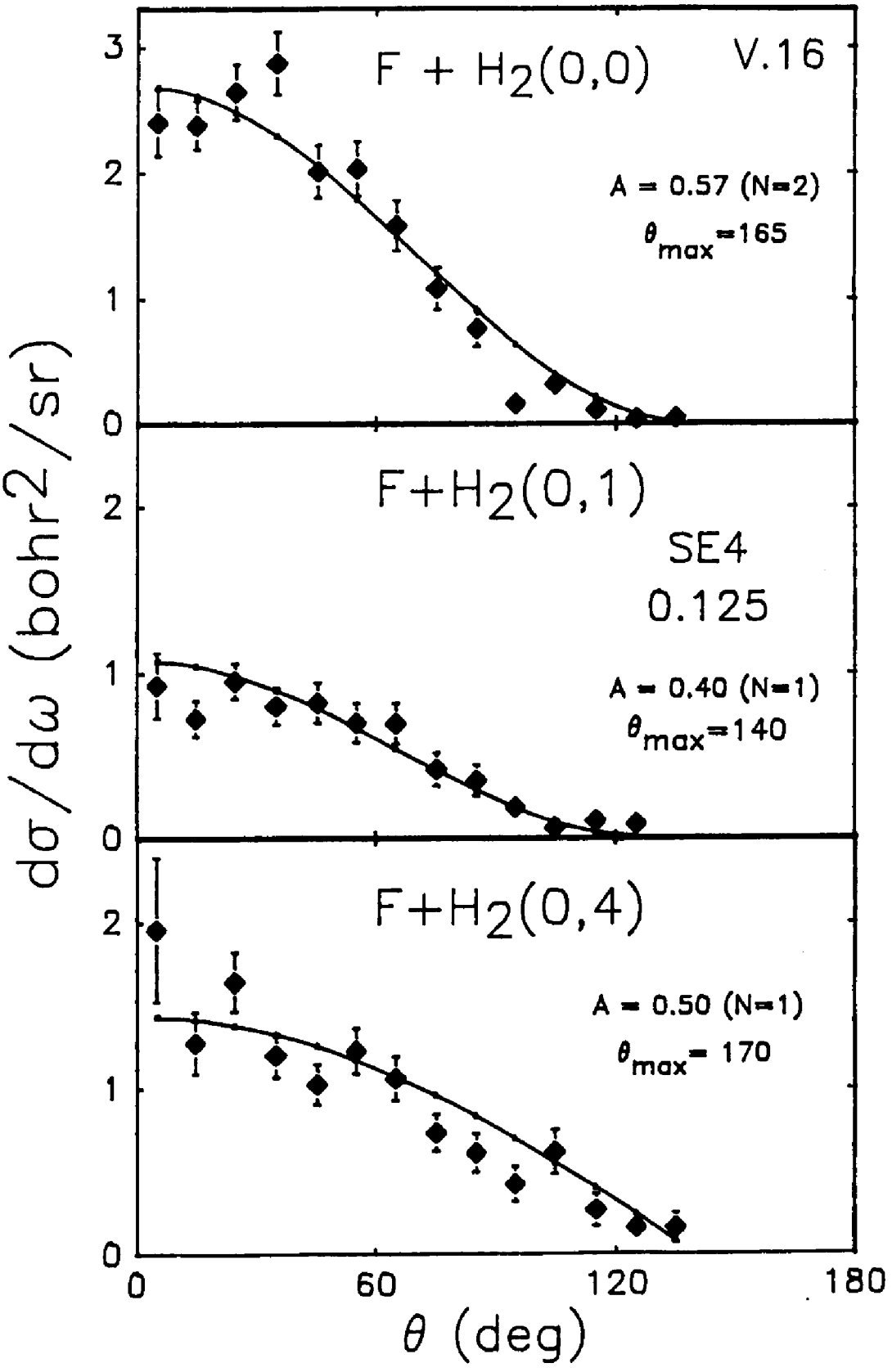
F + H2(0,0)
V.16
A = 0.57 (N=2)
θmax=165
F+H2(0,1)
SE4
0.125
A = 0.40 (N=1)
θmax=140
F+H2(0,4)
A = 0.50 (N=1)
θmax= 170
dσ/dω (bohr2/sr)
θ (deg)
0
60
120
180
0
1
2
3

Fig. V.17 Opacity functions, $P^R(l)$, for $F + H_2(0,j)$ on the SE1 and the SE4 surfaces for j=0, 6, and 12. The translational energy E_t is 0.125 eV. Error bars are about the size of the point.

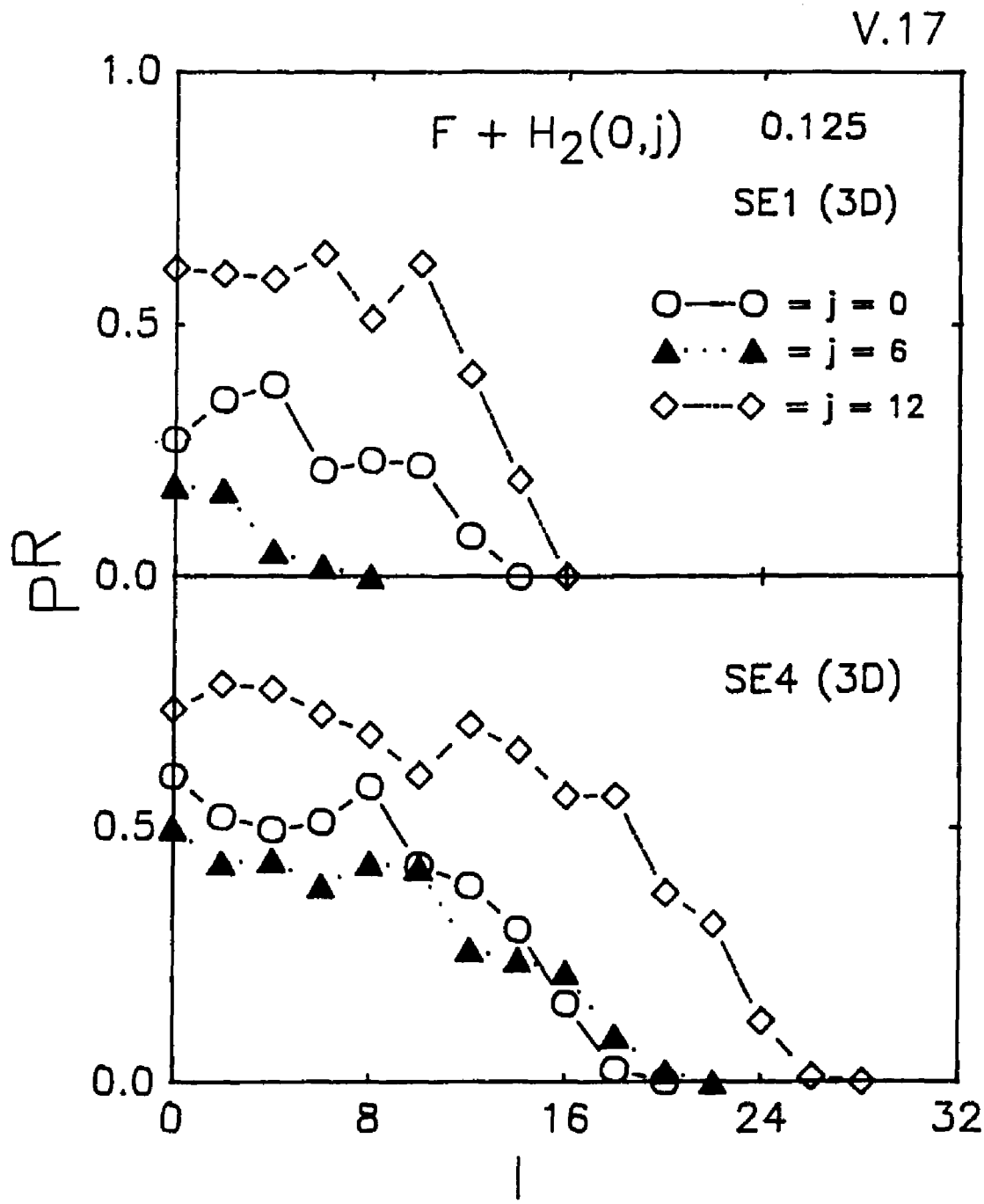
V.17
1.0
F + H2(0,j)
0.125
SE1 (3D)
O—O = j = 0
▲···▲ = j = 6
◇—◇ = j = 12
0.5
0.0
PR
SE4 (3D)
0.5
0.0
0
8
16
24
32
J

Fig. V.18 Maximum impact parameter leading to reaction as a function of j for F + H_2(0,j) on both the SE1 and the SE4 surfaces. The translational energies are 0.200, 0.125, and 0.075 eV. Error bars are about the size of the point.

V.18

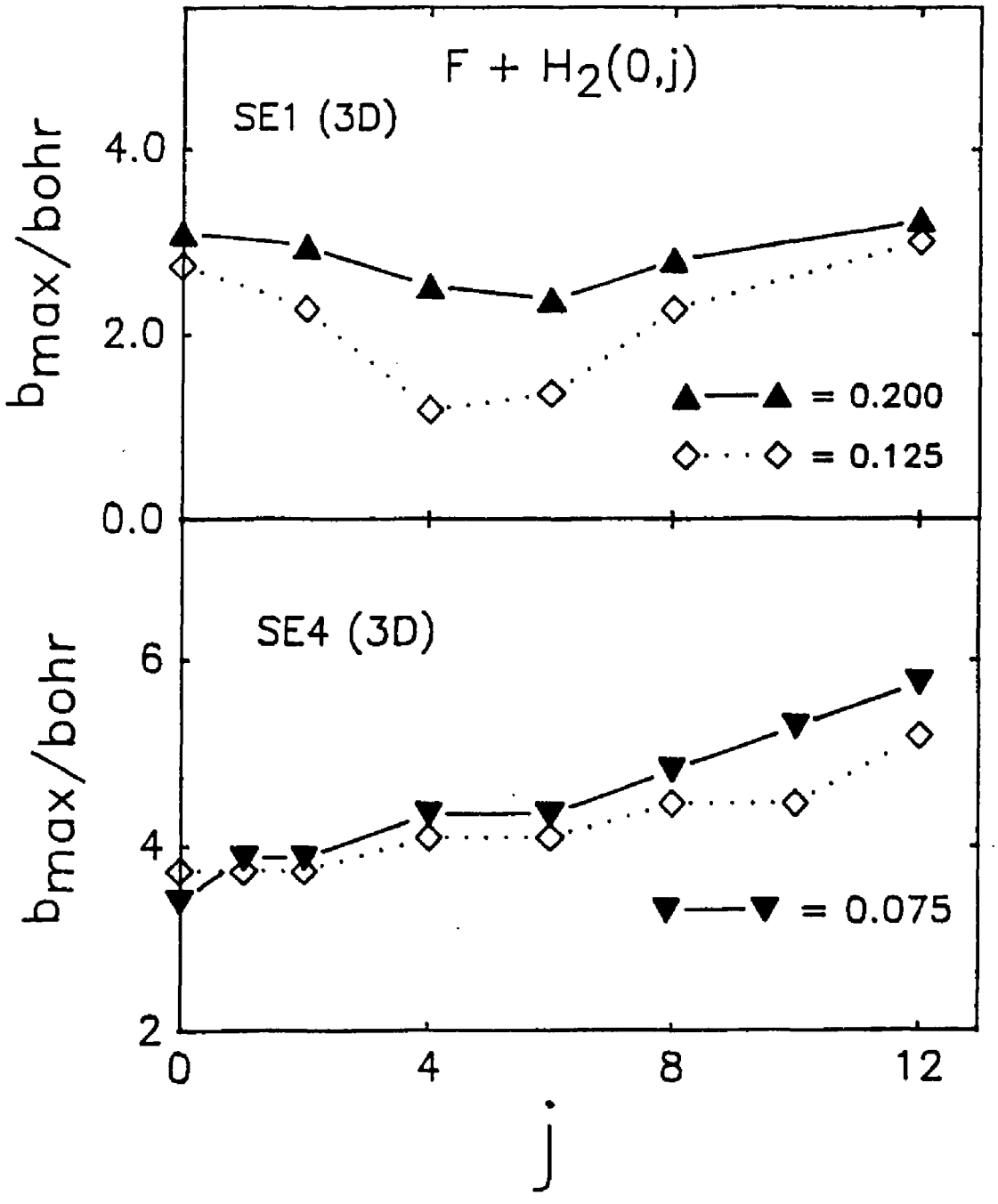
F + H2(0,j)
SE1 (3D)
bmax/bohr
4.0
2.0
0.0
= 0.200
= 0.125
SE4 (3D)
bmax/bohr
6
4
2
= 0.075
0
4
8
12
j

Fig. V.19 Product rotational distributions for F + H_2 and F + D_2 on the SE1 surface for j=0, 4, and 12. The translational energy is 0.125 eV. The peak height is normalized to 1.0.

V.19

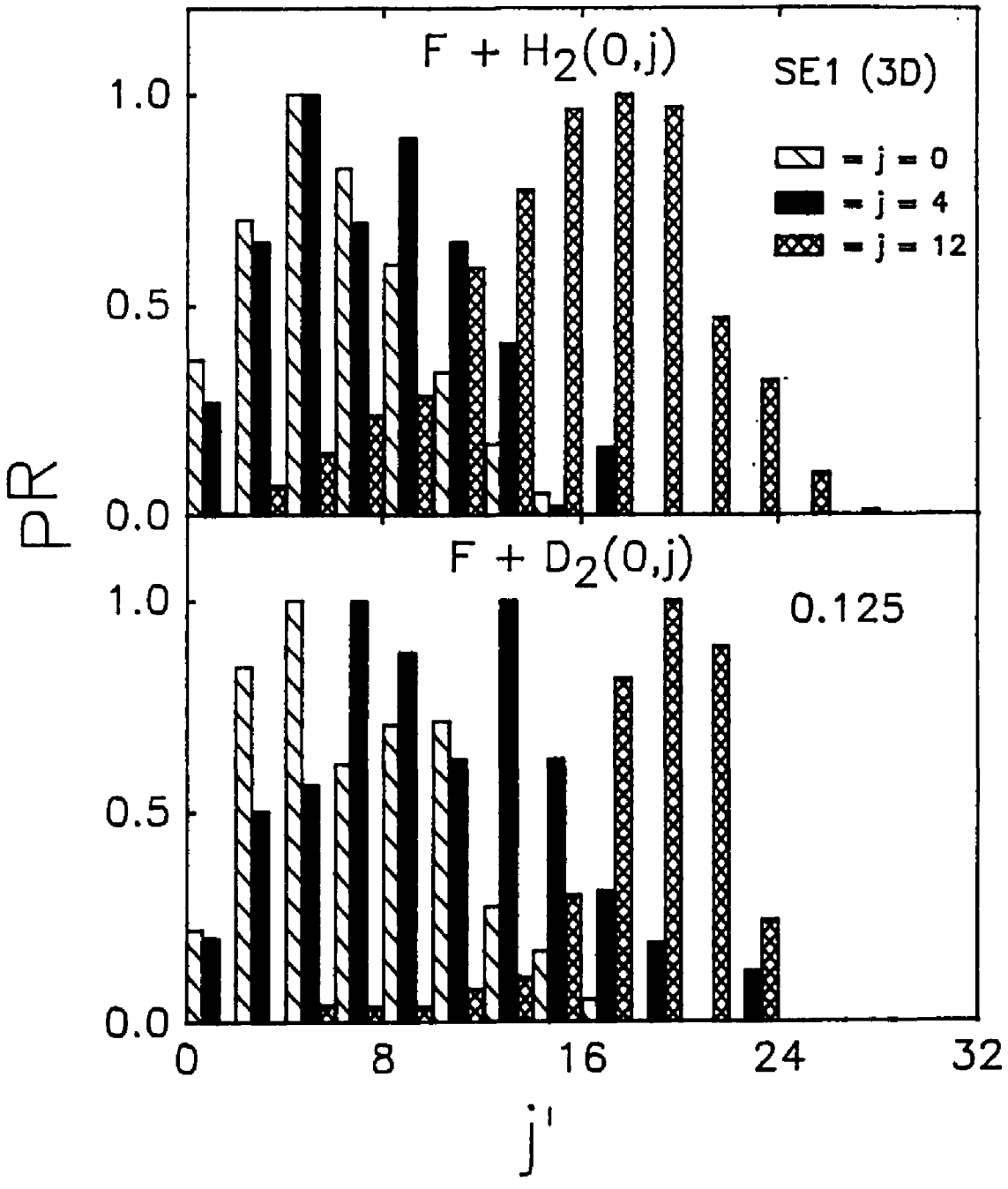

Fig. V.20 Product rotational distributions for F + H_2 and F + D_2 on the SE4 surface for j=0, 4, and 8. The translational energy is 0.125 eV. The peak height is normalized to 1.0.

V.20

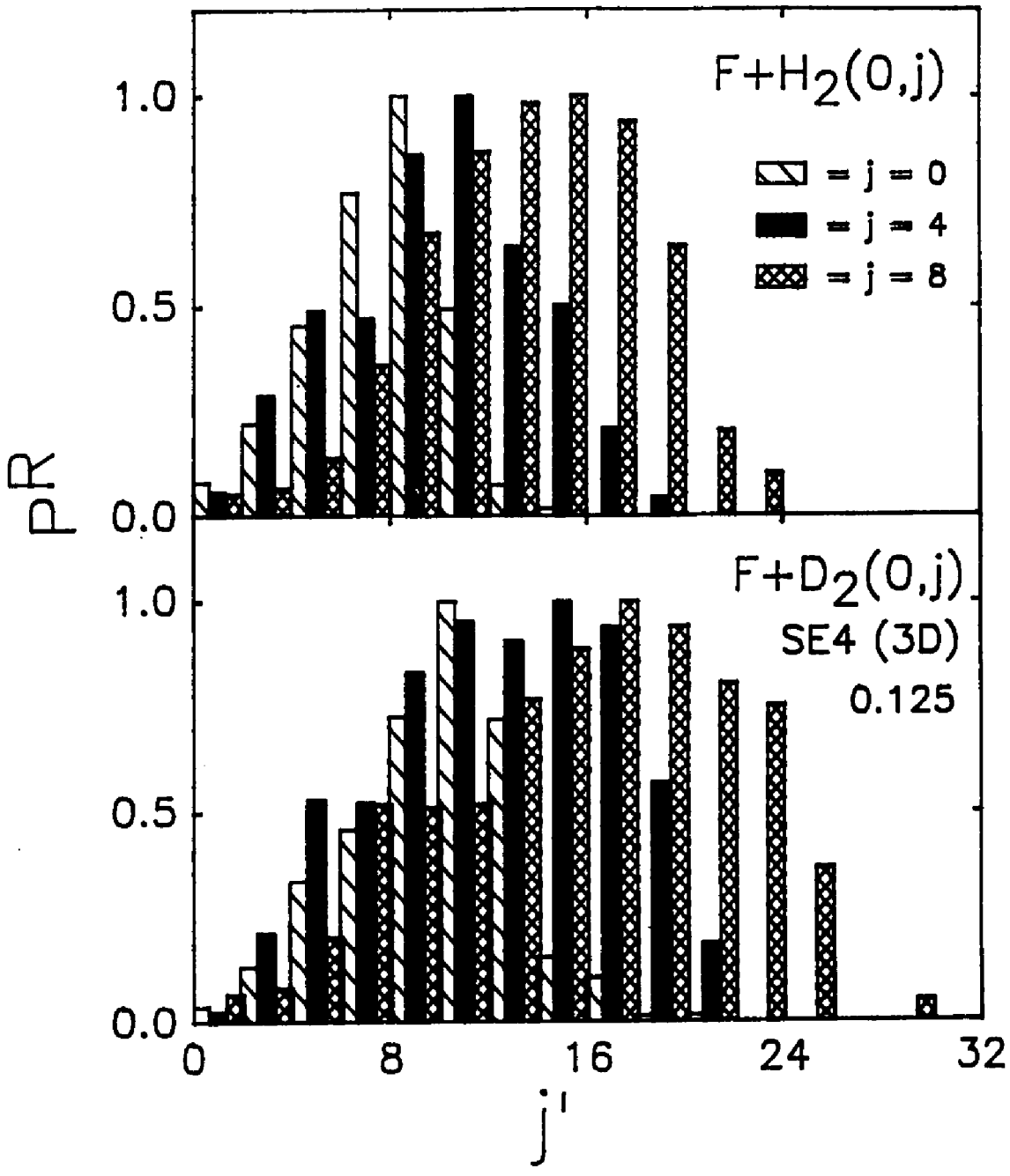

Fig. V.21 First moments of the HF and DF product rotational quantum number, <j'> as a function of j on the SE1 potential. The translational energies are 0.200 and 0.125 eV. Error bars are about the size of the point.

V.21

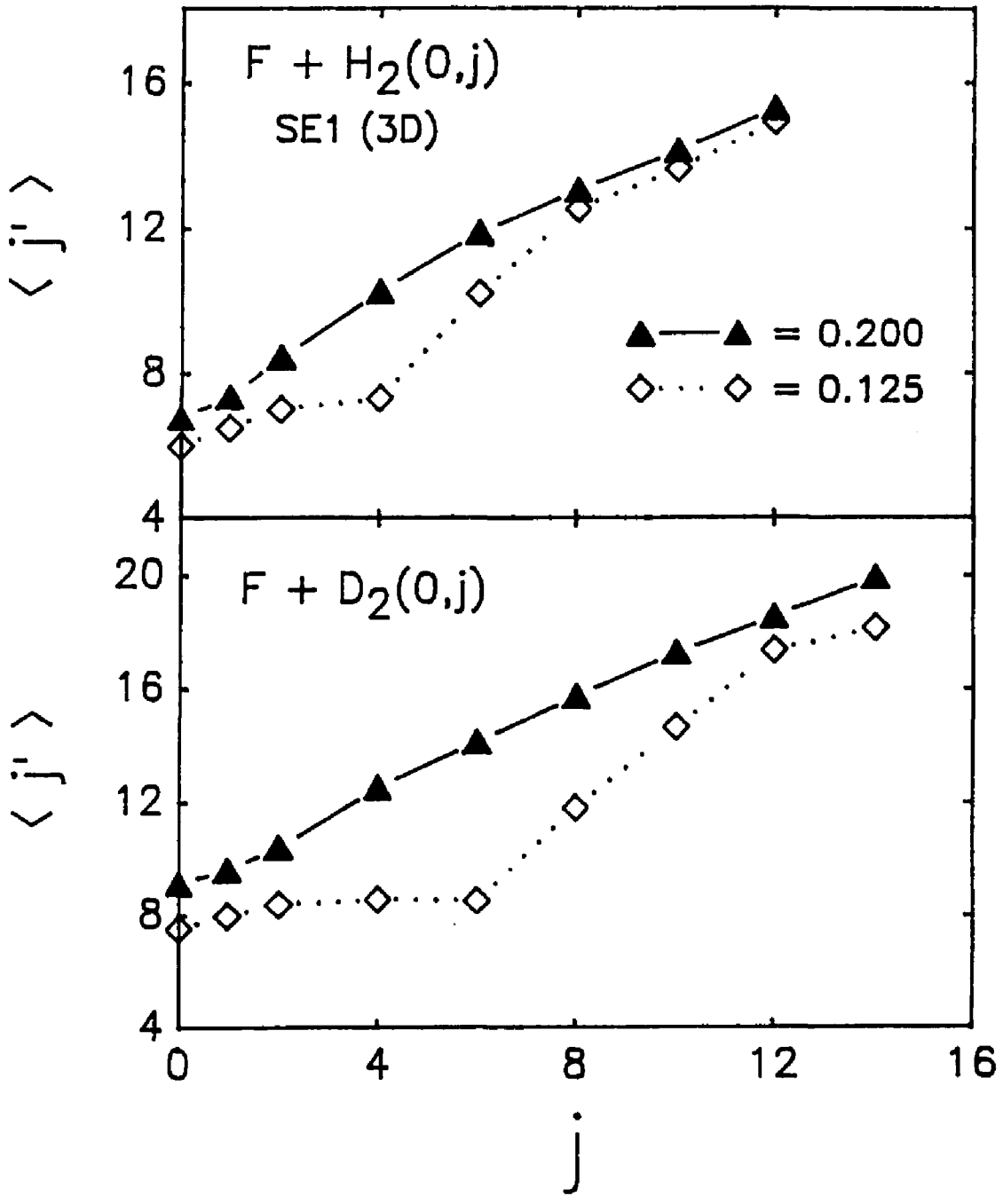

Fig. V.22 First moments of the HF and DF product rotational quantum number, <j'>, as a function of j on the SE4 potential at translational energies 0.125 and 0.075 eV. Error bars are about the size of the point.

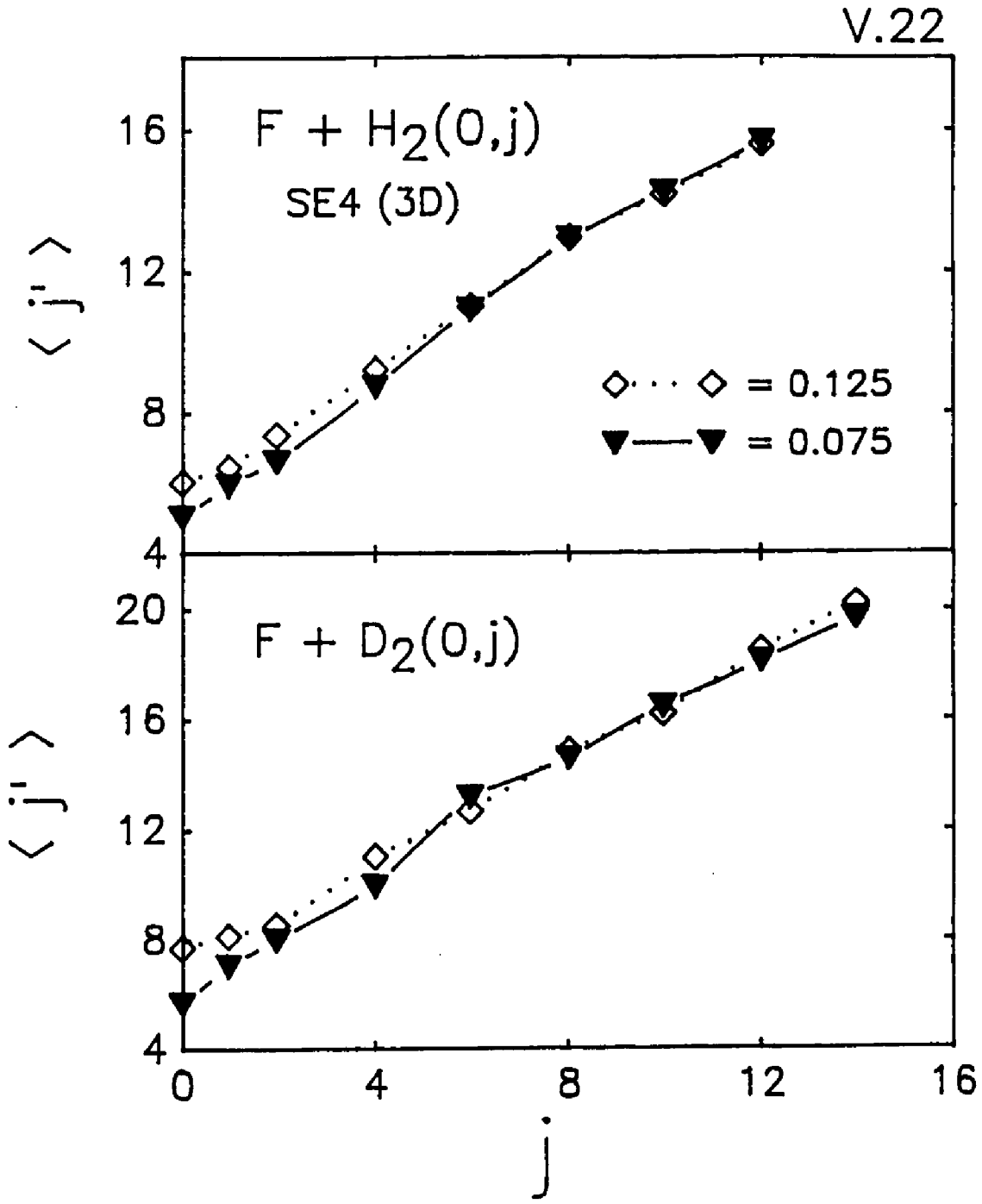
V.22
F + H2(0,j)
SE4 (3D)
◇···◇ = 0.125
▼—▼ = 0.075
F + D2(0,j)
⟨ j ⟩
⟨ j ⟩
16
12
8
4
20
16
12
8
4
0
4
8
12
16
j

Fig. V.23 Product rotational distributions for F + H_2 and F + D_2 for coplanar trajectories on the SE1 surface for j= 0, 4, and 12. The translational energy is 0.125 eV. The peak height is normalized to 1.0.

V.23

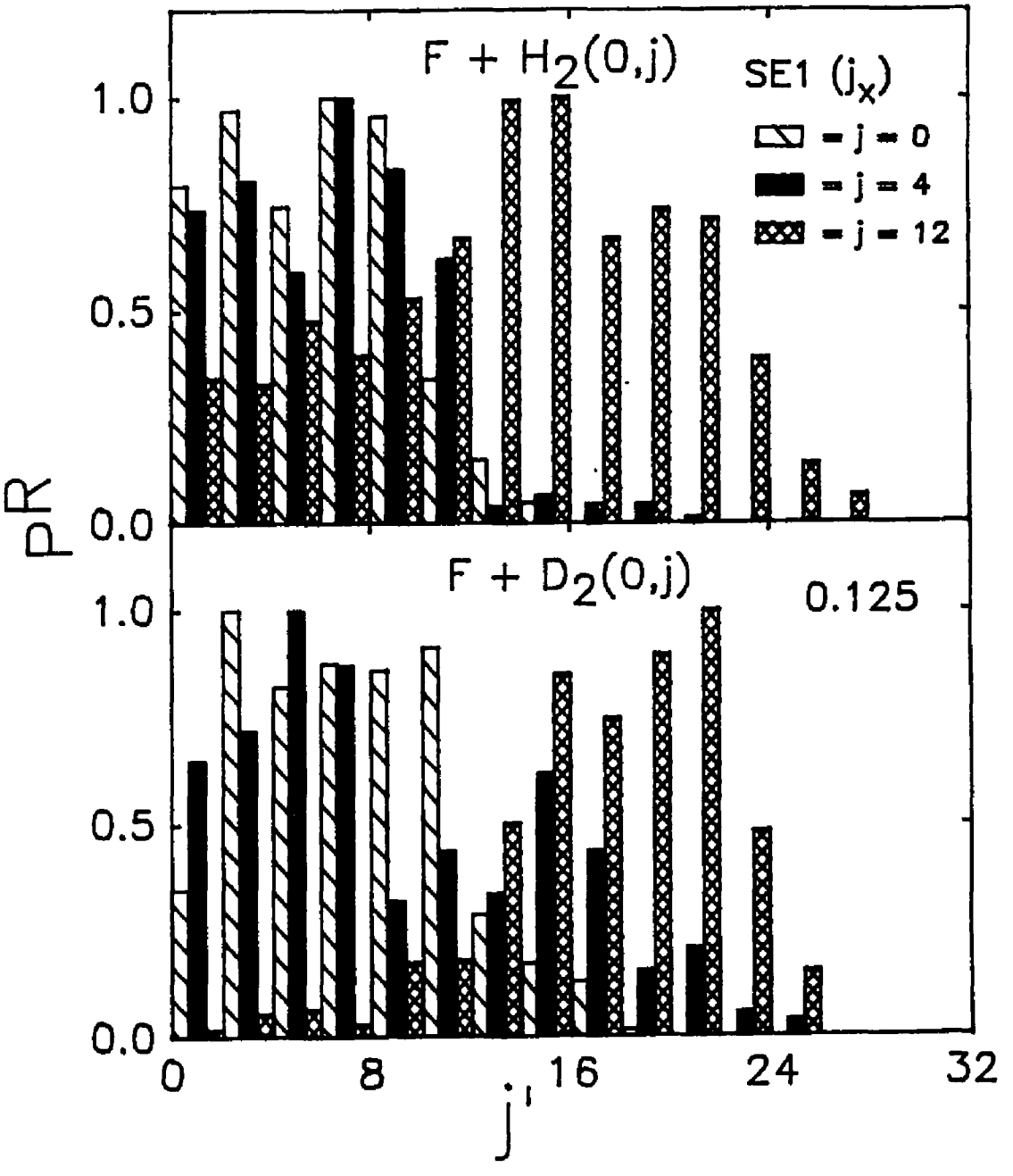

Fig. V.24 Product rotational distributions for F + H_2 and F + D_2 for coplanar trajectories on the SE4 surface for j=0, 4, and 12. The translational energy is 0.125 eV. The peak height is normalized to 1.0.

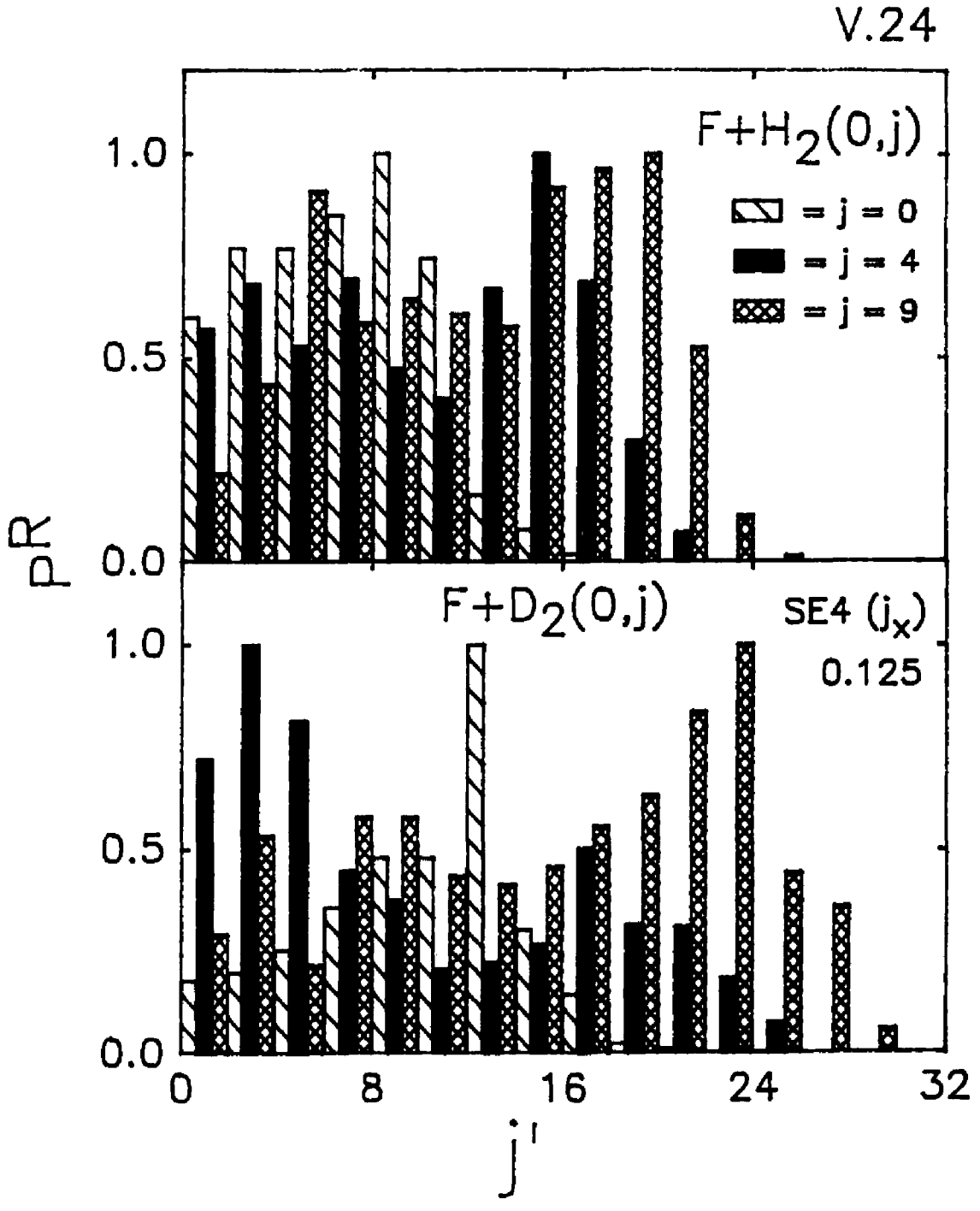
V.24
F+H2(0,j)
= j = 0
= j = 4
= j = 9
F+D2(0,j)
SE4 (jx)
0.125
1.0
0.5
0.0
PR
0
8
16
24
32
j'

Fig. V.25 Product rotational distributions for F + H_2 on the SE1 surface for j = 0, 8, and 12 at fixed center of mass scattering angle. The translational energy is 0.125 eV. The peak height is normalized to 1.0.

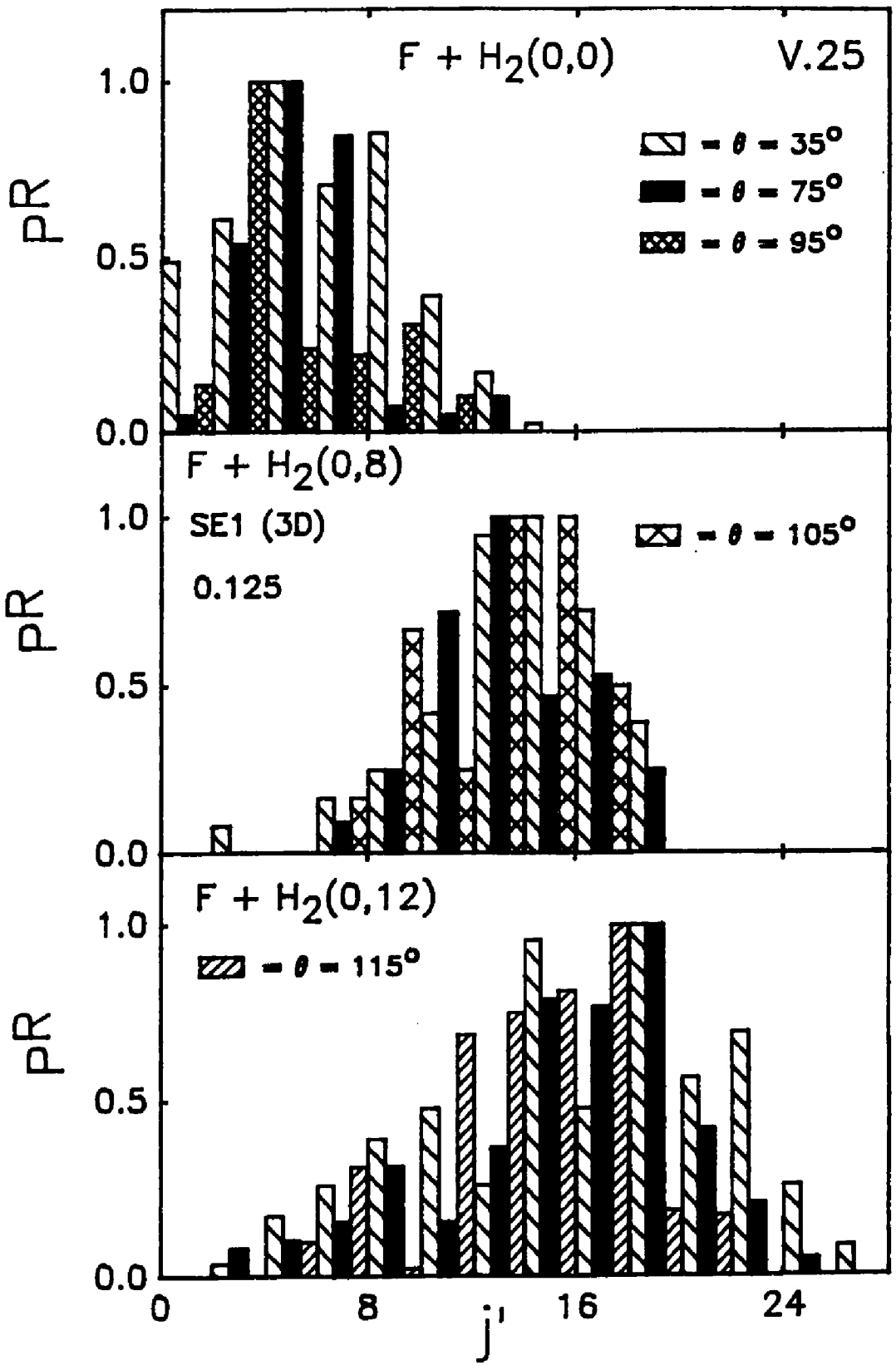
F + H2(0,0)
V.25
= θ = 35°
= θ = 75°
= θ = 95°
F + H2(0,8)
SE1 (3D)
0.125
= θ = 105°
F + H2(0,12)
= θ = 115°
PR
1.0
0.5
0.0
0
8
16
24
j'

CHAPTER VI

CASE STUDY: OH(0,j) + H_2(0,j)

Introduction

Most of the theoretical work which has examined the effect of reagent rotation on reactivity has been concerned with simple 3 atom reactions, e.g. A + BC(j) --> AB + C. As a result of this work on such atom-diatom systems as H + H_2 [21,22,29], O + HCl [24], and F + H_2 [60,121,123,126,128] and in light of results presented here, the effect of rotation in the target diatom is fairly well understood and the circumstances under which rotation will inhibit or enhance reactivity are now predictable with relative certainty. Isotopic substitution of one or both of the target diatomic molecule's atoms has also been investigated, e.g. H + HD [29] and F + D_2 [60,123].

Recently the OH + H_2 --> H_2O + H system has generated interest, for three major reasons. First, it is very important to the combustion process [172], second, it is of astrophysical interest since H_2O is a major source of microwave absorption [173], and third, the isotopic variants of the reaction are of considerable commercial interest, since it is one of the elementary steps in the production of heavy water: [174] The overall reaction being HD(g) + H_2O(l) -->

$HDO(l) + H_2(g)$.

The $OH + H_2 \rightarrow H_2O + H$ system is one of the few systems of more than three atoms for which there is a reasonable potential energy surface. Walch and Dunning [156] carried out ab initio calculations for this system. An analytical fit to their points was first provided by Schatz and Elgersma [57] (SE). The SE surface manifests spurious minima (Figure II.11). Rashed and Brown [58] corrected this problem by adding a cubic spline term to the Morse functions in the SE potential function. However, these functions produce spurious peaks (Figure II.11) which, as will be shown here, seriously affect the dynamics.

Transition state calculations [157-159] have been carried out on this system in order to investigate how well the rate constants agree with experiment. Discrepancies between the experimentally determined rate constants and the theoretically determined rate constants of Isaacson and Truhlar [159] are less than a factor of 2 over the temperature range considered. Truhlar and Isaacson [158] also examined the enhancement of the rate when the H_2 or the OH diatom is vibrationally excited using an extension of variational transition state theory. Their results were in much better agreement with experiment than are calculations based on conventional transition state theory.

Rashed and Brown [160] have investigated intramolecular and intermolecular energy transfer in nonreactive $OH + H_2$

collisions using quasiclassical dynamics. With regard to rotational energy they concluded: 1) There is a greater propensity for the transfer of translational energy to OH rotation than H_2 rotation; 2) Both molecules exhibited intramolecular energy transfer from vibration to rotation; and 3) There is no dominant mechanism for deactivation of H_2 rotation and OH rotation is deactivated by transfer to translation.

Schatz [161] performed quasiclassical trajectory calculations on the OH + H_2 system in which he examined the effect of reagent vibration in both diatoms on the integral cross section and the thermal rate constants. In addition, the partitioning of the reagent energy among the product degrees of freedom, including H_2O, was studied. Vibration in the OH only lead to a small enhancement in the thermal rate constant at 300 K, compared to the large enhancement in thermal rate constant caused by H_2 vibration. Reagent rotation was found to cause a decrease in reaction cross section. The rate of decrease was found to be larger when H_2 was excited than when OH was excited. However, cross sections were only calculated for $j < 6$ (OH) and $j' < 3$ (H_2); for $OH(0,j) + H_2(0,j') \rightarrow H_2O + H$ (note in this case j' denotes rotation in the H_2 diatom not product state rotation as it did in the atom + diatom case). Product state energy partitioning indicated that nearly all of the additional energy coming from reagent vibrational excitation ends up as product vibration. Rashed and Brown [58]

also investigated the effect of reagent vibrational and rotational excitation on the reaction OH + H_2 --> H_2O + H through the use of classical trajectories. They concluded, in agreement with Schatz [161], that rotational excitation of either diatom (j > 8 and j' < 6) serves to suppress reactivity.

The object of this work is to investigate the effect of reagent rotation on the reaction OH(0,j) + H_2(0,j') --> H_2O + H. The range of rotational quantum numbers investigated will be extended to j = 40 and j' = 15. The effects of isotopic substitution in both diatoms will also be discussed.

Method of Calculation

The full three dimensional trajectory calculations reported here were carried out by the method detailed in Appendix A. Reduced dimensionality calculations were carried out by setting the impact parameter, b, to zero, and the rotational projection phase angles QM to 0 (Appendix A), constraining the atoms to lie in a plane.

The model developed in Chapter II for A+BC(j) reactions can also be applied to AB(j) + CD(j') reactions. The form of the classical Hamiltonian in this case is given by (II.10). The method for calculating model trajectories for the AB(j) + CD(j') system is detailed in Chapter II.

Results and Discussion

Effect of H_2 Rotation

Reaction cross sections, calculated on the Rashed-Brown

potential energy surface (RB) for the reaction OH(0,0) + H_2(0,j') --> H_2O + H, as a function of H_2 rotational quantum number for three translational energies are shown in Figure VI.1. At low energy, 0.2 eV, i.e. below the j' = 0 threshold, rotation enhances reaction for sufficiently large j'. At a higher translational energy, 0.5 eV, the $S^R(j')$ take on the now familiar, "dip and climb" functional form. Lastly, at high translational energy, 1.2 eV, the $S^R(j')$ is flat as j' goes from zero to about j' = 5, then the $S^R(j')$ increase with increasing j'. Noting that the OH bond is generally considered to be a "spectator" in this reaction, these results are not surprising in light of the previously presented data. That is, if the OH bond is a "spectator" bond the system now resembles any of the previously described A + BC(j) systems. Thus the potential, $V(s,\phi)$, [Fig (II.12)] resembles the reduced potential $V(s,\gamma)$ obtained from a three body LEPS potential. In light of this, it can be concluded the orientational effect is responsible for the downward trends in the $S^R(j')$ and the energy effect is responsible for the increase in $S^R(j')$ with increasing j'. Both of these effects were fully discussed in Chapter IV.

Effect of OH Rotation

Reaction cross sections for the OH(0,j) + H_2(0,0) --> H_2O + H reaction at three translational energies for the RB surface are shown in Figure VI.2. At 0.3 eV the reaction cross section decreases as j goes from 0 to 10, then it increases

as j goes from 10 to 20, finally the $S^R(j)$ decrease as j goes from 20 to 40. At lower translational energy, 0.2 eV, the $S^R(j)$ have a similar functional form, the difference being the lack of the decrease in the $S^R(j)$ from j = 0 to 10. (The lowest translational energy, 0.2 ev, is near the j = 0 threshold, so the cross section is small). At high translational energy, the $S^R(j)$ decrease as j goes from 0 to 20, then for j > 20 the $S^R(j)$ is flat with increasing j. It is worth noting at this time that these same trends are also present in the $S^R(j)$ calculated on the SE surface (Figure VI.3). In fact, all the trends observed in calculations on the RB surface are also manifested in calculations done on the SE surface. The trends present in the $S^R(j)$, discussed above, are somewhat surprising in light of the fact that the OH bond is a "spectator" bond. If it is indeed a "spectator" bond, why should putting rotation into this diatomic molecule have an effect on the reactivity?

Analysis of the RB reduced potential $V(s,\theta)$ (shown in Figure II.11) yields insight into this question. Unlike $V(s,\phi)$ there are "bumps" in the entrance valley near s = -2 bohr. These are an artifact of the fit arising from the four-body Gaussian term in the potential function (that is, V_{42} in Schatz Elgersma notation [57]). If the V42 term is set equal to zero, the bumps disappear, however they are replaced by minima (Figure VI.4). How do these "bumps" and the minima affect the dynamics on the RB and the RB surface with V42 set equal to

zero?

In order to investigate the effects of these potential energy surface features on the dynamics a test computation was performed. Coplanar trajectories with zero impact parameter were calculated. Further, the vibrational quantum numbers of both the diatomic molecules was set equal to -1/2. Setting the vibrational quantum number to -1/2 serves to minimize any possible vibration to rotation coupling. Additionally, this serves to keep the trajectory on the minimum energy path for as much of the trajectory as possible.

Figure VI.5 is a comparison of these $P^R(j)$ calculated on the RB surface and those calculated with V42 equal to zero on the RB surface (RB-V42). It is worth noting that these trajectories were carried out at a slightly higher E_t than the 3D trajectories to compensate for the lack of the zero point energies in each of the diatomic molecules. On the RB surface, the $P^R(j)$ decrease until it reaches a minimum at about $j = 15$, subsequent to this the $P^R(j)$ increase with j until it peaks at about $j = 25$. The minimum in the $P^R(j)$ at $j = 15$ is much less pronounced when V42 is equal to zero than when it is nonzero. Thus, comparison of these $P^R(j)$ to those obtained when V42 is set to zero suggests that the bumps in the RB surface may, in fact, be the responsible for the strange behavior in the $S^R(j)$. In three dimensions, when V42 is equal to zero, the minimum at $j = 15$ in the $S^R(j)$ is no longer present (Figure VI.6), however there is still a distinct peak at $j = 25$. These

trends can easily be explained with the aid of the model.

Model Calculations

Model calculations were carried out using equation II.10 with j' equal to zero. Since the OH bond is a "spectator" throughout the collision I(s) is constant (equation II.6). This is in contrast to the situation where the bond of interest is broken during the collision and I(s) is given a functional form in s. Therefore the moment of inertia in the "spectator" diatom case is equal to; $I = m\langle r\rangle^2$, where $\langle r\rangle$ is the constant internuclear distance. The PRM (Appendix A) algorithm was used in order to determine the $\langle r\rangle$ value for OH(-1/2,j), which is the average of the inner and outer turning points of r. The $\langle r\rangle$ values for each given j value are given in Table VI.1. Analysis of Figure II.11 or Figure VI.4 reveals that the RB potential has two reaction valleys. In an effort to keep the problem simple, a reduced potential with one reaction valley was used. This single reactive valley is flanked by Gaussian bumps centered at s_o = -2 bohr and $\gamma = \pm\pi/2$. This simplified form was used in order to keep the potential flexible and simple while still retaining the qualitatively important features of the actual surface. The analytic form of the reduced potential is given by equation (II.17) and the parameters are given in Table II.2.

The model $P^R(j)$ for several different peak heights (D_o) are shown in Figure VI.7. When the parameter D_o is zero there are no gaussian peaks and the potential reduces to the

symmetric reduced potential (II.14). The $P^R(j)$ when D_o is zero are almost constant. There is a slight decrease in the $P^R(j)$ as j goes from 0 to 20 subsequently the $P^R(j)$ increase slightly with increasing j. The decrease is due to the increase in χ (Fig IV.12) with j ("orientational" effect Chapter IV). The increase is due to the fact that the OH bond is stretched to some degree by the reagent rotation (Table VI.1).

For nonzero D_o, (that is, when peaks are added) the $P^R(j)$ undergo a dramatic change. For both values of D_o examined the $P^R(j)$ decrease from j equal 0 to 5, then it increases and reaches a maximum when j is equal to 10, and finally the $P^R(j)$ decreases from 10 to 20. After j = 20 the $P^R(j)$ look essentially like the $P^R(j)$ when D_o is zero. This is not surprising since by j = 20 the rotational energy of the system is very much greater than the height of the peak, as a result the trajectories no longer "see" the peaks. Furthermore, when the peaks are added the $P^R(0)$ are significantly larger than the $P^R(0)$ when no peaks are present. Once D_o is nonzero, increasing its value further increases the value of the $P^R(j)$ at the maximum.

This behavior of the $P^R(j)$ is very easily rationalized with the aid of a schematic diagram (Figure VI.8). First, recall if j is equal to zero there is a range of initial γ values which lead to reaction (Figure IV.12) and motion across the surface is parallel to the s axis (i.e. cos (χ) = 0). For

small values of j, where the rotational energy (E_j) is much lower than the size of the bumps, χ begins to increase. In this instance, the bumps tend to deflect otherwise reactive trajectories out of the reaction valley. As a result, the reaction probability decreases.

As j is increased further, χ is also increased. Since χ has increased, there does exist a range of γ values where the bumps deflect trajectories "into" the reaction valley. Thus the reaction probability increases. For very large j, E_j is so large that the bumps do not play a significant role.

Thus the similarity of Figures VI.7 and the middle panel of VI.2 (i.e. 0.3 eV) suggest that the bumps in the reaction valley of the RB potential are indeed responsible for the strange behavior of the $S^R(j)$. Analysis of actual trajectories on the RB surface also confirms this behavior. For those trajectories where the $S^R(j)$ is enhanced, there is strong rotation to translation (i.e. R --> T) coupling. This is due to the bumps deflecting the trajectories and thus transferring motion from the γ coordinate into the s coordinate.

Turning attention to the RB-V42 surface and thus to a consideration of the effect of wells in the reactant valley and their affect on reactivity. Here again, the model will be used in order to elucidate the effect of the wells. Gaussian wells were centered at s_o = -1.0 bohr, $\gamma = \pm\pi/2$. The $P^R(j)$ are shown in Figure VI.9. As one would expect, when D_o is set equal to zero the $P^R(j)$ are identical to those in Figure VI.7.

For nonzero negative D_o the $P^R(j)$ decrease slightly from j = 0 to j = 5, then rise sharply and reach a maximum at about j = 12, and subsequently decrease as j is increased further. It is interesting to note that as D_o is decreased the $P^R(j)$ at the maximum also increase as in the case of positive D_o. In contrast to the situation when bumps were placed in the reagent valley, the $P^R(j)$ distributions are much broader and the position of the maximum has shifted to slightly larger j values. Furthermore, the decrease in the $P^R(j)$ for small values of j is much less here (Fig VI.9) than in the previous case (VI.7).

These effects can be represented by a schematic diagram (Fig VI.10) as in the case of the bumps. For small values of j, trajectories which might otherwise be reactive are "pulled" away from the reactive region by the wells (top panel Fig VI.10) decreasing the reactivity slightly. As j is increased further the wells pull trajectories which would have missed the reaction valley into the reaction valley. The result is an increase in the $P^R(j)$. The functional forms of Figures VI.9, VI.5 (lower panel), VI.6, and VI.2 are all similar. Therefore the following can be concluded. First, wells in the reagent valley, in addition to bumps, are capable of causing the down, up, then down, behavior observed in the $S^R(j)$. Second, the effect of the bumps in the reagent valley seem to be more pronounced than those when wells are present.

Isotope Dependence

Figure VI.11 illustrates the effect of reagent rotation in the reaction OX(0,j) + H_2 --> HXO + H, where X is an isotope of hydrogen. In this work OT, OD, and OL (where L is a fictitious isotope of hydrogen having a mass of 0.5 a.m.u.) have all been examined. Note that the light isotope of hydrogen is used merely to illustrate the trend upon substitution. When tritium (m_X = 3.0) is substituted for hydrogen the $S^R(j)$ decrease gradually from j = 0 to a minimum at j = 30, after which the $S^R(j)$ begin to increase with increasing j. The $S^R(j)$ appear as though they may still be increasing when j = 68. When deuterium is used (m_X = 2.0), the $S^R(j)$ decrease more rapidly reaching a minimum at j = 20 then increasing and finally flattening out by j equal to 55. When m_X is equal to 0.25 a.m.u. the $S^R(j)$ decrease as j goes from 0 to 5, as j is increased further the $S^R(j)$ also increase and reach a maximum at j = 12. As j goes from 12 to 25 the $S^R(j)$ decrease and reach another minimum at j = 25. The minimum in the $S^R(j)$ occur at j = 5, 20, and 30 when m_X is equal to 0.5, 2.0, and 3.0 a.m.u., respectively. From an analysis of Figure VI.11 it appears as though isotopic substitution of a light atom, where reagent rotation is rapid, "compresses" the features observed for OH, whereas substitution of a heavy atom "stretches" them. When reagent rotation is very fast (that is muonium [79] is X, mass = 0.11 amu) these features are so "compressed" that the minimum is very difficult to detect; it is found to be at approximately j = 1, and the maximum occurs

at j = 3 (Figure VI.12). The j values of the minima (j_{min}) as well as the j values of the maxima (j_{max}) in the $S^R(j)$ are roughly linear in m_X. This point is nicely illustrated in Figure VI.13, where j_{min} and j_{max} are plotted versus m_X.

Comparison of these $S^R(j)$ data with model reaction probabilities in which the H of the OH has been isotopically substituted, shown in Figure (VI.14), reveal that the model does, in fact, reproduce qualitative trends observed in the 3D $S^R(j)$. The values of j_{min} in the model $P^R(j)$ occur at j = 2, 3, 5, 10 for m = 0.5, 1.0, 2.0, and 3.0 a.m.u., respectively. As in the actual trajectories the position of the minimum is roughly linear in m. Further, the values of j_{max} in the $P^R(j)$ occur at j = 5, 10, 20, 30 for m = 0.5, 1.0, 2.0, and 3.0 a.m.u., as expected, they are linear in m.

In addition to reproducing the correct qualitative trends, the model can also be used to rationalize the linear behavior of j_{min} and j_{max} in m_X. That the trend on isotopic substitution goes as m is not surprising, since for a diatom consisting of a heavy atom (oxygen) and a light atom (hydrogen and its isotopes) the moment of inertia is roughly proportional to m_X, the mass of the hydrogen isotope. As we have seen, the effects of the bumps on the motion in the (s,γ) plane depend on the angle, χ (Chapter IV), at which the trajectory traverses the plane. For fixed translational energy, ds/dt is a constant. However, as j is increased $d\gamma/dt$ will also increase. Since $d\gamma/dt = j/I$, is proportional to

j/m_χ, in order to achieve the same χ for different m_χ values, the j values must also be scaled by m_χ.

Branching Ratios

In this section the effect of reagent rotation in both diatoms on the hydrogen branching ratio is addressed, i.e. the reactions

$$OH(0,j) + HD(0,0) \quad \text{---}> \quad H_2O + D \qquad \text{(VI.1a)}$$

$$\text{---}> \quad HDO + H \qquad \text{(VI.1b)}$$

and

$$OH(0,0) + HD(0,j' \quad \text{---}> \quad H_2O + D \qquad \text{(IV.2a)}$$

$$\text{---}> \quad HDO + H \qquad \text{(VI.2b)}$$

are both discussed. The primary kinetic isotope effect in reactions involving H atoms has long been used as a test of reaction rate theories [175]. Further, the D/H ratio is important in cosmological theories, and an understanding of the rate of deuterium fractionation in molecular species is crucial to its evaluation [176]. The effect of reagent rotation on the branching ratios of reactions (VI.1) and (VI.2) has never been investigated.

Shown in Figure VI.15 are the $S^R(j)$ for reaction (VI.1). The qualitative shape of both the H_2O (VI.1a) product and the HDO (VI.1b) product $S^R(j)$ are similar. The heavy product (HDO) is preferred for all values of j. In contrast, in reaction (VI.2) at low j the heavy product (VI.2b) is preferred (Fig VI.16), as j is increased, however, the "cross over" first observed by Muckerman [121-123] occurs and the light product

is preferred (VI.2a).

These results can be rationalized as follows. Rotation in the spectator bond does not affect the preference for product formation, since the reactive cross section is the same for all j. Thus, if the OH is treated as an atom Z, then reaction can be thought of in more simple terms as Z + HD. Therefore, the fact the ZD product is preferred over ZH product is a classic case of it being more difficult to transfer a light atom than it is to transfer a heavy one. This phenomenon has been investigated intensively by Polanyi [60,115] and can be summarized as follows. Scaled and Skewed potential energy contour plots (see Appendix B) of the collinear reactions Z + HD and Z + DH reveal why it is more difficult to transfer a light atom than a heavy one. Due to the mass combination, the Z + HD surface has a very sharp corner, on going from the reagent to the product valley, thus making it difficult to pass into the reaction valley. In contrast, the Z + DH reaction potential energy surface is less skewed, making the corner less sharp. This makes reaction less difficult in this case.

The "cross over effect" has also been observed for the F + HD(j) [121-123], the H + HD(j) [21], and the Cl + HD(j) [177] reactions. The cause of this phenomenon, however, is not well understood.

Muckerman's [121-123] explanation was kinematic in nature. He suggested that since the center of mass of the HD

lies closer to the D atom than to the H; then as the molecule rotates, the H atom sweeps out a larger volume than does the D atom, making it a more favorable target for the incoming atom. Mayne [29] examined the branching ratio of reaction H + HY with products HH + Y and HY + H. By systematically varying the mass of the Y atom, Mayne was able to disprove the above hypothesis. Mayne determined that the major distinction between the transfer of the light atom and a heavy one was that the bottleneck to reaction, i.e. the point along the reaction coordinate at which the motion is slowest, occurred earlier in the case of the light atom transfer. This allowed a more rapid increase in the target diatom's moment of inertia when the diatom is rotating, which is precisely the requirement for rotational enhancement of the reaction.

Conclusions

The effect of rotation on reactivity in the OH(0,j) + H_2(j') --> H_2O + H reaction has been investigated. When the H_2 is rotationally excited it is correct to think of the OH bond as a "spectator", and to consider the reaction as a simple A+BC(0,j) type reaction. The trends observed in the $S^R(j)$ are as expected. These trends can be accurately described by the model described in Chapter IV.

When the OH is rotationally excited the $S^R(j)$ has a rather complicated functional form. Model calculations did an equally good job reproducing the $S^R(j)$ in this case as when the is H_2 rotational excited. That is, the model can be used

to represent rotational excitation in either of the diatoms. Further, it was demonstrated that the complicated functional form of the $S^R(j)$ was a result of "bumps" in the case of the RB potential and "wells" in the case of the SE potential in the entrance valley. Thus, it was demonstrated that such "defects" in the potential, although far from the saddle point, can have a profound effect on the dynamics of the system. When the hydrogen atom of the OH was isotopically substituted these trends in the $S^R(j)$ reacted as follows. For lighter isotopes, the $S^R(j)$ became "compressed", that is reactivity decreases much more quickly due to the faster rotation of the diatom. For heavier isotopes the $S^R(j)$ became "stretched", due to the slower rotation. Lastly, it seems that rotational excitation could be a useful tool in detecting "defects", i.e. spurious wells and bumps, present in a potential energy surface.

Fig. VI.1 Reaction cross sections as a function of j', $S^R(j')$, for trajectories on the RB surface at translational energies 1.2, 0.5, and 0.2 eV. Error bars are one standard deviation.

VI.1

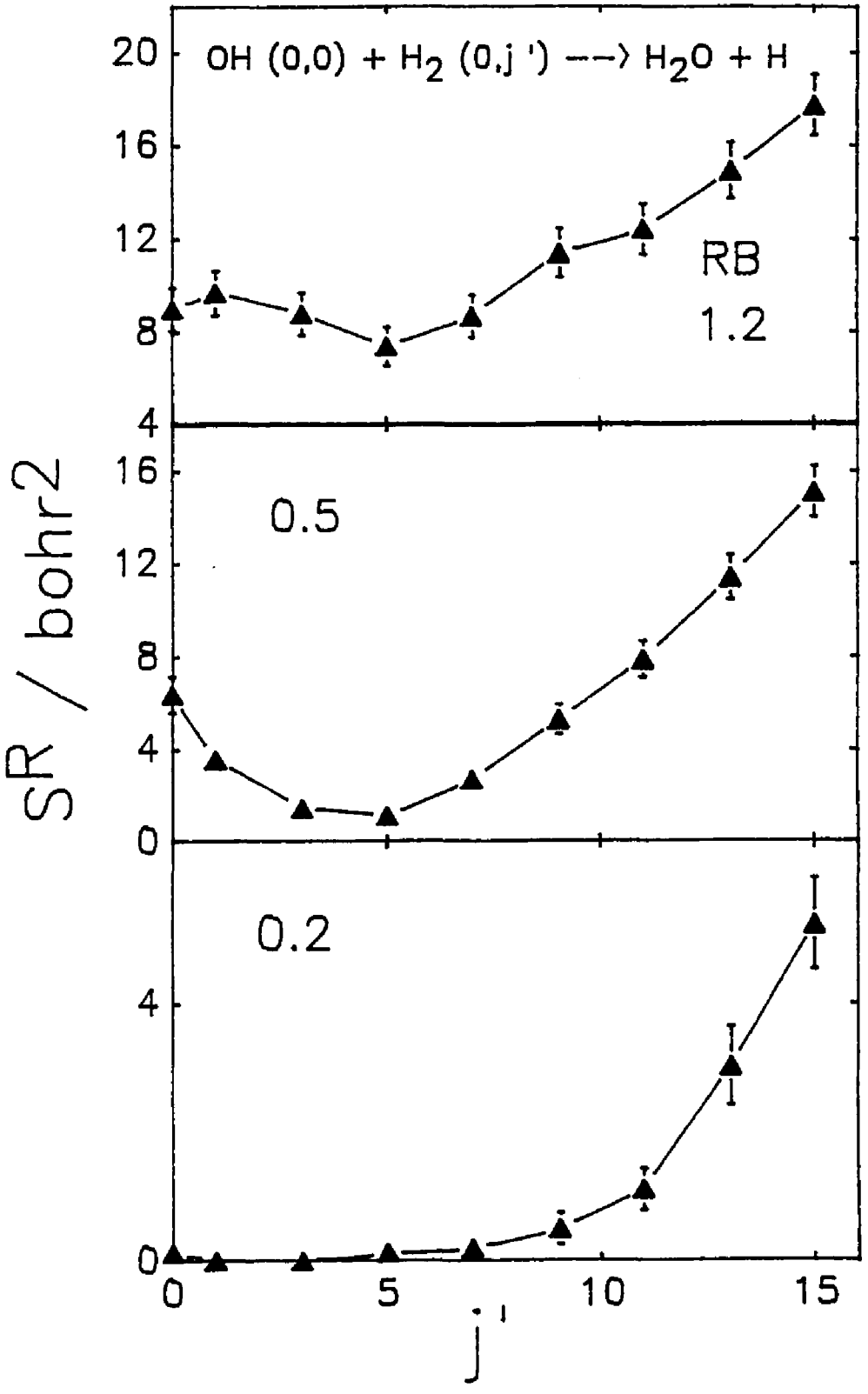

Fig. VI.2 Reaction cross sections as a function of j, $S^R(j)$ for trajectories on the RB surface at translational energies 0.8, 0.3, and 0.2 eV. Error bars are one standard deviation.

VI.2

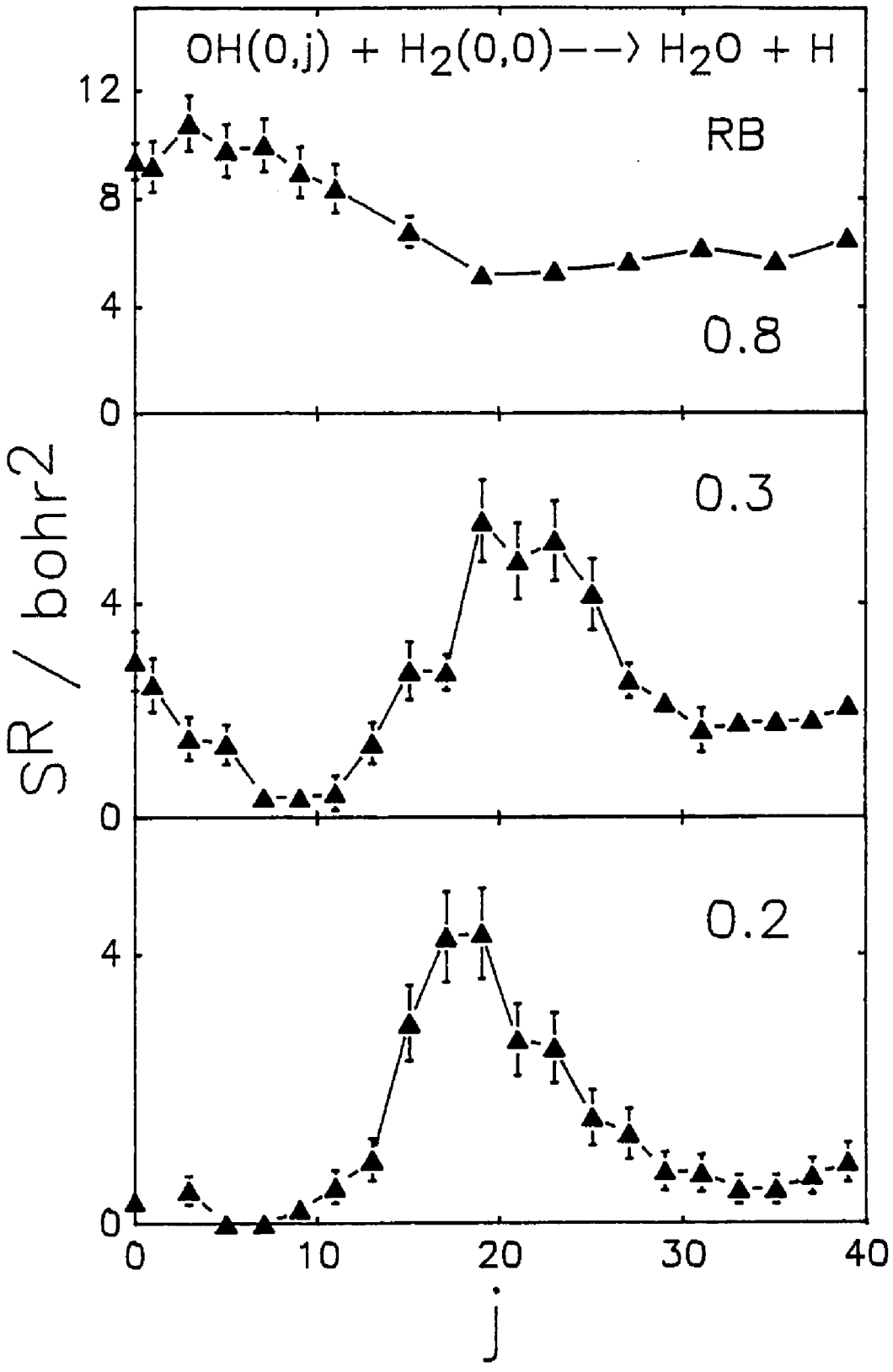

Fig. VI.3 Reaction cross sections as a function of j, $S^R(j)$, for trajectories on the SE surface at translational energies 0.8, 0.3, and 0.2 eV. Error bars are one standard deviation.

VI.3

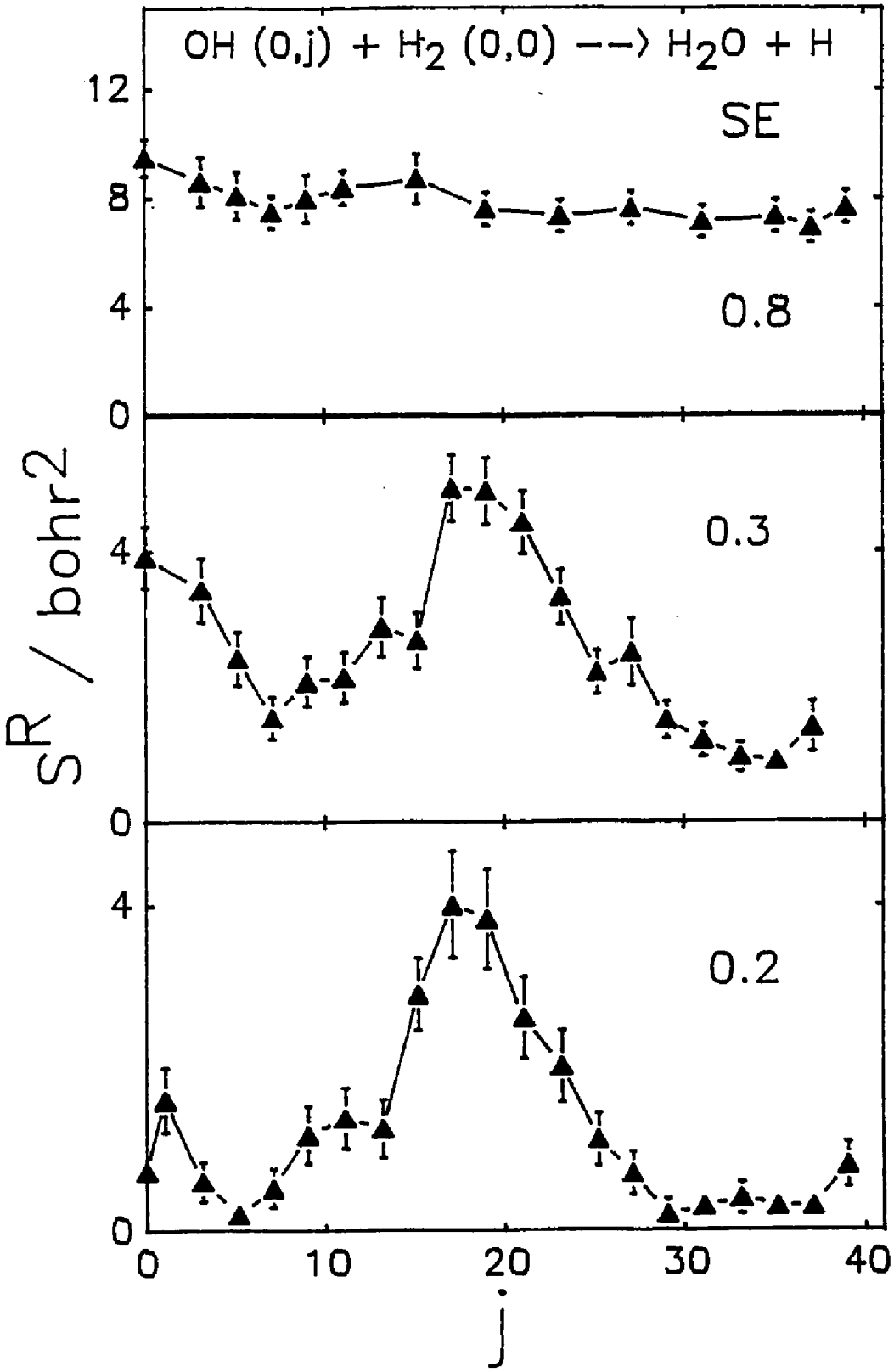

Fig. VI.4 Contour plot in (s,θ) for the RB-V42 potential (RB with the V42 term set to zero). Contour values are -0.4, -0.04, 0.1, 0.2, 0.5 and 0.9 eV. Broken lines signify energies less than zero.

VI.4

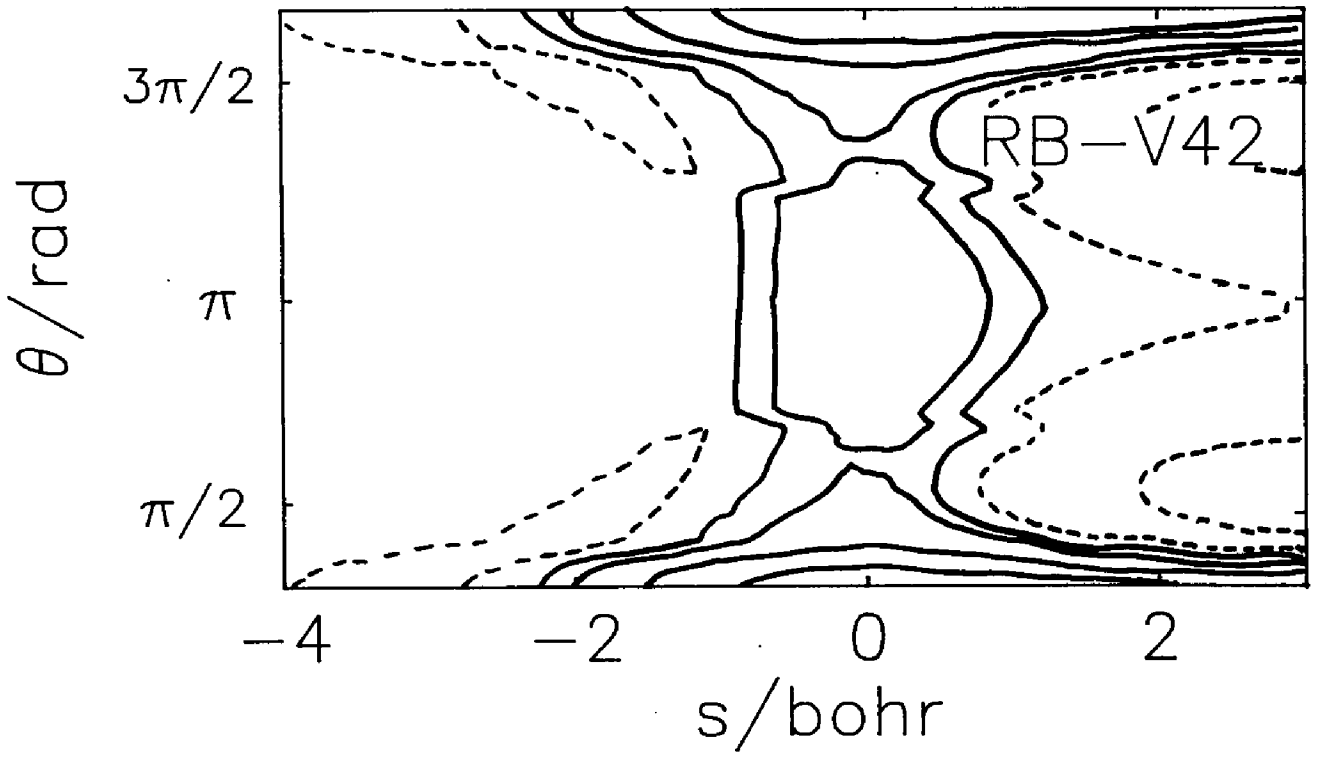

Fig. VI.5 Reaction probability as a function of j for coplanar b=0 trajectories on the RB and RB-V42 potential surfaces. The classical vibrational quantum number is set to -1/2 in both diatoms.

VI.5

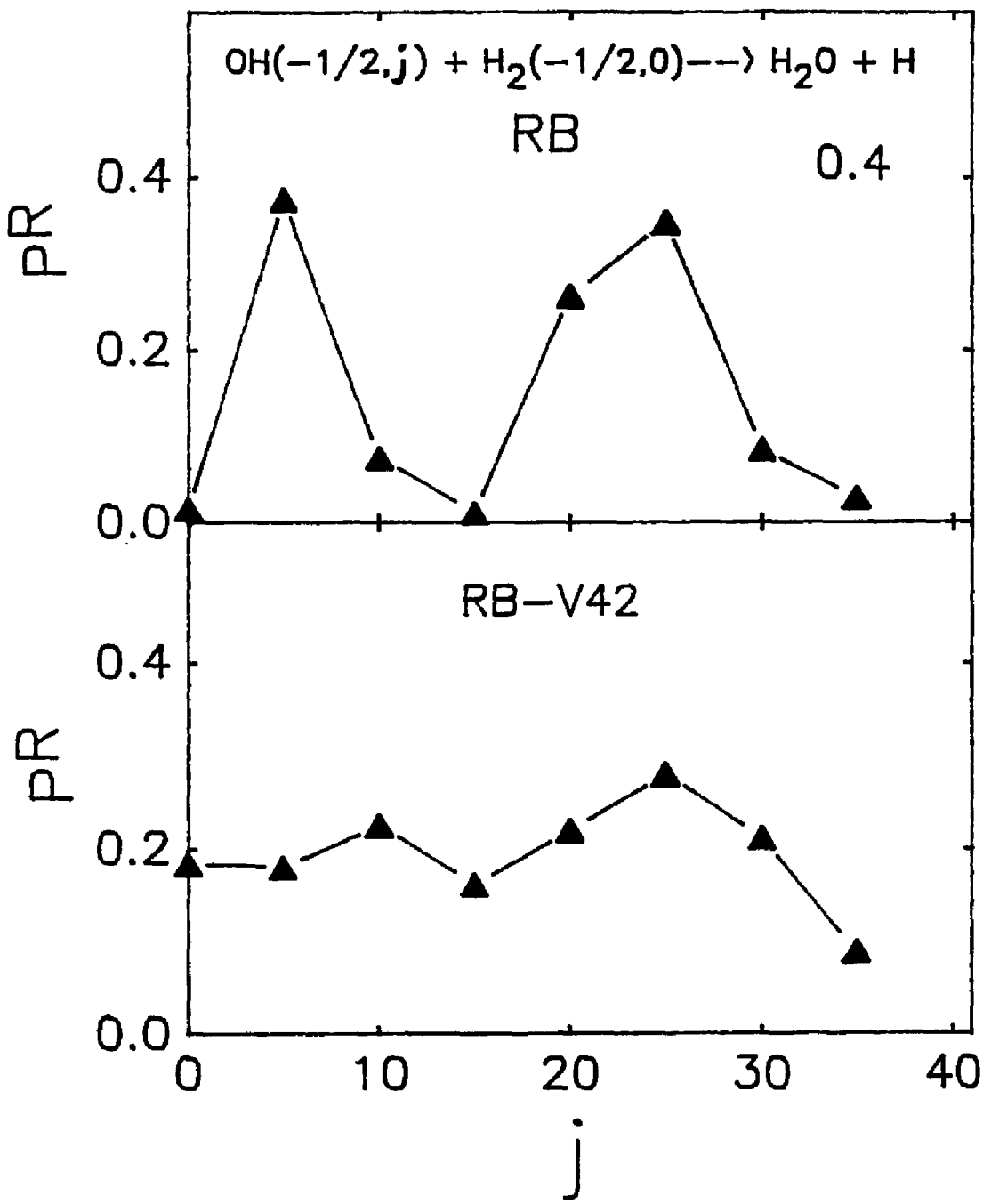

Fig. VI.6 Reaction cross section as a function of j for 3D trajectories on the RB-V42 potential surface at translational energy 0.4 eV. The classical vibrational quantum number is set to -1/2 in both diatoms.

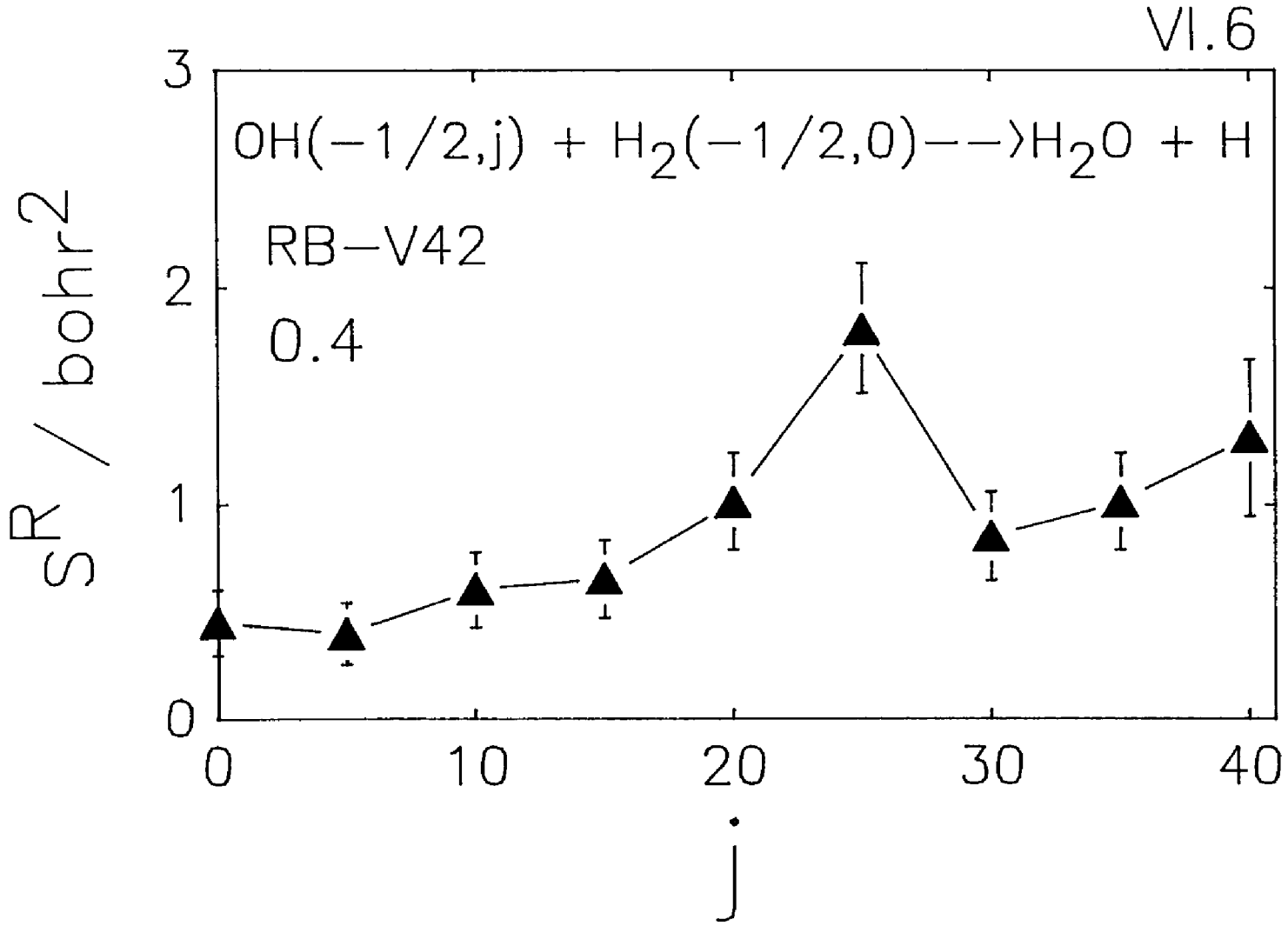
VI.6
OH(−1/2,j) + H2(−1/2,0)−−›H2O + H
RB−V42
0.4
SR / bohr2
0
1
2
3
0
10
20
30
40
j

Fig. VI.7 Reaction probabilities as a function of j for the RB model system. The translational energy is 0.05 eV. Potential parameters are given in Table II.2.

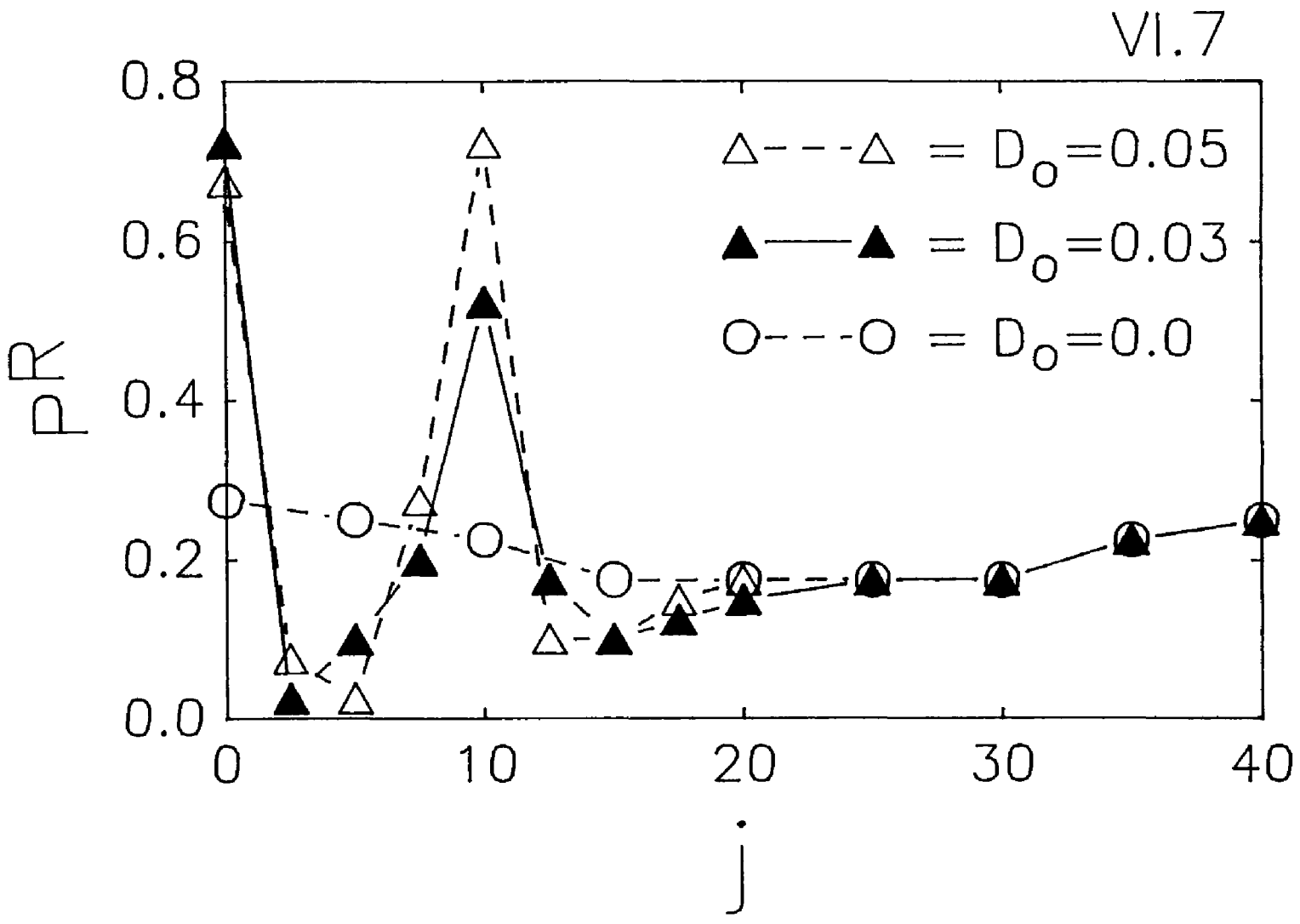
VI.7
0.8
0.6
0.4
0.2
0.0
P_R
△---△ = D_o=0.05
▲——▲ = D_o=0.03
○---○ = D_o=0.0
0
10
20
30
40
j

Fig. VI.8 Potential contour diagram showing effect of bumps in entrance valley of RB model. Top panel: small j. The lower trajectory would have reacted in the absence of bumps. The shading on the γ axis shows the range of values which react in the presence of bumps. Lower Panel: high j. Two trajectories which would be unreactive in the absence of the bumps are deflected by the bumps through the reaction valley.

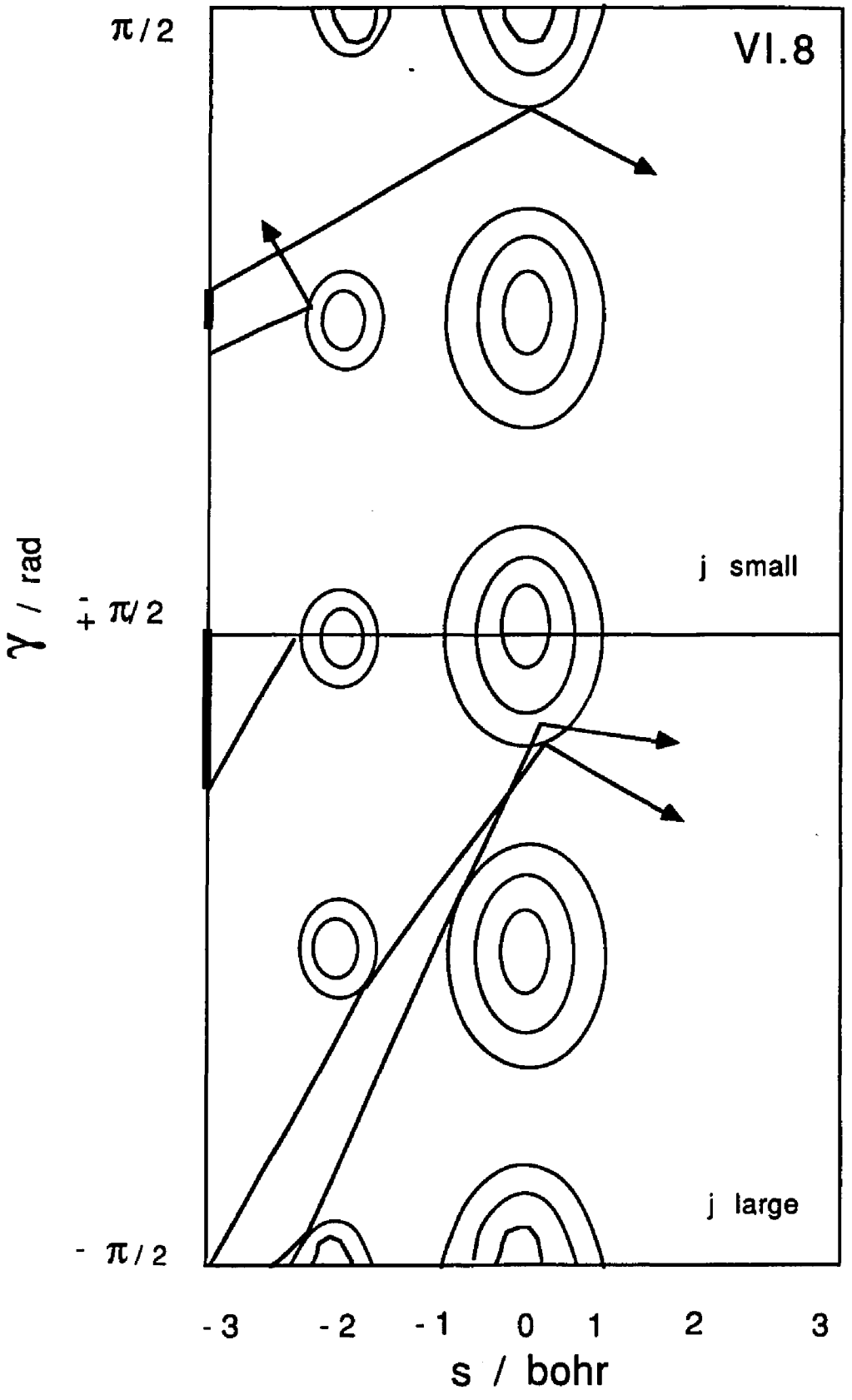
VI.8
π / 2
γ / rad
+ π/ 2
- π / 2
j small
j large
- 3
- 2
- 1
0
1
2
3
s / bohr

Fig. VI.9 Reaction probabilities as a function of j for the SE model system. Potential parameters are given in Table II.2.

VI.9

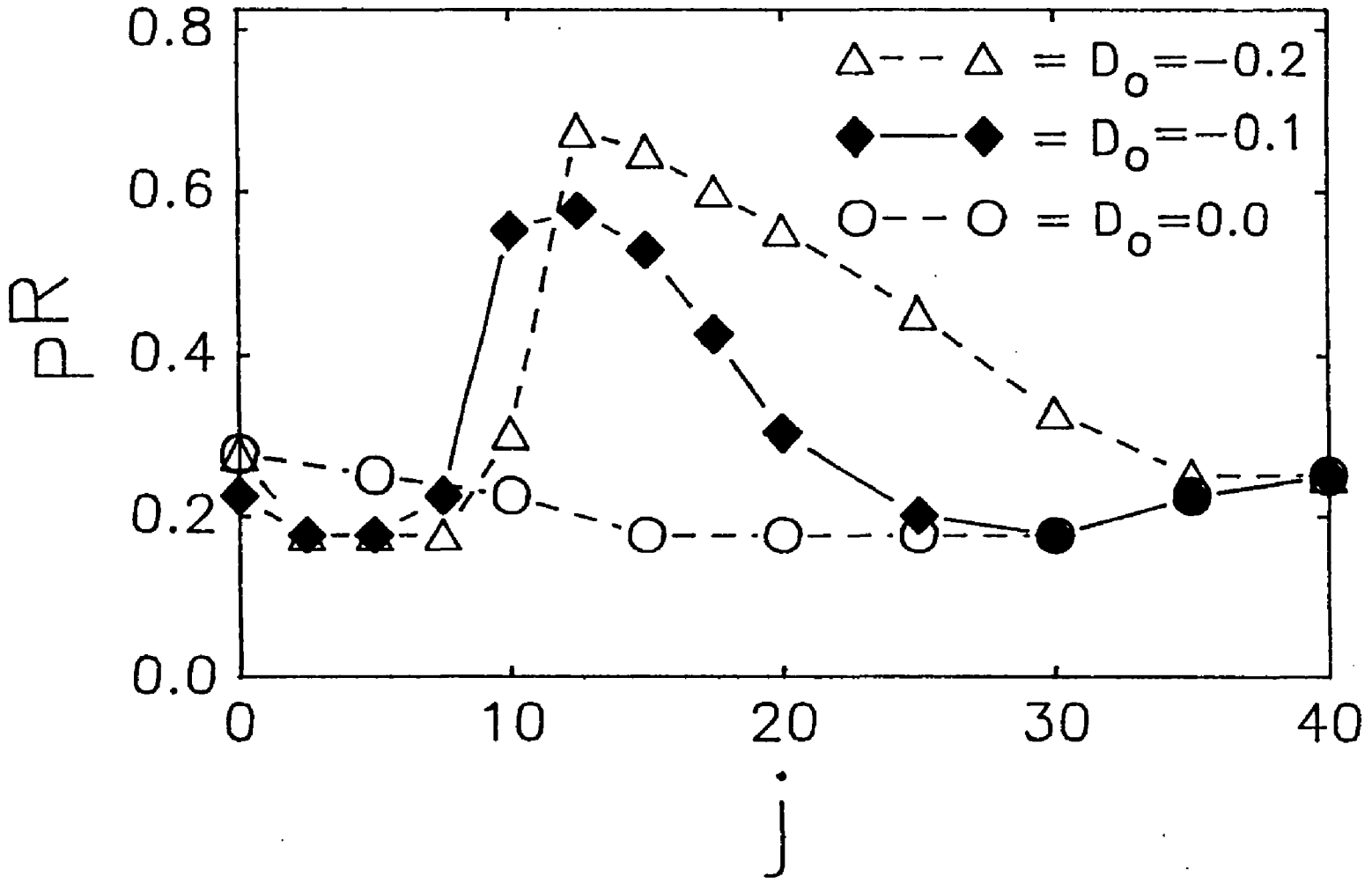

Fig. VI.10 Potential contour diagram showing effect of attractive wells in the entrance valley of model SE potential. Top panel: small j. The lower trajectories would have reacted in the absence of wells. Lower panel: high j. Two trajectories which would be unreactive in the absence of wells are pulled into reactive region.

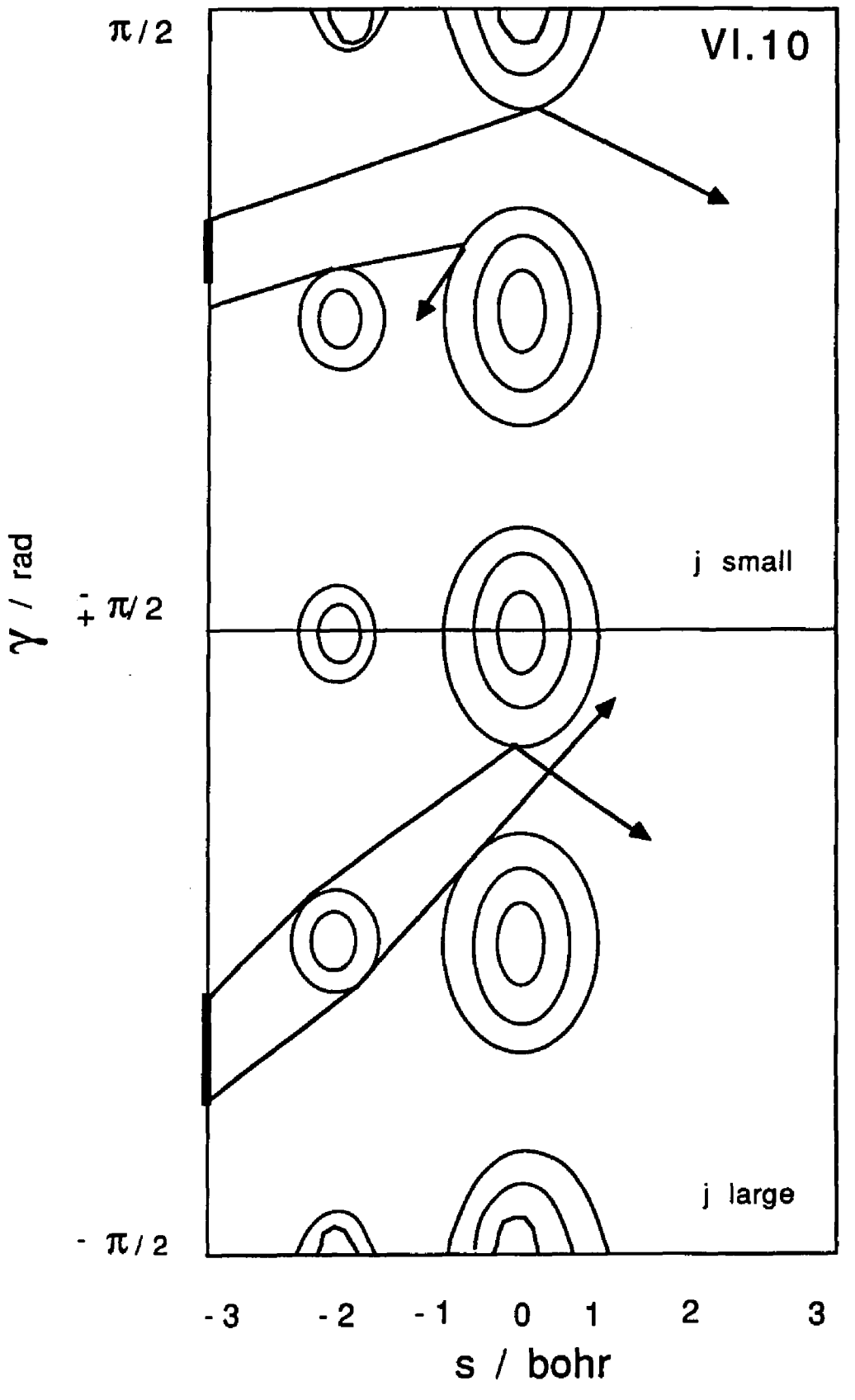
VI.10
π / 2
γ / rad
+ π/ 2
- π / 2
j small
j large
- 3
- 2
- 1
0
1
2
3
s / bohr

Fig. VI.11 Reaction cross sections as a function of j for isotopically substituted H in OH. The masses of substituted H atom are: Top panel, $m_x = 3.0$; middle panel $m_x = 2.0$; Lower panel $m_x = .03$ eV. Error bars are one standard deviation.

VI.11

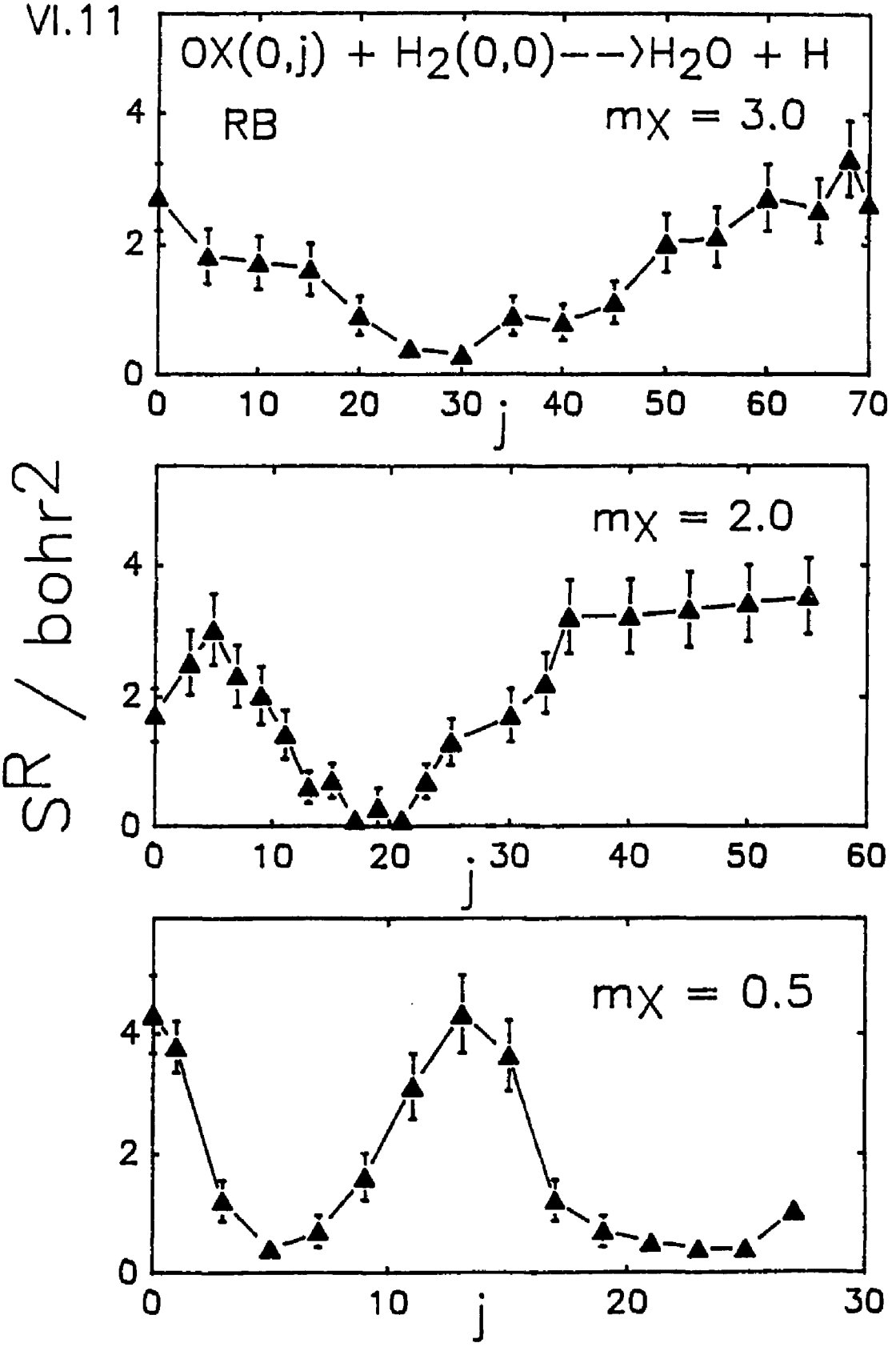

Fig. VI.12 Reaction cross sections as a function of j for $OX(0,j)+H_2$, where X is muonium, mass 0.11 amu. Translational energy is 0.3 eV.

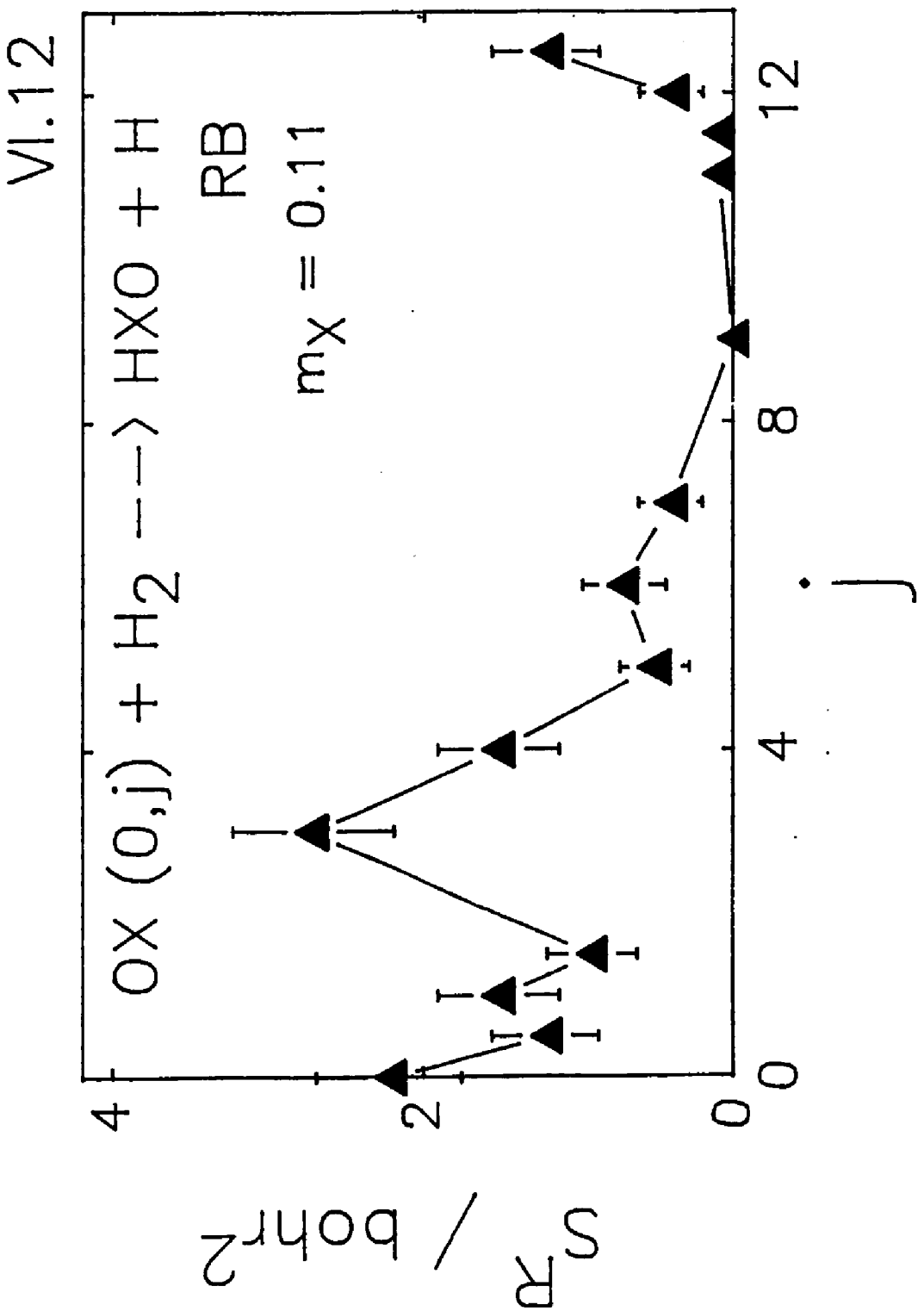
VI.12
OX (0,j) + H2 ---> HXO + H
RB
mx = 0.11
SR / bohr2
J
0
4
8
12
0
2
4

Fig. VI.13 Plot of the classical quantum number j, at the max/min in the SR(j) versus the mass of the isotopically substituted hydrogen in OH. Translational energy is 0.3 eV.

VI.13

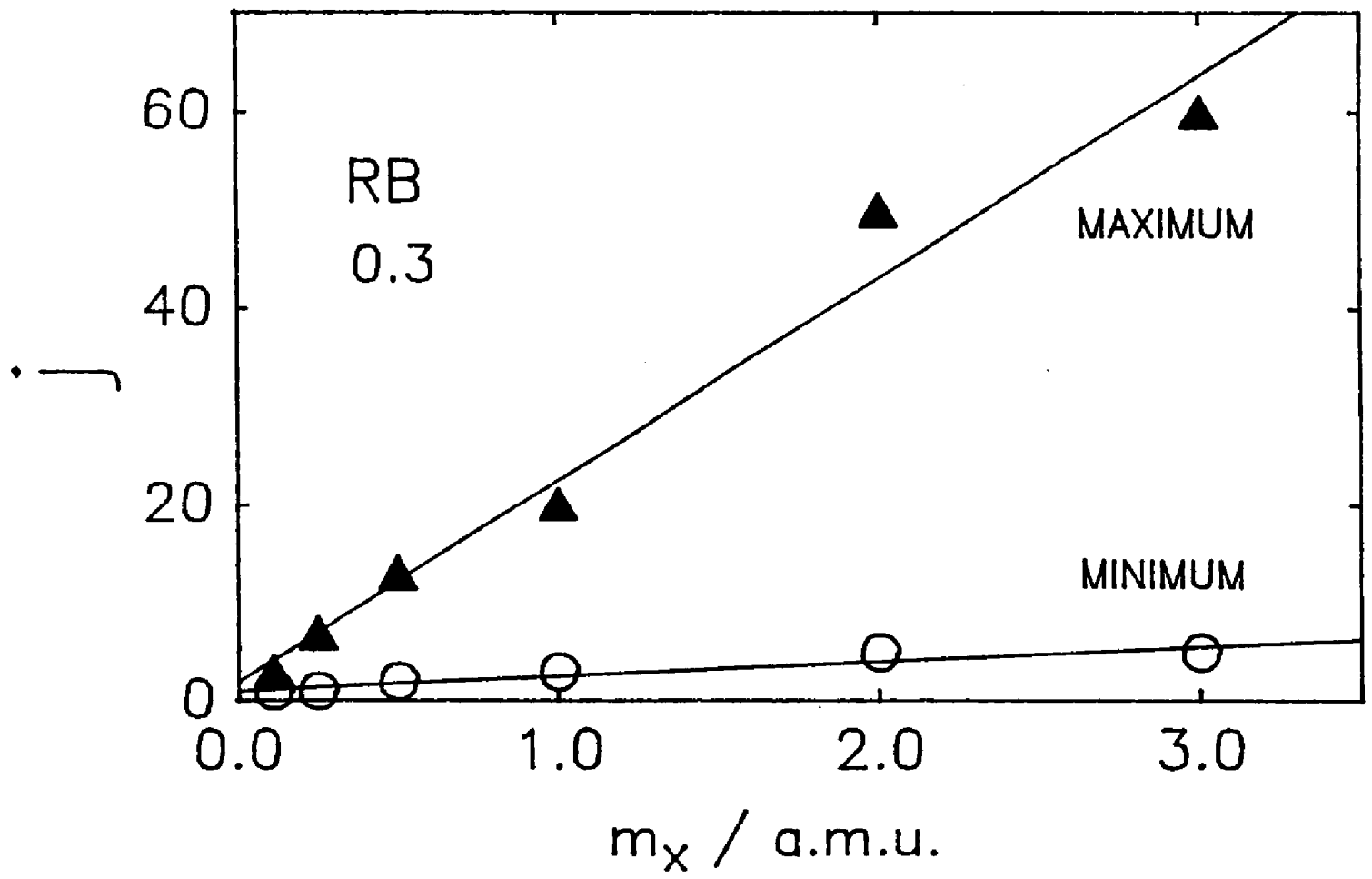

Fig. VI.14 Reaction probabilities on the model RB potential as a function of j for the isotopically substituted H in OH. The potential parameter D_o = 0.03 eV. The masses of the H atom, are on the figure.

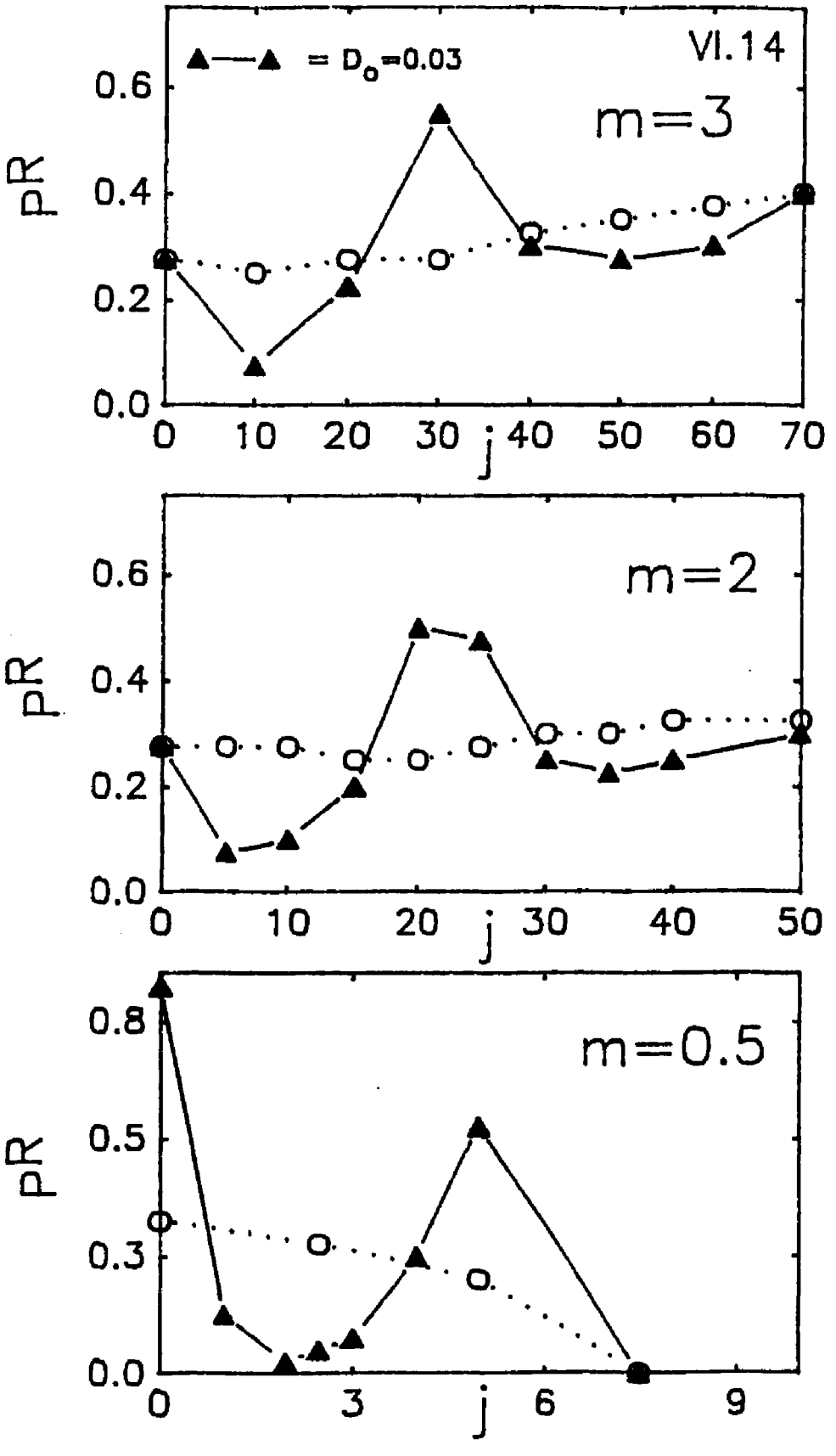
▲—▲ = D_o=0.03
VI.14
m=3
pR
0.6
0.4
0.2
0.0
0
10
20
30
j
40
50
60
70
m=2
pR
0.6
0.4
0.2
0.0
0
10
20
j
30
40
50
m=0.5
pR
0.8
0.5
0.3
0.0
0
3
j
6
9

Fig. VI.15 Reaction cross sections as a function of j calculated on the RB surface for the reaction OH(0,j) + HD(0,0). Error bars are one standard deviation. Translational energy is 0.3 eV.

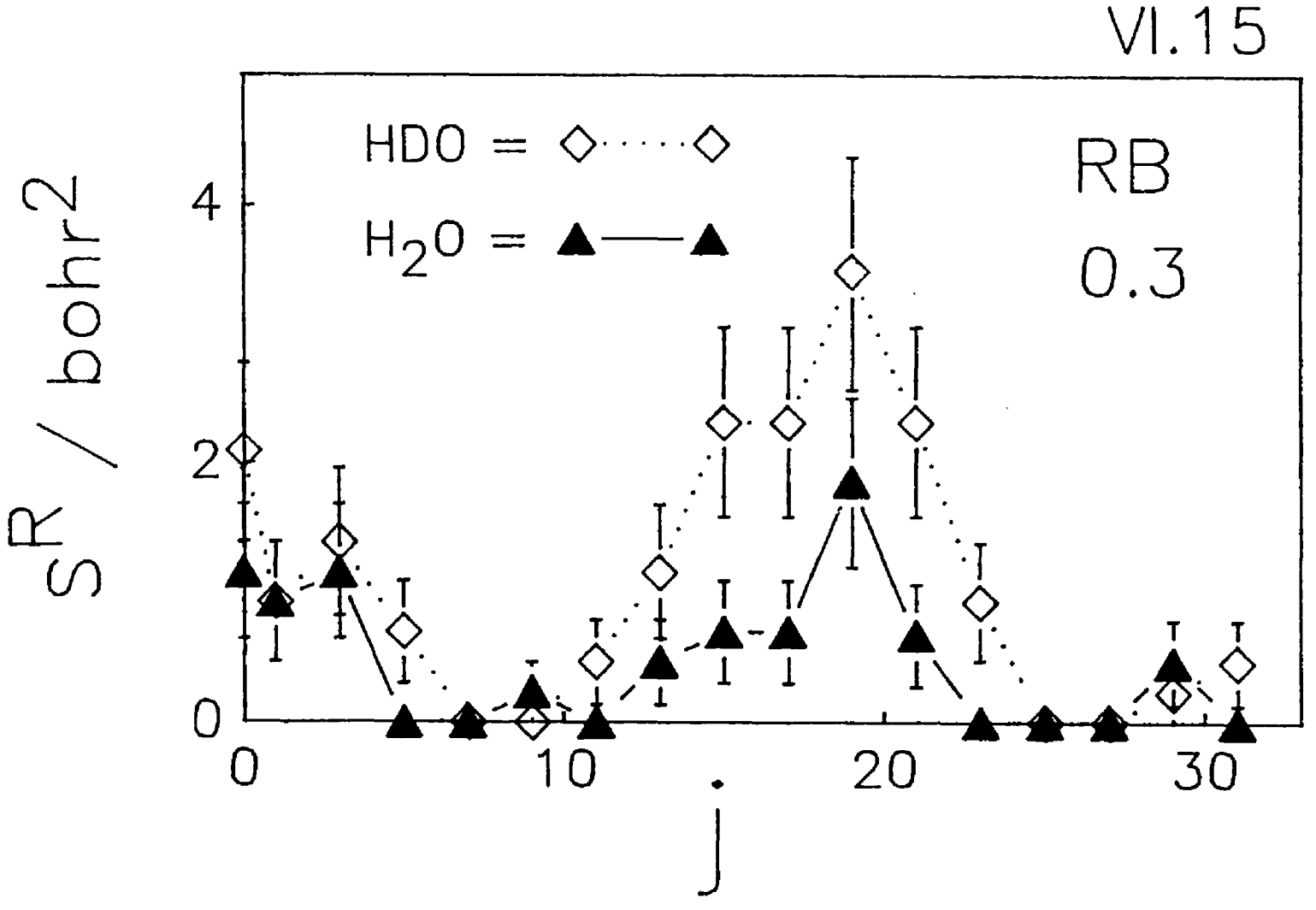
VI.15
HDO =
H2O =
RB
0.3
SR / bohr2
4
2
0
0
10
20
30
J

Fig. VI.16 Reaction cross sections as a function of j calculated on the RB surface for the reaction OH(0,0) + HD(0,j'). Translational energy is 0.38 eV. Error bars are one standard deviation.

VI.16

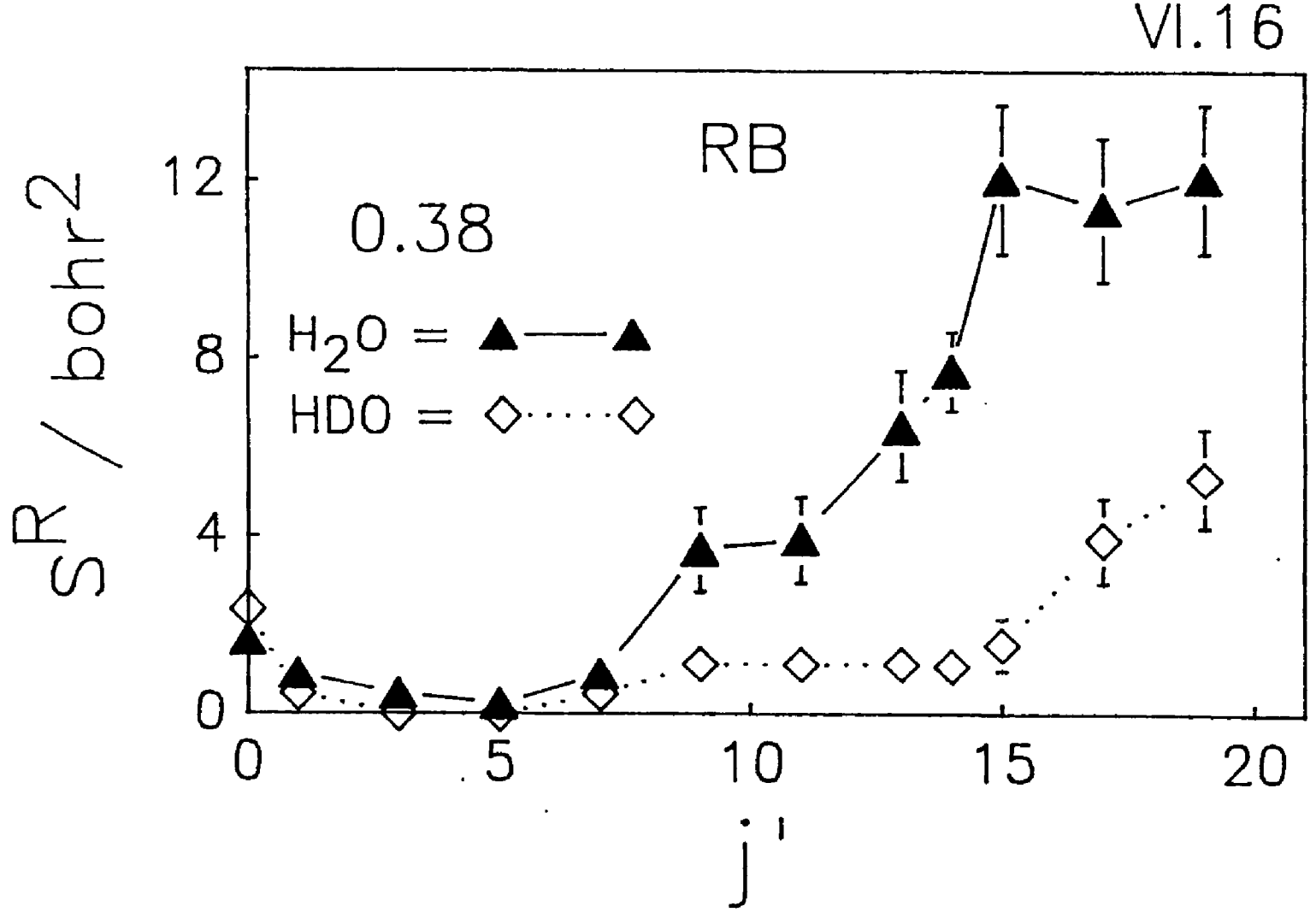

TABLE VI.1

OH(-1/2,j)	< r > / bohr	E_{vj} / (au)
0	1.86330	0.00000
5	1.86902	0.00250
10	1.88456	0.00915
15	1.91070	0.01993
20	1.94890	0.03478
25	2.00191	0.05364
30	2.07428	0.07642
35	2.17505	0.10301
45	2.32479	0.13329

< r > = the average of the inner and outer turning points of r for the diatom OH(-1/2,j). Inner and outer turning points were calculated with the PRM.

APPENDIX A

CLASSICAL TRAJECTORIES: METHOD OF CALCULATION

Introduction

In order to calculate classical trajectories Hamilton's or Newton's equations of motion, which are coupled differential equations [100,101], must be solved numerically. Hamilton's equations, which are functions of position and momenta, are used in this work. Numerical solution of the classical equations of motion is an initial value problem. As such, the solution requires values for the initial positions and momenta present in the Hamiltonian which represents the system. Selection of initial position and momenta requires selection of the so called "action" and "angle" variables. This is illustrated for the rigid rotor below.

In the case of zero potential, the Hamiltonian for the rigid rotor in spherical polar coordinates is given by

$$H(\theta, p_\theta) = p_\theta^2/2I = E \qquad (A.1)$$

where θ is the position, p_θ is the momentum, I is the rotor's moment of inertia, and E is the total energy. Applying the contact transformation, $S'(\theta, p_\theta)$, so that [101]

$$p_\theta = dS'/d\theta \qquad (A.2)$$

$$\bar{\theta} = dS'/d\bar{p}_\theta \qquad (A.3)$$

$$d\bar{p}_\theta/dt = -d\bar{H}/d\bar{\theta}, \qquad \bar{H} = H \qquad (A.4)$$

$$d\bar{\theta}/dt = d\bar{H}/d\bar{p}_\theta \qquad (A.5)$$

The generating function, S', is chosen so that $\bar{p}_\theta$ is a constant of the motion, J, i.e. $\bar{p}_\theta = J$, [101] further, $\bar{\theta} = w$ and from (A.3)

$$w = dS'/dJ. \qquad (A.6)$$

Suppose that θ and p_θ are periodic functions of the time, and let us evaluate the action over one period. This is a constant of the motion, and we choose J to be equal to it [101]

$$J = \oint p_\theta \, d\theta. \qquad (A.7)$$

Substituting for p_θ, expression (A.7) becomes

$$J = (2EI)^{1/2} \oint d\theta. \qquad (A.8)$$

The generating function is given by [101]

$$S'(\theta,\bar{p}_\theta) = \int E \, d\theta = \int (J/2\pi)^2 \, (1/2I) \, d\theta \qquad (A.9)$$

Using the result from integration of (A.9) and (A.6) one obtains the expression for w

$$w = J/I2\pi \qquad (A.10)$$

where w is unitless as required and J has the units of actions, energy X time [100,101]. For such a problem, J is called the "action" variable and w is the corresponding angle variable [101]. The transformed momenta are the classical "actions." This allows for the random scanning of the angle variables conjugate to the action variables in order to randomly select the molecule's initial conditions.

In the case of a rotating diatomic molecule scanning the angles conjugate to the rotational and vibrational actions would allow for initial selection of position and momenta. The

fact that vibration and rotation are coupled make the extraction of good "actions" difficult. If one assumes vibration and rotation are separable the situation is much simpler. Vibration can be approximated by either a harmonic oscillator or a Morse oscillator. Rotation can be described by a rigid rotor approximation. Selection of initial conditions in this case has been discussed by Raff and Thompson [12].

One of the earliest methods for the selection of initial conditions for a rotating Morse oscillator is the method of Karplus, Porter, and Sharma (KPS) [11]. This method was later replaced by the method of Porter, Raff, and Miller (PRM) [162]. The PRM method uses a truncated Hamiltonian for a rotating Morse oscillator to determine the action-angle variables. The results obtained from this method are good except for large values of angular momenta. Recently, Eaker [163] has developed an alternative way to determine the initial Cartesian variables, that is, the initial position and momenta, based on the Fast Fourier transform of the action-angle variables. This method is a vast improvement over the PRM method in that it is exact. As a result, it could be used to select initial conditions for large values of angular momenta where PRM breaks down. Both the KPS and the PRM methods are discussed more fully in subsequent sections.

Here, in addition to the discussion of the selection of initial position and momenta for three particle A+BC(v,j) type

reactions, the coordinate system and the calculation of final state properties is also discussed. The coordinate system and selection of initial conditions for a generalized four particle system is also discussed.

In this work, the KPS method was used in the $F+H_2$ case study and is therefore described in the three particle, A+BC, section. Similarly, the PRM method was used in the $OH+H_2$ investigation and is discussed in the four particle section.

Classical Trajectories: Method of Calculation

Coordinates: A+BC(v,j)

As with any dynamical problem, the choice of a suitable coordinate system is a major concern. The appropriate choice of coordinates allows for a reduction in the number of simultaneous differential equations which must be solved, thus reducing the computational effort required to solve the problem of interest.

For 3 particle, A + BC (j), systems it turns out that Jacobi coordinates ($\underline{R}$,$\underline{r}$) [11,100] are most suited to the problem. These coordinates are shown in Figure A.1, where $\underline{r}$ is a vector which runs along the internuclear axis of the diatom BC and $\underline{R}$ is the vector from the atom A to the center of mass of BC. The length of $|r|$ is referred to as r, the internuclear distance of the BC diatom. This coordinate system was used by Karplus et. al. [KPS,65] to perform a classical trajectory study of $H + H_2$ reaction.

In three dimensions, the use of Jacobi coordinates

instead of Cartesian coordinates, allows for a reduction in the number of simultaneous differential equations, i.e. Hamilton's equations, which must be solved from 18 to 12. In these coordinates, the Hamiltonian is given by:

$$H = \underline{p}_R^2/2\mu + \underline{p}_r^2/2m + V(\underline{R},\underline{r}) \qquad (A.11)$$

where $\underline{p}_R$ is the momentum conjugate to $\underline{R}$, $\underline{p}_r$ is the momentum conjugate to $\underline{r}$, μ is the total reduced mass of A + BC, m is the reduced mass of the diatom, and V is the potential energy. The potential energy is not usually defined in terms of the coordinates $(\underline{R},\underline{r})$, but rather the interatomic distances, i.e. $V(x_1,x_2,x_3)$. The A-B, B-C, and A-C internuclear distances are given by x_1, x_2, and x_3 respectively (also shown in Fig A.1). The form of μ and m are

$$\mu = A * (B+C)/(A + B + C) \qquad (A.12)$$

$$m = (B * C)/(B + C) \qquad (A.13)$$

where A, B, and C represent the masses of atoms A, B, and C respectively. The relationships between the Jacobi coordinates, $\underline{R}$ and $\underline{r}$, and interatomic distances, x_1,x_2, and x_3 are given by the following equations

$$x_1 = (R^2 + (C/(B+C))r^2 - 2 * R * r * \cos(\gamma))^{1/2} \qquad (A.14)$$

$$x_2 = r \qquad (A.15)$$

$$x_3 = (R^2 + (C/(B+C))r^2 + 2 * R * r * \cos(\gamma))^{1/2} \qquad (A.16)$$

where γ is the angle between $\underline{r}$ and $\underline{R}$.

Classical trajectories were run by solving Hamilton's equations [101,102] with a standard Hamming Predictor Corrector [94,178] integration technique. Since the Hamming

Predictor Corrector is not a self-starting integration technique, points needed to begin the integration were obtained by a Runge Kutta integration [94]. Hamilton's equations [100,101] have the general form

$$dq/dt = dH/dp(i) \qquad (A.17)$$

$$dp/dt = -dH/dq(i) \qquad (A.18)$$

where p(i) represents the component of the momentum in the i direction and similarly, q(i) represents the component of the position in the i direction. In this case, Hamilton's equations have the form

$$dr(i)/dt = dH/dp_r(i) \qquad (A.19)$$

$$dp_r(i)/dt = -dH/dr(i) = -dV(x_1,x_2,x_3)/dr(i) \qquad (A.20)$$

$$dR(i)/dt = dH/dp_R(i) \qquad (A.21)$$

$$dp_R(i)/dt = -dV(x_1,x_2,x_3)/dR(i) \qquad (A.22)$$

where i is as above, the x, y, or z direction of the component of interest. The derivatives of the potential with respect to $\underline{R}$ and $\underline{r}$ are obtained by utilizing the chain rule in conjunction with equations (A.14-A.16).

Selection of Initial Position and Momenta: KPS

In accordance with the usual convention, [11] the atom A approaches the diatom from the $\underline{z}$ direction, that is, the z axis is the direction of the initial asymptotic relative velocity vector, $\underline{v}_{cm}$, therefore

$$p^R_x = 0. \qquad (A.23)$$

$$p^R_y = 0. \qquad (A.24)$$

$$p^R_z = \mu \, |\underline{v}_{cm}| = (2 \, E_t/\mu)^{1/2} \qquad (A.25)$$

The initial relative velocity vector, $\underline{v}_{cm}$, is also referred to as the center of mass velocity. Additionally, the coordinate system is oriented so that the atom A and the center of mass of BC lie in the yz plane, therefore

$$R_x = 0. \tag{A.26}$$

$$R_y = b \tag{A.27}$$

$$R_z = -(R_{max}^2 - b^2 - |v_{cm}| \; \tau \; \varsigma \;)^{1/2} \tag{A.28}$$

where E_t is the translational energy, b is the impact parameter, i.e. the distance in the y direction of the atom from the diatom's center of mass, R_{max} is some conveniently large distance between A and the center of mass of BC, where the interaction potential is zero, τ is the vibrational period of the diatom, and ς is a computer generated random number on the interval [0-1]. The impact parameter, b, is randomly chosen from a distribution that is uniform in b^2, i.e. $0 \leq b^2 \leq b^2_{max}$, where b_{max} is the maximum impact parameter, when $b > b_{max}$ the reaction probability is zero [11-13]. The z component of $\underline{R}$, R_z, is randomly selected in the range given by the vibrational period and the initial center of mass velocity. The diatom's internuclear distance is initially set to its inner (r_-) or outer (r_+) turning point, the actual choice makes little difference [13]. By initially setting the diatom's internuclear separation to, say, its outer turning point and varying the initial R_z distance the diatom will have different internuclear separations at the time of collision. In other words, the aforementioned random selection of R_z results in

the random sampling of the vibrational phase of the diatom.

The orientation of the BC molecule is given by the spherical polar coordinates r, θ, and ϕ. Random selection of r_x, r_y, and r_z is achieved by random selection of ϕ from a uniform distribution between [0-2π] and selection of cos(θ) from a uniform distribution between -1 and 1. In order to specify the internal momentum components, a third angle, η, must be randomly selected from a uniform distribution between [0-2π]. The angle, η is the angle of the angular momentum vector relative to an arbitrarily chosen vector that is perpendicular to the molecular axis. This vector is usually taken to be $\underline{r} \times \underline{k}$, where $\underline{r}$ points along the molecular axis and $\underline{k}$ is the unit vector in the z direction.

The Cartesian components of $\underline{r}$ and $\underline{p}_r$ are related to the polar coordinates via

$$r_x = r \sin(\theta) \cos(\phi) \qquad \text{(A.29)}$$

$$r_y = r \sin(\theta) \sin(\phi) \qquad \text{(A.30)}$$

$$r_z = r \cos(\theta) \qquad \text{(A.31)}$$

$$p_x = - p_r(\sin(\phi) \cos(\eta) + \cos(\phi) \cos(\theta) \sin(\eta)) \qquad \text{(A.32)}$$

$$p_y = p_r(\cos(\phi) \cos(\eta) - \sin(\phi) \cos(\theta) \sin(\eta)) \qquad \text{(A.33)}$$

$$p_z = p_r \sin(\theta) \sin(\eta) \qquad \text{(A.34)}$$

where:

$r = r_-$ or r_+

$p_r = p_r$ at r_- or r_+ (eqn 18 of ref [11])

$p_{r-} = j(j+1) \hbar^2 / (r_-)^2$ (substitute r_+ to obtain p_{r+}).

It is now apparent why random selection of cos(θ), ϕ, and η

determine the initial orientation and momenta of the diatomic molecule.

Initial Polarization of the j Vector: KPS

The j vector can be polarized initially to lie in the x, y, or z (Fig A.2) direction. Recall the definition of $\underline{j}$ [100]

$$\underline{j} = \underline{r} \times \underline{p} \tag{A.35}$$

therefore the components of $\underline{j}$ are defined by the following:

$$j_x = (r_y\, p_z - r_z\, p_y) \tag{A.36}$$

$$j_y = (r_z\, p_x - r_x\, p_z) \tag{A.37}$$

$$j_z = (r_x\, p_y - r_y\, p_x)\,. \tag{A.38}$$

Inspection of equations (A.36) through (A.38) yields insight into the conditions which will result in polarization, i.e. only one nonzero $\underline{j}$ component. Polarization in any direction, x, y, or z, is achieved by setting the $\underline{r}$ and $\underline{p}_r$ components in that direction equal to zero. For example, to achieve polarization in the x direction, set r_x and p_x equal to zero. The result is $j_x \neq 0$ and $j_y = j_z = 0$.

By inspection of equations (A.29) through (A.34) it is apparent that setting ϕ equal to $\pi/2$ or $3\pi/2$, η equal to $\pi/2$ or $3\pi/2$, and keeping θ random will result in x polarization. Polarization in the y direction is achieved by setting ϕ equal to 0 or π, η equal to $\pi/2$ or $3\pi/2$, and randomly selecting θ. Lastly, z polarization is achieved by randomly selecting ϕ then setting η equal to 0 or π, and θ equal to $\pi/2$ or $3\pi/2$.

Lastly, allowing θ and ϕ to be randomly chosen and setting η to be equal to $\pi/2$ or $3\pi/2$ causes the j_z component

of angular momentum to be equal to 0 and both the j_x and j_y components to be nonzero. In other words, this situation gives rise to random orientation of the diatom in the plane perpendicular to the z axis, i.e. there is no projection of the angular momentum vector on to the z axis.

Coplanar and Collinear Orientation of the Diatom: KPS

Classical trajectories are often restricted to one or two dimensional collisions. This is done in hopes of making the dynamics of the reaction easier to visualize. For example, in a reaction of the A + BC type if the atom (A) approached from the z direction the diatom (BC) could be made to rotate in the yz plane resulting in a coplanar arrangement of the three atoms. The BC diatom could also be forced to lie along the z axis resulting in a collinear collision geometry.

A coplanar initial geometry is equivalent to the case of x polarization. The criteria for this geometry have been previously discussed.

A collinear initial geometry is achieved by setting ϕ equal to 0 or π, θ equal to 0 or π, and η equal to 0 or π.

Final State Properties: A+BC(v,j)

In this work, the major concern is the change in reactivity, i.e. cross section, with rotational excitation of the diatom. Of additional interest are the product rotational distributions, the product angular distributions, and the product vibrational distributions.

The angular momentum vector of the product diatomic

molecule is easily obtained from the relationship

$$\underline{j}' = \underline{r}' \times \underline{p}'. \qquad \text{(A.38)}$$

Analysis of Figure A.3 reveals that for the product molecule, AB, the product displacement vectors $\underline{r}'_C$ and $\underline{R}'_C$ (where subscript, C, denotes free product atom C) are given by

$$\begin{pmatrix} \underline{r}'_C \\ \underline{R}'_C \end{pmatrix} = \begin{pmatrix} -C/(B+C) & 1 \\ BM/(B+C)(B+A) & A/(B+C) \end{pmatrix} \begin{pmatrix} \underline{r} \\ \underline{R} \end{pmatrix} \qquad \text{(A.39)}$$

where M is the total mass, (A+B+C), and primes denote final quantities. If the product molecule is AC the product displacement vectors are given by

$$\begin{pmatrix} \underline{r}'_B \\ \underline{R}'_B \end{pmatrix} = \begin{pmatrix} B/(B+C) & 1 \\ CM/(B+C)(A+B) & -A/(A+C) \end{pmatrix} \begin{pmatrix} \underline{r} \\ \underline{R} \end{pmatrix} \qquad \text{(A.40)}$$

Product momenta are easily obtained by taking the time derivative of the product displacement vectors given in equations (A.39) and (A.40), then by using equation (A.38) the angular momentum vector of the product molecule, $\underline{j}'$, can be obtained.

The product vibrational quantum number, v', is given by [12]

$$v' = -1/2 + 2/h \int p_r \, dr \qquad \text{(A.41)}$$

where all the variables have been previously defined. In practice, equation (A.41) is solved by simply continuing the trajectory for 1/2 period after locating one of the turning points. Once the $p_r(r)$ values are obtained an appropriate quadrature method is used to obtain v', e.g. Simpson's rule.

A large number of trajectories were calculated for each desired set of initial conditions, the cross section, S^R, and the differential cross section, $d\sigma/d\omega$, are calculated by a Monte Carlo averaging procedure for fixed $\underline{v}_{cm}$, j, and v [11-13].

The cross section is given by [11]

$$S^R (v_{cm},j,v) = 2 \pi \int_0^{b_{max}} P_r (v_{cm},j,v,b)\ b\ db \qquad (A.42)$$

where j is the rotational quantum number, v is the vibrational quantum number, and P_r is the reaction probability. In practice, the integral in equation (A.42) is approximated by using the Monte Carlo relationship

$$\lim_{N\to\infty} N_r(\underline{v}_{cm},j,v)/N(\underline{v}_{cm},j,v) = 1/2\ (b_{max}^2)^{-1} \int_0^{b_{max}} P_r(\underline{v}_{cm},v,j,b)\ b\ db \qquad (A.43)$$

where N_r is the number of reactive trajectories and N is the total number of trajectories. Using (A.43), for finite N, the cross section (A.42) becomes [11]

$$S^R(\underline{v}_{cm},j,v) = \pi\ b_{max}^2\ [N_r(\underline{v}_{cm},j,v)/N(\underline{v}_{cm},j,v)] \qquad (A.44)$$

with the standard error, s_e, given by [11]

$$s_e = S^R(\underline{v}_{cm},j,v)\ [(N - N_r)/N\ N_r]^{-1/2}. \qquad (A.45)$$

The differential cross section, DCS, is by definition [3] the cross section per solid angle volume element. The DCS is a measure of the direction in which the product molecule is scattered. If θ is the center of mass scattering angle, by convention $\theta = 0$ is scattering in the forward direction of the product atom and $\theta = \pi$ is termed backward scattering. The center of mass scattering angle, θ, is given by [12]

$$\theta = \cos^{-1} [\ \underline{v}'_{cm} \cdot \underline{v}_{cm} / |\underline{v}_{cm}| * |\underline{v}_{cm}|\ ] \qquad (A.46)$$

where $\underline{v}'_{cm}$ is the product center of mass velocity. For a given angular width, $\Delta\chi$, (where χ is defined as the absolute value of θ) centered at χ, the Monte Carlo method defines the DCS, in the limit of finite N, as [179]

$$d\sigma/d\omega\ (E_t,j,v,\chi) = \pi\ b_{max}^2/\ [\Delta\Omega(\chi,\Delta\chi] * [N_r(E_t,v,j,\chi,\Delta\chi)/N(E_t,v,j)] \qquad (A.47)$$

where $\Delta\Omega$ is the finite increment of solid angle included in $\Delta\chi$.

Coordinates: AB(v,j) + CD(v,j)

Just as in the three particle system, in the four particle system the use of Jacobi coordinates significantly reduces the number of simultaneous differential equations which must be solved. The four particle Hamiltonian has the form

$$H = \underline{p}_{r1}^2/2m_1 + \underline{p}_{r2}^2/2m_2 + \underline{p}_R^2/2\mu + V(\underline{r}_1,\underline{r}_2,\underline{R}) \qquad (A.48)$$

where $\underline{r}_1$ and $\underline{r}_2$, are the vectors along the AB and CD diatoms, respectively, $\underline{R}$ is the vector from the center of mass of AB to the center of mass of CD, $\underline{p}_{r1}$ and $\underline{p}_{r2}$ are the momenta conjugate to $\underline{r}_1$ and $\underline{r}_2$, $\underline{p}_R$ is the momentum conjugate to $\underline{R}$, m_1 and m_2 are the reduced masses of diatoms AB and CD, respectively, μ is the total AB + CD reduced mass, and V is the potential energy. As in the 3 particle case, the potential energy is defined in terms of the internuclear distances, $V(x_1,x_2,x_3,x_4,x_5,x_6)$. The B-A, D-C, A-C, B-D, B-C, and A-D interatomic distances are given by x_1, x_2, x_3, x_4, x_5, and x_6,

respectively. Defining the interatomic vectors, $\underline{x}_i$, as in Figure A.4, results in the following coordinate transformations

$$\underline{x}_1 = \underline{r}_1 \tag{A.49}$$

$$\underline{x}_2 = \underline{r}_2 \tag{A.50}$$

$$\underline{x}_3 = -B/(A+B)\ \underline{r}_1 + \underline{R} + D/(D+C)\ \underline{r}_2 \tag{A.51}$$

$$\underline{x}_4 = A/(A+B)\ \underline{r}_1 + \underline{R} - C/(D+C)\ \underline{r}_2 \tag{A.52}$$

$$\underline{x}_5 = A/(A+B)\ \underline{r}_1 + \underline{R} + D/(D+C)\ \underline{r}_2 \tag{A.53}$$

$$\underline{x}_6 = -B/(A+B)\ \underline{r}_1 + \underline{R} - C/(D+C)\ \underline{r}_2 \tag{A.54}$$

where A, B, C, and D represent the masses of atoms A, B, C, and D, respectively.

In this case, Hamilton's equations are given by

$$dr_1(i)/dt = dH/dp_{r1}(i) \tag{A.55}$$

$$dp_{r1}(i)/dt = -dV(x_1,x_2,x_3,x_4,x_5,x_6)/dr_1(i) \tag{A.56}$$

$$dr_2(i)/dt = dH/dp_{r2}(i) \tag{A.57}$$

$$dp_{r2}(i)/dt = -dV(x_1,x_2,x_3,x_4,x_5,x_6)/dr_2(i) \tag{A.58}$$

$$dR(i)/dt = dH/dp_R(i) \tag{A.59}$$

$$dp_R(i)/dt = -dV(x_1,x_2,x_3,x_4,x_5,x_6)/dR(i). \tag{A.60}$$

As in the three particle case, the derivatives of V with respect to $\underline{R}$, $\underline{r}_1$, and $\underline{r}_2$ are obtained by making use of the chain rule and equations (A.49-A.54).

For the OH + H_2 case study a fourth order Runge Kutta Gill integrator [94] was used to solve equations (A.55-A.60).

Initial Conditions PRM Method:

The classical Hamiltonian for a rotating Morse oscillator [162] is given by

$$H = p_r^2/2m + l^2/2mr_e^2 + D\ (1-\exp[-\alpha(r-r_e)])^2 \qquad (A.61)$$

where D is the depth of the Morse well, α is the Morse steepness parameter, r_e is the equilibrium internuclear distance of the diatom, l is the angular momentum, and p_r, r, and m have been previously defined.

The PRM algorithm selects the initial position and momenta for the rotating Morse oscillator via random selection of the three "angle" variables QN, QM, and QL. In addition to the three "angle" variables, λ, the projection of the j vector on to the z axis, must also be randomly selected. The vibrational phase is determined by QN. The variables, QM, QL and λ determine the diatom's orientation in space. Random selection of the Cartesian components of $\underline{r}$ (internuclear displacement) and $\underline{p}_r$ (momentum conjugate to $\underline{r}$) follow from the random selection of "angle" variables via the following definitions

$$r_x = r\ (-\sin Q \sin QM + \lambda \cos Q \cos QM) \qquad (A.62)$$

$$p_x = [\ p_r\ (-\sin Q \sin QM + \lambda \cos Q \cos QM) + (l/r) * (-\cos Q \sin QM - \lambda \sin Q \cos QM)\ ] \qquad (A.63)$$

$$r_y = r\ (\sin Q \cos QM + \lambda \cos Q \sin QM) \qquad (A.64)$$

$$p_y = pr\ (\sin Q \cos QM + \lambda \cos Q \sin QM) + (l/r) * (\cos Q \cos QM - \lambda \sin Q \sin QM) \qquad (A.65)$$

$$r_z = r\ [\ (1 - \lambda^2)^{1/2} \cos Q] \qquad (A.66)$$

$$p_z = p_r[(1 - \lambda^2)^{1/2} \cos Q] + (l/r) * [(1 - \lambda^2)^{1/2} \sin Q] \qquad (A.67)$$

where

r = internuclear distance, given by

$r = r_e - [1/\alpha] \ln [\xi]$ (eqn 35 from ref [162])

$\xi = (-2a)[b+(b^2 - 4ac)^{1/2}\sin QN]^{-1}$ (eqn 36 [162])

a,b,c = constants defined by the Morse parameters, D, r_e and α, and the total energy, E_{vj}.

E_{vj} = is obtained from equation (6) of ref [162]

p_r = momentum conjugate to r (eqn 5 of ref [162])

$= \pm (2\ m)^{1/2} (a + b\ \xi + c\ \xi^2)^{1/2}$

$Q = QL + l\Delta$

$l = (j\ (j + 1))^{1/2}$ (i.e. the angular momentum in units of $\hbar$)

j = rotational quantum number

$\lambda = M_j/l$

M_j = projection of λ on to the z axis

Δ = couples vibrational phase to angular momentum, l (eqn 26 of ref [162])

$QM = [0 - 2\pi]$

$QN = [0 - 2\pi]$

$QL = [0 - 2\pi]$.

Thus random initial selection of QN, QM, QL and λ completely define the position and conjugate momenta of the rotating Morse oscillator.

Initial Polarization of j vector: PRM

As before the appropriate $\underline{r}$ and $\underline{p}_r$ components must be set equal to zero in order to obtain polarization in the direction of interest.

The remainder of this section deals with the conditions under which the individual components of $\underline{r}$ and $\underline{p}_r$ will be equal to zero, resulting in polarization of the $\underline{j}$ vector.

Recall in the case of x polarization there is no projection of $\underline{j}$ onto either the y or z axes. Therefore m must be equal to zero. As a result, λ is equal 0. Therefore equations (A.62) and (A.63) become

$$r_x = r\ (-\sin Q \sin QM) \tag{A.68}$$

$$p_x = p_r\ (-\sin Q \sin QM) + 1/r\ (-\cos Q \sin QM) \tag{A.69}$$

It is now apparent that the only remaining term related to the diatom's orientation in space is sin QM. Therefore in order for r_x and p_x to be zero, QM must be set to 0 or π. If QM is set equal to zero, j_x will be negative, further, if QM is set equal to π, j_x will be positive.

As in the case of x polarization, y polarization has no projection on to the x or the z axes (i.e. $M_j = 0$) therefore equations (A.64) and (A.65) become:

$$r_y = r \sin Q \cos QM \tag{A.70}$$

$$p_y = pr\ (\sin Q \cos QM) + 1/r\ (\cos Q \cos QM). \tag{A.71}$$

Setting QM equal to $\pi/2$ causes j_y to be negative, setting QM equal to $3\pi/2$ makes j_y positive. It should be noted at this time QN and QL are still selected randomly, since QN determines the vibrational phase of the oscillator and QL determines the oscillator's orientation in the yz plane.

The situation for polarization along the z axis is different from that of x and y polarization. Here, the

projection of $\mathbf{j}$ on to the z axis is equal to the total angular momentum, i.e. $|M_j|=1$ (Fig A.2). Therefore, in this case, λ can have the value 1 or -1. Analysis of equations (A.66) and (A.67) reveals that when λ equal to 1 or -1 both r_z and p_z being 0. It is important to note that both QM and QL are selected randomly since they have no bearing on the values of the r_z and p_z components. If λ is equal to 1, j_z will be positive and if λ is equal to -1 j_z will be negative.

The last case to consider is random orientation in the xy plane, that is when $j_x \neq 0$, $j_y \neq 0$, and $j_z = 0$. This case is important since quantum mechanically only j_z is quantized. When the rotating diatom is randomly oriented in the xy plane, as in the case of x and y polarization, there is no projection of angular momentum on the z axis. Therefore as before λ is equal to 0. However, unlike the x and y polarization cases, the orientation angle QM, along with QN and QL, must be selected randomly. This results in the two terms in equation (A.38) being equal, therefore the z component of $\mathbf{j}$ will be equal to zero.

Coplanar and Collinear Orientation of the Diatom: PRM

In order to achieve a coplanar collision geometry, the criteria for x polarization must be followed. In order to effect a collinear collision geometry, in addition to the coplanar criteria, one must set QL equal to 0 or π. Further, since rotation of the diatom is not possible in the collinear geometry, l must also equal 0.

Analysis of Products:

In four particle systems AB + CD, e.g. OH + H_2, there are several possible products of a reactive collision. In the OH + H_2 --> H_2O + H reaction OH is a spectator bond. The product H_2O can be formed with the addition of either of the H atoms present in the diatomic molecule. Adopting the more general representation, AB+CD, where AB = OH and CD = H_2 allows a general definition of the criteria for determination of products formed. From an analysis of Figure A.4 it is apparent that if the reaction products are ABD + C the interatomic distances x_1, x_4, and x_6 will remain small after the trajectory has been integrated into the region of zero potential, this is termed reaction TYPE C (here TYPE C represents the atom which flies off). If the reaction products are ABC + D the interatomic distances x_1, x_3, and x_5 will all be small, i.e. reaction TYPE D. In the case of no reaction, i.e. the reaction products are AB + CD, x_1 and x_2 are small after integration of the trajectory.

The total cross section, S^R, was calculated by equation (A.44), with its associated error, s_e',

$$s_e' = S^R / (N_r)^{1/2}. \qquad (A.72)$$

Equations (A.72) and (A.45) give similar results.

Fig. A.1 Definition of coordinate system for a 3 body (A + BC) reaction. Both Jacobi coordinates (R,r,γ) and the internuclear distances x_1, x_2 and x_3 are included.

A.1

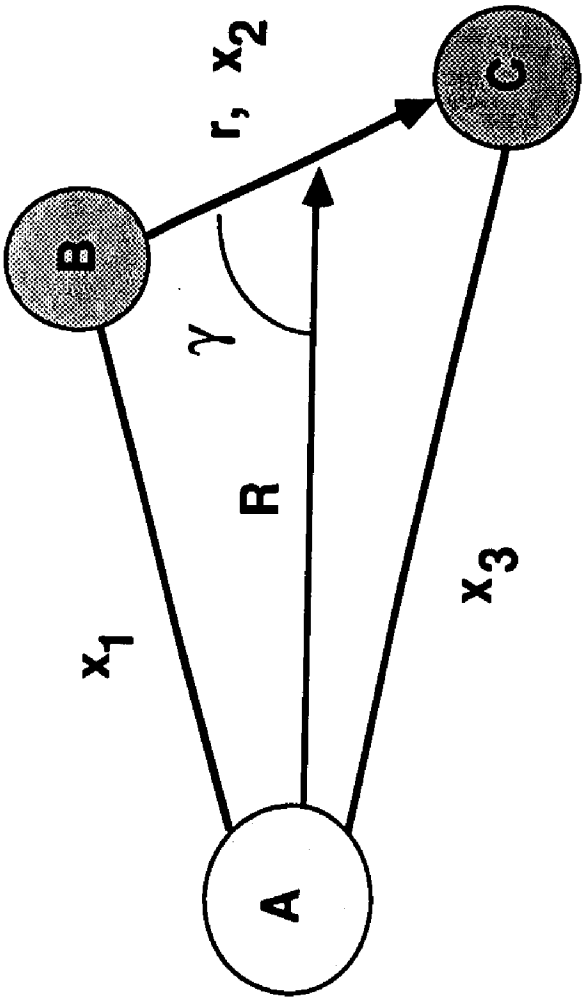

Fig. A.2 Pictorial representations of the polarization of the rotational angular momentum vector of a diatomic molecule.

A.2

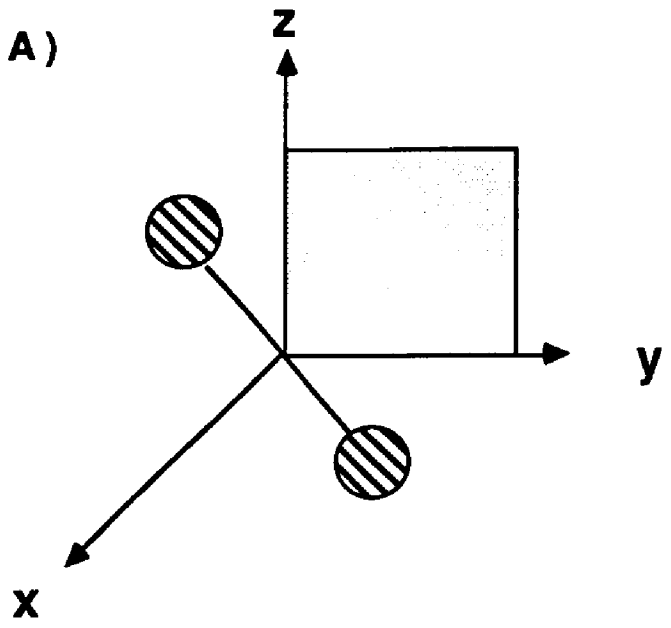

j_x

MOLECULE IN YZ PLANE

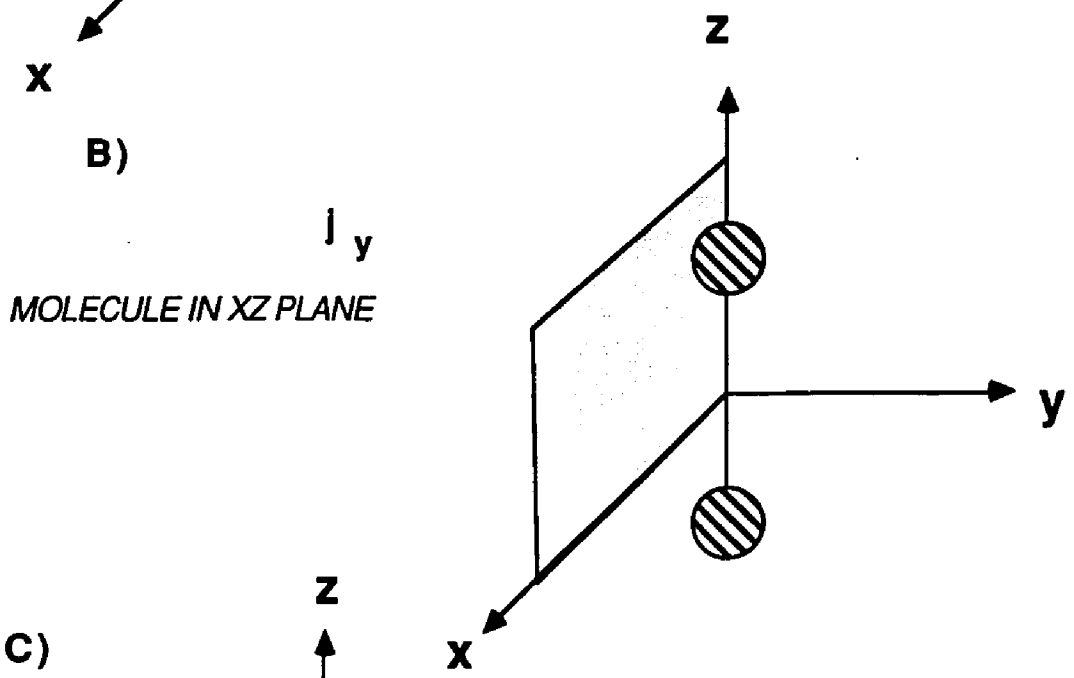

j_y

MOLECULE IN XZ PLANE

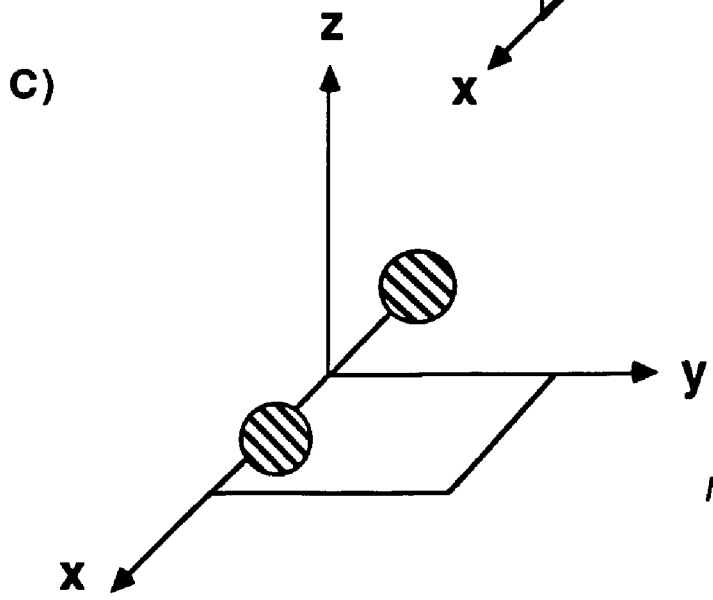

j_z

MOLECULE IN XY PLANE

Fig. A.3 Definition of reagent Jacobi ($\underline{R}$,$\underline{r}$) coordinates and product Jacobi ($\underline{R}_C$,$\underline{r}_C$) coordinates for the 3 body reaction, A + BC --> AB + C.

A.3

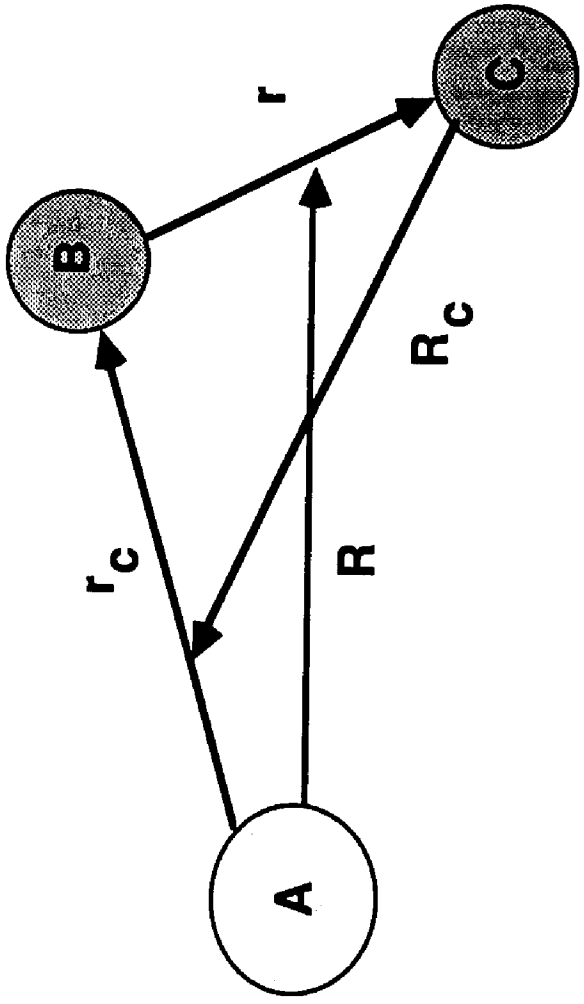

Fig. A.4 Definition of the coordinate system for a 4 body (AB + CD) reaction. Center of mass coordinates, ($\underline{r}_1, \underline{r}_2, \underline{R}$) and the internuclear separations ($x_1, x_2 \ldots x_6$) are both shown.

A.4

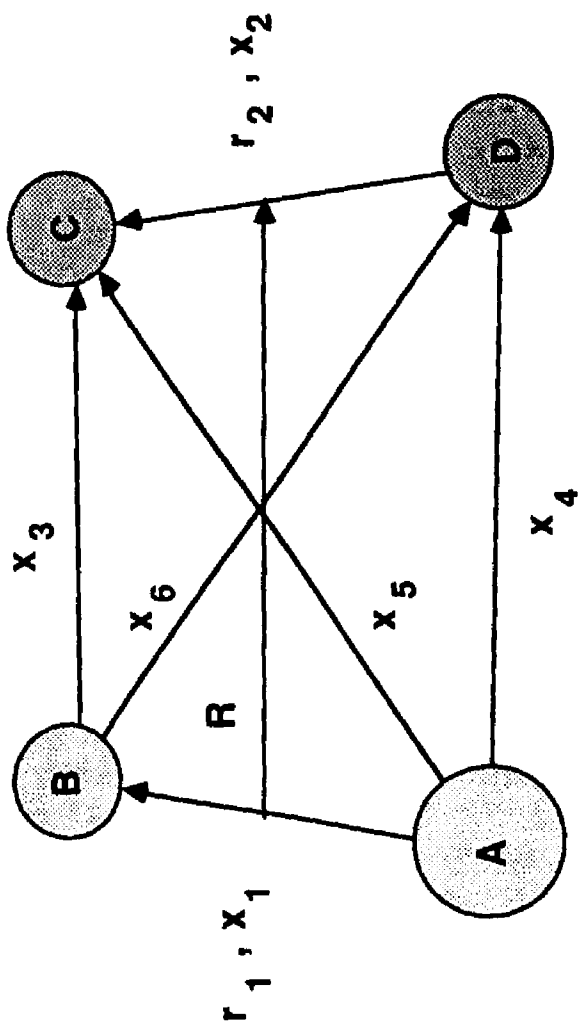

APPENDIX B

SKEWED AND SCALED COORDINATES

Considerable insight into the dynamics of reactive collisions can be obtained from an examination of the potential energy contour diagram for collinear A + BC --> AB + C systems [3,184]. The so-called "skewed and scaled" representation is particularly useful. This representation is explained below.

Consider the collinear geometry A-B-C. There are two independent distances, r_{AB} and r_{BC} ($r_{AC} = r_{AB} + r_{BC}$ in this geometry). The potential energy can be plotted as a contour map $V(r_{AB},r_{BC})$ with the lengths as the usual rectilinear Cartesian axes (see Figure B.1).

Unfortunately, these coordinates are poorly suited to dynamical calculations. To see this, consider the atom, A, to be at rest and well separated from the diatom, BC, whose center of mass is also at rest. It is clear that vibrational motion in the BC diatom will result in a change in the length r_{AB}. Thus, both lengths change, even though plainly only a single mode of motion is involved.

The usual method of removing this difficulty is to separate out the center of mass motion of the entire triatom [100]. The resulting variables are the Jacobi coordinates, (R,r), where $r = r_{BC}$ is the diatom bond length, and R is the

distance from the atom A to the diatom's center of mass. In matrix notation,

$$\begin{pmatrix} R \\ r \end{pmatrix} = \begin{pmatrix} 1 & C/(B+C) \\ 0 & 1 \end{pmatrix} \begin{pmatrix} r_{AB} \\ r_{BC} \end{pmatrix} \qquad (B.1)$$

where A, B, C, denote the masses of atoms A, B, C, respectively.

It is clear that (since r_{AB} must be nonnegative) R is constrained to be greater than or equal to r * B/(B+C). A plot of the potential in these coordinates, V(R,r), is often referred to as "skewed" (see Figure B.2). The "skewing" angle, α, is clearly given by

$$\tan(\alpha) = (B + C)/C \qquad (B.2)$$

It is seen that the rectilinear coordinates (r_{AB},r_{BC}) become appropriate in the limit of B --> ∞.

Visualization of the dynamics of a system in such a coordinate system is complicated by the fact that motion in each of the coordinates is characterized by a different mass: The kinetic energy, T, is given by

$$2T = \mu(dR/dt)^2 + m(dr/dt)^2 \qquad (B.3)$$

where m = BC/(B+C), μ = A(B+C)/M, and M = A + B + C. It is more convenient to have a single mass characteristic of both dimensions. One choice is to prefer μ, and rewrite

$$\begin{aligned} 2T &= \mu[(dR/dt)^2 + m(dr/dt)^2/\mu] \\ &= \mu[(dR/dt)^2 + (dU/dt)^2] \end{aligned} \qquad (B.4)$$

where $U^2 = r^2\ (m/\mu)$ or $U = r(m/\mu)^{1/2}$. The r coordinate is now

said to be "scaled" by the factor $(m/\mu)^{1/2}$.

Another choice, and one which is preferred in the chemical literature, is to scale both the R and r coordinates so that the characteristic mass is unity:

$$2T = (dQ_1/dt)^2 + (dQ_2/dt)^2 \qquad (B.5)$$

By comparison with equation (B.2), it is clear that

$$Q_1 = R\ \mu^{1/2}$$
$$Q_2 = r\ m^{1/2} \qquad (B.6)$$

The length R is scaled by $\mu^{1/2}$; the length r by $m^{1/2}$. The skew angle (Figure B.3) is now given by

$$\tan(\beta) = [(B+C)/C] * (m/\mu)^{1/2}$$
$$= (MB/AC)^{1/2} \qquad (B.7)$$

where the definitions of m and μ have been used. Equation (B.7) has an appealing symmetry: it is obviously invariant to the exchange of the end atoms A <--> C, as it must be. Simple trigonometry yields

$$\sin^2(\beta) = MB/(MB + AC) = MB/[(A+B)(B+C)]$$
$$\cos^2(\beta) = AC/(MB + AC) = AC/[(A+B)(B+C)] \qquad (B.8)$$

where the latter forms once more emphasize the symmetry with respect to A <--> C exchange.

The scaling factors in equation (B.6) can be expressed in terms of the skew angle:

$$Q_1 = R\ \mu^{1/2}$$
$$Q_2 = r\ \mu'^{1/2} \sin(\beta) \qquad (B.9)$$

where $\mu' = C(A+B)/M$ is the reduced mass appropriate to the product rearrangement channel AB + C.

Now from Figure B.4 it can be seen that the scaling factor in the direction parallel to the exit valley is $(\mu')^{1/2}$. We can further compress the information by introducing a scaling ratio

$$s = (\mu'/\mu)^{1/2} = [C(A+B)/A(B+C)]^{/2} \qquad (B.10)$$

which is the ratio of the scaling along the exit valley to that along the entrance valley. A large value of s indicates that the exit valley is elongated compared to the entrance valley, and vice versa.

The skewed and scaled variables, Q_1 and Q_2 are related to the physical lengths, r_{AB} and r_{BC}, via the inverses of equations (B.6) and (B.1):

$$\begin{pmatrix} r_{AB} \\ r_{BC} \end{pmatrix} = \begin{pmatrix} 1 & -C/(B+C) \\ 0 & 1 \end{pmatrix} \begin{pmatrix} R \\ r \end{pmatrix}$$

$$= \begin{pmatrix} (1/u)^{1/2} & -C/(B+C)u^{1/2} \\ 0 & (1/m)^{1/2} \end{pmatrix} \begin{pmatrix} Q_1 \\ Q_2 \end{pmatrix} \qquad (B.11)$$

As was stated previously, analysis of the skewed and scaled collinear potential energy surfaces can yield insight into the dynamics of the reaction of interest. For example, consider the following mass combinations; **L + HH**, **H + LL**, **H + HL**, **H + LH**, and **L + HL**. (where **L** is a light atom with mass 1 a.m.u. and **H** is a heavy atom with mass 20 a.m.u.). These mass combinations have the following values for s and β;

L + HH **H + LL** **H + HL** **H + LH** **L + HL**

s	3.24	0.719	0.308	1.00	1.00
β(deg)	81.1	46.4	81.1	17.8	87.3

For instance, if one were interested in the two mass combinations, **H + HL** and **H + LH**, analysis of the skewing angle, β, immediately reveals that the skew angle is much smaller for the latter. In order for reaction to occur, the mass moving on the skewed and scaled potential must negotiate the bend from the entrance valley into the exit valley. In the case of the small skew angle it will have to make a much more abrupt change of direction than if β is large. Therefore it is more difficult to transfer the light atom than the heavy atom. In general, the smaller β is, the more difficult it is to pass from the entrance valley into the exit valley. Other interesting points include; 1) When atom A and atom C are identical the scaling factor, s, is 1.0 as expected (both entrance and exit channels are identical). and 2) Analysis of the mass combination **L + HL** reveals that is very easy to transfer a heavy atom from a light atom to a light atom (note the skewing angle is very close to 90°).

Plotter Programs

The FORTRAN programs used in this work to generate skewed, V(R,r), and skewed and scaled, $V(Q_1,Q_2)$, representations of LEPS surfaces are know as PLEPSCM.FOR and PSCALED.FOR, respectively. Both are included in this Appendix.

Alternative Scaling Methods

The scaling outlined above is specifically designed for

the collinear reaction A + BC --> AB + C, or its reverse. It does not allow the possibility of the rearrangement channel A + BC --> AC + B. Other scaling schemes have been developed which are more "democratic" in allowing one to consider all possible rearrangement channels equally.

Marcus [53] uses the mass, u, where

$$u = (ABC/M)^{1/2}. \qquad (B.12)$$

Clearly, u is invariant to any exchange of labels, and is therefore equally useful for all rearrangement channels. The kinetic energy is given by

$$2T = u\,[(dx/dt)^2 + (dX/dt)^2] \qquad (B.13)$$

where

$$X = R\,(f)^{-1}$$

$$x = r\,f$$

$$f = [BCM/A(B+C)^2]^{1/4} \qquad (B.14)$$

direct substitution of (B.14) into (B.13) recovers (B.3).

Fig. B.1 Schematic representation of a LEPS potential energy surface in rectilinear coordinates, (r_{AB}, r_{BC}).

B.1

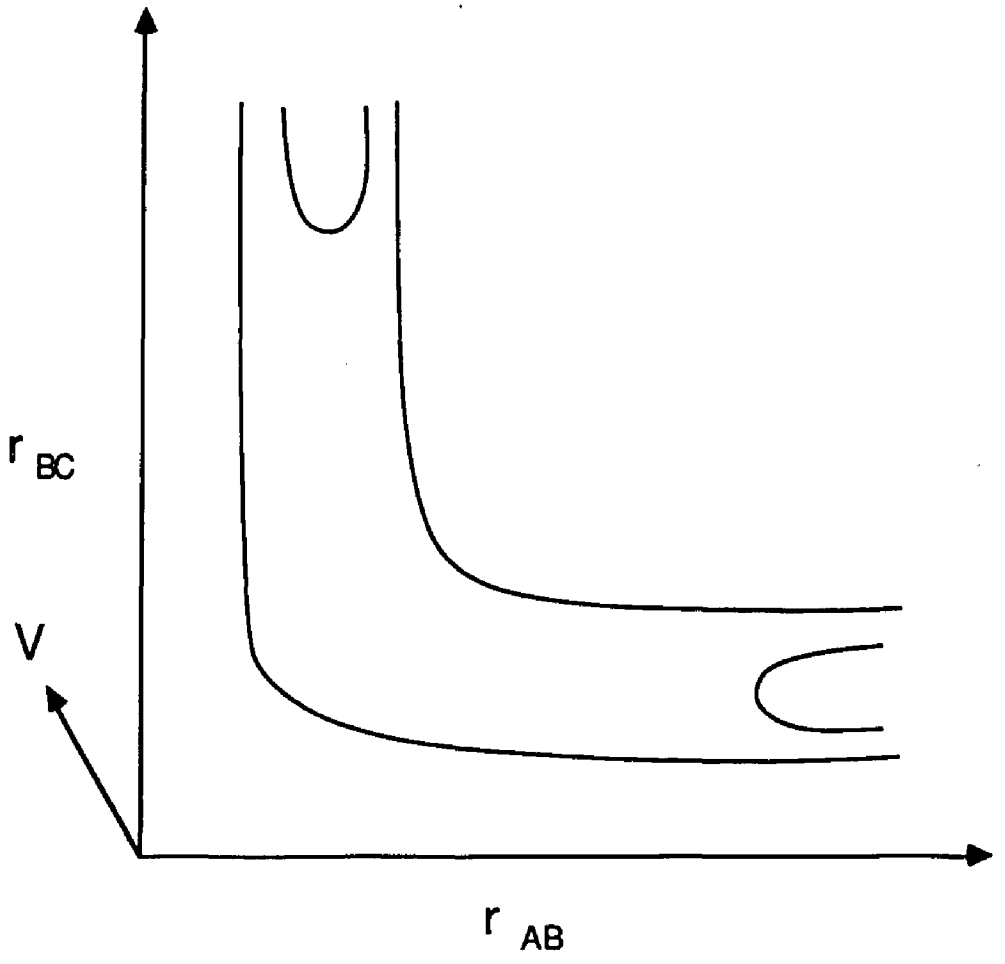

Fig. B.2 Schematic representation of a LEPS potential energy surface in skewed coordinates (R,r). The angle α is the skew angle.

B.2

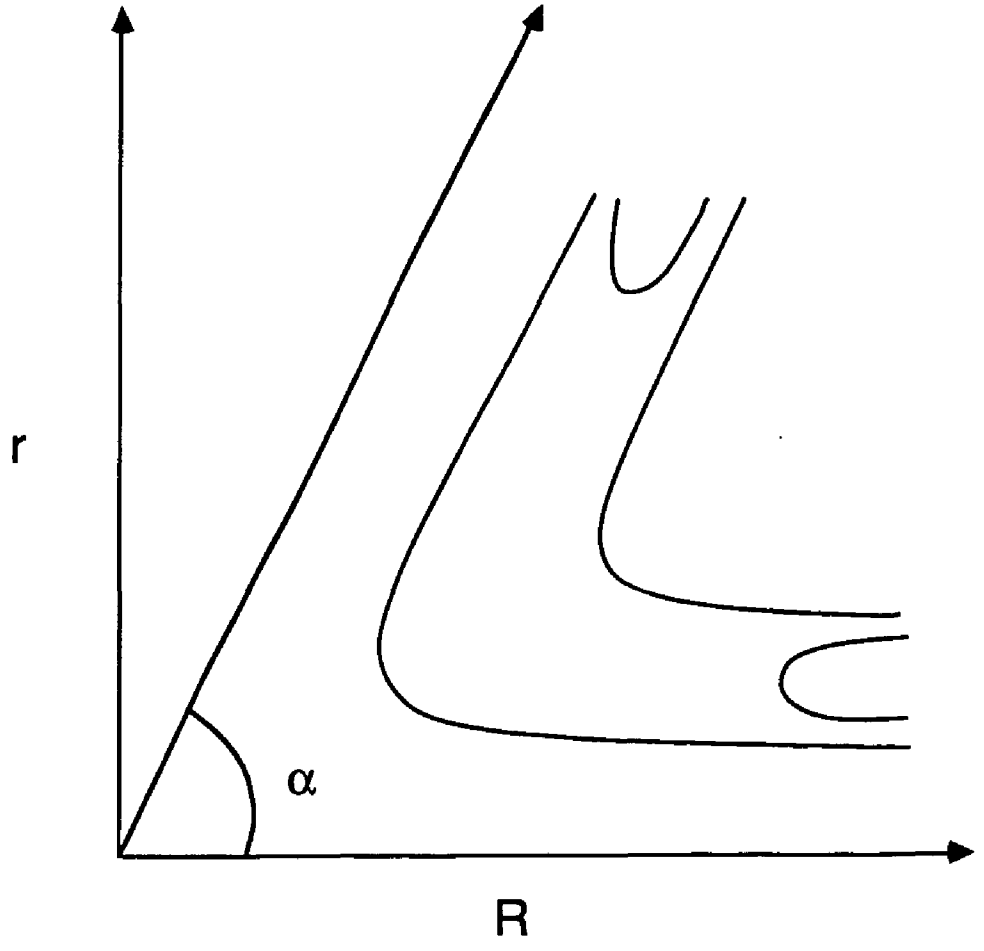

Fig. B.3 Schematic representations of a LEPS potential energy surface in skewed and scaled coordinates, (Q_1,Q_2). The skew angle is β.

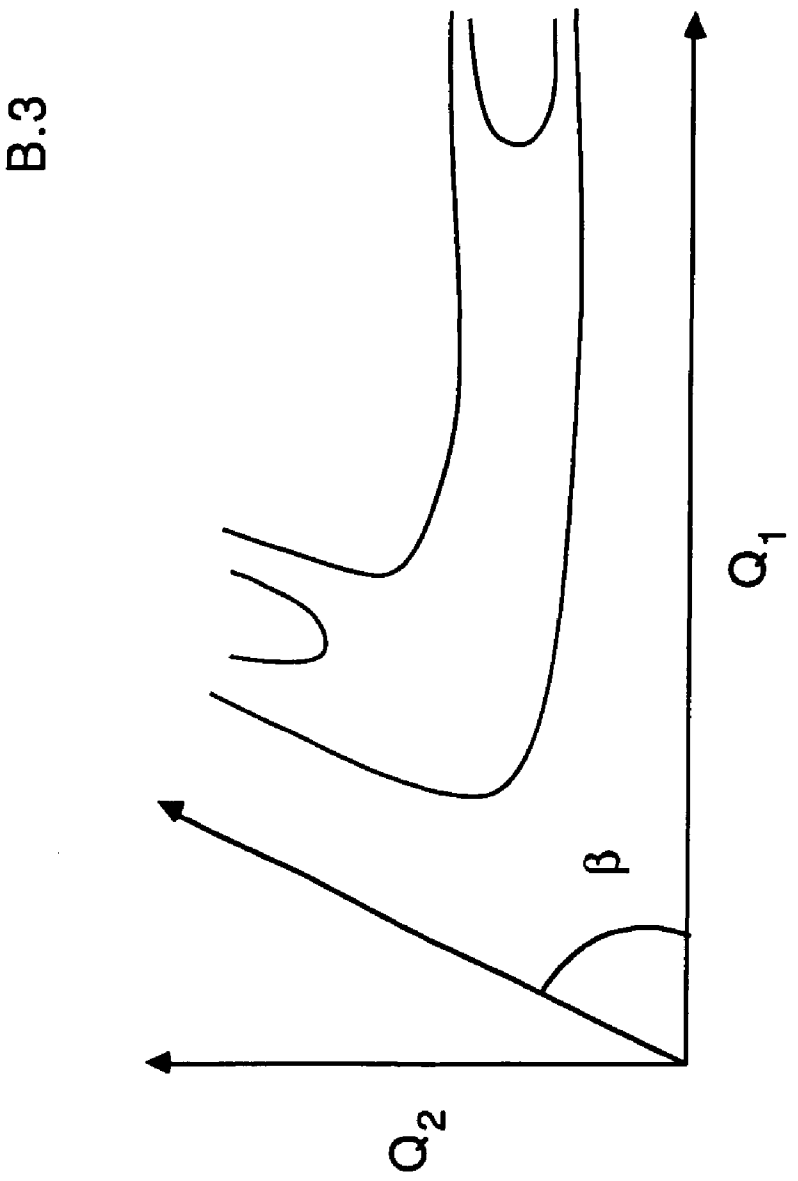
B.3
Q_1
Q_2
β

Fig. B.4 Mathematical definitions of Q_1 and Q_2.

B.4

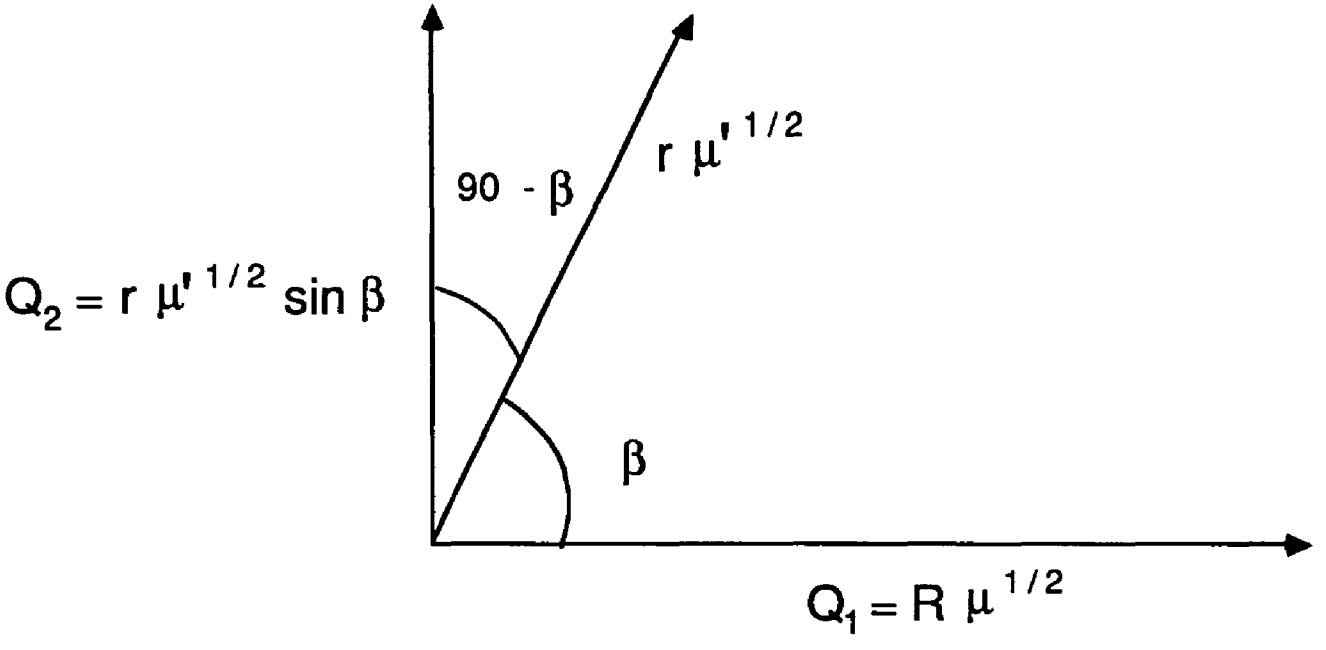

```
C
C               PLEPSCM.FOR
C
c
C       PROGRAM PLOTS  LEPS TYPE SURFACES IN
C         IN "SKEWED" COORDINATES
C            ADAPTED FROM PLEPSCL.FOR
c
C          PLOTTER CALLS ARE FOR CALCOMP PLOTTER
C
C
C        ARRAY SIZES MUST BE CONSISTENT WITH THOSE IN TOPOG.
C        NPTS MUST BE CONSISTENT WITH ARRAY SIZE!
C
C          LINK INFO:
C              TOPOG.FOR      CONTOUR PROGRAM
C              LEPSPOT.FOR, VFHH.FOR     ANY 3 BODY LEPS POTENTIAL
C
C
C
C            CALL TO V() MUST BE CONSISTENT WITH POTENTIAL
C                (LEPS) PROGRAM.
c             NOTE:
C               MASSES (AMA, AMB, AND AMC) MUST BE CHANGED
C                IN DATA STATEMENT FOR SYSTEM OF INTEREST.
C               DIATOMIC BOND LENGTH, RE2, MUST ALSO BE CHANGED
C                  DEPENDING ON SYSTEM OF INTEREST
C
C           RE2 = 1.40142 IS FOR H2
C

      dimension x(80),y(80),pot(80,80),cntr(20),
     #wka(80),wkb(80)
        DIMENSION Z(3)

C             ARRAY DEFINTIONS:
C               X(), Y() = PLOTTER COORDINATES IN INCHES
C               POT() = HOLDS THE VALUE OF THE POTENTIAL AT X(),Y()
C               CNTR() = HOLDS THE CONTOUR VAULES
C               WKA(), WKB() = WORK ARRRAYS USED IN TOPOG
C               Z() = HOLDS THE 3 INTERNUCLEAR DISTANCES
C
        data xmin,xmax,ymin,ymax/0.0,6.0,0.0,6.0/
        data npts/80/
C          MASSES FOR F + H2
         DATA AMA,AMB,AMC/19.,1.,1./
C          MASSES FOR O + HCl
c
c          DATA AMA,AMB,AMC/16.,1.,35.5/
           DATA PI/3.1415927/
c           GAMMA IS THE ANGLE BETWEEN R AND r
c
           DATA GAMMA/0./
        data re2/1.40142/
C
C           RE2 = 2.40942 IS FOR HCL
C
c       data re2/2.40942/
C         NPCHIOCE:
C           DETERMINES POTENTIAL:
```

```
C             INPUT 1 = F+H2 SE* POTENTIALS
C             INPUT 0 = OTHER LEPS TYPE POTENTIALS
C
c          NSE:
C               NSE = INPUT INTEGER OF SE* POTENTIAL DESIRED
        common/pchoice/nse

            TM = AMA + AMB + AMC
            SINB = SQRT(AMB*TM/((AMA+AMB)*(AMB+AMC)))
            BETA = ASIN(SINB)
            BETADG = BETA*180./PI
          xlp = xmax - xmin
          ylp = ymax - ymin

           COSG = COS(GAMMA)
           SING = SIN(GAMMA)

          write(6,80)
80        format(' INPUT THE INTEGER 1 FOR F+H2 P-S TYPE POTENTIALS')
          read(5,81)npchoice
81        format(i1)

          if(npchoice.eq.1)then
            write(6,83)
83          format(' INPUT THE INTEGER SE* VALUE YOU WISH TO RUN')
            read(5,81)nse
          endif

        write(6,60)
60      format(' input a value for BR (x)  min')
        read(5,50)r1min
50      format(1f10.5)
        write(6,61)
61      format(' input a value for BR (x) max')
        read(5,50)r1max
        write(6,62)
62      format(' input a value for r2 (y) min')
        read(5,50)r2min
        write(6,63)
63      format(' input a value for r2 (y) max')
        read(5,50)r2max

         dx = (xmax - xmin)/(npts - 1)
         dy = (ymax - ymin)/(npts - 1)
        dr1=(r1max-r1min)/(npts - 1)
        dr2=(r2max-r2min)/(npts - 1)
        DELTA1=(R1MAX-R1MIN)/(XMAX-XMIN)
        DELTA2=(R2MAX-R2MIN)/(YMAX-YMIN)

c
c       CALCULATING THE ZERO VALUE OF THE POTENTIAL. (TO BE
C         SUBTRACTED OFF ALL POT VALUES.)
C

          R1 = 10.0
          R2 = RE2
          R3 = R1+R2


          z(1) = r1
          z(2) = r2
```

```
        z(3) = r3

           n = 3
        deriv1 = .false.
c
c
C
C            CALL IS FOR STANDARD LEPS TYPE PROGRAMS.
C               EG. OHCL,HOH

c          call v(z,pot,dv1,dv2,dv3,n)

C
C          CALL IS FOR F+HH TYPE LEPS POTENIALS.
C
        call v(z,ea,epot,dv1,dv2,dv3)
C        zero = epot

         write(6,777)zero
777       format(' zero = ',e20.10)


      do 100 ix=1,npts
      x(ix)=xmin+(ix-1)*dx
      BR=r1min+(ix-1)*dr1
        do 200 iy=1,npts
        y(iy)=ymin+(iy-1)*dy
        r2=r2min+(iy-1)*dr2
            CHECK = R2*(AMB/(AMB+AMC))
           IF(BR.LT.CHECK)GOTO 200
         R2CML = (AMC/(AMB+AMC))*R2
         R2CMS = (AMB/(AMB+AMC))*R2
                R1 = SQRT(BR**2 + R2CML**2 - 2.*R2CML*BR*COSG)
                DELTA = PI - GAMMA
                R3 = SQRT(R2CMS**2 + BR**2 -2.*R2CMS*BR*COS(DELTA))

C          write(6,77)gamma,DELTA
77         format(' g,DEL',2f15.6)
C          write(6,78)r1,r2,br,r3,R2CML
78          format(' r1,r2,br,r3,R2CML',5f12.4)
         z(1)=r1
         z(2)=r2
          z(3)=r3
        deriv1=.false.
c
c        June 14,1988
c
c          change call for O + HCL
c

           n = 3
c        call v(z,epot,dv1,dv2,dv3,n)
         CALL V(Z,EA,EPOT,DV1,DV2,DV3)
       pot(ix,iy)=epot - zero
     pot(ix,iy)=pot(ix,iy)/3.6752e-2
c
C      THE POTENTIAL IS PLOTTED IN eV.
C
c
200     continue
100   continue
```

```
C
C      FILLED UP GRID WITH POTENTIAL VALUES
C
      write(6,66)
66    format(' input the # of contours you want drawn')
      read(5,52)ncntr
52    format(i2)
      write(6,67)
67    format(' input the values of the contours by line')
      read(5,53) (cntr(i),i=1,ncntr)
53    format(f10.5)

      call plots(0,0,9)
       call plot(1.0,1.0,-3)
       CALL AXIS(0.0,0.0,'BR  (AU)',-7,xlp,0.,rlmin,DELTA1)
       CALL AXIS(0.0,0.0,'R2  (AU)',7,ylp,BETADG,r2min,DELTA2)
      call topog(pot,x,y,wka,wkb,npts,npts,cntr,ncntr)
c      call traj
      call plot(0.0,0.0,999)
      stop
      end
```

```
      subroutine topog(v,x,y,ra,rb,m,n,cntr,ncntr)
c
c      v is a mxn input array whose values are represented by
c      contour lines.
c          ra and rb must be dimensioned at least m in the calling
c      program
c      x and y arrays are the values at which v is calculated
c      contour values are contained in the array cntr
c
       common/axcom/sx,firstx,deltax,sy,firsty,deltay
       dimension v(80,80),x(80),y(80),ra(80),rb(80),CNTR(50)
       rb(1)=v(1,1)
       do 27 j=2,m
 27    rb(j)=v(j,1)
       do 118 k=2,n
       do 30 j=1,m
        ra(j)=rb(j)
 30     rb(j)=v(j,k)
        do 118 j=2,m
        assign 112 to l
        rr=ra(j)
       xx=x(j)
       yy=y(k-1)
  37   rl=rr
      xl=xx
      yl=yy
      if(rl-ra(j-1))41,40,40
40    if(rl-rb(j))42,50,50
41    rl=ra(j-1)
      xl=x(j-1)
      yl=y(k-1)
      goto 40
42    rl=rb(j)
      xl=x(j)
      yl=y(k)
50    rs=rr
      xs=xx
      ys=yy
      if(rs-ra(j-1))52,52,53
52    if(rs-rb(j)) 60,60,54
53    rs=ra(j-1)
      xs=x(j-1)
      ys=y(k-1)
      goto 52
54    rs=rb(j)
      xs=x(j)
      ys=y(k)
60    rm=rr
      xm=xx
      ym=yy
      if(rm-rs)62,62,61
 61   if(rm-rl) 70,62,62
 62   rm=ra(j-1)
      xm=x(j-1)
      ym=y(k-1)
      if(rm-rs)64,64,63
63    if(rm-rl) 70,64,64
 64   rm=rb(j)
      xm=x(j)
      ym=y(k)
```

```
 70   continue
      do 100 icntr=1,ncntr
      rc=cntr(icntr)
      if(rc.ne.rm) goto 91
      if(rm.ne.rs) goto 91
      if(r1.eq.rm)goto 100
91    if(rc-rs)100,95,92
92    if(rc-rm) 96,93,94
93    xpa=xm
      ypa=ym
      goto 99
94    if(rc-r1) 106,103,110
103   xpa=x1
      ypa=y1
      goto 99
106   q=(rc-rm)/(r1-rm)
      xpa=xm-q*(xm-x1)
      ypa=ym-q*(ym-y1)
      goto 99
95    q=0.
      goto 97
 96   q=(rc-rs)/(rm-rs)
 97   xpa=xs-q*(xs-xm)
      ypa=ys-q*(ys-ym)
 99   q=(rc-rs)/(r1-rs)
      xpb=xs-q*(xs-x1)
      ypb=ys-q*(ys-y1)
      if(rc) 10115,10116,10116
10115 xpb1=.5*(xpa+xpb)
      ypb1=.5*(ypa+ypb)
      if(abs(xpa-xpb1)-1.e-2)5001,5002,5002
5001  if(abs(ypa-ypb1)-1.e-2)100,5002,5002
5002  call plot(xpa,ypa,3)
      call plot(xpb1,ypb1,2)
       goto 100
10116  if(abs(xpa-xpb)-1.e-2)5003,5004,5004
5003   if(abs(ypa-ypb)-1.e-2)100,5004,5004
5004   call plot(xpa,ypa,3)
       call plot(xpb,ypb,2)
100    continue
110    goto 1,(112,118)
112    assign 118 to 1
       rr=rb(j-1)
       xx=x(j-1)
       yy=y(k)
       goto 37
118    continue
       return
       end
```

```
C                PSCALED.FOR
C
c
C      PROGRAM PLOTS  LEPS TYPE SURFACES IN
C      SKEWED AND SCALED COORDINATES.
C           ADAPTED FROM PLEPSCM.FOR
C
C         CALL'S TO PLOTTER ROUTINES ARE FOR CALCOMP PLOTTER
C
C          SKEWED AND SCALED DEFINITIONS TAKEN FROM
C           LEVINE AND BERNSTEIN p. 165
c
c
C
c          NEEDED AT LINK:
C              TOPOG.FOR         WRITES CONTOURS
C              LEPSPOT.FOR     LEPS POTENTIAL (ANY 3 BODY POTENTIAL)
C
C       ARRAY SIZES MUST BE CONSISTENT WITH THOSE IN TOPOG.
C       NPTS MUST BE CONSISTENT WITH ARRAY SIZE!
C
C
C           CALL TO V  MUST BE CONSISTENT WITH POTENTIAL
C               (LEPS) PROGRAM.
c            NOTE:
C              MASSES (AMA, AMB, AND AMC) MUST BE CHANGED
C               IN DATA STATEMENT FOR SYSTEM OF INTEREST.
c               RE2 MUST BE APPROPRIATE FOR BC DIATOM
C
C          RE2 = 1.40142 IS FOR H2
C

      dimension x(80),y(80),pot(80,80),cntr(20),
     #wka(80),wkb(80)
        DIMENSION Z(3)
C           ARRAY DEFINITIONS:
C            x , y  = plotter coordinates in inches
c            pot = contains the value of the potential
c                        at x ,y .
c            wka , wkb  = work arrays needed by topog
c            cntr  = holds contour values
C            Z    = HOLDS THE 3 INTERNUCLEAR DISTANCES

        data xmin,xmax,ymin,ymax/0.0,8.0,0.0,8.0/
        data npts/80/
C         MASSES FOR O + HCl
c        data ama,amb,amc/16.,1.,35.5/
c         MASSES FOR F + H2
         DATA AMA,AMB,AMC/19.,1.,1./
          DATA PI/3.1415927/
C         GAMMA IS THE ANGLE BETWEEN R AND r (denoted BR AND R2
C          IN THE PROGRAM). GAMMA = 0. IS FOR THE COLLINEAR
C          GEOMETRY.
          DATA GAMMA/0.0/
        data re2/1.40142/
C
C          RE2 = 2.40942 IS FOR HCL
C
c       data re2/2.40942/
C        NSE IS FOR F + H2 POTENTIALS. IT DETERMINES WHICH
```

```
      x(ix)=xmin+(ix-1)*dx
      BRS=r1min+(ix-1)*dr1
        do 200 iy=1,npts
        y(iy)=ymin+(iy-1)*dy
        R2S=r2min+(iy-1)*dr2
         BR = BRS/AS
         R2 = R2S/(BS*SINB)
c         write(6,605)br,r2,brs,r2s
605       format(' br,r2  brs r2s',4f10.4)
         R2CML = (AMC/(AMB+AMC))*R2
         R2CMS = (AMB/(AMB+AMC))*R2
                R1 = SQRT(BR**2 + R2CML**2 - 2.*R2CML*BR*COSG)
                DELTA = PI - GAMMA
                R3 = SQRT(R2CMS**2 + BR**2 -2.*R2CMS*BR*COS(DELTA))

         z(1)=r1
         z(2)=r2
          z(3)=r3
        deriv1=.false.
c
c
c


           n = 3
C          CALL V(Z,EPOT,....) IS FOR LEPS POTENTIALS
C             CONTAINED IN LEPSPOT.FOR

c         call v(z,epot,dv1,dv2,dv3,n)

C           CALL V(Z,EA,....) IS FOR F+H2 SEC TYPE POTENTIALS
          CALL V(Z,EA,EPOT,DV1,DV2,DV3)
         pot(ix,iy)=epot - zero
        if(r2.gt.br*2.) then
         pot(ix,iy)=0.0
        endif
      pot(ix,iy)=pot(ix,iy)/3.6752e-2
c
C     THE POTENTIAL IS PLOTTED IN eV.
c
200     continue
100   continue
c     filled up grid with potential values
      write(6,66)
66    format(' input the # of contours you want drawn')
      read(5,52)ncntr
52    format(i2)
      write(6,67)
67    format(' input the values of the contours by line')
      read(5,53) (cntr(i),i=1,ncntr)
53    format(f10.5)

      call plots(0,0,10)
       call plot(1.0,1.0,-3)
       CALL AXIS(0.0,0.0,'BR (AU)',-7,xlp,0.,r1min,DELTA1)
       CALL AXIS(0.0,0.0,'R2 (AU)',7,ylp,betadg,r2min,DELTA2)
      call topog(pot,x,y,wka,wkb,npts,npts,cntr,ncntr)
      call plot(0.0,0.0,999)
      stop
      end
```

```
C         SE* SURFACE YOU WILL BE PLOTTING. * CAN EQUAL 1,2
C          3,4, OR 5.
          common/pchoice/nse


C         SKEWING AND SCALING VARIABLES
C           LEVINE AND BERNSTEIN NOTATION = PROGRAM NOTATION
C                 a = as
c                 b = bs
c                 M = tm
c                 beta = beta
            tm = ama + amb + amc
            as = sqrt(ama*(amb+amc)/tm)
            bs = sqrt(amc*(ama+amb)/tm)
            sinb = sqrt(amb*tm/((ama+amb)*(amb+amc)))
            beta = asin(sinb)
            betadg = beta*180./pi
          xlp = xmax - xmin
          ylp = ymax - ymin

           COSG = COS(GAMMA)
c            NPCHOICE = 1 TO RUN SE* TYPE POTENTIALS
C            NPCHOICE = 0 FOR OTHER LEPS TYPE SURFACES
          write(6,80)
80        format(' INPUT THE INTEGER 1 FOR F+H2 P-S TYPE POTENTIALS')
          read(5,81)npchoice
81        format(i1)

          if(npchoice.eq.1)then
            write(6,83)
83          format(' INPUT THE INTEGER SE* VALUE YOU WISH TO RUN')
            read(5,81)nse
          endif

        write(6,60)
60      format(' input a value for BR (SCALED) (x)  min')
        read(5,50)rlmin
50      format(1f10.5)
        write(6,61)
61      format(' input a value for BR (SCALED) (x) max')
        read(5,50)rlmax
        write(6,62)
62      format(' input a value for r2 (scaled) (y) min')
        read(5,50)r2min
        write(6,63)
63      format(' input a value for r2 (SCALED) (y) max')
        read(5,50)r2max

         dx = (xmax - xmin)/(npts - 1)
         dy = (ymax - ymin)/(npts - 1)
        dr1=(r1max-r1min)/(npts - 1)
        dr2=(r2max-r2min)/(npts - 1)
        DELTA1=(R1MAX-R1MIN)/(XMAX-XMIN)
        DELTA2=(R2MAX-R2MIN)/(YMAX-YMIN)


C
C         LOOPING ON SCALED COORDINATES (X,Y AND BR,R2)
C
C
        do 100 ix=1,npts
```

APPENDIX C

ATOMIC UNITS

Throughout this work atomic units have been used. This was because atomic units are the most convenient unit for dealing with problems involving atoms and molecules, in that they avoid the huge and tiny exponents that are encountered in computations involving more conventional units, e.g. SI. This is a major concern when dealing with machine (computer) computation where the storage of very small numbers may lead to significant roundoff error. This is true with one exception, the mass unit which is most often used is the atomic mass unit, amu, that is 1/12 the mass of Carbon (not the atomic unit of mass). In this work, for the sake of simplicity, the mass of hydrogen is approximated as 1 amu instead of the actual value of 1.00091 amu.

What follows is a brief description of atomic units, a sample calculation, as well as some of the more frequently used conversion factors.

Definitions

Three quantities have been specified as basic, e, h, and m, and the other quantities are derived from them (where e is charge on the electron, $\hbar$ is Planck's constant divided by 2π, and m_e is the mass of the electron [164]. The atomic unit of length is the bohr, denoted a_o. The bohr radius is defined as

the mean distance of the hydrogen atom electron in its innermost orbit from the H nucleus. It is obtained from the relationship

$$r = n^2 \epsilon_o h^2 / \pi m_e e^2 Z \qquad (C.1)$$

where ϵ_o = permittivity in a vacuum

= 8.854187(-12) $J^{-2} C^{-2} m^{-1}$

h = Planck's constant

= 6.626176(-31) J-s

n = radial quantum number (n = 1 for lowest orbit)

Z = atomic number (Z = 1 for hydrogen

m_e = 9.10953(-31) kg

e = 1.602189(-19) C

Substitution of these values into equation (C.1) yields the bohr radius, r = 5.2917(-11) meters = 0.52917 Ang = 1 a_o.

The atomic unit of energy is a hartree, au. It is defined as twice the energy of the ground state hydrogen atom. It can be calculated using the relationship

$$E_n = - me Z^2 e^4 / 8 \epsilon_o^2 n^2 h^2 \qquad (C.2)$$

where all the variables have been previously defined. For the ground state hydrogen atom E_1 = 2.1799(-18) J = 13.6069 eV = 13.6069 rydbergs. Therefore, since 1 rydberg = 1/2 hartree, one atomic energy unit is equal to 27.212 eV.

The atomic unit of mass is equal to the mass of an electron, 1 au(mass) = 9.1095(-31) kg. Therefore one a.m.u. or one proton having mass 1.6606(-27) kg is equivalent to 1832 au (mass).

Finally one atomic time unit is equal to 2.4187(-17) s and h is equal to 1.0. These results are summarized in Table C.1.

Sample Calculation

Rotational Energy Levels for H_2:

Rotational energy levels are given by $E_j = Bj(j+1)$

where $B = \hbar^2/2\ \mu\ r_e^2$

now, $\mu = 1*1/(1+1)$ amu = 0.5 * 1823 au(mass)

r_e = 0.7408 Ang = 1.40 a_o

therefore

B = 2.807(-4) au(energy) = 7.638(-3) eV.

Energy Conversions

	kJ/mol	eV	cm^{-1}	au
kJ/mol	1	1.036(-2)	83.61	3.807(-4)
eV	96.49	1	8066	3.675(-2)
cm^{-1}	1.196(-2)	1.2398(-4)	1	4.556(-6)
au	2627	8.617(-5)	0.6949	1

Table C.1

ATOMIC UNIT (au)		
length	=	0.52917 Ang
mass	=	9.1095(-31) kg
time	=	2.4187(-17) s
energy	=	27.212 eV
$\hbar$	=	1.0

LIST OF REFERENCES

1. J.O. Hirschfelder, C.F. Curtiss, and R.B. Bird, "Molecular Theory of Gases and Liquids", John Wiley and Sons, Inc., NY, 1954

2. "Atom-Molecule Collision Theory. A Guide for the Experimentalist.", ed. R.B. Bernstein, Plenum Press, NY, 1979

3. R.D. Levine and R.B. Bernstein, "Molecular Reaction Dynamics and Chemical Reactivity",, Oxford University Press, NY, 1987

4. M.S. Child, "Molecular Collision Theory", Academic Press, NY, 1974

5. "Theory of Chemical Reaction Dynamics", Volume I-IV, ed. M. Baer, CRC Press, Inc., Boca Raton Florida, 1985

6. M. Kneba and J. Wolfrum, Ann. Rev. Phys. Chem., 31 (1980) 47

7. S. Leone, Ann. Rev. Phys. Chem., 35 (1985) 109

8. J.C. Polanyi, Acc. Chem. Res., 5 (1972) 161

9. J.C. Polanyi, Angew. Chem. Int. Ed. Eng., 26 (1987) 952

10. B.A. Hodson and J.C. Polanyi, J. Chem. Phys., 55 (1971) 4745

11. M. Karplus, R.N. Porter, and R.D. Sharma, J. Chem. Phys., 43 (1965) 3259

12. L.M. Raff and D.L. Thompson, in ref 5, Volume III, p1, p42-47

13. D.G. Truhlar and J.T. Muckerman, in ref 2, p505

14. N. Sathyamurthy, Chem. Rev., 83 (1983) 601

15. M. Hoffmeister, L. Potthast, and H.J. Loesch, Chem. Phys., 78 (1983) 369.

16. W. Grote, M. Hoffmeister, R. Schleysing, H. Zerhau-Dreihoefer and H.J. Loesch, in "Selectivity in Chemical Reactions", ed J.C. Whitehead, Kluwer, 1988, p 47.

17. R.I. Altkorn, F.E. Bartoszek, J. DeHaven, G. Hancock, D.S. Perry, and R.N. Zare, Chem. Phys. Lett., 98 (1983) 212.

18. R. Zhang, D.J. Rakestraw, K.G. McKendrick, and R.N. Zare, J. Chem. Phys., 89 (1988) 6283.

19. D.J. Rakestraw, K.G. McKendrick, and R.N. Zare, J. Chem. Phys., 87 (1987) 7341.

20. H. Jalink, F. Harven, D. van den Ende, and S. Stolte, Chem. Phys., 108 (1986) 391

21. C.A. Boonenberg and H.R. Mayne, Chem. Phys. Lett., 108 (1984) 67

22. H.R. Mayne and S.K. Minick, J. Phys. Chem., 91 (1987) 1400.

23. N. Sathyamurthy and J.P. Toennies, Chem. Phys. Lett., 143 (1988) 323

24. A. Persky and M.Broida, J. Chem. Phys., 81 (1984) 4352.

25. H. Kornweitz, M. Broida, and A. Persky, J. Phys. Chem., 93 (1989) 251.

26. B. Amaee, J.N.L. Connor, J.C. Whitehead, W. Jakubetz, and G.C. Schatz, Faraday Disc. Chem. Soc., 84 (1987) 387.

27. J.M. Alvarino and A. Lagana, Chem. Phys. Lett., 144 (1988) 588.

28. M. Menendez, L. Banares, A. Gonzalez-Urena, and J.C. Whitehead, J. Chem. Soc. Faraday Trans. 2, 84 (1988) 1765.

29. H.R. Mayne, J. Phys. Chem., 92 (1988) 6289

30. H. Loesch, Chem. Phys., 104 (1986) 213.

31. H. Loesch, Chem. Phys., 112 (1987) 85.

32. L.S. Rodberg and R.M. Thaler, "Introduction to the Quantum Theory of Scattering", Academic Press, NY, 1967, p 278-320

33. A.M. Arthurs and A.Dalgarno, Royal Soc. Proc. Series A, 256 (1960) 540

34. R.B. Bernstein, A. Dalgarno, Sir H. Massey, and I.C. Percival, Royal Soc. Proc. Series A, 274 (1963) 427

35. G.C. Schatz and A. Kuppermann, J. Chem. Phys., 65 (1976) 4642

36. R.N. Zare, "Angular Momentum: Understanding Spatial Aspects in Chemistry and Physics", John Wiley and Sons, NY, 1988, p 43-65

37. A. Kuppermann and G.C. Schatz, J. Chem. Phys., 62 (1975) 2502

38. G.C. Schatz and A.Kuppermann, J. Chem. Phys., 65 (1976) 4668

39. A.B. Elkowitz and R.E. Wyatt, J. Chem. Phys., 62 (1975) 2504

40. A.B. Elkowitz and R.E. Wyatt, J. Chem. Phys., 63 (1976) 702

41. R.B. Walker, E.B. Stechel, and J.C. Light, J. Chem. Phys., 69 (1978) 2922

42. F. Webster and J.C. Light, J. Chem. Phys., 90 (1989) 265, 300.

43. M. Zhao, M. Mladenovic, D.G. Truhlar, D.W. Schwenke, Y. Sun, D.J. Kouri, and N.C. Blais, J. Am. Chem. Soc., 111 (1989) 852.

44. "The Theory of Chemical Reaction Dynamics", ed. D.C. Clary, Reidel, Dordrecht, 1986.

45. R.T Pack and G.A. Parker, J. Chem. Phys., 87 (1987) 3888.

46. G.C. Schatz, Ann. Rev. Phys. Chem., 39 (1988) 317.

47. G.C. Schatz, in ref 44, p1 and references therein.

48. M. Baer and D.J. Kouri, in ref 44, p167, and references therein.

49. D.J. Kouri in ref 2, p301, and references therein

50. M. Baer, Adv. Chem. Phys., 49 (1982) 191

51. H.R. Mayne, Chem. Phys. Lett., 130 (1986) 249.

52. R.A. Marcus, J. Chem. Phys., 45 (1966) 4493.

53. R.A. Marcus, J. Chem. Phys., 49 (1968) 2610

54. F. London, Z. Electrochem, 35 (1929) 552

55. H. Eyring and M. Polanyi, Z. Phys. Chem. B, 12 (1931) 279

56. S. Sato, J. Chem. Phys., 23 (1955) 592

57. G.C. Schatz and J. Elgersma, Chem. Phys. Lett., 73 (1980) 21

58. O. Rashed and N.J. Brown, J. Chem. Phys., 82 (1985) 5506

59. R.P. Bell, "The Tunnel Effect in Chemistry", Chapman Hall, NY, 1980, p27

60. J.C.Polanyi and J.L.Schreiber, Faraday Disc. Chem. Soc., 62, (1977) 267

61. E.M. Mortensen, J. Chem. Phys., 48 (1968) 4029

62. J.C. Light, Meth. Comp. Phys., 10 (1971) 111

63. C.C. Rankin and J.C. Light, J. Chem. Phys., 51 (1969) 1701

64. G. Miller and J.C. Light, J. Chem. Phys., 54 (1971) 1635

65. S-F. Wu and R.D. Levine, Mol. Phys., 22 (1971) 881

66. J.C. Light in ref 2, p 467, and references therein

67. R.B. Walker and J.C. Light, Ann. Rev. Phys. Chem., 31 (1980) 401

68. A. Kuppermann, Chem. Phys. Lett., 32 (1975) 374

69. G.C. Schatz and A. Kuppermann, J. Chem. Phys., 65 (1976) 4642

70. A. Kuppermann, G.C. Schatz, and M. Baer, J. Chem. Phys., 65 (1976) 4596

71. D.G.Truhlar and C.J. Horowitz, J. Chem. Phys., 68 (1978) 2466; ibid. 71 (1979) 1514E

72. P. Siegbahn and B. Liu, J. Chem. Phys., 68 (1978) 2457

73. D.G. Truhlar and R.E. Wyatt, Ann. Rev. Phys. Chem., 27 (1976) 1, and references therein

74. D.J. Diestler, J. Chem. Phys., 54 (1971) 4547

75. G.C. Schatz and A. Kuppermann, J. Chem. Phys., 59 (1973)

946

76. J.W. Duff and D.G. Truhlar, Chem. Phys. Lett., 23 (1973) 327

77. Z. Top and M. Baer, Chem. Phys., 10 (1975) 95

78. R.I. Altkorn and G.C. Schatz, J. Chem. Phys., 72 (1980) 3337

79. G.C. Schatz, in ref 44, p1

80. D.C. Clary, Mol. Phys., 48 (1982) 618

81. P. McGuire and D.J. Kouri, J. Chem. Phys., 60 (1974) 2488

82. R.T. Pack, J. Chem. Phys., 60 (1974) 633

83. A.B. Elkowitz and R.E. Wyatt, Mol. Phys., 31 (1976) 189

84. A. Kuppermann, G.C. Schatz, and J. Dwyer, Chem. Phys. Lett., 45 (1977) 71

85. D. Secrest, J. Chem. Phys., 62 (1975) 710

86. J.M. Bowman and S.C. Leasure, J. Chem. Phys., 66 (1977) 288

87. G-D. Barg and G. Drolshagen, Chem. Phys., 47 (1980) 209

88. J.M. Bowman, J. Chem. Phys., 66 (1977) 296

89. J. Jellinek and M. Baer, J. Chem. Phys., 76 (1982) 4883

90. P.A.M. Dirac, "Aspects of Quantum Chemistry", ed. A. Salum and E.P. Wigner, Cambridge University Press, 1972, p137

91. A. Messiah, "Quantum Mechanics", North Holland Publishing Co., Amsterdam, 1970, p246

92. M.J. Redmon and R.E. Wyatt, Int. J. Quant. Chem., 11 (1977) 343

93. J.C. Light and R.B. Walker, J. Chem. Phys., 65 (1976) 4272

94. W.H. Press, B.P. Flannery, S.A. Teukolsky, W.T. Vetterling, in "Numerical Recipes. The Art of Scientific Computing", Cambridge University Press, 1986

95. M.E. Riley and A. Kuppermann, Chem. Phys. Lett., 1 (1968)

96. J.M. Bowman, Int. J. Quant. Chem., 13 (1979) 487

97. G. Drolshagen, Masters Thesis, Max-Planck Institut fur Stromungsforchung, 1979, p 50

98. IMSL Math Library, Routine FFTCF

99. R. Schinke and P. McGuire, Chem. Phys., 31 (1978) 391

100. H. Goldstein, "Classical Mechanics", Addison-Wesley Publishing Company, Inc., 1950, p 245

101. H.C. Corben and P. Stehle, "Classical Mechanics", second edition, John Wiley and Sons, Inc., 1950, p 156, 188-190

102. W.H. Miller, Adv. Chem. Phys., 30 (1975) 77

103. T. Mulloney and G.C. Schatz, Chem. Phys., 45 (1980) 213.

104. S. Green, Chem. Phys., 31 (1978) 425

105. T.P. Tsien, G.A. Parker, and R.T Pack, J. Chem. Phys., 59 (1973) 5373.

106. B.A. Blackwell, J.C. Polanyi, and J.J. Sloan, Chem. Phys., 30 (1978) 299

107. J.B. Anderson, Adv. Chem. Phys., 41, (1980) 229

108. H.F. Schaefer III, J. Phys. Chem., 89, (1985) 5336

109. J.H. Parker and G.C. Pimentel, J. Chem. Phys., 51, (1969) 91

110. T.D. Schafer, P.E. Siska, J.M. Parson, F.P. Tully, Y.C. Wong, and Y.T. Lee, J. Chem. Phys., 53, (1970) 3385

111. Y.T. Lee, Ber. Bunges. Phys. Chem., 86, (1982) 378

112. J.C. Polanyi and D.C. Tardy, J. Chem. Phys., 51, (1969) 5717

113. N. Jonathan, C.M. Melliar-Smith, and D.H. Slater, Mol. Phys., 20, (1971) 93

114. J.C. Polanyi and K.B. Woodall, J. Chem. Phys., 57, (1972) 1574

115. D.S. Perry and J.C. Polanyi, Chem. Phys., 12, (1976) 37, 12, (1976) 419

116. D.J. Douglas and J.C. Polanyi, Chem. Phys., 16, (1976) 1

117. F.S. Klein and A. Persky, J. Chem. Phys., 61, (1974) 2422

118. D.M. Neumark, A.M. Wodtke, G.N. Robinson, C.C. Hayden and Y.T. Lee, J. Chem. Phys., 82, (1985) 3045

119. D.M. Neumark, A.M. Wodtke, G.N. Robinson, C.C. Hayden, K. Shobatake, and Y.T. Lee, J. Chem. Phys., 82, (1985) 3067

120. R.L. Jaffe and J.B. Anderson, J. Chem. Phys., 54, (1971) 2224; J. Chem. Phys.,56, (1972) 682

121. J.T. Muckerman, J. Chem. Phys., 54, (1971) 1155

122. J.T. Muckerman, J. Chem. Phys., 56, (1972) 2997

123. J.T.Muckerman, in "Theoretical Chemistry", Vol 6A, ed. H.Eyring and D. Henderson, Academic Press, New York, 1981 1-77

124. R.L. Wilkins, J. Chem. Phys., 67, (1977) 5838

125. R.L. Wilkins, J. Chem. Phys., 57, (1972) 912

126. R.L. Wilkins, Mol. Phys., 28, (1974) 21

127. J.C. Polanyi and J.L. Schreiber, Chem. Phys. Lett., 29, (1974) 319

128. N.C. Blais and D.G. Truhlar, J. Chem. Phys., 58, (1973) 1090

129. D.G. Truhlar, B.C. Garrett, and N.C. Blais, J. Chem. Phys., 80, (1984) 232

130. R.B. Walker, N.C. Blais, and D.G. Truhlar, J. Chem. Phys., 80 (1984) 246

131. R.L. Wilkins, J. Phys. Chem., 77, (1973) 3081

132. S. Ron, M. Baer, and E. Pollak, J. Chem. Phys., 78, (1983) 4414

133. N.C. Blais and D.G. Truhlar, J. Chem. Phys., 76, (1982) 4490

134. G.C. Schatz, J.M. Bowman, and A. Kuppermann, J. Chem. Phys., 63, (1975) 674

135. M.J. Redmon and R.E. Wyatt, Chem. Phys. Lett., 63 (1979) 209

136. J.N.L. Connor, W. Jakubetz, and J. Manz, Mol. Phys., 35 (1978) 1301

137. S.L. Latham, J.F. McNutt, and R.E. Wyatt, J. Chem. Phys., 69 (1978) 3746

138. Y. Shan, B.H. Choi, R.T. Poe, and K.T. Tang, Chem. Phys. Lett., 57, (1978) 379

139. S.H. Suck, Chem. Phys. Lett., 77, (1981) 390

140. J.F. McNutt, M.J. Redmon, and R.E. Wyatt, J. Chem. Phys., 81, (1984) 1692

141. J. Romelt, Chem. Phys. Lett., 87, (1982) 259

142. J.M. Launay and M.L. Dourneuf, J. Phys. B, 15, (1982) L455

143. B. Lepetit, J.M. Launay, and M.L. Dourneuf, Chem. Phys., 106, (1986) 111

144. B. Lepetit, J.M. Launay, and M.L. Dourneuf, J. Phys. B, 19, (1986) 2779

145. M.J. Redmon and R.E. Wyatt, Int. J. Quant. Chem., 9 (1975) 403

146. J.M. Bowman, K-T Lee, and G-Z Ju, Chem. Phys. Lett., 86 (1982) 384

147. M. Baer, J. Jellinek, and D.J. Kouri, J. Chem. Phys., 78 (1983)

148. M. Baer and J. Jellinek, J. Chem. Phys., 78 (1983) 4494

149. J.L. Schreiber, Ph.D. Thesis, University of Toronto, 1977

150. H. Kornweitz, A. Persky, and R.D. Levine, Chem. Phys. Lett., 128, (1986) 443

151. H.R.Mayne and J.A.Harrison, Chem. Phys. Lett., 133, (1987) 185

152. N. Sathyamurthy and I. Noorbatcha, J. Am. Chem. Soc., 104, (1982) 1766

153. G-D. Barg, H.R. Mayne, and J.P. Toennies, J. Chem. Phys.,

74, (1981) 1017

154. H.R. Mayne and J.P. Toennies, J. Chem. Phys., 75, (1981) 1794

155. H.R. Mayne, Chem. Phys. Lett., 86, (1982) 33

156. S.P. Walch and T.H. Dunning, Jr., J. Chem. Phys., 72 (1980) 1303

157. G.C. Schatz and S.P. Walch, J. Chem. Phys., 72 (1980) 776

158. D.G. Truhlar and A.D. Isaacson, J. Chem. Phys., 77 (1982) 3516

159. A.D. Isaacson and D.G. Truhlar, J. Chem. Phys., 76 (1982) 1380

160. N.J. Brown and O. Rashed, J. Chem. Phys., 85 (1986) 4348

161. G.C. Schatz, J. Chem. Phys., 74 (1981) 1133

162. R.N. Porter, L.M. Raff, and W.H. Miller, J. Chem. Phys., 63 (1975) 2214 [NOTE: Error in equation (30b). The last term should be $-p_z\ r\ \sin(\theta)$ not $p_z\ r\ \cos(\theta)$.]

163. C.W. Eaker, J. Chem. Phys., 90 (1989) 105

164. H. Shull and G.G. Hall, Nature, 184 (1959) 1559

165. F. Pilar, "Elementary Quantum Chemistry", McGraw Hill Book Company, NY, 1968, p169

166. M. Baer, in ref 5, Volume I, p91

167. D.J. Kouri, in ref 5, Volume I, p163

168. N.F. Mott and H.S.W. Massey, "The Theory of Atomic Collisions", third edition, Clarendon Press, Oxford, 1965

169. H. Rabitz, J. Chem. Phys., 57 (1972) 1718

170. L.D. Thomas et. al., J. Compt. Phys., 41 (1981) 407

171. L.J. Isakson, B.A. Thesis, University of New Hampshire, 1989

172. R. Zellner, in "Combustion Chemistry", ed W.C. Gardiner, Jr., Springer, NY, 1984, p173

173. C.H. Townes and A.L. Schawlow, "Microwave Spectroscopy", McGraw Hill Book Company, NY, 1955, p49

174. W. Spindel, in "Isotopes and Chemical Principles", ed. P.A. Rock, ACS Symposium Series, No. 11, 1975, p77

175. R.V. Wagner, Astrophys. J., 179 (1973) 343

176. H.R. Mayne and S.S. Prasad, Int. J. Chem. Kinet., 18 (1986) 977

177. A. Persky, J. Chem. Phys., 70 (1979) 3910

178. R.W. Hamming, "Numerical Methods for Scientists and Engineers", second edition, Dover Publications, Inc., 1973, p383-406

179. W.R. Gentry, in ref 2, p395

180. H.R. Mayne, J. Chem. Phys., 73 (1980) 217

181. J.M. Bowman and K-T. Lee, Chem. Phys. Lett., 64 (1979) 291

182. IMSL Math Library, Routine FFTCB

183. The step function F(s) is given by: $F(s) = (1 - \tanh[a(|s| - 3)]/2)$

184. N. Sathyamurthy and T. Joseph, J. Chem. Ed., 61 (1984) 968

185. The functional form of the LEPS [60] is given by: $V(x_1,x_2,x_3) = \Sigma Q_i - (0.5 \Sigma_{i>j} (J_i - J_j)^2)^{1/2}$ where $Q(x_i) = 0.5[{}^1E(x_i) + {}^3E(x_i)]$, $J(x_i) = 0.5[{}^1E(x_i) - {}^3E(x_i)]$, ${}^1E(x_i) = {}^1DX(X-2)$, $X(x_i) = \exp[-{}^1\beta(x_i - x_e)]$, ${}^3E(x_i) = {}^3DX'(X'+2)$, $X'(x_i) = \exp[-{}^3\beta(x_i - x_e)]$, and ${}^3D = {}^1D(1-S)/2(1+S)$. The values ${}^1D$, β, S, and x_e are given in ref [60].